# DISSERTATION | DOCTORAL THESIS

Titel | Title

Distribution of Permian pegmatites and spodumene pegmatites in the Austroalpine Unit - geochemical and geochronological investigations

verfasst von | submitted by

Tanja Knoll BSc MSc

angestrebter akademischer Grad | in partial fulfilment of the requirements for the degree of

Doktorin der Naturwissenschaften (Dr.rer.nat.)

Wien | Vienna, 2024

| | |
|---|---|
| Studienkennzahl lt. Studienblatt \| Degree programme code as it appears on the student record sheet: | UA 796 605 426 |
| Dissertationsgebiet lt. Studienblatt \| Field of study as it appears on the student record sheet: | Erdwissenschaften |
| Betreut von \| Supervisor: | Ralf Schuster Privatdoz. |

*for mum, grandma and Lucia - my biggest role models*
*for all who joined and helped me during this journey*

*In geology, as in history, the material in hand remains silent if no questions are asked. The nature of these questions depends on the "school" to which the geologist belongs and on the objectivity of his investigations. Hans Cloos called this way of interrogation "the dialogue with the earth".*

*Reinout Willem van Bemmelen, geologist*

*In every outthrust headland, in every curving beach, in every grain of sand there is the story of the earth.*

*Rachel Carson, biologist*

*View towards Weiße Spitze and Hochalmspitze in Defereggental Valley, Defereggental pegmatite field, acrylic on canvas, Tanja Knoll („Tanja Knollić“), 2021*

## ACKNOWLEDGMENTS

I could not have undertaken this journey without my supervisor Dr. Ralf Schuster, and I would like to express my deepest appreciation to him for sharing his knowledge and experience in regional geology, petrography, mapping and geochronological investigation with me over the past years. I am extremely grateful to Dr. Heinrich Mali for the knowledge he has brought to the project and for his constant feedback. Without him and his diligence, we would never have been able to obtain this enormous amount of samples and data. I would like to express my deepest gratitude to Dr. Benjamin Huet. His skills in petrographic modeling have made this work what it is. I would also like to thank him for his guidance, constructive criticism, and many hours of writing and discussion.

I am deeply honored to have had the opportunity to learn over the past few years from the great mentors and scientists listed above. Each of them has a different expertise and working with them has helped me grow as a scientist and as a person. In addition to their professional contribution, they have always supported me mentally during difficult times.

My special thanks also go to my defense committee, who generously shared their knowledge and experience with me. Furthermore, this work would not have been possible without the financial support of the “Mineral and Raw Materials Initiative” of the Federal Ministry of Science, Research and Economy (BMWFW).

I would also like to thank Dr. Holger Paulick, Prof. Jürgen Konzett, Prof. Theodoros Ntaflos, and Prof. Rainer Abart for their continuous support and belief in our project and our work as well as to Prof. Richard Göd, Prof. Frank Melcher, Prof Axel Bernd Müller, Prof. Walter Pohl and Prof. Harald Dill for their constructive discussions and advice. My heartfelt thanks go to my colleagues from Geosphere Austria, Gerald Schuberth-Hlavac M.Sc., Mag. Christine Hörfarther, Dr. Christoph Iglseder and Mag. Julia Weilbold for their great moral support, their help with editing and proofreading and their inspiration. I would like to acknowledge the laboratory teams at the University of Vienna, the Montanuniversität Leoben, Geosphere Austria and the University of Graz for preparing our samples and measurements. Many thanks to my colleagues from the Department of Mineral Resources and Geoenergy not only for their suggestions and proposals, but also for their kindness and humanity over the years.

Finally, I would like to mention my family and friends, whose support has not let me down even in difficult situations and times. Above all, I am very grateful to my mother Sloba for her motivation and support in all situations and for being the best possible role model. Without her, I would not be the person I am today. I cannot express in words my gratitude to my husband Johann for his tireless support and motivation. Due to that I would like to thank my little daughter Lucia for showing me, through her childlike nature, not to always take things seriously and sometimes to let go. I would be remiss if I didn't mention Caro for her acceptance and support.

I am so grateful to have you all in my life and to be able to learn from you.

Thank you

## ABSTRACT

Lithium (Li) is a metal that has become essential in today's society and the demand for lithium is constantly rising. For this reason, small Li-deposits like spodumene pegmatite dikes in the Austroalpine Unit might become of economic importance in the future. This PhD-Thesis focuses on their investigation.

A database of pegmatites in the basement of the Austroalpine Unit has been developed building on the results of the MRI Peg I and Peg II projects, in the framework of a consortium driven by GeoSphere Austria (formerly Geological Survey of Austria) and the Montanuniversität Leoben. More than 1400 pegmatite bodies were documented and analyzed systematically with high-end chemical methods. This includes several newly found bodies of spodumene pegmatite. This allows a graphic representation of the fractionation trends over a large area and at different scales. New geochemical and geochronological investigation indicate a contemporaneous and cogenetic formation of simple pegmatites, fractionated pegmatites, spodumene pegmatites and leucogranites, whereby the spodumene pegmatites are most fractionated and occur in highest structural levels. Due to the field work and the resulting large number of samples (>1000) as well as the geochemical and geochronological investigations in the entire Austroalpine Unit, it was possible for the first time to classify individual pegmatite fields. Based on their contemporaneous and cogenetic formation, these fields were grouped into a pegmatite province and thus the Austroalpine Pegmatite Province (AUPP) was formulated. Fractionated pegmatites and spodumene pegmatites contain several minerals hosting critical trace elements, like cassiterite, columbite-tantalite, monazite, apatite and zircon. However, except spodumene the rarity of these minerals and their small grain size argue against their commercial use.

Additionaly, the genetic relationships between simple pegmatite, pegmatitic leucogranite, fractionated pegmatite and spodumene pegmatite and their host rocks has been investigated in a few key zones of the Austroalpine Unit Pegmatite Province. Using an approach integrating results from field work, geochronology, mineralogical and chemical analyses as well as geochemical modelling we developed a new genetic model for the formation of spodumene pegmatite. The melts crystallizing as spodumene pegmatite formed by anatexis of Al-rich, staurolite-bearing metapelites at metamorphic conditions of about 675°C and 6.45 kbar. In Permian time, these melts were primarily enriched in Li and fractional crystallization of simple granites and leucogranites increased the Li content up to 5,000-10,000 ppm, allowing spodumene to crystallize. This genetic model does not require large granite bodies genetically linked to the pegmatites, which are absent in the Austroalpine Unit. It suggests that metamorphic units with anatectic mica schists and paragneisses should also be taken into account when prospecting for spodumene pegmatites. The view that certain pegmatite types of the rare-element class represent anatectic formations without granitic “mother plutons” is currently spreading rapidly among experts, and the results on the pegmatites occurring in the Austroalpine Unit Pegmatite Province have accordingly received very positively.

## ZUSAMMENFASSUNG

Lithium ist ein Metall, das in der heutigen Gesellschaft unverzichtbar geworden ist, und die Nachfrage nach Lithium steigt ständig. Aus diesem Grund könnten kleine Lithiumvorkommen wie Spodumen-Pegmatite aus dem Ostalpinen Kristallin in Zukunft von wirtschaftlicher Bedeutung sein. Die vorliegende Dissertation beschäftigt sich mit deren Erforschung.

Aufbauend auf den Ergebnissen der Projekte MRI Peg I und Peg II wurde eine Datenbank der Pegmatite des Ostalpinen Kristallins entwickelt. Mehr als 1400 Pegmatitkörper wurden dokumentiert und systematisch mit chemischen High-End-Methoden analysiert. Darunter befinden sich auch mehrere neu gefundene Spodumen-Pegmatite. Dies ermöglicht auch eine graphische Darstellung der Fraktionierung über ein großes Gebiet und auf verschiedenen Skalen. Neue geochemische und geochronologische Untersuchungen deuten auf eine zeitgleichen und kogenetische Bildung von Pegmatiten, fraktionierten Pegmatiten, Spodumenpegmatiten und Leukograniten hin, wobei die Spodumenpegmatite am stärksten fraktioniert sind. Aufgrund der Kartierung und der daraus resultierenden großen Anzahl von Proben (>1000) sowie der geochemischen und geochronologischen Untersuchungen im gesamten Ostalpinen Kristallin war es erstmals möglich, einzelne Pegmatitfelder zu klassifizieren. Aufgrund der zeitgleichen und kogenetischen Bildung wurden diese Felder zu einer Pegmatitprovinz zusammengefasst und somit die Austroalpine Pegmatitprovinz (AUPP) definiert.

Die fraktionierten Pegmatite und Spodumen-Pegmatite enthalten verschiedene Minerale mit kritischen Spurenelementen wie Kassiterit, Kolumbit-Tantalit, Monazit, Apatit und Zirkon. Das seltene Vorkommen dieser Minerale im Gestein und ihre geringe Korngröße sprechen aber gegen eine wirtschaftliche Nutzung.

Im Rahmen dieser abgeschlossenen Projekte wurde der Fraktionierungsgrad von spodumenfreien Pegmatiten umfassend untersucht und es wurden mehrere neue Spodumen-Pegmatite gefunden. Darüber hinaus wurden die genetischen Beziehungen von einfachen Pegmatiten, pegmatitischen Leukograniten, fraktionierten Pegmatiten und Spodumen-Pegmatiten zueinander und zu ihren jeweiligen Muttergesteinen herausgearbeitet. Mineralogische und chemische Analysen deuten darauf hin, dass die Schmelzen der Spodumen-Pegmatite durch Anatexis von Al-reichen, staurolithhaltigen Metapeliten bei metamorphen Bedingungen von etwa 675°C und 6,45 kbar entstanden sind. Diese Schmelzen waren in erster Linie mit Li angereichert, und die fraktionierte Kristallisation von einfachen Pegmatiten und Leukograniten erhöhte den Li-Gehalt auf 5000-10000 ppm und ermöglichte die Kristallisation von Spodumen. Dieses genetische Modell setzt keine großen Granitkörper voraus, die genetisch mit den Pegmatiten verbunden sind, welche in den ostalpinen Einheiten auch nicht vorhanden sind. Es legt nahe, dass auch metamorphe Einheiten mit anatektischen Glimmerschiefern und Paragneisen bei der Suche nach Spodumen-Pegmatiten berücksichtigt werden sollten. Die Ansicht, dass es sich bei bestimmten Pegmatit-Typen der Seltene-Elemente-Klasse um anatektische Bildungen ohne granitische "Mutterplutone" handelt, verbreitet sich derzeit in der Fachwelt rasant, und die Ergebnisse zu den in der Austroalpine Unit Pegmatite Province (AUPP) vorkommenden Pegmatiten wurden dementsprechend sehr positiv aufgenommen.

## TABLE OF CONTENT

# 1. INTRODUCTION

## 1.1. INITIAL SITUATION AND GENERAL REMARKS

In recent years, interest in lithium (Li) deposits has risen sharply due to the growing demand for lithium-ion batteries. In Austria, several pegmatites are known to contain the Lithium-bearing pyroxene spodumene ($LiAl(SiO_3)_2$). As a result, prospecting for Lithium in Austria has become a high priority in recent years. For this reason, the projects MRI Peg I (2015-2018) and MRI Peg II (2019-2023), in the course of which this dissertation was written, were funded as part of the "Mineral und Rohstoffinitiative" (MRI) of the Bundesministerium für Wissenschaft, Forschung und Wirtschaft (BMWFW) and were based at the Geosphere Austria (formerly Geological Survey of Austria). I made the present PhD thesis in this framework.

It should be noted that the peer-reviewed publications (Chapters 2-4) as well as the published field trip guide (Chapter 5) have not been changed in terms of content or editorial. Only the font and font size have been adjusted. To make the text better readable the tables in Chapters 3 and 4 have been placed at the end of the respective article.

### 1.1.1. PERSONAL AIM

It has always been assumed that the genesis of the Permian pegmatites of the Austroalpine Unit are related to large granite plutons, following the classical model of Černý & Ercit, (2005). However, mapping and geochronological analyses in the last decades have shown a regional geological and time discrepancy between possible parent plutons and pegmatites. In parallel, new investigations at international scale showed that rare element pegmatites could crystallize from melts deriving from partially molten metasediments, so called pegmatites of anatectic origin (f.e. Melleton et al., 2012; Dill, 2016; Simmons et al., 2016; Kaeter et al., 2018; Barros et al., 2020; Fei et al., 2020). Hence emerged the theory of an anatectic origin for the Permian pegmatites in the Austroalpine Unit. In this framework and based on published data and own field observations, Dr. Ralf Schuster developed the idea for the MRI Peg I project, which we wrote together and which became the basis of my PhD project. The project team was completed by Dr. Heinrich Mali from the Montanuniversität of Leoben and Dr. Konstantin Petrakakis and Monika Horschinegg from the University of Vienna. The aims of the project were (1) to find unknown rare-element pegmatites, (2) to use geochemical "fingerprints" to investigate the distribution of differently fractionated pegmatites across various nappes of the Austroalpine Unit and (3) to develop a model for the genesis of spodumene pegmatites formed in Permian times.

The project was successfully completed in 2018. Over 800 pegmatites have been collected and analyzed. In addition, three new spodumene pegmatites were found and known occurrences were expanded. This also resulted in the publication Knoll et al. 2018 (Chapter 3). The notion that the genesis of the Permian pegmatites is anatectic became increasingly apparent. With the help of Dr. Benjamin Huet, who replaced Dr. Konstantin Petrakakis in the course of the project, the first geochemical model showing the plausibility of an anatectic origin was also carried out. The results were presented at numerous conferences. As international interest in the pegmatites of the Austroalpine Unit Pegmatite Province (AUPP) has increased significantly, Dr. Ralf Schuster and me also organized and hosted an excursion during the EGU 2019. An excursion guide was also published as part of this (Chapter 5).

I subsequently wrote and submitted the MRI Peg II project with the help of Dr. Ralf Schuster. This project has been granted since (1) the project MRI Peg I was able to generate large amounts of data and answer many questions, (2) the project team was very well coordinated, (3) the interest of the international pegmatite community was very high (4) the work also raised open questions and (5) a synthesis paper presenting the new genetic model remained to be published. In the course of this second project, Dr. Jürgen Konzett from the University of Innsbruck joined the team. The MRI Peg II project built on the results of the completed MRI Peg I project. The

main objectives were to complete the area-wide sampling of pegmatite-bearing units to determine the distribution of the degree of fractionation and to refine and publish the model for anatectic genesis. Among other objectives, both the important goals for this PhD thesis of completing the sampling and the paper on anatectic genesis (Knoll et al., 2023, Chapter 4) were successfully completed.

#### 1.1.2. DISSERTATION OBJECTIVES

The main objectives of the dissertation were (1) to analyse white mica systematically, to use the results as geochemical "fingerprints" and to investigate the distribution of differently fractionated pegmatites across various geological units within the Eastern Alps, (2) to find additional rare-element pegmatites and (3) to develop a model for the genesis of Permian spodumene pegmatites in the Austroalpine Unit.

#### 1.1.3. METHODS

Following methods were used mainly during this research: Scanning Electron Microscope (SEM), Electron Probe Micro Analyser (EPMA), Laser Ablation ICP-MS (LA ICP-MS), Whole Rock Geochemistry and Sm-Nd and Rb-Sr Geochronology. A more detailed description of the methods applied can be found in chapters 3-4 and in the Appendix.

#### 1.1.4. DESCRIPTION OF THE COOPERATION SYNERGIES

As the projects were based at the GeoSphere Austria (formerly the Geological Survey of Austria) and I also led the Peg II project, the scientific expertise of Geosphere Austria in the field of "battery metals" has been deepened and expanded. The strengthening of basic research as a goal of the Austrian RTI strategy was covered by the networked cooperation with other institutions. The proven cooperation with partners from the Montanuniversität Leoben and the University of Innsbruck ensured the scientific expertise in the field of raw materials geology. This cooperation and networking made it possible to use the research infrastructure of the Geosphere Austria, the University of Vienna, the Montanuniversität Leoben and the University of Innsbruck. In addition, there has been cooperation synergies with the University of Graz (LA ICP-MS and microprobe measurements). The skills and competencies in the field of pegmatite research have also been expanded and a scientific, national and international comprehensive platform and a working group for future projects has been formed.

### 1.2. RAW MATERIALS POLICY SITUATION

In recent years, the demand for decentralized electrical storage capacities such as lithium-ion batteries has risen sharply (Tabelin et al., 2021). It is expected that the demand for Li will continue to increase rapidly in the coming years (Fig. 1). Corresponding price increases for lithium carbonate are also reflected in rising exploration activity (Fig. 1). Currently, Lithium is mainly extracted from brines of salt lakes in South America and pegmatites in Australia (Kesler et al., 2012). Exploration activities are widely dispersed globally (SP Global, 2017) and even smaller deposits have the potential to play an important role in the future. In this sense, the geological framework conditions for a European "local supply" of lithium are a fundamental issue for the development of a sustainable energy future. In Europe, there are several deposits of pegmatites that, in addition to lithium, may also contain other special metals that are classified as critical by the European Union (Mancheri et al., 2018; Mackay & Simandl, 2015; European Commission, 2017). Hence, Li-bearing pegmatites are currently being explored in Spain, Portugal, Ireland, Finland, Serbia, Bosnia and Hercegovina and Austria. Spodumene pegmatite of the Weinebene deposit in the Koralpe Mountains (Carinthia) have been known since the 1980s. The $Li_2O$ content is approximately 1.6 wt% and the indicated resources amount

to >200,000 t $Li_2O$ (Göd, 1989). In addition, almost all of Austria's other spodumene pegmatite deposits have been covered with exploring permission in the past three years.

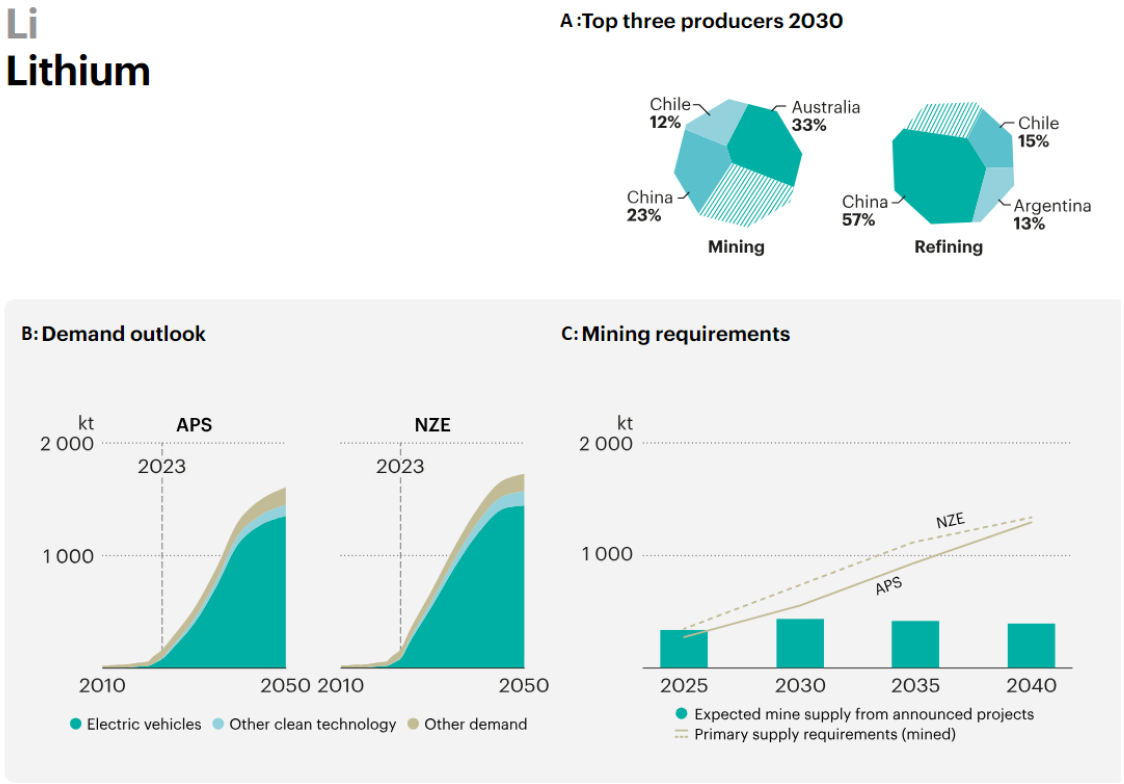


*Figure 1: Forcast of different Lithium demand scenario (IEA, 2024, Lithium, IEA, Paris https://www.iea.org/reports/lithium). A: The top three producers in mining are expected to be Australia, China and Chile, whereas the top three producers in 2030 for refining are expected to be mainly China, Chile and Argentina. B: Due to the increasing importance of electrical storage capacities, the primary supply requirement for lithium is C: forcasted to double in both the Net Zero Scenario (NZE) and the Announces Pledges Scenario (APS).*

### 1.3. GENESIS MODELS AND CLASSIFICATION OF PEGMATITES

Two competing models are currently used to explain the formation of Li-rich pegmatites, often classified as LCT pegmatites (lithium-cesium-tantalum pegmatites). The widely accepted model assumes that rare element-containing pegmatite bodies with economic concentrations of Li and additional Cs, Be, Ta and Nb originate from large fertile granite intrusions through fractionation, immiscibility of the melt and enrichment with volatiles (Černý, 1991; Černý et al. 2012; London 2008). In this model, pegmatite swarms ideally occur concentrically around the overriding intrusion, with the degree of fractionation, concentration of volatile elements and complexity of zonation increasing at higher structural levels (Černý, 1991). Exploration projects are therefore focused on areas that offer corresponding geological conditions. This classical genetic model is challenged by a model in which anatexis plays an important role. Melting of low-percentage Li-rich metasediments can produce Li-rich melts, presumably at lower temperatures than those of the solidus in Li-absent systems (Stewart, 1978). This alternative model can explain the formation of Li-rich pegmatite bodies that (1) are not contemporaneous or genetically linked to a neighboring fertile granite, (2) occur in close temporal and spatial relation to anatectic metasediments and (3) share important geochemical patterns with anatectic melts. Stewart´s alternative model was long considered as not plausible (Černý, 1991). Černý´s arguments against an anatectic model are therefore addressed and discussed in the chapter “Discussion of the arguments against the anatectic model” of this work. In recent years more and more studies postulated the anatectic formation of pegmatite melts and the crystallization of certain types of

rare-element pegmatites without the presence of large-scale granitic plutons (e.g. Simmons & Webber, 2008; Simmons et al., 2016; Müller et al., 2017; Konzett et al., 2018).

Pegmatites are coarsely crystalline dykes of magmatic rocks (Le Maitre et al., 2002). The main minerals of granitic pegmatites are alkali feldspar, plagioclase, quartz and mica and the overall rock composition is alkali granitic to granitic. Depending on the degree of fractionation and the content of rare elements, other minerals of economic importance may be present (London, 2008). Numerous classification schemes can be found in the literature (Müller et al., 2018, Wise et al., 2022). According to Černý & Ercit (2005), granitic pegmatites are divided into the LCT (Li, Cs, Ta) and NYF (Nb, Y, F) families. In this classification, these groups derive from S-type and A-type granites respectively. Furthermore, there are five classes that differ in their mineralogical composition and intrusion level. The melts of the abyssal and muscovite class are formed by partial anatexis in granulite-facies, eclogite-facies and amphibolite-facies rock units and can intrude into higher crustal levels. The muscovite rare element class represents a link to the rare element class, whereby pegmatites of the latter class are formed by fractional crystallization of granitic parent plutons. These pegmatites often contain minerals containing Li, Rb, Cs, Be, Ga, SEE, Sn, Ti, U, Th, Hf, Nb, and Ta. Some types and subtypes of this class contain spodumene and/or other Li-bearing minerals such as petalite ($LiAl(Si_4O_{10})$), lepidolite ($K(Li_{1.5}Al_{1.5})(AlSi_3O_{10})(F,OH)_2$) and elbaite ($Na(Li_{1.5}Al_{1.5})Al_6(Si_6O_{18})(BO_3)_3(OH)_3(OH)$). Miarolitic pegmatites are characterized by the occurrence of druse cavities. They are formed in shallow, greenschist-facies crustal levels from all other classes of granitic pegmatites (London, 2008).

### 1.4. Problem definition and preliminary work of the Austroalpine Unit Pegmatite Province

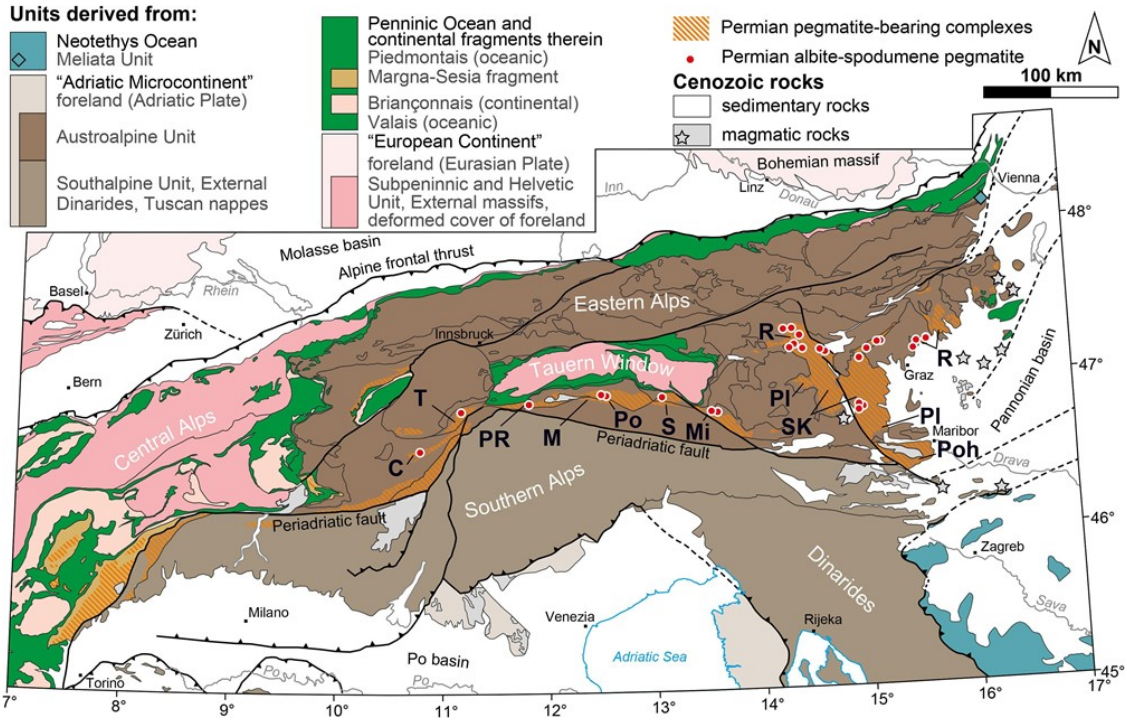


*Figure 2. The Austroalpine Unit pegmatite province with pegmatite-bearing lithostratigraphic complexes and albite-spodumene pegmatite occurrences shown on a simplified tectonic map of the Eastern Alps (modified after Knoll et al., 2018). The lithostratigraphic complexes mentioned in the text and figures are located on the map: C (Campo Complex), M (Michelbach Complex), Mi (Millstatt Complex), Pl (Plankogel Complex), Po (Polinik Complex), Poh (Pohorje area), PR (Petzeck-Rothenkogel Complex), R (Rappold Complex), S (Strieden Complex), SK (Saualpe-Koralpe Complex) and T (Texel Complex). Notice that a few complexes occur in different geographic localities as part of different nappes due to the complex alpine tectonics.*

### 1.4.1. Regional geology and distribution of Permian spodumene pegmatites in the Eastern Alps

Permian pegmatites are widespread in the eastern Alps over an E-W extension of approximately 400 km (Fig. 2).They are common in some complexes with aluminosilicate-bearing, migmatic mica schists and paragneisses and staurolite-rich mica schists, while they are absent in others. The mineralogy and intrusive contacts of the pegmatites were overprinted by deformation and metamorphism to varying degrees during the Eoalpine Event. In less overprinted areas (e.g. Kreuzeck Group, Carinthia), the andalusite and sillimanite formed during the Permian high temperature/low pressure (HT/LP) metamorphism is well preserved (Hoke, 1990; Fig. 3A, B, C), while in other areas (Niedere Tauern, Styria) these minerals have been transformed to kyanite (Schuster et al., 2001). Signs of local anatexis are present in the structurally deepest, sillimanite-bearing parts (Fig. 3D). There are networks of mm- to cm-thick feldspar-quartz veins (Fig. 3E), irregularly shaped and often diffusely bounded pegmatitic neosomes and isolated sprouting muscovite porphyroblasts up to 3 cm in size (Fig. 3F).

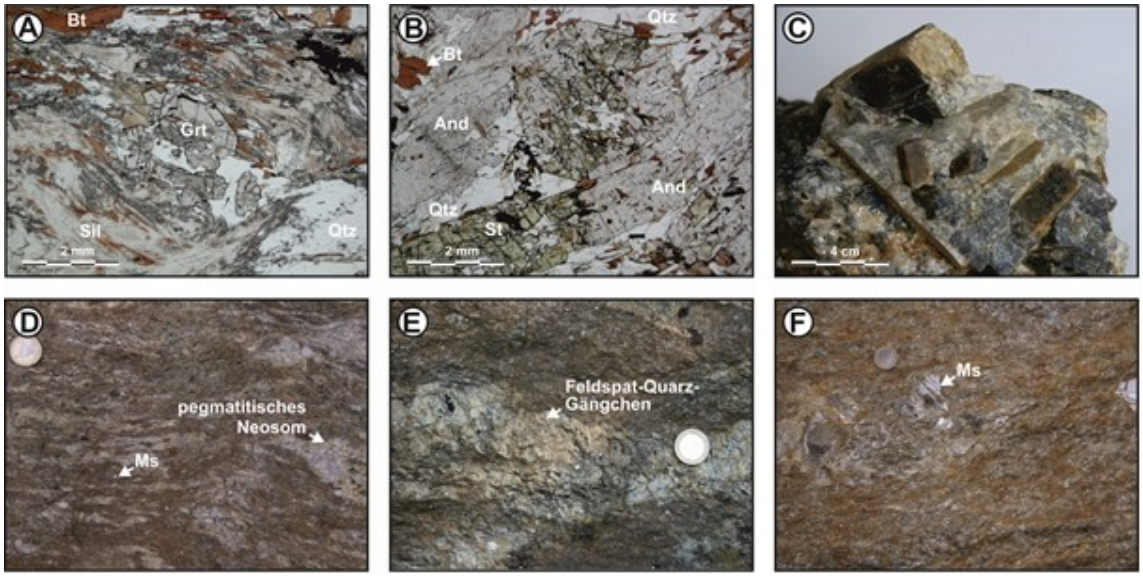


*Figure 3: A-B thin sections of metapelites from the Kreuzeck Mountains (Carinthia): A) Variscan garnet overgrown by Permian sillimanite, B) Variscan staurolite displaced by Permian andalusite; C) Idiomorphic andalusite in a vein with quartz, albite and white mica (Kreuzeck Group, Carinthia). D-F: Lithologies from the Rappold Complex (Niedere Tauern, Styria): D) migmatic paragneiss with muscovite several millimeters in size and pegmatitic neosome of quartz + feldspar ± muscovite ± tourmaline; E) feldspar-quartz vein; F) cm-sized muscovite in migmatic mica schist.*

### 1.4.2. Characterization of the Permo-Triassic event in the Austroalpine Unit

The Permian pegmatites were formed during the Permo-Triassic event, which can be attributed to stretching of the lithosphere (Habler & Thöni, 2001; Gaidies et al., 2006; Schuster & Stüwe, 2008). Due to this stretching, basaltic melts formed in the mantle, which accumulated close to the Moho discontinuity (magmatic underplating) and caused an increased heat flow and high-temperature/low-pressure metamorphism in the lower crust. This led to the melting of metapelites under amphibolite to granulite-facies metamorphic conditions at lower crustal levels. S-type melts were formed and they crystallized in some units at lower crustal levels as simple pegmatites (without significant enrichment of rare elements), leucogranites, evolved pegmatite and spodumene pegmatites. In other units, granodiorites and granites were formed at mid-crustal levels (Fig. 4). Acidic to intermediate volcanics were predominantly formed on the earth's surface. The slow cooling of the lithosphere during the Triassic resulted in continuous subsidence and the deposition of Triassic sediments up to 3000 m in thickness (Schuster & Stüwe, 2008).

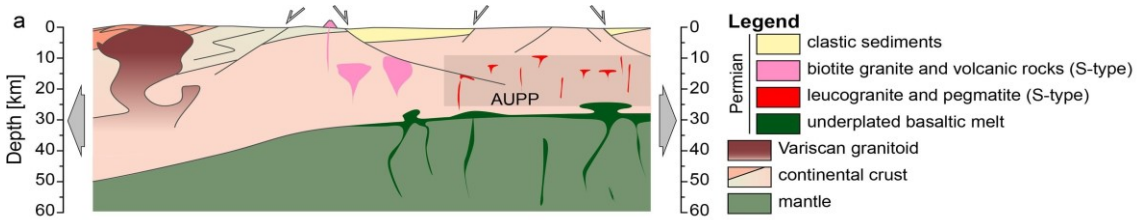


*Figure 4: Geodynamic situation during the Permo-Triassic Event (adapted after Knoll et al., 2023/Chapter 4)*

### 1.4.3. Mineralogy of pegmatites, leucogranites and spodumene pegmatites in the Austroalpine Unit

The main mineral composition of simple pegmatites and leucogranites includes potassium feldspar, albite, quartz and, to a lesser extent, muscovite, black tourmaline and garnet. Accessory minerals include biotite, cassiterite, columbite-tantalite, monazite, apatite and zircon (Mali, 2004; Ertl et al., 2010; Chapter 3). Simple pegmatites are on average 2 m thick, occur concordantly with the existing schistosity even in areas weakly overprinted by Eoalpine deformation and show no or only weak zonation (Chapter 4). The leucogranites with a thickness of 50 to several hundred meters are heterogeneous, with fine-grained, aplitic and coarse-grained, pegmatitic parts. Quartz, feldspar and muscovite are the main minerals in higher fractionated pegmatites and spodumene pegmatites. Accessory minerals are garnet, tourmaline and beryl. Depending on the zoning, spodumene contents of up to approximately 30 percent by volume are present in spodumene pegmatites. Holmquistite $(Li_2)(Mg_3Al_2)(Si_8O_{22})(OH)_2$ and liddicoatite $(Ca(Li_2Al)Al_6(Si_6O_{18})(BO_3)_3(OH)_3(OH))$ occur as further lithium minerals in subordinate form. Pollucite $((Cs,Na)_2(Al_2Si_4O_{12})\ 2H_2O)$ has been observed very rarely as inclusions in spodumene (Mali, 2004). In addition, cassiterite $(SnO_{2)}$, columbite-tantalite group minerals, fersmite $((Ca,Ce,Na)(Nb,Ta,Ti)_2(O,OH,F)_{6)}$, pyrochlore group minerals, apatite $(Ca_5(PO_4)_3(Cl/F/OH))$, allanite group minerals, chrysoberyl $(BeAl_2O_4)$, elbaite, galena (PbS), monazite $(REE(PO_4))$, pyrite $(FeS_2)$, uraninite $(UO_2)$, xenotime $(Y(PO_4))$, zircon $(Zr(SiO_4))$ and aeschynite group minerals occur accessory in evolved pegmatites and spodumene pegmatites (Niedermayr & Göd, 1992; Mali, 2004; Ahrer, 2014; Chapter 3). The thickness is between 0.5 and 12 m. Spodumene forms crystals up to 41 cm long (Niedermayr & Göd, 1992; Mali, 2004; Ahrer, 2014; Chapter 3).

### 1.4.4. Rock chemistry, mineral chemistry and radiometric age dating

In general, pegmatites have high $SiO_2$ (70-75 wt%) and $Al_2O_3$ contents (14-22 wt%) with low contents of $TiO_2$, FeO, MgO, MnO and CaO. $Na_2O$ and $K_2O$ vary ($Na_2O+K_2O$ = 5.0-11.4 wt%), with $Na_2O/K_2O$ ratios mostly larger than 1 (Stöckhert, 1987; Göd, 1989; Niedermayr & Göd, 1992; Mali, 2004; Ahrer, 2014). Most simple pegmatites contain 5-30 ppm Li, which corresponds approximately to the concentration in the continental crust (~20 ppm; Gao et al., 1998). Muscovites in simple pegmatites can contain up to 500 ppm Li (Koller et al., 1983). The Rb and Sr contents of the pegmatites are variable, but the Rb/Sr ratios are generally high (3.5-84; Mali, 2004; Stöckhert, 1987). The initial Sr and Nd isotope ratios of the simple pegmatites and spodumene pegmatites are largely the same (87Sr/86Sr = 0.707-0.720; 143Nd/144Nd = 0.512-0.523). Radiometric age dating ranges between 225 and 280 Ma (Thöni & Miller, 2000; Schuster et al., 2001; Thöni et al., 2008; Habler et al., 2007).

## 1.5. REFERENCES


Ahrer, S. (2014). Geowissenschaftliche und aufbereitungstechnische Untersuchungen an ausgewählten Pegmatiten und deren Nb-Ta-Vererzungen in den Ostalpen, Steiermark, Österreich. Unveröffentlichte Masterarbeit, Montanuniversität Leoben: 105 S.

Barros, R., Kaeter, D., Menuge, J. F., & Škoda, R. (2020). Controls on chemical evolution and rare element enrichment in crystallising albite-spodumene pegmatite and wallrocks: Constraints from mineral chemistry. Lithos, 352, 105289.

Černý, P., 1991. Rare-element granitic pegmatites. Part I: Anatomy and internal evolution of pegmatite deposits. Geoscience Canada. 18(2), 49-67.

Černý, P., & Ercit, T. S. (2005). The classification of granitic pegmatites revisited. The Canadian Mineralogist, 43(6).

Černý, P., Halden, N.M., Ferreira, K., Meintzer, R.E., Brisbin, W.C., Chackowsky, L.E., Corkery, M.T., Longstaffe, F.J., Trueman, D.L., 2012. Extreme fractionation and deformation of the leucogranite-pegmatite suite at Red Cross Lake, Manitoba, Canada. II. Petrology of the leucogranite and pegmatite. Canadian Mineralogist. 50, 1807–1822.

Dill, H.G., 2016. The CMS classification scheme (Chemical composition-Mineral assemblage-Structural geology)-linking geology to mineralogy of pegmatitic and aplitic rocks. Neues Jahrbuch für Mineralogie-Abhandlungen. 193, 231–263.

Ertl, A., Mali, H., Schuster, R., Körner, W., Hughes, J. M., Brandstätter, F., & Tillmanns, E. (2010). Li-bearing, disordered Mg-rich tourmaline from a pegmatite-marble contact in the Austroalpine basement units (Styria, Austria). Mineralogy and Petrology, 99, 89-104.

Fei, G., Menuge, J. F., Li, Y., Yang, J., Deng, Y., Chen, C., Yang, Y., Yang, Z., Qin, L., Zheng, L., Tang, W., 2020. Petrogenesis of the Lijiagou spodumene pegmatites in Songpan-Garze Fold Belt, West Sichuan, China: Evidence from geochemistry, zircon, cassiterite and coltan U-Pb geochronology and Hf isotopic compositions. Lithos. 364, 105555.

Gaidies, F., Abart, R., De Capitani, C., Schuster, R., Connolly, J. A. D., & Reusser, E. (2006). Characterization of polymetamorphism in the Austroalpine basement east of the Tauern Window using garnet isopleth thermobarometry. Journal of Metamorphic Geology, 24(6), 451-475.

Göd, R. (1989). The spodumene deposit at “Weinebene”, Koralpe, Austria. Mineralium Deposita, 24, 270-278.

Habler, G., Thöni, M., & Miller, C. (2007). Major and trace element chemistry and Sm–Nd age correlation of magmatic pegmatite garnet overprinted by eclogite-facies metamorphism. Chemical Geology, 241(1-2), 4-22.

Hoke, L., 1990. The Altkristallin of the Kreuzeck Mountains, SE Tauern Window, Eastern Alps; basement crust in a convergent plate boundary zone. Jahrbuch der Geologischen Bundesanstalt. 133(1), 5-87.

Kaeter, D., Barros, R., Menuge, J.F., Chew, D.M., 2018, The magmatic-hydrothermal transition in rare-element pegmatites from southeast Ireland: LA-ICP-MS chemical mapping of muscovite and columbite-tantalite: Geochimica et Comochimica Acta, v. 240, p. 98–130.

Kesler, S. E., Gruber, P. W., Medina, P. A., Keoleian, G. A., Everson, M. P., & Wallington, T. J. (2012). Global lithium resources: Relative importance of pegmatite, brine and other deposits. Ore geology reviews, 48, 55-69.

Koller, F., Götzinger, M. A., Neumayer, R., & Niedermayr, G. (1983). Beiträge zur Mineralogie und Geochemie der Pegmatite des St. Radegunder Kristallins und der Gleinalpe. Archiv für Lagerstättenforschung der Geologischen Bundesanstalt, 3, 47-65.

Konzett, J., Schneider, T., Nedyalkova, L., Hauzenberger, C., Melcher, F., Gerdes, A., & Whitehouse, M. (2018). Anatectic granitic pegmatites from the Eastern Alps: A case of variable rare-metal enrichment during high-grade regional metamorphism–I: Mineral assemblages, geochemical characteristics, and emplacement ages. The Canadian Mineralogist, 56(4), 555-602.

Le Maitre, R.W. (ED .) (2002): Igneous rocks. A classification and glossary of terms, 2 nd edition. Cambridge University Press, Cambridge: 236 pp.

London, D. (2008). Pegmatites, the Canadian mineralogist, special publication 10, the mineralogical association of Canada.

Mackay, D. A. R., & Simandl, G. J. (2015). Niobium and tantalum: Geology, markets, and supply chains. In Symposium on critical and strategic materials. British Columbia Geological Survey Paper (Vol. 3, p. 13).

Mali, H. (2004). Die Spodumenpegmatite von Brettstein und Pusterwald (Wölzer Tauern, Steiermark, Österreich). Joannea-Mineralogie, 2, 5-53.

Mancheri, N. A., Sprecher, B., Deetman, S., Young, S. B., Bleischwitz, R., Dong, L., Kleijn, R. & Tukker, A. (2018). Resilience in the tantalum supply chain. Resources, Conservation and Recycling, 129, 56-69.

Mathieux, F., Ardente, F., Bobba, S., Nuss, P., Blengini, G. A., Dias, P. A., ... & Solar, S. (2017). Critical raw materials and the circular economy. Publications Office of the European Union: Bruxelles, Belgium.

Melleton, J., Gloaguen, E., Frei, D., Novak, M., Breiter, K., 2012. How are the emplacement of rare-element pegmatites, regional metamorphism and magmatism interrelated in the Moldanubian Domain of the Variscan Bohemian Massif, Czech Republic. Canadian Mineralogist. 50, 1751–1773.

Müller, A., Romer, R. L., & Pedersen, R. B. (2017). The Sveconorwegian pegmatite province–thousands of pegmatites without parental granites. The Canadian Mineralogist, 55(2), 283-315.

Müller, A., Simmons, W., Beurlen, H., Thomas, R., Ihle, P.M., WISE, M., RODA -ROBLES, E., Neiva, A.M.R. & Zagorsky, V. (2018). A proposed new mineralogical classification system for granitic pegmatites – Part 1: history and the need for a new classification. The Canadian Mineralogist, 56: 1-25.

Niedermayer, G. & Göd, R. (1992): Das Spodumenvorkommen auf der Weinebene und seine Mineralien. Carinthia II, 182/102: 21-35.

Schuster, R., Scharbert, S., Abart, R., & Frank, W. (2001). Permo-Triassic extension and related HT/LP metamorphism in the Austroalpine–Southalpine realm. Mitt. Ges. Geol. Bergbaustud. Österr, 45, 111-141.

Schuster, R., & Stüwe, K. (2008). Permian metamorphic event in the Alps. Geology, 36(8), 603-606.

Simmons, W. B. S., & Webber, K. L. (2008). Pegmatite genesis: state of the art. European Journal of Mineralogy, 20(4), 421.

Simmons, W., Falster, A., Webber, K., Roda-Robles, E., Boudreaux, A. P., Grassi, L. R., & Freeman, G. (2016). Bulk composition of Mt. Mica pegmatite, Maine, USA: Implications for the origin of an LCT type pegmatite by anatexis. The Canadian Mineralogist, 54(4), 1053-1070.

Stöckhert, B. (1987). Das Uttenheimer Pegmatit-Feld (Ostalpines Altkristallin, Südtirol). Genese und alpine Überprägung.

Stewart, D. B. (1978). Petrogenesis of lithium-rich pegmatites. American Mineralogist. 63, (9-10), 970-980.

Tabelin, C. B., Dallas, J., Casanova, S., Pelech, T., Bournival, G., Saydam, S., & Canbulat, I. (2021). Towards a low-carbon society: A review of lithium resource availability, challenges and innovations in mining, extraction and recycling, and future perspectives. Minerals Engineering, 163, 106743.

Thöni, M., & Miller, C. (2000). Permo-Triassic pegmatites in the eo-Alpine eclogite-facies Koralpe complex, Austria: age and magma source constraints from mineral chemical, Rb–Sr and Sm–Nd isotope data. Schweizerische Mineralogische und Petrographische Mitteilungen, 80(2), 169-186.

Thöni, M., Miller, C., Zanetti, A., Habler, G., & Goessler, W. (2008). Sm–Nd isotope systematics of high-REE accessory minerals and major phases: ID-TIMS, LA-ICP-MS and EPMA data constrain multiple Permian–Triassic pegmatite emplacement in the Koralpe, Eastern Alps. Chemical Geology, 254(3-4), 216-237.

Wise, M. A., Müller, A., & Simmons, W. B. (2022). A proposed new mineralogical classification system for granitic pegmatites. The Canadian Mineralogist, 60(2), 229-248.

## 2. Die Genese der permischen Lithium-Pegmatite des Ostalpinen Kristallins

*Tanja Knoll[1], Ralf Schuster[1], Heinrich Mali[2] & Benjamin Huet[1]*

*[1]Geologische Bundesanstalt, Neulinggasse 38, 1050 Wien*

*[2]Montanuniversität Leoben, Peter-Tunnerstraße 5, 8700 Leoben*

*Corresponding author: tanja.knoll@geologie.ac.at*

---

➔ *Manuscript status: no open access publication*
➔ *Berg-und hüttenmännische Monatshefte 2021, Volume 166, pages 175–180; https://doi.org/10.1007/s00501-021-01093-3*
➔ *Published: 04.03.2021*

---

ZUSAMMENFASSUNG

Lithium ist ein Metall, das in der heutigen Gesellschaft unverzichtbar geworden ist und dessen Bedarf weiter steigt. Dadurch könnten in Zukunft auch kleinere Lagerstätten, wie die Spodumen-Pegmatite im Ostalpinen Kristallin eine wirtschaftliche Bedeutung erlangen. Diese Pegmatite entstanden im Perm, während eines temperaturbetonten Metamorphoseereignisses. Detaillierte mineralogische und chemische Analysen sprechen dafür, dass die Schmelzen der Spodumen-Pegmatite durch Anatexis von Al-reichen, Staurolith-führenden Metapeliten, bei Metamorphosebedingungen von ca. 675°C und 6,45 kbar gebildet wurden. Diese Schmelzen waren primär an Li angereichert und durch fraktionierte Kristallisation von einfachen Graniten und Leukograniten erhöhte sich der Li-Gehalt auf über 7000 ppm, sodass letztendlich Spodumen kristallisieren konnte. Dieses Genesemodell kommt ohne große, mit den Pegmatiten genetisch verbundene Granitkörper aus, welche im Ostalpinen Kristallin fehlen. Es legt nahe, dass bei der Prospektion auf Spodumen-Pegmatite auch metamorphe Einheiten mit teilweise aufgeschmolzenen Glimmerschiefern und Gneisen beachtet werden sollten.

SCHLÜSSELWÖRTER

Lithium, Spodumen, Ostalpines Kristallin, Anatexis, Genesemodell

ABSTRACT

Lithium is a metal that has become essential in today's society and the demand for lithium is constantly rising. For this reason small Li-deposits like the spodumene pegmatite dikes in the Austroalpine unit might become of economic importance in the future. These pegmatite dikes formed in Permian time during a temperature dominated metamorphic event. Detailed mineralogical and geochemical investigations suggest melt formation by anataxis of Al-rich, staurolite bearing metapelites at about 675°C and 6.45 kbar. These melts were characterized by elevated Li contens and were continuously enriched by the fractional crystallization of simple pegmatite and leucogranite. Finally, the Li-contend reached 7000 ppm and crystallization of spodumene initiated. The proposed genetic model gets along without huge, genetically linked parental intrusions, which are missing in the Austroalpine unit. It suggests that areas composed of anatectic micaschists and paragneisses might be interesting for prospection on spodumene pegmatite.

KEYWORDS

Lithium, Spodumene, Austroalpine Unit, Anatexis, genesis model

## 1. EINLEITUNG

Der Bedarf an Lithium (Li) ist in den letzten Jahren stark gestiegen. Li wird vor allem für Batterien (z. B. in Smartphones) aber auch in der Keramik- und Glasindustrie (z. B. CERAN-Kochplatten) sowie in Schmieröl und für Medikamente verwendet. Insbesondere durch die zunehmende Bedeutung der Elektromobilität steigt der Bedarf an Lithium stetig an.

Lithium wird hauptsächlich aus Salzseen in Südamerika, in Australien und China aus Pegmatiten, welche den Lithium-Pyroxen Spodumen ($LiAl(SiO_3)_2$) führen, gewonnen [1]. Durch die wachsende Nachfrage könnten in Zukunft auch kleinere Vorkommen eine wirtschaftliche Bedeutung gewinnen. In Europa gibt es mehrere Pegmatit-Provinzen, die neben Lithium auch andere, als kritisch eingestufte Sondermetalle enthalten können [2, 3, 4]. Eine der größten derartigen Pegmatit-Provinzen befindet sich im Ostalpinen Kristallin in Österreich und Italien [5]. Diese entstand im Perm während einer temperaturbetonten Metamorphose [6].

Spodumen-Pegmatite gehören nach der Klassifikation von Černý & Ercit [7] zur LCT-Familie bzw. zur Selten-Element-Klasse [8, 9]. Die klassische Vorstellung ist, dass solche Gesteine durch fraktionierte Kristallisation von Restschmelzen großer granitischer Plutone entstehen [10]. Im Ostalpinen Kristallin sind jedoch keine permischen Granite vorhanden, die als Mutterplutone der Pegmatite in Frage kommen. Alle bekannten Granitvorkommen sind räumlich getrennt und liegen, bezogen auf die permische Stratigraphie, zumeist in höheren Krustenniveaus als die Pegmatite.

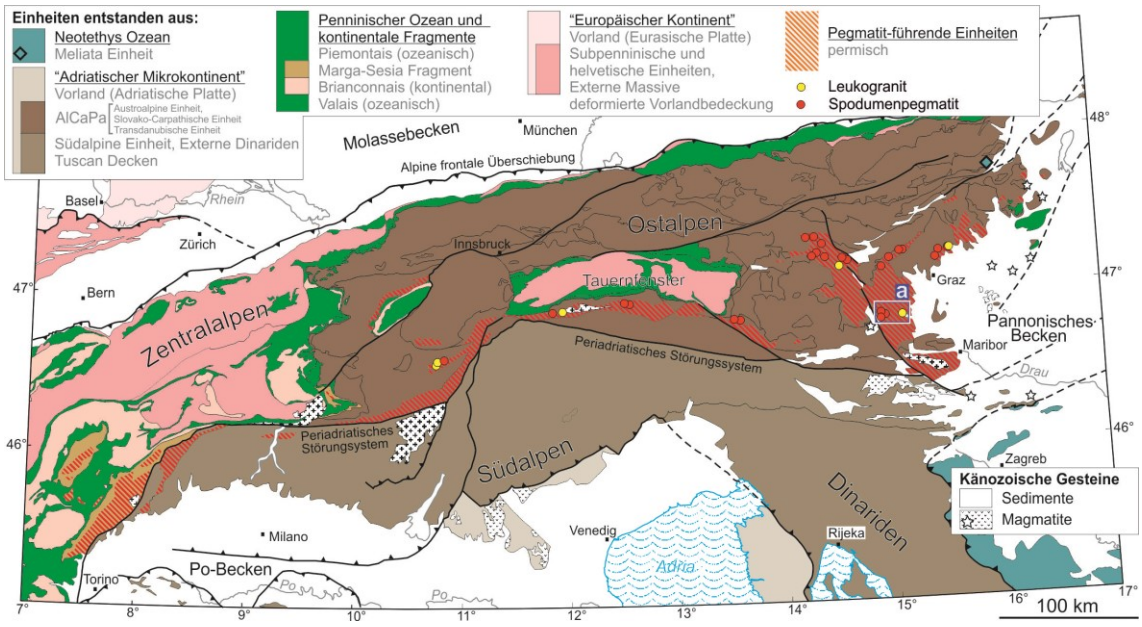


*Abb. 1 Tektonische Übersichtskarte der Alpen nach Froitzheim et al., [12]. Die Verteilung der Pegmatit-führenden Einheiten sowie der Spodumenpegmatit – und Leukogranitvorkommen sind hervorgehoben. (a) Spodumenpegmatit-Vorkommen des Brandrückens/Koralpe.*

Um die Verbreitung, die Genese und das Lagerstättenpotential der permischen Pegmatite in Österreich genauer zu untersuchen, hat sich eine Kooperation zwischen der Geologischen Bundesanstalt, der Montanuniversität Leoben, der Universität Innsbruck und der Universität Wien gebildet, welche seit 2015 laufend in den Projekten PEG I (2015-2018) und PEGII (2019-2022) zusammenarbeitet. Diese durch die „GBA-Forschungspartnerschaft Mineralrohstoffe" geförderten Projekte, haben folgende drei Hauptziele: (1) Ermittlung der genetischen Beziehungen von einfachen (Spodumen-freien) Pegmatiten, Leukograniten und Spodumen-Pegmatiten zueinander und zu ihren jeweiligen Nebengesteinen, (2) Kartierung der Verbreitung und Bestimmung des Fraktionierungsgrades von einfachen Pegmatiten, Leukograniten und

Spodumen-Pegmatiten, (3) Klärung des Lagerstättenpotentials der Pegmatite für kritische Spurenelemente.

Aufbauend auf den Ergebnissen dieser Untersuchungen wurde ein Genesemodell entwickelt, welches zeigt, wie und unter welchen Bedingungen Li von den Nebengesteinen bis in die Spodumen-Pegmatite angereichert werden kann. Im Folgenden werden die vorhandenen Daten zu den Pegmatiten zusammengefasst und das Genesemodell kurz beschrieben.

## 2. Ausgangslage

### 2.1. Die genetischen Beziehungen von einfachen Pegmatiten, Leukograniten und Spodumen-Pegmatiten im Gelände

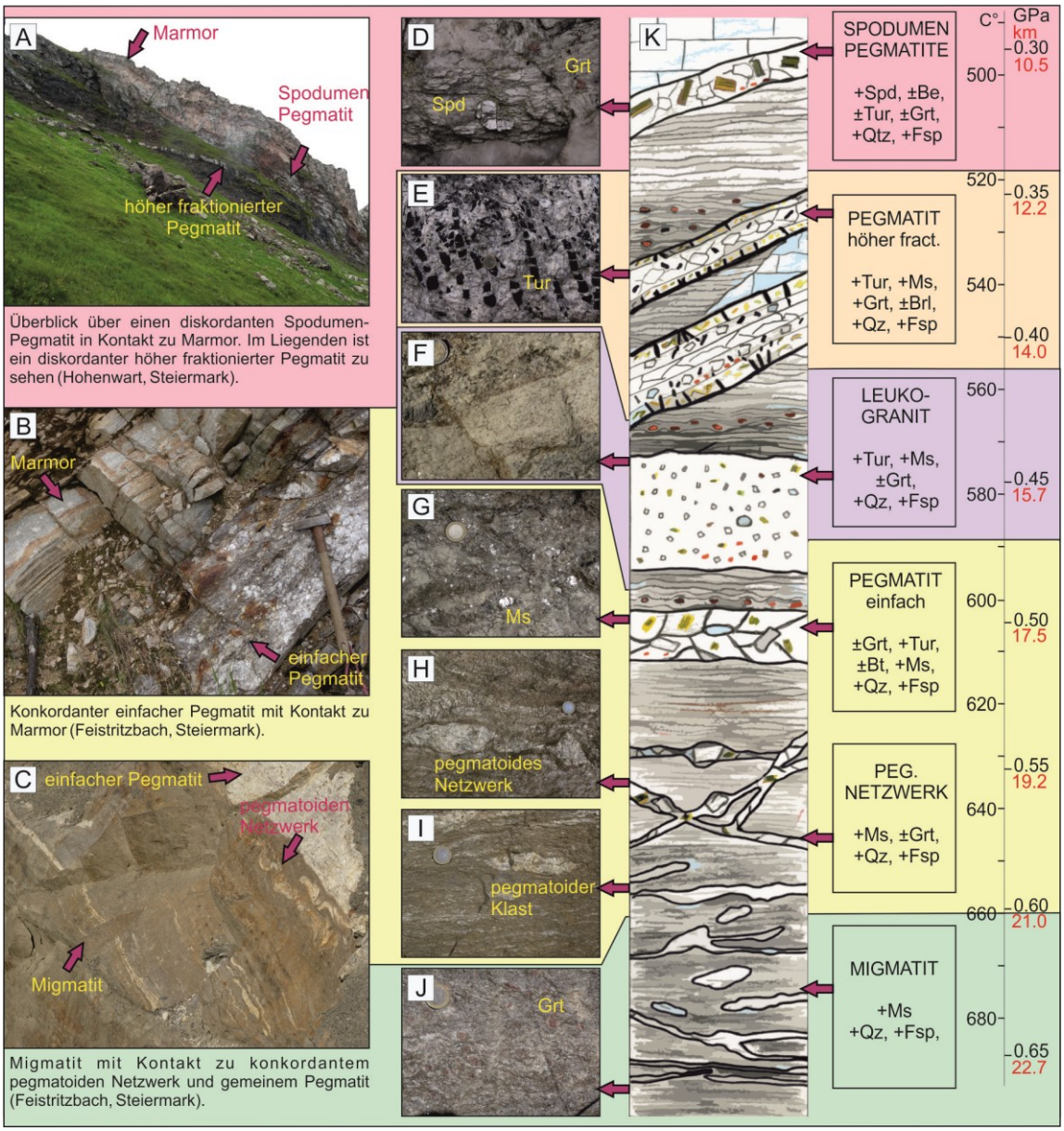


*Abb. 2: Überblick über die Geländebeobachtungen zwischen Migmatiten, einfachen Pegmatiten, Leukograniten, höher fraktionierten Pegmatiten und Spodumenpegmatiten.*

Im Ostalpin sind die permischen Pegmatite auf bestimmte lithostratigraphische Komplexe beschränkt (z.B. Rappold Komplex, Strieden Komplex, oder Silvretta Komplex) [5, 11] Abb.1). Pegmatit-führende Einheiten bestehen hauptsächlich aus Alumosilikat-führenden, zum Teil migmatischen Glimmerschiefern und Paragneisen und Staurolith-führenden Glimmerschiefern. Im Gelände kann man die kartierten Gebiete in drei Bereiche teilen [13, 14]:

(1) Die strukturell tiefsten Bereiche bestehen aus migmatischen Glimmerschiefern und Paragneisen (Abb. 2.C, J-H). Darin befinden sich unregelmäßig und diffus begrenzte pegmatitische Neosome, isolierte Muskovit- oder Alkalifeldspatporphyroblasten oder Netzwerke von cm-dicken Feldspat-Quarz-Gängchen. Weiters liegen zumeist geringmächtige Feldspat-reiche, einfache Pegmatite konkordant in der Schieferung.

(2) Die mittleren Bereiche sind durch das Vorkommen von nicht zonierten, einfachen Pegmatiten charakterisiert, welche mit scharfem Kontakt hauptsächlich konkordant im Nebengestein liegen (Abb. 2. B, G). In manchen Bereichen treten zum Teil mehrere hundert Meter mächtige, heterogene Leukogranitkörper mit pegmatitischer und/oder aplitischer Textur auf (Abb. 2. F). Glimmerschiefer und Paragneise, die permischen Staurolith oder Andalusit (kretazisch zum Teil in Kyanit umgewandelt) führen, bilden hier das Nebengestein.

(3) Die strukturell höchsten Bereiche sind durch höher fraktionierte, zonierte Pegmatite (Abb. 2. E) und Spodumen-Pegmatite (Abb. 2. A, D) charakterisiert. Der Kontakt zu Granat-Glimmerschiefern und Paragneisen ist scharf und konkordant oder diskordant ausgebildet.

## 2.2. Fraktionierungsgrad und Alter von einfachen Pegmatiten, Leukograniten und Spodumen-Pegmatiten

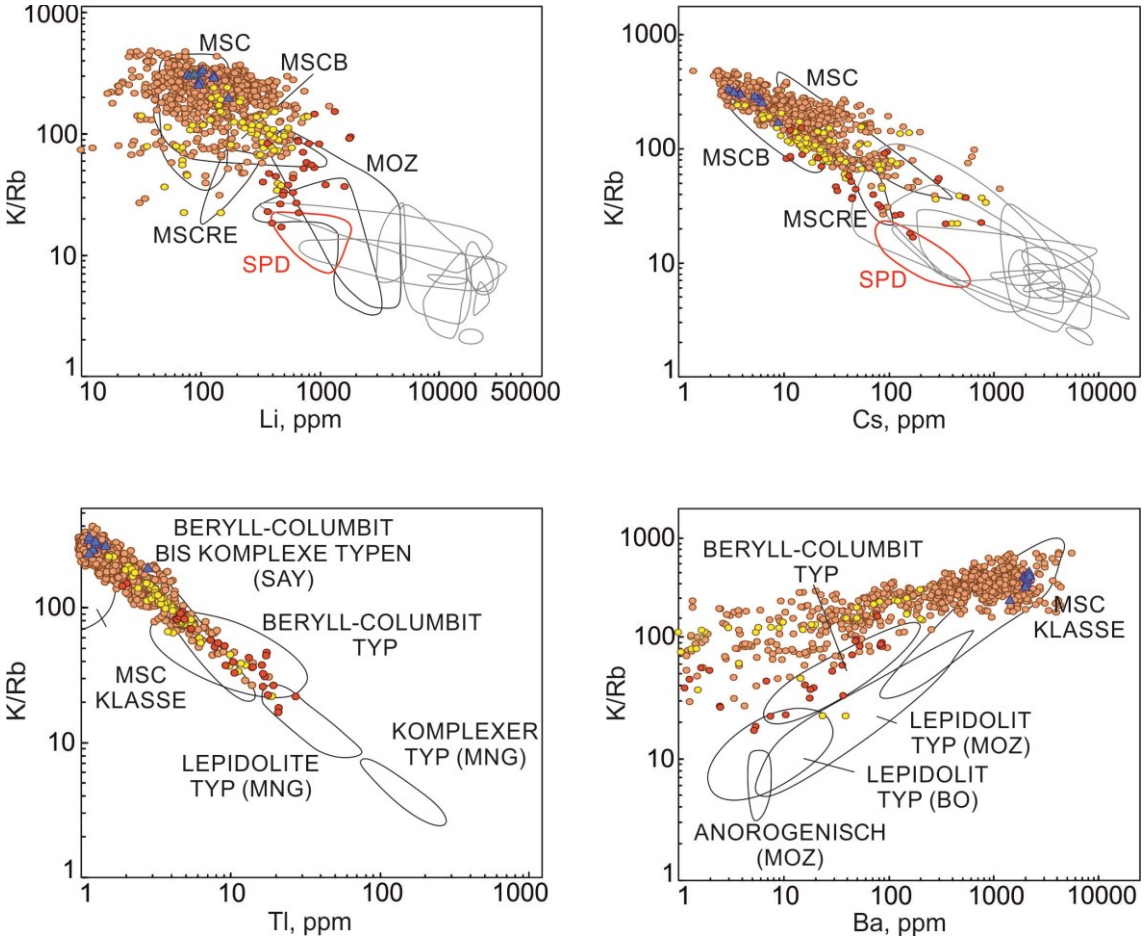


*Abb. 3: Spurenelement-Analysen an Muskoviten aus Migmatiten (blaue Punkte), einfachen bis höher fraktionierten Pegmatiten (orange Punkte), Leukograniten (gelbe Punkte) und Spodumenpegmatiten (rote Punkte) geplottet nach der Pegmatitklassifikation nach Černý & Burt [15].*

Um den Fraktionierungsgrad der Gesteine zu ermitteln wurden Spurenelementgehalte von magmatischen Muskoviten aus mehr als 600 Proben mittels LA-ICP-MS an der MUL analysiert (Abb. 3). Im Zuge der Fraktionierung steigen das K/Rb-Verhältnis, sowie die Li, Cs- und Tl-Gehalte an, während der Ba-Gehalt absinkt. Betrachtet man die Diagramme in Abb. 3 so sieht man einen kontinuierlichen Abfall des K/Rb-Verhältnisses in den Muskoviten von den migmatitischen Glimmerschiefern und einfachen Pegmatiten, hin zu den Leukograniten und Spodumen-Pegmatiten [5]. Die Li, Cs- und Tl-Konzentrationen korrelieren negativ, während die Ba-Konzentration einen positiven Trend zeigen. Die Streuung der Datenpunkte im K/Rb-Li-

Diagramm (Abb. 3. A) ist wahrscheinlich auf unterschiedliche Li-Gehalte in den teilweise aufgeschmolzenen Nebengesteinen und die eoalpidische metamorphe Überprägung zurückzuführen. Zusammenfassend lässt sich sagen, dass die Spurenelementgehalte in den Muskoviten einen kontinuierlichen Fraktionierungstrend zeigen, was auf eine co-genetische Bildung der Gesteinstypen hindeutet.

Eine co-genetische Bildung der magmatischen Gesteine ist nur möglich, wenn diese im gleichen Zeitintervall kristallisiert sind. Tatsächlich ergaben Sm/Nd Granatalter und einige wenige Zirkonalter für einfache Pegmatite 247 bis 288 Millionen Jahren (Ma) [11, 16], für drei Spodumen-Pegmatite 265 bis 268 Ma und für Leukogranite 259 bis 287 Ma (Abb. 1) [5]. Alle diese Altersspannen überlagern und fallen auch in den Zeitraum, der für das permische Metamorphoseereignis angegeben wird [6].

## 3. Genese der Spodumenpegmatite und das anatektische Lithium-Transfer-Modell

Laser Ablation ICP-MS Untersuchungen an Mineralen und Gesamtgesteinsanalysen von Al-reichen Glimmerschiefern aus dem Ostalpinen Kristallin zeigen, dass diese 70-170 ppm Li enthalten und Staurolith mit bis zu über 800 ppm der Hauptträger des Li ist. Li-reicher Muskovit und Staurolith könnten daher als Lithium-Quelle für Spodumen-Pegmatite dienen [12, 17]. Um diese Möglichkeit zu prüfen, wurden Modellrechnungen mit dem Programm Theriak-Domino (18) und der thermodynamischen Datenbank von Holland & Powell (19) und White et al. (20) angestellt.

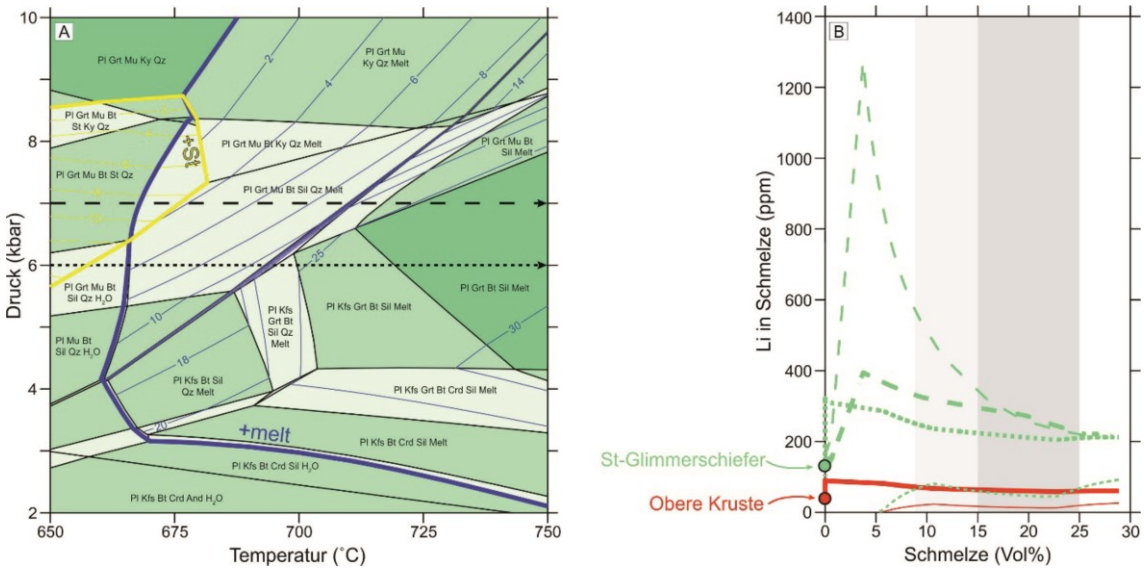


*Abb. 4: Abbildung 4. (A) P/T-Phasendiagramm eines Staurolith-Granatglimmerschiefers berechnet mit der Software Theriak-Domino [18] und der thermodynamischen Datenbank von Holland & Powell [19] und White et al. [20]. Chemisches System: Na-Ca-K-Fe-Mg-Al-Si-$H_2O$. (B) Modellierung des Li-Inhalts in der Schmelze. Der Partitionierungskoeffizient wurden anhand von in situ LA-ICP-MS Messungen berechnet. Zwei angenommene Endgliedermodelle: „batch melting" (dicke Kurven), Aufschmelzung mit Li-Fraktionierung (dünne Kurven).*

Im berechneten P-T-Diagramm zeigt sich, dass Staurolith bei einer Temperatur von 675 °C und einem Druck von 6,45 kbar instabil wird und sich gleichzeitig Schmelze bildet (Abb. 4). Dabei geht das im Staurolith enthaltene Li in die Schmelze über. Wenn man annimmt, dass bei einem Aufschmelzungsgrad von 15 – 20% Schmelze aus dem Migmatit entweichen kann, so ergibt sich, dass in dieser Ausgangsschmelze etwa 250 ppm Li enthalten sind (Abb. 4). Kristallisieren aus dieser Schmelze einfache Pegmatite, Leukogranite und höher fraktionierte Pegmatite ohne Spodumen, mit einem Li-Gehalt von etwa 100 ppm, so reichert sich Li in der Restschmelze an.

Eine Berechnung der Li-Massenbilanz zeigt, dass die letzten 1-5% der Schmelze nach einer derartigen fraktionierten Kristallisation 7.000 ppm Li enthalten. Das ist der Schwellenwert, der die Kristallisation von Spodumen, erlaubt [10]. Tatsächlich ist das Verhältnis von einfachen Pegmatiten zu Spodumen-Pegmatiten im Gelände größer als 1:100.

Dieses genetische Modell kann die Bildung von Li-Pegmatiten erklären, die nicht zeitlich und räumlich mit einem fertilen Granit verbunden sind, in enger zeitlicher und räumlicher Beziehung zu anatektischen Metasedimenten auftreten und wesentliche geochemische Muster mit anatektischen Schmelzen teilen.

## 4. AUSBLICK

Das berechnete Lithium-Transfer-Modell stützt eine anatektische Genese der Spodumen-Pegmatite im Ostalpinen Kristallin und könnte auch auf ähnliche Pegmatit-Provinzen anzuwenden sein. Möglicherweise ist das Explorationspotential von Gebieten mit einer mittel- bis hochgradigen, temperaturbetonten Metamorphose für bestimmte Pegmatittypen neu zu bewerten. Das Modell passt in eine Reihe von modernen Genesemodellen, die auch für andere Typen von Pegmatiten der Selten-Element-Klasse von einer anatektischen Bildung ausgehen. Es steht jedoch außer Frage, dass viele, vor allem proterozoische und archäische Pegmatite aus Restschmelzen großer Plutone entstanden.

## LITERATUR


1. Kesler, S.E.; Gruber, P.W.; Medina, P.A.; Keoleian, G.A.; Everson, M.P.; Wallington, T.J.: Global lithium resources: relative importance of pegmatite, brine and other deposits, Ore Geology Reviews, 48 (2012), pp 55–69

2. Mancheri, N. A.; Sprecher, B. S.; Deetman, S.; Young, S. B.; Bleischwitz, R.; Dong, L.; Kleijn, R.; Tukker, A.: Resilience in the tantalum supply chain, Resources, Conservation and Recycling, 129 (2018), pp 56-69

3. Mackay, D. A. R.; Simandl, G. J.: Niobium and tantalum: geology, markets and supply chains, in: Simandl, G. J.; Neetz, M. (eds.): Symposium on strategic and critical materials proceedings, Victoria, British Columbia Geological Survey Paper, 2015, pp 13-22

4. European Commision: Study on the review of the list of Critical Raw Materials, Final Report, (2017), p 93

5. Knoll, T.; Schuster, R.; Huet, B.; Mali, H.; Onuk, P.; Horschinegg, M.; Ertl, A.; Giester, G.: Spodumene Pegmatites and Related Leucogranites from the Austroalpine Unit (Eastern Alps, Central Europe): Field Relations, Petrography, Geochemistry, and Geochronology, The Canadian Mineralogist, 56 (2018), no. 4, pp 489-528

6. Schuster, R.; Stüwe, K.: The Permian Metamorphic Event in the Alps, Geology, 36 (2008), no. 8, pp 303-306

7. Černy, P.; Ercit, T. S.: The classification of granitic pegmatites revisited, The Canadian Mineralogist, 43 (2005), no. 6, pp 2005-2026

8. Mali, H.: Die Spodumenpegmatite von Brettstein und Pusterwald (Wölzer Tauern, Steiermark, Österreich), Joannea Mineralogie, 2 (2004), pp 5-53

9. Göd, R.: The spodumene deposit at “Weinebene”, Koralpe, Austria, Mineralium Deposita, 24 (1989), pp 270–278

10. London, D.: Pegmatites, The Canadian Mineralogist Special Publication, 10 (2008), pp 347

11. Schuster, R.; Scharbert, S.; Abart, R.; Frank W.: Permo-Triassic extension and related HT/LP metamorphism in the Austroalpine – Southalpine realm, Mitteilungen der Gesellschaft der Geologie und Bergbaustudenten Österreichs, 44 (2001), pp 111-141

12. Froitzheim, N.; Plasienka, D.; Schuster, R.: Alpine tectonics of the Alps and Western Carpathians, in: McCann, T. (ed.): The Geology of Central Europe, Mesozoic and Cenozoic, 2 ed., London, Geological Society of London, 2008, pp 1141-1232

13. Huet, B.; Knoll, T.; Schuster, R.; Paulick, H.: Albite-spodumene pegmatites without large granite intrusions? Exploring the feasibility of the alternative anatectic model, in: Koukal, V; Wagreich, M (eds.): Pangeo Austria 2018 - Abstracts, Vienna, Geologische Bundesanstalt, 2018, p 62

14. Ilickovic, T.; Schuster, R.; Mali, H.; Huet, B.; Horschinegg, M.: Genesis of Permian pegmatites and spodumene bearing pegmatites during regional scale, high temperature/low pressure metamorphism in the Austroalpine unit, in: Cvetkovic, V.; Saric, K. (eds.): Abstract Volume, 2nd Emile Argand Conference on Alpine Geology, Zlatibor, 2017, p 47

15. Černy, P.; Burt, D.M.: Paragenesis, crystallochemical characteristics, and geochemical evolution of micas in granite pegmatites, in: Bailey, S. W. (ed.): Micas, Reviews in Mineralogy, 1 ed., Blacksburg, Mineralogical Society of America, 1984, pp 257-297

16. Thöni, M.; Miller, C.; Zanetti, A.; Habler, G.; Goessler, W.: Sm–Nd isotope systematics of high-REE accessory minerals and major phases: ID-TIMS, LA-ICP-MS and EPMA data constrain multiple Permian–Triassic pegmatite emplacement in the Koralpe, Eastern Alps, Chemical Geology, 254 (2008), no. 3-4, pp 216-237

17. Konzett, J.; Schneider, T.; Nedyalkova, L.; Hauzenberger, CH.; Melcher, F.; Gerdes, A.; Whitehouse, M.: Anatectic granitic pegmatites from the Eastern Alps: a case of variable rare-metal enrichment during high-grade regional metamorhism – I. Mineral assemblages, geochemical characteristics, and emplacement ages, The Canadian Mineralogist, 56 (2018), no. 4, pp 555-602

18. De Capitani, C.; Petrakakis, K.: The computation of equilibrium assemblage diagrams with Theriak/Domino software, American Mineralalogist, 95 (2010), pp 1006-1016

19. Holland, T. J. B.; Powell, R.: An improved and extended internally consistent thermodynamic dataset for phases of petrological interest, involving a new equation of state for solids, Journal of Metamorphic Geology, 29(2011), no. 3, pp 333-383

20. White, R.W.; Powell, R.; Holland, T.J.B.; Johnson, T.E.; Green, E.C.R.: New mineral activity–composition relations for thermodynamic calculations in metapelitic systems, Journal of Metamorphic Geology, 32 (2014), no. 3, pp 261-286

## 3. SPODUMENE PEGMATITES AND RELATED LEUCOGRANITES FROM THE AUSTROALPINE UNIT (EASTERN ALPS, CENTRAL EUROPE): FIELD RELATIONS, PETROGRAPHY, GEOCHEMISTRY AND GEOCHRONOLOGY

*Tanja Knoll[1], Ralf Schuster[1], Benjamin Huet[1], Heinrich Mali[2], Peter Onuk[2], Monika Horschinegg[3], Andreas Ertl[4] & Gerald Giester[4]*

*[1]Geological Survey of Austria, Neulinggasse 38, 1030 Vienna, Austria*

*[2]Department of Applied Geosciences and Geophysics, Montanuniversität Leoben, Peter-Tunnerstraße 5, 8700 Leoben, Austria*

*[3]Department of Lithospheric Research, Geocenter, University of Vienna, Althanstraße 14, 1090 Vienna, Austria*

*[4]Institut für Mineralogie und Kristallographie, Geocenter, University of Vienna, Althanstraße 14, 1090 Vienna, Austria*

*Corresponding author: tanja.knoll@geologie.ac.at*

---

➔ *Manuscript status: no open access publication*
➔ *The Canadian Mineralogist 2018, 56 (4): 489–528.; https://doi.org/10.3749/canmin.1700092*
➔ *Published: 23.10.2018*

---

ABSTRACT

In the Eastern Alps (Central Europe), about two dozen spodumene pegmatite bodies spread heterogeneously over the Austroalpine Unit. They are spatially associated with leucogranites and simple pegmatites formed during the Permian extensional event. The pegmatites and leucogranites were overprinted during the Alpine orogeny with differing intensity, leading to various structural and chemical changes of the magmatic features. The magmatic assemblage consists of K-feldspar, quartz, plagioclase, muscovite, garnet, tourmaline with additional spodumene in the pegmatites. Beryl is rarely present and other accessory phases like apatite, cassiterite or Nb-Ta phases are exceptional. Mineral compositions indicate that magmatic garnet is rich in Mn and Fe and has Ca-rich and Mn-poor Alpine metamorphic overgrowths. Sm-Nd ages of carefully separated magmatic garnet from the leucogranites and spodumene pegmatites fall in the range of 245–280 Ma. These Permian-Early Triassic ages are in good agreement with previously published results from associated simple pegmatites. Tourmalines from spodumene pegmatites belong to the elbaite-schorl series, containing an unusual but significant dravite component. The occurrence of tourmaline at the absence of biotite may be due to the low Ti content (< 0.06 wt.% $TiO_2$) in the melt of both rock tyes. Trace element compositions (Rb, Li, Cs, Tl or Ba) of magmatic muscovite show that the leucogranites and spodumene pegmatites belong to the same fractionation trend, with more fractionated signatures in the spodumene pegmatites. Whole rock geochemical compositions indicate that both lithologies have a common granitic peraluminous geochemistry, similar minor and trace element distribution patterns and share a fractionation trend of trace elements including Be, Li, Rb, Cs, Sn, Ge, Ba and REE. Positive and negative Eu anomalies in analyzed leucogranites and spodumene pegmatites, respectively, are interpreted with extraction of Eu in plagioclase crystallizing in leucogranite during the melt evolution. Values of $\varepsilon(t)_{Nd}$ (approximately –8) and initial $^{87}Sr/^{86}Sr$ ratios (0.7098–0.7353) indicate a crustal origin for the primary melts. Using the Permian metamorphic conditions of the country rock as a proxy, the spodumene pegmatites intruded at more than 10 km depth in somewhat higher structural levels than the leucogranites. This set of field and petrographic observations as well as geochemical and geochronological data suggests that the leucogranites and spodumene pegmatites of the Austroalpine Unit are contemporaneous and

cogenetic, whereby the spodumene pegmatites show a higher degree of chemical evolution and concentration of rare metals.

KEYWORDS: spodumene pegmatite, leucogranite, Eastern Alps, geochemistry, Sm-Nd garnet age;

## INTRODUCTION

Recent changes in the demand for lithium for batteries has triggered re-evaluation and re-investigation of the Li-pegmatites in the Eastern Alps. Projected increases in this demand has the implication that even small Li-pegmatite deposits might become economically viable (Kesler *et al.* 2012). About two dozen individual spodumene ($LiAlSi_2O_6$) pegmatite bodies spread heterogeneously in the Austroalpine Unit of the Eastern Alps over an E–W distance of more than 400 km. These pegmatites may be classified as albite-spodumene pegmatites of the rare element class of Černý & Ercit (2005), and have been previously thought to be products of fractional crystallization of parent plutonic bodies (Göd 1989, Mali 2004). However, no large parent granitic plutons have been identified to date, this problem having being ruled out by assuming that Alpine tectonics removed the crustal level including these intrusions. The spodumene pegmatites of the Austroalpine Unit are always spatially associated with simple pegmatites. In some pegmatite fields additionally relatively small, inhomogeneous leucogranitic bodies occur. The simple pegmatites yielded Permian to Triassic ages and are considered to be products of anatexis (Stöckert 1987, Thöni & Miller 2000, Habler *et al.* 2007) in contrast to the spodumene pegmatites. A similar age and origin was assumed for some of the leucogranites (Stöckert 1987). Age data are only available for the Weinebene spodumene pegmatites, indicating a Middle Triassic emplacement at about 240 Ma (Heede 1997, Thöni & Miller 2000). Understanding the genesis of the spodumene pegmatites of the Austroalpine Unit therefore requires that their relation to the simple pegmatites and leucogranites is clarified and their main characteristics are well understood.

In this article, we provide a summary of the available data on spodumene pegmatite and leucogranite occurences from the Austroalpine Unit. We report new detailed petrographic observations, whole rock and mineral chemical analyses determined by electron probe microanalyser and laser ablation ICP-MS, Sm-Nd garnet and Rb-Sr muscovite ages as well as whole rock Sr and Nd isotopic ratios. This data allows us to characterise the time and genetic relationships between spodumene pegmatites and leucogranites, evaluate the extent of fractionation and estimate their intrusion depth as well as their geochemical fingerprint. The genetic relationship between the spodumene pegmatites and leucogranites with respect to simple pegmatites and migmatites is not the aim of the present study, because this topic would have to be discussed with additional data from the country rocks.

## GEOLOGICAL SETTINGS

The Alpine orogen developed from two continental and two oceanic realms existing in Late Jurassic to Cretaceous times (Fig. 1a). The lowermost tectonic units have formed since the Eocene from the former continental margin of Europe. They are represented by the Helvetic nappes appearing along the northern front and the Subpenninic nappes present in the more internal part of the orogenic belt. The overlying Penninic nappes derived from the Penninic Ocean (Alpine Tethys) and continental fragments therein. Together with the Subpenninic nappes they experienced Alpine tectonics and metamorphism mainly in the Eocene to Miocene. The Austroalpine and the Southalpine units, separated by the Periadriatic fault, are both derived from the Adriatic continental margin and now occur on top of the previously described units. The Austroalpine nappes were sheared off during the Cretaceous and the individual nappes experienced a various tectonic and metamorphic overprint during nappe stacking. They represent the northwest verging pro-wedge of the Alpine orogeny, whereas the Southalpine Unit formed as a south verging retro-wedge since the Oligocene. Tectonic slices derived from the Neotethys oceanic realm referred as the Meliata Unit occur within the Austroalpine nappe

pile. They were mobilized in the Jurassic and reached their present position by out of sequence thrusting in the Cretaceous (Schmid *et al.* 2004).

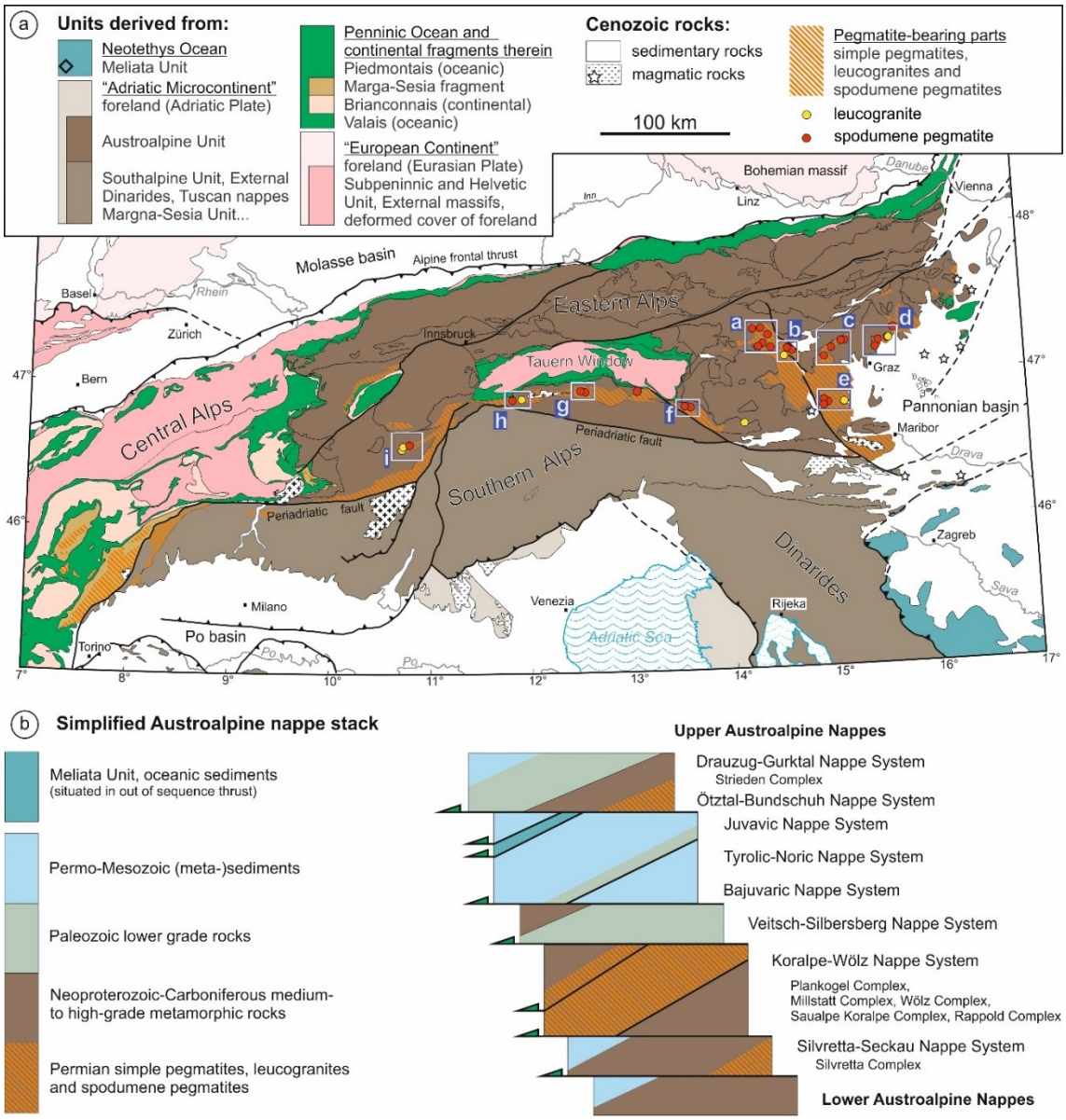


*Fig. 1. Regional geology. (a) Tectonic map of the Alps (modified after Froitzheim et al. 2008) with pegmatite-bearing parts (orange overlay), main occurrences of leucogranites (yellow dots) and spodumene pegmatites (red dots). Rectangles indicate the position of pegmatite fields described in the text. [a] Wölzer Tauern pegmatite field with Hohenwart and Lachtal spodumene pegmatites, [b] Falkenberg pegmatite field with Geißrücken leucogranite, [c] Gleinalm pegmatite field with Mitterberg spodumene pegmatite,[d] St. Radegund pegmatite field with Garrach and Schöcklkreuz spodumene pegmatites. [e] Koralpe pegmatite field including the Weinebene spodumene pegmatite group and the Trahütten leucogranite, [f] Millstätter Seenrücken pegmatite field, [g] Defereggental pegmatite field, [h] Uttenheim pegmatite field with Schlösselberg leucogranite and [i] Martelltal pegmatite field with the Martell leucogranite. (b) Simplified profile of the Cretaceous nappe stack of the Austroalpine Unit. Spodumene pegmatites include occurrences from Angel (1933), Angel & Meixner (1953), Höller (1959), Meixner (1966), Koller et al. (1983), Marsch (1983), Heritsch (1984), Esterlus (1983), Moser et al. (1987), Walter (1998), Schulz (2000), Mali (2004) and Pestal et al. (2005).*

Several thousand pegmatites are variably distributed within the Austroalpine nappe pile (Fig. 1). Beside a few Ordovician (Thöni & Miller 2004), Variscan (Handler *et al.* 1999), Cretaceous (Thöni & Miller 2010) and Oligocene occurrences, the majority is Permian in age (Schuster *et al.* 2001, Schuster & Stüwe 2008). They formed during the Permian extensional event, which reflects thinning of the whole continental lithosphere (Schuster & Stüwe 2008). Decompression melting in the mantle caused crustal basaltic underplating that induced partial melting of metasediments at granulite or high amphibolite- facies conditions in lower crustal levels.

In middle crustal levels, at amphibolite to greenschist-facies metamorphic conditions these melts crystallized in form of pegmatites in some units, whereas different melts generated granitoides in other units. Meanwhile, sedimentary basins in extensional grabens and rhyolitic volcanic edifices formed at the surface. During the Alpine collisional event in the Cretaceous the Austroalpine nappes formed associated to a SE dipping, intracontinental subduction within the Adriatic continental lithosphere. Peak metamorphic conditions reached the greenschist- to eclogite-facies in the individual units (Froitzheim *et al.* 2008).

Simple Permian pegmatites are common in some lithostratigraphic complexes (in the sense of the North American Commission on Stratigraphic Nomenclature, 2005; *e.g.*, Rappold, Saualpe-Koralpe, Plankogel, Strieden, and basal Silvretta complexes), but completely absent from other ones (Fig. 1b). Pegmatite-bearing units consist predominantly of micaschist and paragneisse, often containing staurolite and/or aluminosilicate-rich layers. The protoliths are expected to be Neoproterozoic to earliest Carboniferous. Spodumene pegmatites appear as dikes up to a few meters thick, and lengths up to more than one kilometer (Göd 1989, Mali 2004) or alternatively as boudins with several decimeter size within country rocks (Ahrer, 2014). Leucogranites are present as inhomogeneous bodies with pegmatitic and aplitic zones with a maximum dimension of hundreds of meters to a few kilometers, covering areas up to 2100 $km^2$. In some units primary spatial relationships between the Permian pegmatites and their country rocks are well preserved, whereas in others they are overprinted to a varying extent by the Alpine deformation and metamorphism (Thöni & Miller 2000).

## METHODS

The methods used in this study are described in this section.

### SCANNING ELECTRON MICROSCOPE (SEM)

Back-scattered electron (BSE) images were acquired on a Vega-II Tescan SEM at the Geological Survey of Austria, Vienna. The following settings were used: 15 kV acceleration voltage, 70 nA beam current and a working distance of approximately 10 mm. This SEM is equipped with an X-Max 50 $mm^2$ Oxford Instrument EDS detector controlled by the AZTec software. Accessory phases were identified by their X-ray spectrum measured with the EDS detector (15 kV acceleration voltage, 50–70 nA beam current, 27 mm working distance). The chemical zoning of garnet was characterized by semiquantitative X-ray elemental mapping by EDS (15 kV acceleration voltage, 70 nA beam current, 27 mm working distance, 0–10 keV range, 1024 bins). The raw count data for elements Mn and Ca were first smoothed with a median filter and 3×3 averaging kernel, then normalized to enhance elemental distributions within garnet and were plotted using a gamma correction with exponent values between 0.9 and 1.9 (Heilbronner & Barrett 2013). Major element compositions of muscovite were carried out on a Zeiss EVO MA 10 SEM equipped with a Bruker Nano X-Flash EDS detector and Esprit Standalone software at the Department of Applied Geosciences and Geophysics, Montan University of Leoben, Austria. The following settings were used: 15 kV acceleration voltage, 50–70 nA beam current and working distance of approximately 10 mm. Peak calibration was carried out on well characterized natural and synthetic standards, and beam calibration was done with pure Cu.

### Electron Probe Micro Analyser (EPMA)

Major element compositions of garnet, feldspar and tourmaline were performed using a Cameca SX Five FE EPMA equipped with 5 Wavelength- and one Energy-Dispersive Spectrometers at the Department of Lithospheric Research, University of Vienna, Austria. Well characterized homogeneous natural and synthetic minerals were used as standards. All analyses were performed using a focused beam at 15 kV accelerating voltage and 20 nA beam current. The counting time was 20 s at the peak position and 10 s at each background position. In order to avoid Na migration in feldspar and tourmaline analyses, a defocused beam of 7 µm diameter with a 10 s counting time was used on the peak position. For matrix correction, the PAP method (Pouchou & Pichoir 1991) was applied to all acquired data. The relative error of the laboratory internal standard is below 1% (Ntaflos *et al.* 2017).

### Laser ablation ICP-MS (LA ICP-MS)

*In situ* major and trace element analyses of phases investigated by Sm-Nd and Rb-Sr methods (garnet, feldspar, muscovite, tourmaline) were performed with an Agilent 8800 (QQQ)-ICP-MS at the Department of Applied Geosciences and Geophysics, Montan University of Leoben, Austria. The laser probe consists of the Laser System ESI NWR213 Nd:YAG with a TwoVol2 ablation cell and a wave length of 213 nm. Spot diameter was typically between 60 and 80 µm with a RF power of 1280 W. Argon was used as a carrier gas with a flow rate of 0.85 L/min. Silicon (measured from EPMA or SEM analyses, see above) was used as an internal standard for garnet, feldspar, muscovite and tourmaline.

### Whole rock geochemistry

Large samples (> 5 kg for fine-grained rocks with up to 2 cm large grains and > 10 kg for coarse-grained rocks with more than 2 cm large grains) with typical mineral assemblages were selected to obtain representative geochemical analyses. Sample preparation for whole rock chemical analyses was performed at the Geological Survey of Austria in Vienna. The samples were processed by standard methods involving crushing and ultra-fine grinding with an agate disc mill. Whole-rock chemical analyses were carried out by Activation Laboratories Ltd. (Ancaster, Ontario, Canada). Major and trace elements were analyzed with the 4Litho package. Material was first diluted and analyzed by a Perkin Elmer Sciex ELAN 9000 ICP-MS by using a Lithium Metaborate/Tetraborate fusion. Three blanks and five control samples were analyzed per group of samples. Duplicates were fused and analyzed every 15 samples. For Lithium analyses (package 5D) samples were digested with four acids beginning with hydrofluoric, followed by a mixture of nitric and perchloric acids, heated using precise programmer controlled heating in several ramping and holding cycles, which took the samples to incipient dryness. After incipient dryness was attained, samples were brought back into solution using hydrochloric acid. In-lab standards (traceable to certified reference materials) or certified reference materials were used for quality control.

### Sm-Nd and Rb-Sr geochronology

For isotopic analyses we considered mineral separates of garnet, feldspar+quartz, tourmaline, muscovite and spodumene, as well as whole rock powders. Minerals were separated by standard methods involving crushing, grinding, sieving and magnetic separation, with hand-picking of grains under the binocular microscope from specified sieved and magnetic fractions. All minerals were picked from the 0.2–0.3 mm sieve fractions except garnet from samples RS32/1 and RS33/01, which were selected from the 0.2–0.45 mm size fraction. Weights of analyzed fractions were about 150–200 mg for whole rock powder, tourmaline, muscovite and feldspar and 30–50 mg for garnet. All mineral separates were washed in acetone and deionized water, to remove surface contaminants. Afterwards the mineral fractions were leached in 2.5 N HCl at *ca.* 80°C for *ca.* 30 minutes, except garnet which was leached in 6 N HCl. Decomposition was achieved with ultra-pure acids ($HF:HClO_4$=4:1) for 3 weeks at 100°C. The chemical sample preparation procedure followed the method described in Sölva *et al.* (2005). Element concentrations were determined by isotope dilution using mixed Sm-Nd and Rb-Sr spikes.

Isotopic measurements were done at the Department of Lithospheric Research at the University of Vienna, Austria. All isotopic ratios were analyzed at a Thermo Finnigan Triton MC-TIMS using Re double filaments, except for Rb which was evaporated from Ta single filaments. Overall blank contributions were < 0.3 ng for Nd and Sm and < 1 ng for Sr and Rb. During the periods of measurements the La Jolla (Nd) international standard yielded $^{143}Nd/^{144}Nd$ = 0.511846±0.000001 (n = 30; 2 σ standard deviation, in 2015–2016) whereas the NBS987 standard yielded $^{87}Sr/^{86}Sr$ = 0.71072±0.00005 (n = 38; 2σ standard deviation, in 2015–2016). Error for the $^{147}Sm/^{144}Nd$ ratio is lower than 1%, based on iterative sample analysis and spike recalibration. Ages were calculated with the analytical errors on the individual measurements, using the software ISOPLOT/Ex (Ludwig 2003). Ages are based on decay constants 6.54 $10^{-12}$ $a^{-1}$ for $^{147}Sm$ and 1.42 $10^{-12}$ $a^{-1}$ for $^{87}Rb$ (Ludwig 2003).

### TOURMALINE SINGLE CRYSTAL-STRUCTURE

Fragments (approximate size ~0.15×0.15×0.15 mm) of three different tourmaline crystals from the spodumene pegmatites (04R45 rim, 14R16 core, 15R42 core) were separated and studied on a Bruker APEXII diffractometer equipped with a CCD area detector and an Incoatec Microfocus Source IμS (30 W, multilayer mirror, Mo-Kα) at the Department of Mineralogy and Crystallography, University of Vienna. Single-crystal X-ray diffraction data were collected at room temperature (up to 80° 2θ), integrated and corrected for Lorentz and polarization factors with an absorption correction by evaluation of partial multiscans. The structure was refined with SHELXL97 (Sheldrick 1998) using scattering factors for neutral atoms and a tourmaline starting model from Ertl *et al.* (2016). The H atom bonded to the O3 cluster was located from a difference-Fourier map and subsequently refined. Refinement was performed with anisotropic displacement parameters for all non-hydrogen atoms. Site occupancies were refined according to well-known characteristics of the tourmaline structure (Na was refined at the *X* site, Al and Fe were refined at the *Y* and *Z* site). The refinements converged at *R*1(*F*) values of ~1.2–1.4% (Table 8a, b).

### ABBREVIATIONS

The mineral and endmember abbreviations of Whitney & Evans (2010) are used in tables and figures: Spd (spodumene), Tur (tourmaline), Ms (muscovite), Grt (garnet), Alm (almandine), Sps (spessartine), Prp (pyrope), Grs (grossular), Adr (andradite), Qz (quartz), Fsp (feldspar), Kfs (K-feldspar), Pl (plagioclase), Or (orthoclase), Ab (albite), An (anorthite), Brl (beryl), Aln (allanite), Ap (apatite), Gn (galena), Lm (limonite), Mnz (monazite), Py (pyrite), Urn (uraninite), Xtm (xenotime) and Zrn (zircon). Abbreviations for microtextural observations follow the terminology of Passchier & Trouw (2005): SR (subgrain rotation), GBM (grain boundary migration) and SPO (shape preferred orientation).

### FIELD OCCURRENCES OF SPODUMENE PEGMATITES AND LEUCOGRANITES

This section summarizes the main macroscopic field and petrological characteristics of spodumene pegmatites and related leucogranites from the Austroalpine Unit in the Eastern Alps. All pegmatite occurences together define a pegmatite province, which can be divided into fields and groups using the hierarchy suggested by Černý (1993). Each field described in the following contains simple pegmatites, spodumene pegmatites and in some cases also a leucogranite body situated within a single lithostratigraphic complex and nappe, respectively. Pegmatite fields and important spodumene pegmatite and leucogranite bodies therein are mentioned with a local name characterizing the latter as lithodemic units in the sense of the North American Commission on Stratigraphic Nomenclature (2005).

The extension of the Permian pegmatite province of the Alps and the pegmatite fields are shown in Figure 1. Main pegmatite fields and important spodumene pegmatite dikes and leucogranite bodies are listed in Table 1. They include the Wölzer Tauern pegmatite field with the Hohenwart and Lachtal spodumene pegmatites (location [a] in Fig. 1), Falkenberg pegmatite field containing

the Geißrücken leucogranite (location [b] in Fig. 1), Gleinalm pegmatite field with Mitterberg spodumene pegmatite (location [c] in Fig. 1) and St. Radegund pegmatite field with the Garrach and Schöcklkreuz spodumene pegmatites (location [d] in Fig. 1).

Further the Koralpe pegmatite field including the Weinebene spodumene pegmatite group and the Trahütten leucogranite (location [e] in Fig. 1), Millstätter Seenrücken pegmatite field (location [f] in Fig. 1), Defereggental pegmatite field (location [g] in Fig. 1), Uttenheim pegmatite field with the Schlösselberg leucogranite (location [h] in Fig. 1) and Martelltal pegmatite field with the Martell leucogranite (location [i] in Fig. 1).

In general spodumene pegmatites occur as dikes ranging in length from several tens of meters up to more than 1 km, with thicknesses from a few decimeters to several meters. Their contact with their host rocks is sharp, sometimes with narrow, millimeters to a few centimeters wide reaction zones. Within paragneiss, micaschist, quartzite and amphibolite they form discrete dikes mostly concordant with respect to the Alpine schistosity, whereas in contact with marble they often show intricate geometries with “bubbly” boudinage-like structures.

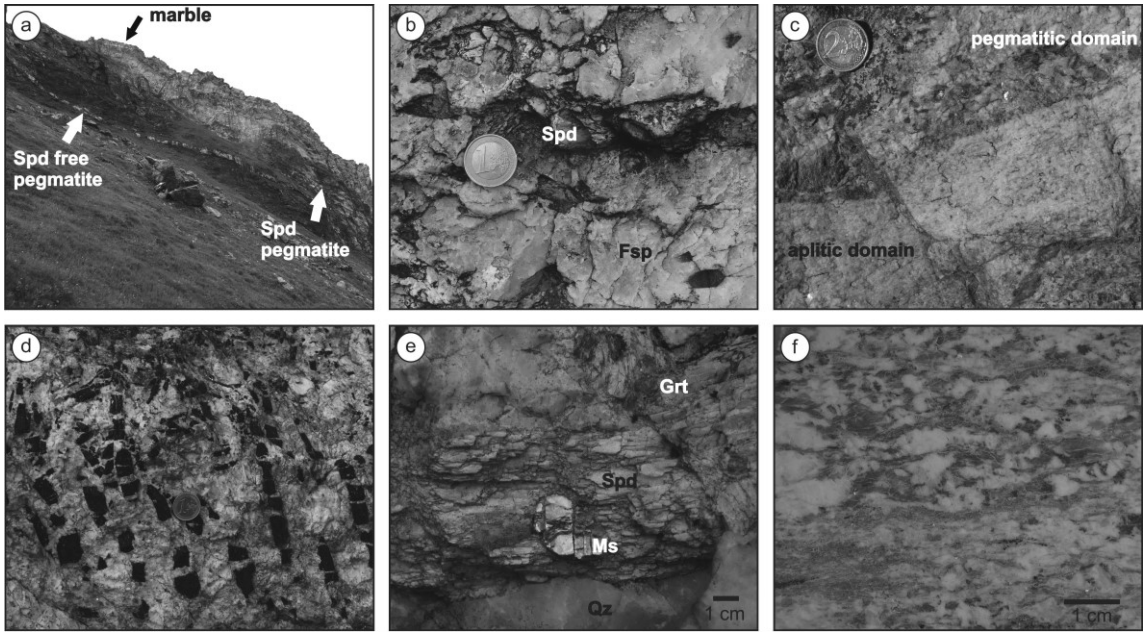


*Fig. 2. Field and sample photographs. (a) View over a discordant spodumene pegmatite in sharp contact with a marble. In the footwall a discordant simple pegmatite is visible (Mount Hohenwart spodumene pegmatite). (b) Weathered, up to 3 centimeters large spodumene crystals associated with feldspar (Lachtal spodumene pegmatite). (c) Contact between a pegmatitic and aplitic zone within Geißrücken leucogranite. Both, the aplitic and the pegmatitic zone consist of quartz, feldspar, muscovite and garnet. At the contact between the pegmatitic and aplitic parts garnet is accumulated in a certain layer. (d) Comb structures of brittle deformed tourmaline within quartz and feldspar (Mitterberg spodumene pegmatite). (e) 7 cm long spodumene associated with euhedral garnet, quartz and muscovite (Mitterberg spodumene pegmatite). (f) Textural detail of deformed, fine- to medium-grained Schlösselberg leucogranite. The assemblage comprises K-feldspar, plagioclase, muscovite, quartz and garnet (dated sample 15R69).*

The phases visible to the naked eye in spodumene pegmatites are spodumene, K-feldspar, plagioclase, quartz, muscovite, tourmaline and garnet. In the field, spodumene is not always easy to recognise, but its strong cleavage is characteristic. When fresh, the spodumene crystals are whitish and slightly translucent, whereas increasing alteration causes milky white, greenish and brownish colors. Grayish coloration is due to graphite, which may also appear as tiny black aggregates. Within mylonitic pegmatites, spodumene forms elongated clasts parallel to the mylonitic lineation. Milky and slightly pale bluish or greenish beryl with a crystal size up to a few

centimeters in size can be found exceptionally. The accessory minerals described in the following petrography section are very rarely visible to the naked eye.

Magmatic zoning within pegmatites is controlled by systematic changes in proportion and size of the minerals. It may be distinct or diffuse, symmetric or irregular. The spodumene pegmatites may be roughly subdivided into a border zone and four internal zones. Internal zone 1 is composed of quartz, plagioclase and K-feldspar crystals of millimeter to a few centimeters size, with minor amounts of muscovite. In this zone K-feldspar can form megacrysts up to a few decimeter in size, with a grayish color. Internal zone 2 is similar to zone 1 and additionally contains crystals of spodumene of up to cm-size, which are mostly anhedral to subhedral with a tabular or blocky shape. Within these two zones, a few centimeters wide elongated tourmaline- and garnet-rich layers may be present. Internal zone 3 consists of very coarse-grained quartz, spodumene, K-feldspar, plagioclase and muscovite, from which some spodumene and feldspar crystals may grow into a quartz core that corresponds to zone 4. In most cases, not all textural zones are developed or only a single zone may be dominant. Miarolitic cavities or indications of collapsed cavities were not observed in any of the studied pegmatites.

Generally, only a thin border zone with a width of a few centimeters to decimeters is developed. Typically, it is aplitic and consists of quartz, muscovite, plagioclase, garnet and tourmaline assemblages and very rarely apatite, beryl, titanite, ilmenite, magnetite and pyrite. The host rock lithology has in some cases an influence on the pegmatite mineralogy. For example a layer with pale blue dravite tourmaline with a significant Li content has been described from a contact zone towards marble (Ertl *et al*. 2009), whereas in the vicinity of amphibolite, holmquistite may be present (Niedermayr & Göd 1992, Steiner 2017).

The leucogranites form intrusive bodies less than hundred to a few hundred meters in thickness and up to more than 10 km in length. The larger bodies contain heterogeneous parts with a fine- to medium-grained aplitic texture and parts with a coarse-grained pegmatitic texture often in a narrow layering. Both consist of a mineral assemblage of K-feldspar, quartz, plagioclase, muscovite and small amounts of garnet and tourmaline. The boundaries between the aplitic and pegmatitic parts are diffuse in most cases (*e.g.*, Geißrücken leucogranite). Contrary to spodumene pegmatites it was not possible to define a consistent internal zoning for leucogranites.

In most cases, both spodumene pegmatite and leucogranite are affected by Alpine deformation, which is heterogeneous at outcrop and regional scale (*e.g.* Esterlus 1993, Mali 2004). Spodumene pegmatite and leucogranite can display proto- to ultramylonitic textures from ductile deformation, or proto- to ultracataclastic textures from brittle deformation.

### Petrography

The petrography of spodumene pegmatites and leucogranites is presented here with special attention given to microtextures. Key samples used for further analyses are also briefly described.

### COMMON MACROSCOPIC AND MICROSCOPIC FEATURES

All spodumene pegmatites and leucogranites are characterized by an assemblage containing quartz (30–60 vol.%), K-feldspar (30–50 vol.%), plagioclase (20–50 vol.%), tourmaline (< 10 vol.%), muscovite (< 30 vol.%) and garnet (< 2 vol.%) and additional spodumene (5–30 vol.%) in pegmatites. Even if some of the samples appear undeformed in hand specimen, microscopic observation shows that all are at least weakly deformed and recrystallized. Frequently they display protomylonitic or mylonitic microtextures.

K-feldspar is euhedral to subhedral with a maximum size of 3 cm (Fig. 3a, b, c). It can be intergrown with fine-grained muscovite or replaced by plagioclase-quartz myrmekites (Wenger & Armbruster 1990, Mali 2004). Plagioclase is subhedral to anhedral and up to 2 cm in size. It shows dynamic recrystallization into small uniform sized and elongated grains. Quartz has a sweepy and/or patchy undulose extinction and is totally recrystallized. The coarser grains have highly irregular grain boundaries and show pinning, dragging and left-over grain structures. Additionally small grains that occur between coarser crystals have a slightly elongated shape. Spodumene shows a euhedral to subhedral shape, an average size of 3 cm up to a maximum of 40 cm (Senzenberger 2001, Mali 2004, Ahrer 2014) and displays brittle fractures. In mylonitic samples it may be deformed into patches with core-mantle structures, very fine-grained elongated aggregates (Fig. 3c) or dispersed fragments (Fig. 3d). Spodumene-quartz symplectites having sharp and straight boundaries to the spodumene crystals but convex inward boundaries into the K-feldspar crystal are also common (Fig. 3a, b). Muscovite is on the one hand present in form of large (0.5–4 cm) crystals with random orientation or a weak shape preferred orientation. It can be kinked or fractured. On the other hand it occurs as small (< 0.3 cm), euhedral crystals with a shape preferred orientation or as fine-grained aggregates parallel to the schistosity. Garnet is euhedral to subhedral, sometimes amoeboid or coronitic, with quartz and rarely zircon inclusions. Its average size is 0.2 cm but it can reach up to 2 cm in diameter. It is often fractured with fracture spacing generally larger than 100 µm. Healed cracks are revealed by BSE images and contain inclusions trails (Fig. 3d–e). In most samples, garnet shows a discontinuous overgrowth, which is characterized by a higher amount of fine-grained quartz and muscovite as well as zircon inclusions (Fig. 3). The thickness of the overgrowth is about 50–80 µm (see also Table 3). Classification of garnet types is also based on chemistry and is therefore described in a following section. Tourmaline is present as euhedral to subhedral, 0.1–10 cm large fractured crystals (Fig. 3e). In some samples a zoning with a blue core and a greenish-blue rim is observed. Zircons are generally small (20–80 µm), subhedral to anhedral and often intergrown with other accessory phases. In general, accessory phases include allanite, apatite, beryl, cassiterite, galena, Fe-hydroxide (pseudomorph after pyrite), monazite, pollucite, pyrite, uraninite and xenotime (Fig. 3g–i). In sample 04R45 one Nb-Ta phase from the pyrochlore-supergroup was identified with SEM (Fig. 3g). Additionally columbite and tantalite were reported by Niedermayr & Göd (1992), Mali (2004) and Ahrer (2014).

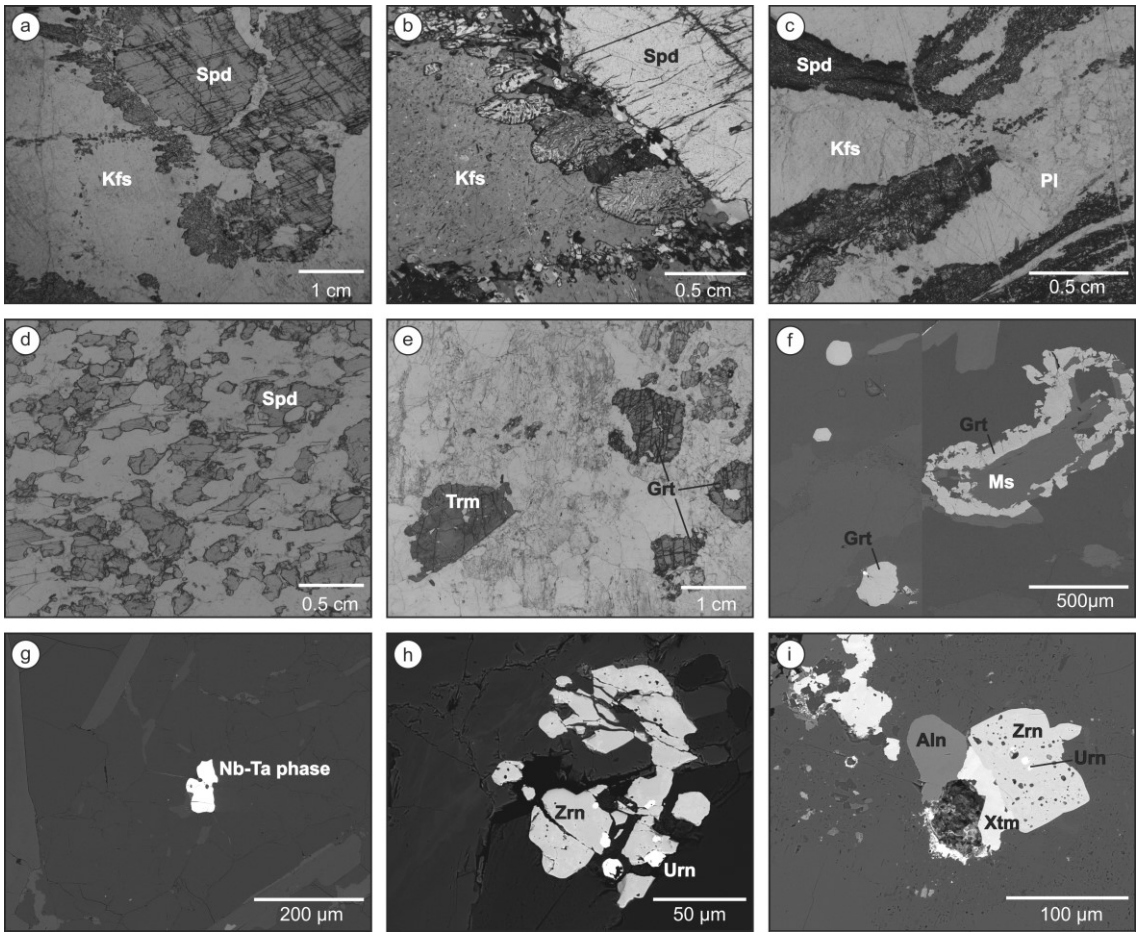


*Fig. 3. Thin section micrographs and BSE images. (a) Large spodumene crystals at the contact to a spodumene-quartz symplectite overgrowing K-feldspar (parallel polarizers; sample 04R45). (b) Detail of the spodumene-quartz symplectite (crossed polarizers; sample 04R45). (c) Patches of very fine-grained spodumene in association with deformed K-feldspar and plagioclase from a mylonitized pegmatite (parallel polarizers; sample PEG200 from Garrach spodumene pegmatite). (d) Mylonitic spodumene pegmatite with fine-grained recrystallized texture (parallel polarizers; sample 15R50 from Weinebene spodumene pegmatite group). (e) Tourmaline and garnet crystals in a fine-grained recrystallized matrix composed of quartz and feldspar (parallel polarizers; sample 04R45). (f) BSE image of type B garnet forming small euhedral grains and coronas overgrowing magmatic muscovite (sample PEG25-1). (g) Nb-Ta phase from the pyrochlore-supergroup in association with quartz (dark gray) and muscovite (light gray) (sample 04R45). (h) Allanite, zircon, xenotime and uraninite cluster overgrowing xenotime within feldspar and quartz (sample PEG25-1). (i) Zircon and uraninite within feldspar and quartz (sample RS33/01).*

### DESCRIPTION OF ANALYZED SAMPLES

As mentioned above the spodumene pegmatite dikes and leucogranite bodies show a variable Alpine deformational overprint. In order to avoid possible chemical changes associated to an Alpine overprint, samples from homogeneous zones with limited deformation were selected for further investigations. Hence, macroscopically, the dated samples of spodumene pegmatites only show semi-brittle deformation while the dated leucogranites are slightly sheared and recrystallized to protomylonitic. Important samples are listed in Table 1 and characteristic features are summarized in Table 2.

Sample 04R45 from the Hohenwart spodumene pegmatite (location [a] in Fig. 1) represents a garnet- and tourmaline-rich, fine- to medium-grained, spodumene-bearing internal zone 2. It shows a weak deformation imprint with euhedral to subhedral garnet, tourmaline, K-feldspar, muscovite and spodumene porphyroclasts within recrystallized plagioclase, quartz and fine-grained muscovite.

Sample 15R42 from the Lachtal spodumene pegmatite (location [a] in Fig. 1) was taken from a boulder with a coarse-grained texture and incipient schistosity. Tourmaline and garnet are subordinate species, with the latter reaching 0.5–2 mm in diameter. Three samples from the Mitterberg spodumene pegmatite (location [c] in Fig. 1) were investigated.

Sample 14R16 comes from a weakly deformed garnet- and tourmaline-rich internal zone 1 close to the spodumene-bearing internal zone 2. From the latter, K-feldspar and spodumene of sample 14R23 were taken from several centimeter-sized crystals.

From the margin of the internal zone 1 toward the border zone, K-feldspar and coarse-grained muscovite of sample 14R24 were extracted from centimeter-sized euhedral crystals embedded in a matrix composed of quartz and plagioclase.

Schlösselberg leucogranite 15R69 from the Uttenheim pegmatite field (location [h] in Fig. 1) is a medium to coarse-grained augengneiss with a continuous to mylonitic schistosity. Subordinate garnet and tourmaline are present as porphyroclasts with a 0.5–3 mm grain-size. From the Martell leucogranite (location [i] in Fig. 1) two samples previously mentioned in Meair & Schuster (2003) were investigated. Sample RS32/01 represents a fine-grained leucogranite with 0.4–2 mm sized garnet and tourmaline as ferromagnesian minerals.

RS33/01 comes from a coarse-grained pegmatitic layer close to the contact to the country rocks. Tourmaline forms several centimeters large, euhedral (-subhedral) crystals, whereas garnet is 0.5–5 mm in diameter. Accessory zircon with uraninite inclusions is common (Fig. 3h).

PEG25-1 was sampled from a marginal aplitic zone of the Geißrücken leucogranite (location [b] in Fig. 1). It is the only sample that contains additional type B garnet (see following section) as up to 0.2 mm large euhedral crystals and 0.1–0.2 mm thick coronas surrounding coarse-grained muscovite (Fig. 3f). As accessory minerals allanite, zircon, xenotime and uraninite have been found as inclusions in garnet overgrowths (Fig. 3i).

Sample PEG57-1 was collected from the Trahütten leucogranite (location [e] in Fig. 1) and represents an inhomogeneous aplitic gneiss with diffuse pegmatitic domains. While the aplitic parts are relatively rich in garnet and tourmaline needles with a characteristic length of a few millimeters, the pegmatitic domains mostly consist of quartz and feldspar. The garnet crystals are about 2 mm in diameter subhedral and intergrown with quartz.

WHOLE ROCK AND MINERAL GEOCHEMISTRY

This section focuses on results of main and trace element compositions of whole rocks and minerals.

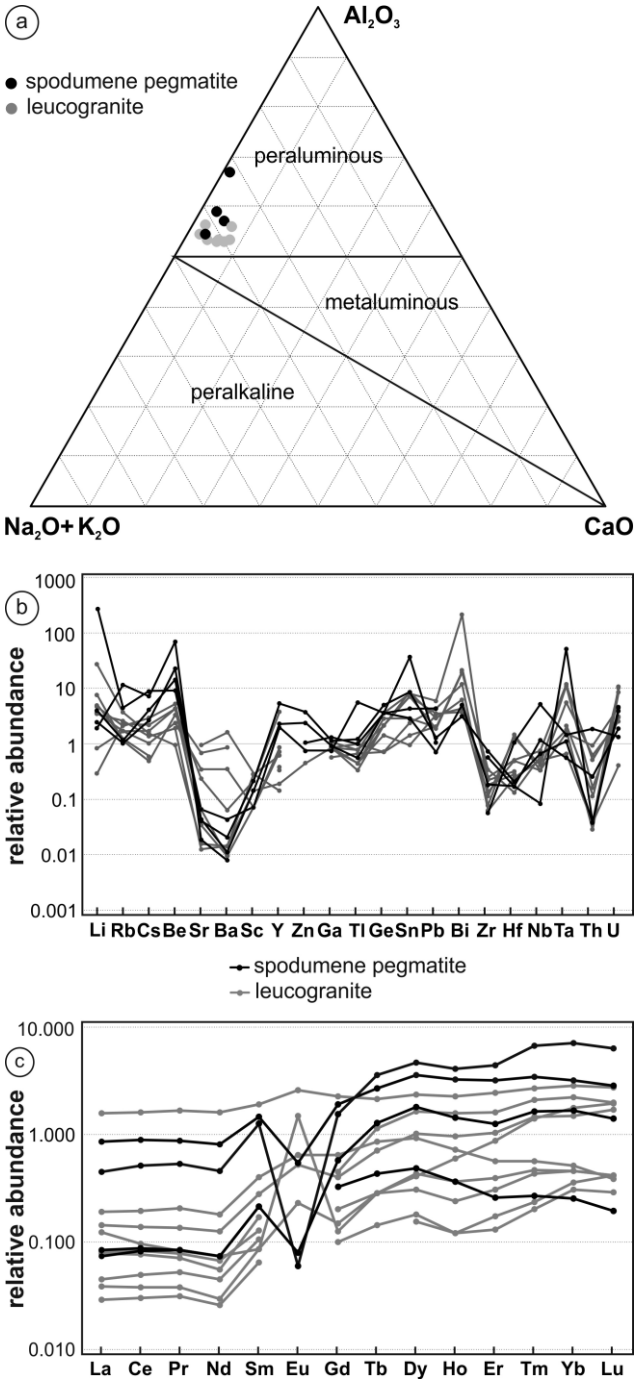


*Fig. 4. Whole rock geochemistry of the spodumene pegmatites and leucogranites. (a) Ternary plot with normalized Al2O3-Na2O+K2O-CaO oxide components in mol.% after Irvine & Baragar (1971) indicating a peraluminous character of the investigated rocks. (b) Pattern of selected elements normalized to the average composition of the upper continental crust after Rudnick & Gao (2003). Notice the lower Ba and Zr contents as well as the relative higher Cs, Be, Tl and Th contents in leucogranites with respect to the spodumene pegmatites. (c) REE patterns normalized to the average composition of upper continental crust after Rudnick & Gao (2003). Leucogranites show a positive Eu anomaly, whereas spodumene-pegmatites are characterized by a negative Eu anomaly Interpretation see text.*

WHOLE ROCK GEOCHEMISTRY

The spodumene pegmatites and leucogranites have the following geochemical characteristics (Table 4): $SiO_2$ is between 70.5 and 77.7 wt.% and $Al_2O_3$ is in the range of 12.5–15.2 wt.%. $TiO_2$, MgO and CaO contents are low and $Na_2O+K_2O$ is in the range of 5.3–8.5 wt.%. The compositions plot in the field of granite in the diagram of Middlemost (1994) and in the peraluminous field in the diagram of Irvine & Balagar (1971) (Fig. 4a). The $K_2O$ content (0.65–0.90 wt.%) is low in spodumene pegmatites (except for sample 15R42; $K_2O$=3.70 wt.%), whereas leucogranites have a medium to high $K_2O$ content of 2.5–4.0 wt.%. In average the $Na_2O/K_2O$ ratios are higher in the spodumene pegmatites (1.18–7.28) than in the leucogranites (0.32–1.74. In comparison with the values of the upper continental crust (Rudnick & Gao 2003) spodumene pegmatites are enriched in Be, Li and Sn and slightly enriched in Cs and Ge (Fig. 4b). For these elements the leucogranites show lower values but similar trends. In both rock types Sc, Ba and Sr are depleted, however Ba is less depleted in the eucogranites. The high field strength elements show the following systematics: U is slightly enriched, Ta is scattered around the value of the upper continental crust and Nb, Zr, Hf, and Th are depleted. REE are in the range of the upper continental crust with a slight depletion in the light REE. Spodumene pegmatites are characterized by a negative Eu anomaly, whereas leucogranites show a slightly positive Eu anomaly (Fig. 4b).

MINERAL MAJOR AND TRACE ELEMENT CHEMISTRY

Garnet: In all dated samples, garnet was characterized by BSE imaging and semiquantitative X-ray elemental maps (Fig. 5) as well as quantitative measurements with the EPMA (Tables 5a and 6a). These methods revealed two types (A, B) of garnet, each one being characterized by a particular habitus and chemistry. Type A is present in all samples, whereas type B only occurs in sample PEG25-1 (Table 3). Irrespective of the garnet type the andradite component is less than 1 mol.% and the uvarovite component is absent.

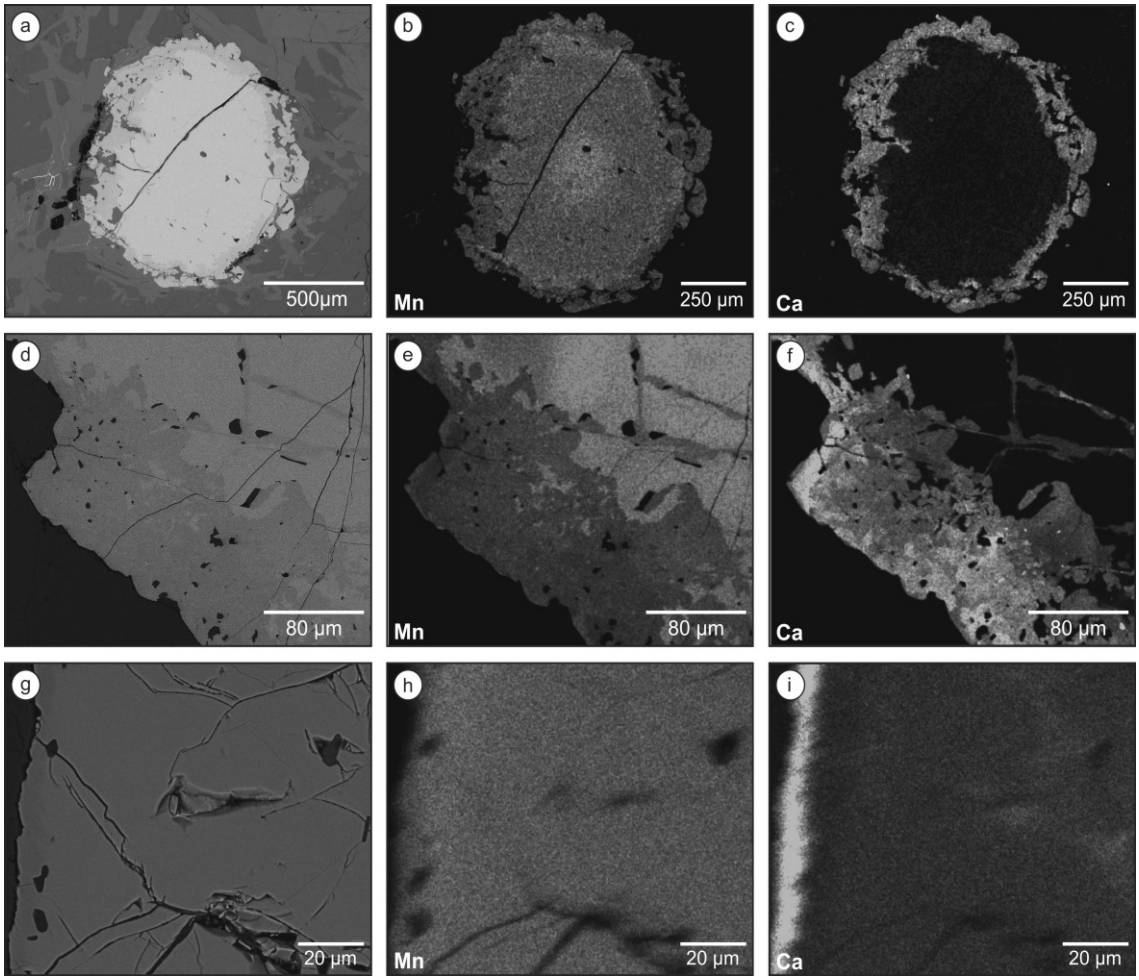


*Fig. 5. BSE images (a, d, g) and X-Ray elemental maps (Mn: b, d, h; Ca: c, f, i) of type A garnet showing a Mn-rich core and a Ca-rich overgrowth. (a) The core shows less inclusions than the overgrown rim (sample 04R45). (b) Mn is enriched in the garnet inner core and locally at the contact to the Ca-rich rim (lighter gray areas). (c) Ca is depleted in the core, but abundant in the overgrowth (lighter gray areas). (d–f) Detail of a sharp and partly toothed overgrowth enriched in Ca and depleted in Mn in comparison to the core. The Mn content is elevated at the contact to the Ca-rich rim. The Ca content in the overgrowth increases from the inner to the outer part. Cracks are healed with a Ca-rich garnet (sample 04R45). (g–i) Detail of an extremely thin and sharp Ca-rich overgrowth (sample RS33/01).*

Type A garnet is characterized by a relatively large inclusion-poor core zone and a relatively thin inclusion-rich overgrowth (Fig. 5a–c). As the core zone is dominated by the almandine and spessartine endmembers (more than 90 mol.%) with low grossular (1.7–3 mol.%) and pyrope (0.4–1.5 mol.%) it appears brighter than the overgrowth in BSE-images. The core zone may be continuously zoned with core-to-rim decrease of the spessartine proportion, balanced by an increase of the almandine component. The overgrowth is grossular-rich (30–45 mol.%), and relatively poor in the almandine (25–47 mol.%) and spessartine (13–42 mol.%) components. It contains abundant inclusions of quartz and zircon as well as fine-grained muscovite. The contact

between the core and the overgrowth is sharp, sometimes toothed and irregular. The core shows corrosion patterns sometimes associated with a local increase of the spessartine component (Fig. 5b, h). In sample PEG57-1, the overgrowth is just a few µm thick and could not be measured by EPMA (Fig. 5g–i). However, elemental maps typically show a slight enrichment of Ca on the margin. The core can also be crosscut by thin (5–10 µm) and elongated (80 µm at maximum) domains that have a similar grossular-rich composition as the overgrowth and contain very fine inclusions (Fig. 5d–f). They are interpreted as healed cracks infilling fractures at the same time as the formation of the overgrowth.

Type B garnet was only found in sample PEG25-1, together with type A. It has a similar grossular-rich composition (almandine: ~52 mol.%, spessartine: ~15 mol.%, grossular: ~31 mol.%, pyrope: ~1 mol.%) as the overgrowth of Type A garnet. Type B garnet occurs either as small euhedral to rounded grains or larger corona garnets around magmatic muscovite (Fig. 3f). The origin of the two types of garnet is crucial for the interpretation of the Sm-Nd ages and is discussed later.

In-situ trace element compositions of garnet from dated spodumene pegmatites and one leucogranite revealed variable transition metal contents: Cr (1.9–3.2 ppm), Co (< 0.1 ppm) and Ni (< 0.52 ppm, except sample 15R69 rim with 4.93 ppm) are low, whereas for Zn moderate to high contents (270–725 ppm) have been measured. The Li content systematically decreases from core (600–780 ppm) to rim (233–750 ppm). The largest difference was measured in sample 15R42 (712 ppm in core, 233 ppm in rim) (Table 6a).

K-feldspar and plagioclase (Fig. 6a, Tables 5 and 6): Microprobe analyses on K-feldspar show the same endmember composition ($Or_{90–98}Ab_{2–10}An_{0–0.1}$) for all samples. In all samples, except 04R45, the albite component decreases slightly from core to rim. Plagioclase shows similar endmember compositions ($Ab_{90–98}An_{2–10}Or_{0.4–2}$) in all investigated samples. No particular chemical zoning was detected. In sample 15R69 the iron content (1490 ppm) is somewhat larger than in the other samples. Except for Ba and Sr, the plagioclase tends to be depleted in trace elements in comparison to the whole rock.

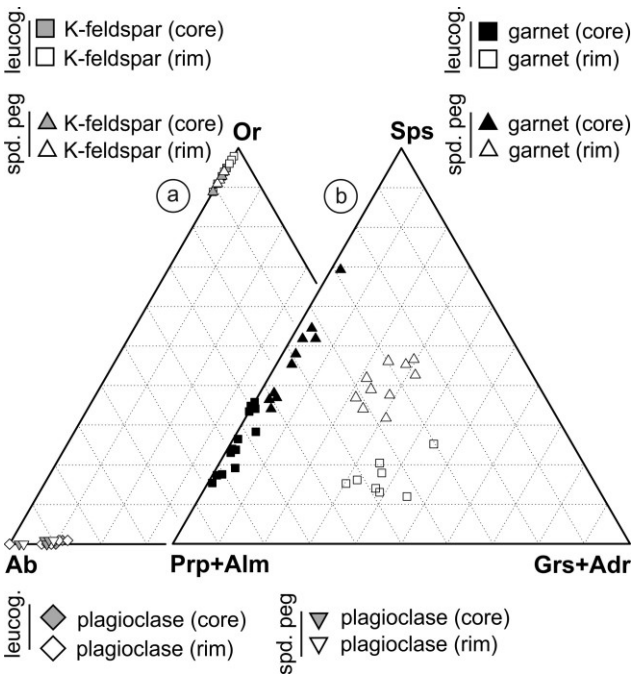


*Fig. 6. Ternary plots of compositional endmembers for feldspar and garnet from spodumene pegmatites and leucogranites. (a) The endmembers of K-feldspar and plagioclase are orthoclase (Or), albite (Ab) and anorthite (hidden vertex of the triangle). Measured K-feldspar crystals shows a high orthoclase component, whereas plagioclase shows a high albite component. (b) The endmembers of garnet are spessartine (Sps), pyrope+almandine (Prp+Alm) and grossular+andradite (Grs+Adr). The garnet cores are dominated by the almandine and spessartine endmembers, whereas the rims (overgrowth) show an enrichment in the grossular component.*

Tourmaline: Black tourmaline crystals from spodumene pegmatite samples 04R45, 14R16 and 15R42 were investigated in detail with EPMA, LA ICP-MS and single-crystal structure determination (Tables 5d and 6c). The chemical composition of these tourmalines is characterized by relatively high Na and Fe and significant Li and also minor Mg contents. Because of the relatively high <*Y*–O> distances with ~2.04 Å

(Table 8b) most of the Fe is present as $Fe^{2+}$. This allows a classification of the analyzed crystals mainly as members of the schorl-elbaite solid solution series with a dominant schorl component and a minor dravite component. Such dravite component together with significant amounts of $Fe^{3+}$, which were also reflected by increased <*Z*–O> distances of ~1.92 Å (Table 8b), can only rarely be observed in tourmalines of the schorl-elbaite series (Ertl *et al.* 2016). Tourmaline from sample 14R16, which has a relatively high $Fe^{2+}$ content in combination with a lower Li content compared with the other tourmaline samples, can be assigned to Li-bearing oxy-schorl. Because of measured <*T*–O> distances, which are close to 1.620 Å (Table 8b), it can be excluded that significant amounts of Al or B occupy the Si-position. The structural formula of the investigated tourmalines, in which the cations were assigned to the different sites based of the average distances (Table 8b), are presented in Table 8a. The amount of OH was calculated based on charge-balanced formulae. *In-situ* trace element data of tourmaline from spodumene pegmatites revealed an increase in Li content from core (350–3600 ppm) to rim (570–4200 ppm). However, core to rim decrease of Li was measured in sample 15R42 (1348 ppm in core and 713 ppm in rim). Lower amounts of Li were measured in tourmaline from the leucogranite sample 15R69 (354 ppm in core and 570 ppm in rim).

Muscovite (Table 7): Chemical compositions characterise the investigated white mica as muscovite. Trace element analyses with LA ICP-MS were carried out on large muscovite crystals from more than 40 samples of leucogranites and spodumene pegmatites. They show progressively decreasing K/Rb ratios from leucogranites (63–193) to spodumene pegmatites (16–149). Similar trends can be seen in the K/Tl and K/Cs ratios. The K/Rb ratios are slightly negatively correlated with the Li content (28–780 ppm in leucogranites and 375–1744 in spodumene pegmatites) (Fig. 7a) as well as the Tl content (2–20 ppm in leucogranites and 2–28 ppm in spodumene pegmatites) (Fig. 7b). Cs concentrations in coarse-grained muscovite are in the range of 4–750 ppm in leucogranites and 11–788 ppm in spodumene pegmatites. The measured Ba values in muscovite are in the range of 1–200 ppm in leucogranites and somewhat lower values of 1–79 ppm were determined in the spodumene pegmatites. With respect to the pegmatite classification of Černý & Burt (1984), muscovite from leucogranites plot in fields of muscovite-barren and muscovite-bearing pegmatite classes (bright gray dots in Fig. 7a, b), whereas spodumene pegmatites reach the fields of moderately evolved pegmatites (black dots in Fig. 7a, b).

Spodumene: In order to keep low Li blanks in the mass spectrometer, spodumene was not analyzed with LA ICP-MS. Chemical compositions of spodumene from the literature (including wet chemical analyses) are reported here for a few occurrences. In spodumene from the Koralpe and Wölzer Tauern pegmatite fields the contents of $Li_2O$ and $Fe_2O_3$ typically range from 6.05–7.70 wt.% and 0.32–1.19 wt.%, respectively (Heritsch 1984, Moser *et al.* 1987, Wenger & Armbruster 1990, Senzenberger 2001). Spodumene from the St. Radegund pegmatite field shows a larger variation in $Li_2O$ ranging from 5.83–7.90 wt% and the highest measured values of $Fe_2O_3$ are up to 1.19 wt.% (Koller *et al*. 1983, Senzenberger 2001, Gotthardt 2015). A pure stoichiometric spodumene contains 8.03 wt.% of $Li_2O$ and no $Fe_2O_3$. Therefore, Mali (2004) the interpreted the values reported in the literature to reflect variable alteration of spodumene.

## Sm-Nd AND Rb-Sr ISOTOPE GEOCHEMISTRY AND AGES

This section focuses on the results of Sm-Nd and Rb-Sr isotope analyses and calculated ages.

### SM-ND AND RB-SR ISOTOPIC DATA

Results of Sm-Nd and Rb-Sr isotopic analyses on spodumene pegmatites and leucogranites presented in this section are listed in Tables 9 and 10. Sm-Nd data show clear systematics. While Sm and Nd contents of the whole rock are variable in the range of 0.3–6.7 ppm and 0.8–21 ppm, respectively, the whole rock analyses yield scattering Rb and Sr contents and high $^{87}Rb/^{86}Sr$ ratios. However, the initial $^{87}Sr/^{86}Sr$ ratios calculated with the ages of the corresponding sample

given in Table 9 lie in a relatively narrow range (0.7098–0.7353, except for sample RS33/01, which gives an unrealistic ratio of 0.7007). Spodumene is characterized by a low concentration of Rb and Sr and a relatively low $^{87}Rb/^{86}Sr$ ratio of approximately 75. Due to high Rb concentrations in the measured K-feldspar and muscovite fractions, their $^{87}Rb/^{86}Sr$ ratios are several hundred in K-feldspar and more than 8000 in muscovite.

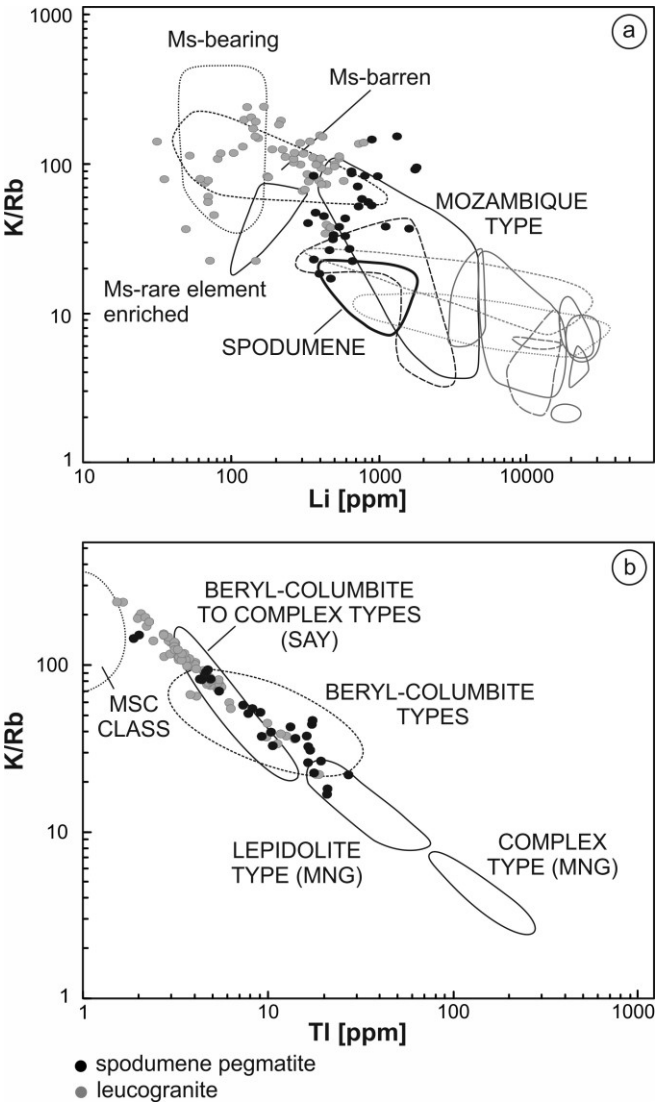


*Fig. 7 1 FIG. 7. Trace element characteristics of magmatic muscovite from spodumene pegmatites (black dots) and leucogranites (bright gray dots) plotted in the diagrams (a) Li content versus K/Rb ratio and (b) Tl content versus K/Rb. Muscovite crystals from leucogranites shows a higher K/Rb ratio and less lithium than those from spodumene pegmatites. With respect to the reference fields for different types of pegmatites (Černý & Burt 1984) muscovite from spodumene pegmatites does not plot in the field of spodumene type pegmatites. For fields of white mica from highly fractionated pegmatites see Černý & Burt (1984). MNG: Mongolia, SAY: Sayan Mountains.*

### Sm-Nd ages

Results of Sm-Nd geochronology on spodumene pegmatites and leucogranites presented in this chapter are listed in Table 9 and the calculated ages are plotted in Figure 8. Both assessment of result quality and age interpretation are presented in the discussion.

Sample 04R45 (Hohenwart spodumene pegmatite): Two garnet fractions, one tourmaline fraction and the whole rock powder were analyzed. Selected garnet grains were broken pieces of larger crystals with a bright orange-pinkish color. Most of them were water clear, but some were slightly turbid. Some grains contained very fine black inclusions, identified as graphite. Two-point isochron age calculations of tourmaline with the garnet2 and garnet3 fractions yield 264.8±2.7 Ma and 258.6±2.6 Ma, respectively. All data points together tightly plot along a regression line corresponding to an age of 261±13 Ma (MSDW=18, initial $^{143}Nd/^{144}Nd$=0.51189±0.00040, Fig. 8a).

Sample 15R42 (Lachtal spodumene pegmatite): Two garnet fractions and the whole rock powder were analyzed. Both garnet fractions (garnet1 and garnet2) represent fragments of larger crystals. Grains were pinkish, water-clear and had smooth surfaces. A few of them contained tiny black inclusions or adherences of iron oxide. The latter were removed during the leaching procedure. A best-fit three-point isochron yields an age of 267.5±2 Ma (MSWD=1.14, initial $^{143}Nd/^{144}Nd$=0.511875±0.000009, 8b).

Sample 14R16 (Mitterberg spodumene pegmatite): Two garnet fractions, one tourmaline fraction and one whole rock powder were analyzed. The garnet fractions (garnet1 and garnet2) consisted of fragments of garnet crystals with an orange-pinkish color. They had smooth surfaces and were water-clear. Some grains of fraction garnet2 contained tiny black inclusions or adherences of iron oxides, which were removed during the leaching procedure. Ages calculated from garnet1 with the whole rock and tourmaline yield two-point isochron ages of 266.5±2.8 Ma and 266.2±2.7 Ma, respectively, those for garnet2 are 261.9±2.7 Ma and 261.7±2.6 Ma. The best-fit isochron calculated with all four data points shows an age of 263.4±8.6 Ma (MSWD=5.7, initial $^{143}Nd/^{144}Nd$=0.51190±0.00023, Fig. 8c).

Sample 15R69 (Schlösselberg leucogranite): Two garnet fractions and a whole rock powder were investigated. Fraction garnet1 consisted of angular pieces of larger crystals with an orange color, whereas garnet2 was pinkish and contained several complete garnet grains with a ball shape. All data points are aligned tightly along a regression line with an age of 270±2.1 Ma (MSWD=0.63, initial $^{143}Nd/^{144}Nd$=0.511839±0.000007, Fig. 8d).

Sample RS32/01 (Martell leucogranite): Two garnet fractions (0.20–0.45 mm), one feldspar+quartz fraction (0.20–0.30 mm) and a whole rock powder were analyzed. The garnet2 fraction was picked after the results for garnet1 were measured so that a fraction as pure as possible was analyzed. For both fractions grains were water-clear, pinkish colored and had shapes like slivers of broken glass with wavy or rough surfaces. Very few grains of garnet1 had fine intergrowths of quartz or inclusions of black unidentified opaque phases. Ages calculated from the whole rock and garnet1 and garnet2 yield 291.2±3.2 Ma and 276.8±2.8 Ma, respectively. All three data points result in an age of 276±69 Ma (MSWD=44, initial $^{143}Nd/^{144}Nd$=0.5120±0.0018). An age calculation including the feldspar+quartz fraction yields 279±24 Ma (Fig. 8e).

Sample RS33/01 (pegmatitic layer within the Martell leucogranite): Fractions of garnet (0.20–0.45 mm), feldspar+quartz (0.2–0.3 mm) and whole rock powder were used. Garnet grains were water-clear, had a pinkish color and were shaped like glass slivers. There were a few tiny intergrowths of quartz or black unidentified opaque phases. Calculations of garnet with WR gives an age of 273.0±2.9 Ma (initial $^{143}Nd/^{144}Nd$=0.512073±0.000006, Fig. 8f). The feldspar+quartz fraction does not plot on the regression line and was not taken into account for age calculation (see discussion).

PEG25-1 (Geißrücken leucogranite): Two garnet fractions and the whole rock powder were investigated. Selected garnet grains represented broken pieces of larger crystals with a bright pinkish color. They were water-clear or slightly turbid and mostly showed rough surfaces. In a second step, this separate was split into an optically pure fraction and a second one with very few remnants of quartz and feldspar as well as black dots of graphite or other opaque minerals. The best-fit three point isochron gives an age of 259±2.3 Ma (MSWD=0.41, initial $^{143}Nd/^{144}Nd$=0.511891±0.000006, Fig. 8g).

Sample PEG57-1 (Trahütten leucogranite): Two garnet fractions, one tourmaline fraction and the whole rock were analyzed. All selected garnet grains were broken pieces of larger crystals with an orange-pinkish color and rough surfaces. Most of them were water clear, but some were slightly turbid. In a second step, this separate was split into an optically pure fraction and a second one with very few black dots representing graphite or other opaque minerals. All data points are aligned tightly along a regression line with an age of 250.4±5.3 Ma (MSWD=0.41, initial $^{143}Nd/^{144}Nd$=0.51192±0.00009, Fig. 8h).

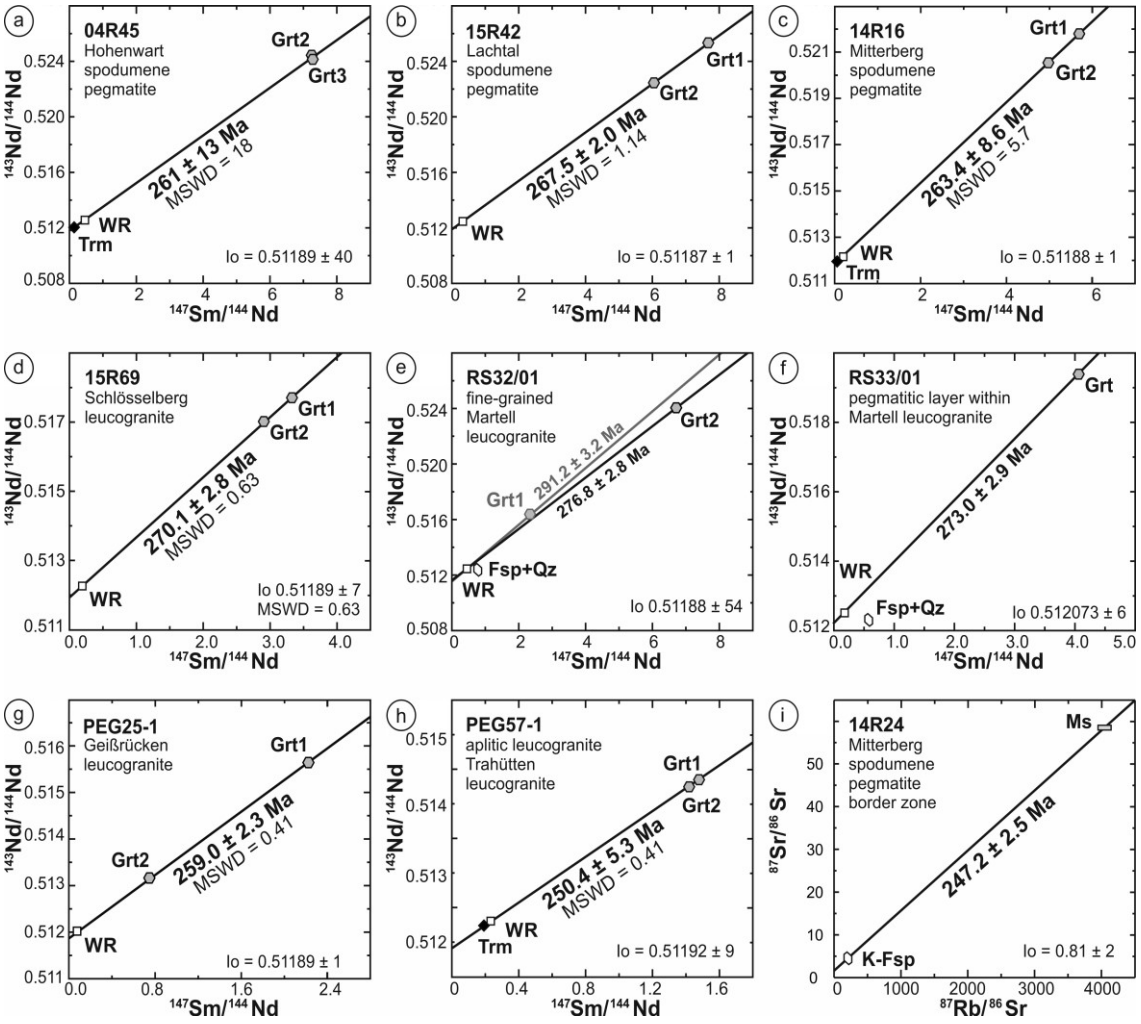


*Fig. 8. Geochronological data. (a–c) Spodumene pegmatites yield Sm-Nd garnet ages in the range of 245–275 Ma and garnets are characterized by high 147Sm/144Nd ratios (5.5–7.5). (d–h) Sm-Nd garnet ages of leucogranites spread between 255–280 Ma. (i) Rb-Sr age calculated from muscovite and K-feldspar from the border zone of Mitterberg spodumenne pegmatite. I0 represents the initial Nd or Sr isotopic ratio calculated for the determined age.*

### Rb-Sr ages

Rb-Sr-ages calculated from Mitterberg spodumene pegmatite are listed in Table 10 and plotted in Fig. 8i. From spodumene and K-feldspar of sample 14R23 (internal zone), an age of 272.2±3.0 Ma with an initial $^{87}Sr/^{86}Sr$ ratio of 0.629 can be determined. K-feldspar and muscovite of sample 14R24 (border zone) yield an age of 247.2±2.5 Ma and an initial $^{87}Sr/^{86}Sr$ ratio of 0.81.

### Discussion

In the following discussion, we address the interpretation of the observed assemblages and microstructures with respect to their magmatic *versus* tectono-metamorphic origin. We also interpret the isotopic and age data as well as the relationships between spodumene pegmatites and leucogranites. Finally, we discuss briefly the classifications of the investigated spodumene pegmatites from the Eastern Alps with respect to the nomenclature by Černý & Ercit (2005).

### Interpretation of mineral assemblages and microtextures: magmatic or tectono-metamorphic?

Inherto existing macroscopic and microscopic investigations on pegmatites of the Austroalpine Unit show a polyphase crystallization and deformation history during the Permian and Alpine events (Thöni & Miller, 2000; Habler & Thöni, 2001; Schuster & Stüwe, 2008, Gaidies *et al.,*

2008). The microtextures of spodumene pegmatites and leucogranites investigated in this study also underline the occurrence of a two phased history. The primary assemblages in the investigated samples include K-feldspar, quartz, plagioclase, muscovite (larger than 0.5 cm), tourmaline, garnet and additional spodumene in spodumene pegmatites. These minerals are often coarse-grained, show a euhedral to subhedral shape and no or limited shape preferred orientation. The observed primary assemblages are typical magmatic assemblages for spodumene pegmatites (Simmons *et al.* 2016, Roda-Robles *et al.* 2016) and leucogranites (Searle & Fryer 1986, Černý *et al.* 2012). Therefore, also following Habler *et al.* (2007) and Thöni *et al.* (2008), we interpret the primary assemblages as magmatic and products of crystallization during the Permian extensional event (see interpretation of ages below).

The Alpine overprint had a structural and chemical impact on the pegmatitic and leucogranitic microtextures and minerals therein. In the investigated samples, magmatic tourmaline, spodumene and K-feldspar are less affected by recrystallization, but are often fractured and/or form porphyroclasts. Large magmatic muscovite is typically kinked and due to its shape slightly orientated in the Alpine schistosity. Fine-grained muscovite is dispersed along the Alpine schistosity and has a shape preferred orientation. It is interpreted as the result of grain-size reduction by recrystallization of magmatic muscovite and/or formation by hydration of feldspar during the Alpine overprint. Dynamic recrystallization was also observed in quartz and plagioclase. Two types of recrystallization mechanisms can be inferred from the microstructures (Passchier & Trouw 2009). Highly irregular grain-boundaries, pinning structures and left-over grains in quartz indicate grain boundary migration. Additionally, small uniform sized, slightly elongated quartz and feldspar grains argue for subgrain rotation. In absence of any overprinting evidence, we suggest that both recrystallization mechanisms were active at the same time. These observations are consistent with deformation at upper greenschist- to eclogite-facies conditions, which are proved for the Alpine metamorphism of the country rocks (Thöni & Miller 2000, Habler *et al.* 2007, Thöni & Miller 2010).

Garnet occurs in two different generations. In type A garnet, the first generation is represented by Mn-rich, euhedral to subhedral cores with a diameter of 0.5 to 5 mm. Such a chemistry is typical of magmatic garnet (Selway *et al.* 2005, London 2008). The second generation corresponds to Ca-rich overgrowths and healed cracks within cores of type A garnet as well as type B garnet, represented by small euhedral grains within the matrix and coronas around magmatic muscovite. Inclusions of fine-grained, recrystallized muscovite and quartz that are the result of Alpine deformation and metamorphism are common within garnet overgrowths.

Ca-rich garnet in metagranitoids typically forms during metamorphism along pressure-dominated gradients (Rubbo *et al.* 1999, Proyer 2003). Similar garnet, as described herein, has already been reported from Permian simple pegmatites of the Austroalpine Unit (Miller & Thöni 1997, Miller *et al.* 2007) and has been interpreted as products of the Alpine metamorphic overprint, due to investigations on REE patterns of garnet cores and overgrowths (Thöni *et al.* 2008) and a detailed study of healed cracks within garnet cores (Griffiths *et al.* 2014). We therefore conclude that the observed garnet overgrowths, corona garnets and healed cracks in the magmatic garnet cores of the spodumene pegmatites and leucogranites also formed during the Alpine orogenic event.

Pinning the formation of the spodumene-quartz symplectites to an event is not straightforward. They have sharp and straight boundaries to the spodumene crystals, but convex inward boundaries to the K-feldspar crystals, indicating that they propagated into the K-feldspar, similarly to myrmekites. The straight boundary to the spodumene without evidence for reaction might indicate that these symplectites grew as overgrowth over spodumene. The origin of quartz in the symplectites is however difficult to explain with new spodumene growth alone. A possible explanation is that the symplectites formed according to the reaction $Li^{+}$+K-

feldspar=spodumene+quartz+$K^+$+$Na^+$ (Mali 2004). That would be evidence for Li transfer, either by late magmatic fluids or during Alpine metamorphic processes.

### Nd and Sr isotopic systematics

First of all, the whole rock Nd and Sr isotopic ratios indicate a crustal origin of the melts out of which the leucogranites and spodumene pegmatites crystallized (Philpotts & Ague 2009). The similar $^{147}Sm/^{144}Nd$ ratios, $\varepsilon(t)_{Nd}$ values and the initial $^{87}Sr/^{86}Sr$ isotopic ratios of the investigated samples indicate that they are typical for the spodumene pegmatites and leucogranites and related to their genesis. In contrast, the strongly different REE contents will be due to heterogeneously distributed REE-rich minerals and whole rock powders, which are only representative for a certain zone of the magmatic body. This interpretation is in line with the problematics of measuring an average composition of zoned pegmatites and other coarse-grained magmatic rocks. The somewhat different Nd and Sr isotopic ratios in sample RS33/01 may be a result of this problem.

Generally, the $^{147}Sm/^{144}Nd$ ratios of garnet fractions are positively correlated with the Nd contents (*e.g.*, Thöni *et al.* 2008). This observation can be explained by tiny inclusions of REE-rich phases like monazite, xenotime, zircon or apatite, which are not enriched in heavy REE. Following this hypothesis, the garnet fractions of the leucogranites should have been less pure than those of the spodumene pegmatites. Further, such inclusions seem to be the reason why the $^{147}Sm/^{144}Nd$ ratios of the garnet 2 fraction from leucogranite PEG25-1 and the garnet1 fraction from leucogranite RS32/01 are lower (0.83 and 2.3, respectively) than in the other investigated garnet fractions. In fact, in sample PEG25-1 many zircon inclusions have been found in garnet by SEM investigations. However, as there is a positive correlation of the $^{147}Sm/^{144}Nd$ ratios between the garnet fractions and the corresponding whole rock powders, higher $^{147}Sm/^{144}Nd$ ratios in the spodumene pegmatites in comparison to the leucogranites may also be due to the REE composition of the whole rock. The $^{147}Sm/^{144}Nd$ ratios of garnet fractions exceeding 7 are in the range of the highest values reported in the literature and indicate a high sample purity (Sölva *et al.* 2003, Habler *et al.* 2007).

### Remarks on garnet Sm-Nd geochronology on pegmatites

The Sm-Nd method is highly suitable for dating garnet-bearing granitic rocks (Prince *et al.* 2003, Thöni *et al.* 2008, Zeitlhofer *et al.* 2013). It is an alternative when zircon dating is problematic due to a low quantity, an inherited origin, a small grain-size or intense metamictization of the available zircon. Magmatic garnet is usually inclusion-poor and shows high $^{147}Sm/^{144}Nd$ ratios due to fractionation of heavy REE (*e.g.*,Thöni et al. 2008). Furthermore, in Fe-Mn-rich garnet the Sm-Nd isotopic system is robust during metamorphic overprint and deformation. According to Thöni (2002; and references therein), Nd and Sm diffusion in mm-sized garnet is insignificant up to 700°C. Metamorphic overgrowths are more problematic. On the one hand, they can easily be detected by SEM and EPMA, but on the other hand it is not straightforward to remove them during separation of the garnet fractions.

In our case, two types of garnet could be distinguished in the investigated samples (Fig. 5). The cores of type A garnet is magmatic while its overgrowths and type B garnet formed during the Alpine metamorphic overprint (see above). As this metamorphic garnet contains less Fe, it is less magnetic and grains containing metamorphic overgrowths could be removed by magnetic separation. Further, metamorphic garnet contains frequent minute inclusions, which allowed us to remove it from the separates by hand-picking under the binocular microscope. Another problem are submicroscopic inclusions of REE-rich phases (Thöni 2002). In the investigated rocks most apatite, monazite or xenotime inclusions are thought to have crystallized more or less

contemporaneously with magmatic garnet, inducing an insignificant disturbance on the Sm-Nd ages. In contrast, zircon may contain older inherited cores, which could have an effect on the calculated age.

INTERPRETATION OF SM-ND AND RB-SR AGES

Calculations of Sm-Nd ages show that whole rock powders, tourmaline and garnet fractions usually fit to isochrones with errors of about 1% of the age value. In contrast, both feldspar+quartz mixtures plot below the regression line. This effect is most probably due to a disturbance of the isotopic system during recrystallization and decomposition of feldspar in the course of the Alpine overprint. The sensitivity of feldspar (and especially K-feldspar) to this processes has already been documented (*e.g.*, Kruger *et al.* 1998, Sölva *et al.* 2003). Therefore, the feldspar+quartz fractions were not used for age calculations.

The errors in the range of 1% on the age value are due to the expected maximum errors on the $^{147}Sm/^{144}Nd$ ratio (samples 15R42, 15R69, 14R16, PEG25-1, PEG57-1). Larger errors for samples 04R45 and 14R16 result from slightly different age values of the individual garnet fractions. This effect is even larger in sample RS32/01. For this sample, a distinctly lower $^{147}Sm/^{144}Nd$ ratio in combination with a higher Nd content and a higher age value argues for contamination of fraction garnet1 by an older REE-rich phase, which could be zircon according to the SEM observations (Table 4). For this reason, we interpret the age calculated with garnet2 as geologically meaningful (Table 9). The large MSWD values for samples 04R45 and 14R16 are also an effect of the small analytical errors on the individual isotopic measurements, inducing that not all error bars are overlapping the regression line. Enlargement of the errors on the $^{143}Nd/^{144}Nd$ ratios to a value covering the long-term range of the La Jolla standard (±0.00001) reduces the MSWD value significantly without an effect on the age value or error on the age value (see also Dickin 1995).

Both Rb-Sr ages were measured from Mitterberg spodumene pegmatite, from which also a Sm-Nd garnet age is available. The garnet age of sample 14R16 is 263.4±8.6 Ma and the initial $^{87}Sr/^{86}Sr$ ratio calculated from the whole rock is 0.71335. In contrast, one of the Rb-Sr ages is higher and gives an unrealistic low initial $^{87}Sr/^{86}Sr$ ratio (sample 14R23: 272.2±3.0 Ma, initial $^{87}Sr/^{86}Sr$=0.629), whereas the other age is lower, but the initial $^{87}Sr/^{86}Sr$ ratio is much higher (sample 14R24: 247.2±2.5 Ma, initial $^{87}Sr/^{86}Sr$=0.81). This systematics indicate a slight disturbance of the Rb-Sr isotopic system. Overall, the Rb-Sr ages are in the range of the Sm-Nd garnet age, but, taken alone, they have to be considered with care. Somewhat problematic Rb-Sr data on spodumene from the Weinebene spodumente pegmatite group are also reported in Thöni & Miller (2000).

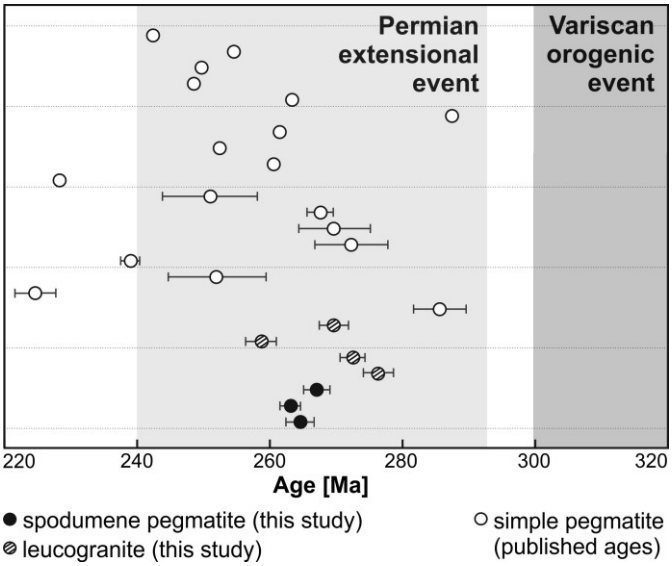


*Fig. 9. Compilation of Sm-Nd garnet ages from spodumene pegmatites, leucogranites and simple pegmatites of the Austroalpine Unit (this study, Thöni & Miller 2000, Habler & Thöni 2001, Schuster et al. 2001, Sölva et al. 2003, Habler et al. 2007, Thöni et al. 2008).*

Since the dated material corresponds to magmatic minerals, we interpret the Sm-Nd garnet ages given in Table 9 as crystallization ages. Taking all calculated errors into account, this implies a formation of the spodumene pegmatites and leucogranites in Permian to Early Triassic time

between 245 and 280 Ma (Figure 9). A somewhat younger Middle Triassic age of about 240 Ma has been published for the Weinebene spodumene pegmatite group. It is based on a zircon U-Pb (multigrain, upper intercept) age of 240+1.5 Ma (Heede 1997) and two Rb-Sr ages calculated from spodumene and whole rock yielding 238.5+2.6 Ma and 242.8+1.7 Ma (Thöni & Miller 2000). The age for the Martell leucogranite earlier mentioned in Mair & Schuster (2003) fits with the Rb-Sr WR-isochron of 271 Ma published by Bockemühl (1988). In general, the ages determined for the spodumene pegmatites and leucogranites reported in here overlap with those from previously published data on simple pegmatites from the Austroalpine unit (Schuster *et al.* 2001, Thöni *et al.* 2008).

### Relationships between the spodumene pegmatites and the leucogranites

The spodumene pegmatites occur within country rocks partly showing a Variscan (Carboniferous) amphibolite-facies metamorphism and in any case a Permian greenschist- to amphibolite-facies overprint (Froitzheim *et al.* 2008). For example, the Weinebene spodumene pegmatite group is situated within micaschists with Permian andalusite, which has been transformed into kyanite during the Alpine (Cretaceous) eclogite-facies metamorphism (Schuster & Stüwe 2008). The andalusite partly formed several centimeter- up to decimeter-sized chiastolites and Permian garnet is also present. These observations indicate Permian metamorphism at upper greenschist-facies conditions. For the micaschists of the rappold Complex in the close vicinity of the Hohenwart spodumene pegmatite metamorphic conditions of 5.3±0.3 kbar and 525±15°C have been determined by Gaidies *et al.* (2006) for the initial growth of Permian garnet. Geochronological age data (Schuster *et al.*, 2001, Gaidies *et al.* 2006) indicate emplacement of the pegmatite during metamorphism in the country rocks and therefore an intrusion depth of more than 10 km is assumed. Additionally, elevated pressures are in agreement with the fact that no petalite (*cf.* Li-aluminosilicate stability fields of London 1984, 2008) or miarolitic cavities have been found in the spodumene pegmatites.

The data presented here indicate that the investigated spodumene pegmatites and leucogranites of the Austroalpine Unit share many similarities, indicating a genetic relationship. In the field, both lithologies occur always in association with simple pegmatites within the same lithostratigraphic complexes. They also show similar geochemical characteristics, including a peraluminous granitic composition and continuous fractionation trends of several trace elements (Fig. 4b). Additionally, Be, Li, Rb, Cs, Sn and Ge contents are higher in spodumene pegmatites than in leucogranites whereas Ba shows an opposite trend. Analyzed leucogranites have a positive Eu anomaly whereas spodumene pegmatites show a negative one. These features argue for a fractionation trend from the leucogranites to the spodumene pegmatites with Ba and Eu extraction in feldspar during the melt evolution, while the light elements Li and Be, the large-ion lithophile elements Rb and Cs as well as Sn and Ge get progressively enriched in the remaining melt.

Spodumene pegmatites and leucogranites are also characterized by a similar magmatic mineral assemblage of K-feldspar, quartz, plagioclase, muscovite, garnet and tourmaline, with spodumene being only present in the pegmatites. A magmatic origin of garnet cores can be inferred from the high Mn and Fe contents typical for crystallization of a peraluminous melt in general (Whitworth & Feely 1994) and for fractionated pegmatites in particular (Selway *et al.* 2005). The occurrence of muscovite and tourmaline and absence of biotite can be explained by crystallization from a melt with a low $TiO_2$ content (average of 0.01 wt.% in the rocks) and sufficient B (Nabelek & Liu 2004). According to Nabelek & Liu (2004) biotite usually crystallizes in melts and fluids with more than 0.06 wt.% $TiO_2$ whereas otherwise tourmaline develops dominantly. The trends inferred from Rb, Li, Cs, Tl and Ba contents measured in magmatic muscovite are in line with those in the whole rocks. These trend are particulary notable for muscovite on the K/Rb *versus* Li and K/Rb *versus* Tl diagrams of Figure 7. Finally, the significant Mg content (dravite component) of tourmaline of the elbaite-schorl series indicates crystallization from an evolved melt (Ertl *et al.* 2009).

Hence, both whole rock and mineral geochemical arguments indicate that at least the larger spodumene pegmatites crystallized from melts fractionated by relatively small, inhomogeneous leucogranite bodies. This is in agreement with the field relations indicating that spodumene pegmatites occur at somewhat higher structural levels. A genetic relationship of the spodumene pegmatites to granites is partly consistent with the model of Göd (1989) for the formation of the the Weinebene pegmatite group. We however disagree with the hypothesis that the spodumene pegmatites derived from large granitic bodies that disappeared during the Alpine orogenic event. The result presented in here should be the basis for the development of a new genetic model for the Permian spodumene pegmatites of the Austroalpine Unit.

### Classification of the spodumene pegmatites from the Austroalpine Unit

According to the K/Rb *versus* Li and K/Rb *versus* Tl diagrams (Fig. 7), but also other discrimination plots by Černý & Burt (1984), the Permian spodumene pegmatites from the Austroalpine Unit do not plot in the expected field of spodumene-bearing pegmatites. Considering the fact that the albite component in the plagioclase is high in the investigated spodumene pegmatites, they can be classified as members of the albite spodumene class (Černý & Ercit 2005). Other albite spodumene class pegmatites are described for example from Little Nahanni field (Northwest Territory, Canada; Groat *et al.* 2003), Galicia (Spain; Fuertes-Fuente & Martin-Izard 1998) or Kings Mountain (North Carolina, USA; Kesler & Vine 1976). However, the Permian pegmatites described here show some differences with respect to the abundance and size of typical minerals like beryl or Nb-Ta phases and the grade of fractionation. This might be due to different geodynamic settings, genetic processes or country rocks. These divergences imply, that further investigations are needed to prove that albite-spodumene pegmatite represent a homogeneous subclass (Černý & Ercit 2005). Alternatively, further investigations on the genesis of these rocks may help to explain these differences in the future.

## CONCLUSIONS

Investigations on spodumene pegmatites and leucogranites from the Austroalpine Unit (Eastern Alps, Central Europe) yield the following results:

- Field observations show that both rock types occur in the same lithostratigraphic complexes always associated with simple pegmatites.

- The magmatic mineral assemblages consists of K-feldspar, quartz, plagioclase, muscovite, garnet and tourmaline and additional spodumene in the pegmatites. As accessories rare beryl, REE minerals (monazite, allanite, xenotime), apatite, zircon, uraninite as well as traces of Nb-Ta phases and cassiterite appear.

- They have a peraluminous, granitic composition, similar element distribution patterns and show continuous fractionation trends for trace elements including Be, Li, Rb, Cs, Sn, Ge, Ba and REE.

- Magmatic garnet is rich in Mn and Fe and the occurrence of tourmaline in the absence of biotite may be due to a low $TiO_2$ content in the melts. The composition of tourmaline in spodumene pegmatites indicates that they crystallized from evolved melts. Trace elements (Rb, Li, Cs, Tl or Ba) in magmatic muscovite show similar fractionation trends with more fractionated signatures in the spodumene pegmatites.

- With respect to the trace elements in muscovite classification diagrams of Černý & Burt (1984) the leucogranites fall in the fields of less evolved muscovite-bearing and muscovite-barren pegmatites, whereas spodumene pegmatites barely reach fields of moderately evolved spodumene pegmatites.

- The $\varepsilon(t)_{Nd}$ of about –8 and initial $^{87}Sr/^{86}Sr$ ratios in the range of 0.7098–0.7353 indicate a crustal origin of the primary melts. $^{147}Sm/^{144}Nd$ ratios are lowest in tourmaline followed by whole rock powder, quartz+feldspar and finally garnet fractions. In garnet, the ratios are very high (up to 7.7), indicating high purity of the analyzed material.

- Our Sm-Nd garnet ages indicate that the investigated rocks intruded in Permian time at 255–280 Ma. This range fits within those reported for the simple pegmatites.

- The spodumene pegmatites from the Austroalpine Unit are inferred to have intruded at more than 10 km depth in country rocks at upper greenschist- to amphibolite-facies conditions.

- All these features taken together indicate a contemporaneous and cogenetic formation of spodumene pegmatites and leucogranites, whereby the spodumene pegmatites are more fractionated and occur in higher structural levels.

## ACKNOWLEDGEMENTS

This research has been supported financially by the “Mineral und Rohstoffinitiative“ of the Bundesministerium für Wissenschaft, Forschung und Wirtschaft (BMWFW). A part of this research (tourmaline single-crystal structure determination) was funded by Austrian Science Fund (FWF) project no. P 31049-N29 (to A.E.). The authors would like to thank Theodoros Ntaflos for his help at the microprobe and the pursued discussions, Christian Auer for his support at the SEM, Konstantin Petrakakis for his scientific input through the whole project run and Richard Göd for the critical and constructive input. The authors would also like to thank Stanislav Grabala for processing the samples as well as Ilka Wünsche, Andreas Wunderlich and Franz Allram for preparing the thin sections. The authors are finally very grateful to the special editor Radek Skoda and the two reviewers Julian Menuge and Marcus T. Sweetapples, who provided very detailed and constructive comments, which were a crucial input for improving the quality of the manuscript.

TABLE 1A. IMPORTANT PEGMATITE FIELDS, SPODUMENE PEGMATITE DIKES, LEUCOGRANITES AND SAMPLES, INCLUDING INFORMATION ABOUT THE LOCATION AND THE COUNTRY ROCKS

| pegmatite field | Niedere Tauern pegmatite field | | | Falkenberg pegmatite field | | | Defferegggen-tal pegmatite field |
|---|---|---|---|---|---|---|---|
| district | Styria | | | Styria | | | Tyrol |
| country | Austria | | | Austria | | | Austria |
| lithostrati-graphic unit | Rappold Complex | | | Rappold Complex | | | Petzeck-Rothenkogel Complex |
| host rock | paragneiss, micaschist, marble | paragneiss, micaschist | paragneiss, micaschist, marble | paragneiss, micaschist | | paragneiss, micaschist, marble | paragneiss, micaschist |
| important dike or body | Hohenwart spodumene pegmatite | Lachtal spodumene pegmatite | | Geißrücken leucogranite | | spodumene pegmatite | Rotes Kögele spodumene pegmatite |
| length [m] | > 500 | > 100 | >10 | 1000 | | >5 | > 100 |
| thickness [m] | 2 | 3 | 5 | > 150 | | 1 | 1,5 |
| sample no. | 04R45 | 15R42 | PEG73 | PEG25-1 | 16R13 | SW1 | RADZ1 |
| locality | Hohenwart (mountain) | Lachtal (valley) | Bretstein (village) | Quarry at Geißrücken (ridge) | Quarry at Geißrücken (ridge) | Falkenberg (ridge) | Rotes Kögele (mountain) |
| sample location (WGS 84) | | | | | | | |
| Lat (N) | 47°19'27.92" | 47°15'59.87" | 47°18'36.76" | 47°10'1.33" | 47°12'16.50" | 47°12'5.76" | 46°55'54.77" |
| Lon (E) | 14°14'28.94" | 14°21'30.47" | 14°29'9.85" | 14°34'47.39" | 14°35'49.39" | 14°35'25.44" | 12°32'43.30" |
| lithology | spodumene pegmatite | spodumene pegmatite | spodumene pegmatite | leucogranite gneiss | leucogranite gneiss | spodumene pegmatite | spodumene pegmatite |

TABLE 1B. IMPORTANT PEGMATITE FIELDS, SPODUMENE PEGMATITE DIKES, LEUCOGRANITES AND SAMPLES, INCLUDING INFORMATION ABOUT THE LOCATION AND THE COUNTRY ROCKS

| pegmatite field | St. Radegund pegmatite field | | Koralpe pegmatite field | | Gleinalm pegmatite field | | Millstätter Seenrücken pegmatite field |
|---|---|---|---|---|---|---|---|
| district | Styria | | Carinthia, Styria | | Styria | | Carinthia |
| country | Austria | | Austria | | Austria | | Austria |
| lithostrati-graphic unit | Rappold Complex | | Saualpe-Koralpe Complex | | Rappold Complex | | Millstatt Complex |
| host rock | paragneiss, micaschist | | paragneiss, micaschist, eclogite-amphibolite | | paragneiss, micaschist, marble | | paragneiss, micaschist |
| important dike or body | Garrach spodumene pegmatite | Schöcklkreuz spodumene pegmatite | Weinebene spodumene pegmatite group | Trahütten leucogranite | Mitterberg spodumene pegmatite | | Lug ins Land spodumene pegmatite |
| length [m] | > 15 | > 20 | 1400 | 1400 | > 10 | | > 80 |
| thickness [m] | < 1.5 | > 3 | > 200 | > 200 | 5 | | 4 |
| sample no. | PEG200 | GM22 | 15R50 | PEG57-1 | 14R16 | PEG51 | MRP-4 |
| locality | Garrach (village) | Schöcklkreuz (ridge) | Weinebene (ridge) | Trahütten (village) | Mitterberg (hill), Übelbach | Mitterberg (hill), Übelbach | Lug ins Land (restaurant) |
| sample location (WGS 84) | | | | | | | |
| Lat (N) | 47°10'42.28" | 47°12'35.40" | 46°0'20.70" | 46°49'44.41" | 47°14'0.55" | 47°14'0.55" | 46°46'55.07" |
| Lon (E) | 15°28'19.16" | 15°29'34.20" | 15°50'9.12" | 15°10'31.84" | 15°12'11.19" | 15°12'11.19" | 13°33'39.51" |
| lithology | spodumene pegmatite gneiss | spodumene pegmatite | spodumene pegmatite mylonite | leucogranite (aplitic) | spodumene pegmatite | spodumene pegmatite | spodumene pegmatite |

TABLE 1C. IMPORTANT PEGMATITE FIELDS, SPODUMENE PEGMATITE DIKES, LEUCOGRANITES AND SAMPLES FROM SOUTH TYROL/ITALY, INCLUDING INFORMATION ABOUT THE LOCATION AND THE COUNTRY ROCKS

| pegmatite field | Uttenheim pegmatite field | | | | Martelltal pegmatite field | | |
|---|---|---|---|---|---|---|---|
| district | South Tyrol | | | | South Tyrol | | |
| country | Italy | | | | Italy | | |
| lithostrati-graphic unit | Petzeck-Rothenkogel Complex | | | | Campo Complex | | |
| host rock | paragneiss, micaschist | | | | paragneiss, micaschist | | |
| important dike or body | Schlösselberg leucogranite | | | | Martell leucogranite | | |
| length [m] | > 5000 | | | | > 300 | | |
| thickness [m] | 200 | | | | 7000 | | |
| sample no. | 16R69 | UTT1 | UTT7 | RS32/01 | RS33/01 | MAR1 | MAR2 |
| locality | Schlössel-berg (ridge) | Schlössel-berg (ridge) | Schlössel-berg (ridge) | Martelltal (valley) | Zufrittsee (Lake), Martelltal (valley) | Martelltal (valley) | Zufrittsee (Lake), Martelltal (valley) |
| sample location (WGS 84) | | | | | | | |
| Lat (N) | 46°50'51.54" | 46°51'30.56" | 46°52'24.92" | 46°30'21.47" | 46°31'32.95" | 46°30'19.48" | 46°31'33.31" |
| Lon (E) | 11°58'20.65" | 11°55'38.28" | 11°56'7.48" | 10°43'12.07" | 10°44'16.22" | 10°43'11.06" | 10°44'16.04" |
| lithology | leucogranite gneiss | leucogranite gneiss | leucogranite gneiss | leucogranite gneiss | peg.domain in leucogranite | leucogranite gneiss | peg.domain in leucogranite |

TABLE 2. SAMPLE LIST OF DATED LEUOCGRANITES AND SPODUMENE PEGMATITES, WITH INFORMATION ABOUT THE PETROLOGICAL AND MINERALOGICAL CHARACTERISTICS

| sample no. | 04R45 | 14R16 | 15R42 | 15R69 | RS32/01 | RS33/01 | PEG25-1 | PEG57-1 |
|---|---|---|---|---|---|---|---|---|
| dike or body | Hohenwart spodumene pegmatite | Mitterberg spodumene pegmatite | Lachtal spodumene pegmatite | Schlössel-berg leucogranite | Martell leucogranite | Martell leucogranite (pegmatitic domian) | Geißrücken leucogranite | Trahütten leucogranite |
| outcrop type | in-situ | boulder | in-situ | in-situ | in-situ | in-situ | in-situ | in-situ |
| Alpine deformation imprint | weak | weak to incipient schistosity | weak to incipient schistosity | well developed schistosity | weak to incipient schistosity | incipient schistocity | weak to incipient schistosity | well developed schistosity |
| K-feldspar | mag., euhedral to subhedral | mag., euhedral to subhedral | mag., subhedral, fine Ms inclusions, frac., myrmektite | mag., subhedral, fine Ms inclusions, frac., myrmektite | mag., euhedral with sharp contacts, fine Ms inclusions | mag., subhedral, dyn. recr. (SR) | mag., subhedral, dyn. recr. (SR), fine Ms inclusions | mag., subhedral, dyn. recr. (SR) |
| plagioclase | mag. and met., subhedral, dyn. recr. (SR) | mag. and met., subhedral to anhedral, dyn. recr. (SR) | mag. and met., subhedral to anhedral, dyn. recr. (SR) | mag. and met., subhedral to anhedral, dyn. recr. (SR) | mag. and met., subhedral to anhedral, dyn. recr. (SR) | mag. and met., subhedral, fine Ms inclusions, dyn. recr. (SR) | mag. and met., euhedral to subhedral, dyn. recr. (SR) | mag. and met., euhedral to subhedral, dyn. recr. (SR) |
| muscovite (mag.) >0.5 cm | euhedral, no prefered orientation | euhedral, slightly oriented | euhedral, no prefered orientation | euhedral, SPO | euhedral, slightly oriented | not present | euhedral, SPO, kinked, fractured | euhedral, SPO |
| muscovite (met.) <0.3 | euhedral, SPO | euhedral, SPO | euhedral, SPO | euhedral, SPO | euhedral, SPO | euhedral, SPO | euhedral, SPO | euhedral, SPO |
| quartz | mag. & met., dyn. recr. (primary GBM, secondary SR), static recr. | mag. & met., dyn. recr. (primary GBM, secondary SR) | mag. & met., dyn. recr. (primary GBM, secondary SR) | mag. & met., fully recr., dyn. recr. (mainly SR, GBM) | mag. & met., dyn. recr. (GBM, SR) | mag. & met., dyn. recr. (GBM, SR) | mag. & met., dyn. recr. (GBM, SR) | mag., fully recr., dyn. recr. (GBM, SR) |
| tourmaline | mag., eu-hedral, zoned, frac. | mag., eu-hedral, zoned, frac. | mag., eu-hedral, zoned | mag., eu-hedral, zoned, frac. | not present | mag., eu-hedral, zoned, frac. | not present | mag., eu-hedral, zoned, frac. |
| garnet | mag., euhedral - subhedral, frac. | mag., euhedral - subhedral, frac. | mag., euhedral - subhedral, frac. | mag., euhedral - subhedral, frac. | mag., euhedral - subhedral, frac. | mag., euhedral - subhedral, frac. | mag., eu-hedral - sub-hedral, slightly frac. | mag., euh-edral - sub-hedral, frac. |
| spodumene | mag., euhedral - subhedral, frac. | mag., euhedral - subhedral, frac. | mag., euhedral - subhedral, frac. | not present | not present | not present | not present | not present |
| accessories | Aln, Gn, Lm, Nb-Ta phase, Py, Urn, Zrn | Mnz, Urn, Xtm, Zrn | Aln, Ap, Lm, Mnz, Py, Zrn | Ap, Mnz, Zrn | Ap, Mnz, Urn, Xtm, Zrn | Ap, Gn, Mnz, Urn, Zrn | Aln, Ap, Mnz, Urn, Xtm, Zrn | Ap, Mnz, Zrn |

mag.: magmatic, met.: metamorphic, dyn.: dynamic, frac.: fractured, recr.: recrystalized, peg.: pegmatitic
SPO.: shape prefered orientation, SR.: subgrain rotation, GBM.: grain boundary migration

TABLE 3. CHARACTERISTICS (SIZE, ENDMEMBER COMPOSITION, MICROSTRUCTURES AND INCLUSIONS) OF GARNET FROM DATED SAMPLES

| sample no. | 04R45 | 14R16 | 15R42 | 15R69 | RS32/01 | RS33/01 | PEG25-1 | PEG57-1 |
|---|---|---|---|---|---|---|---|---|
| *magmatic garnet* | | | | | | | | |
| diameter range [mm] | 1 - 3 | 0.5 - 4 | 0.5 - 2 | 0.5 - 3 | 0.4 - 2 | 0.5 - 5 | 1 - 3 | 0.5 - 2 |
| micro-structure | healed cracks, fresh cracks | slightly cracked | slightly cracked | healed cracks, fresh cracks | healed cracks, fresh cracks | healed cracks, fresh cracks | cracked | cracked and poikoblastic |
| average endmember composition in % | | | | | | | | |
| XAlm | 25 - 45 | 45 - 65 | 40 - 60 | 65 - 80 | 60 - 75 | 70 - 80 | 40 - 55 | 60 - 65 |
| XSps | 50 - 70 | 35 - 50 | 35 - 55 | 15 - 30 | 20 - 35 | 16 - 25 | 10 - 15 | 30 - 35 |
| XPrp | 0.3 - 0.8 | 0.1 - 0.7 | 0.3 - 1.3 | 1 - 1.5 | 0.5 - 1.5 | 2 - 2.5 | 1 - 1.5 | 0.5 - 1 |
| XGrs | 2.5 - 5.5 | 2 - 4 | 2.5 - 4 | 2.5 - 4 | 1.5 - 2.5 | 1.5 - 2 | 30 - 40 | 0.5 - 0.8 |
| inclusions | Qtz, very rare Zrn | Qtz, very rare Zrn | Qtz, very rare Zrn | Qtz | Qtz, very rare Zrn | Qtz | Qtz, Ms, Zrn | Qtz, very rare Zrn |
| *garnet overgrowth* | | | | | | | | |
| av. width (max. width) [µm] | 80 (200) | 30 (200) | 5 (30) | 30 (70) | 40 (80) | 50 (200) | 60 (100) | _ |
| | | | | | | | type B Grt | |
| average endmember composition in % | | | | | | | | |
| XAlm | 20 - 25 | 55 - 60 | 45 - 60 | 40 - 50 | 30 - 50 | 70 - 80 | 40 - 50 | _ |
| XSps | 40 - 50 | 30 - 40 | 35 - 50 | 13 - 20 | 10 - 25 | 15 - 20 | 10 - 17 | _ |
| XPrp | 0.2 - 0.3 | 0.3 - 0.7 | 0.5 - 1 | 0.5 - 1.5 | 0.5 - 2 | 2 - 2.5 | 0.5 - 1 | |
| XGrs | 25 - 31 | 3 - 4 | 4 - 5.5 | 30 - 40 | 40 - 50 | 1 - 2 | 25 - 35 | |
| inclusions | Qtz | Qtz and very rare Zrn | _ | Qtz | Qtz | Qtz | Qtz, Ms, Zrn | _ |

TABLE 4. WHOLE ROCK GEOCHEMICAL COMPOSITIONS FROM DATED SPODUMENE PEGMATITE AND LEUCOGRANITE SAMPLES (MEASURED BY ICP-MS)

| sample no. | 04R45 | 14R16 | 15R42 | 15R69 | RS32/01 | RS33/01 | PEG25-1 | PEG57-1 |
|---|---|---|---|---|---|---|---|---|
| SiO2 [wt.%] | 77,73 | 70,51 | 73,91 | 76,12 | 73,50 | 74,02 | 74,90 | 74,71 |
| Al2O3 | 12,64 | 16,86 | 14,43 | 14,80 | 14,99 | 14,79 | 14,13 | 15,14 |
| Fe2O3(T) | 1,42 | 3,41 | 0,85 | 0,76 | 1,13 | 0,94 | 1,05 | 0,90 |
| MnO | 0,38 | 0,72 | 0,30 | 0,08 | 0,12 | 0,10 | 0,09 | 0,20 |
| MgO | 0,13 | 0,12 | 0,05 | 0,05 | 0,07 | 0,09 | 0,12 | 0,07 |
| CaO | 0,55 | 0,48 | 0,51 | 0,67 | 0,87 | 0,56 | 1,02 | 0,37 |
| Na2O | 4,73 | 6,04 | 4,35 | 4,87 | 4,90 | 4,62 | 3,47 | 4,76 |
| K2O | 0,65 | 0,90 | 3,70 | 2,72 | 2,98 | 3,85 | 3,31 | 3,11 |
| TiO2 | 0,03 | 0,02 | 0,01 | 0,01 | 0,01 | 0,01 | 0,02 | 0,01 |
| P2O5 | 0,01 | 0,05 | 0,03 | 0,01 | 0,13 | 0,10 | 0,03 | 0,35 |
| LOI | 0,57 | 0,75 | 0,42 | 0,72 | 1,07 | 0,55 | 0,99 | 0,78 |
| Total | 98,84 | 99,86 | 98,57 | 100,80 | 99,76 | 99,64 | 99,13 | 100,40 |
| Sc [ppm] | 2 | 3 | 1 | < 1 | 1 | < 1 | 3 | 2 |
| Be | 48 | 30 | 19 | 10 | 11 | 9 | 9 | 4 |
| V | < 5 | 6 | < 5 | < 5 | < 5 | < 5 | 8 | < 5 |
| Ba | 7 | 13 | 27 | 7 | 6 | 6 | 40 | 9 |
| Sr | 14 | 13 | 21 | 16 | 21 | 11 | 75 | 4 |
| Y | 48 | 112 | 41 | 27 | 15 | 8 | 80 | 4 |
| Zr | 109 | 142 | 35 | 42 | 48 | 35 | 66 | 26 |
| Cr | 160 | < 20 | < 20 | < 20 | < 20 | < 20 | < 20 | < 20 |
| Co | 1 | < 1 | < 1 | 1 | < 1 | < 1 | < 1 | < 1 |
| Ni | 90 | < 20 | < 20 | < 20 | < 20 | < 20 | < 20 | < 20 |
| Cu | < 10 | < 10 | < 10 | < 10 | < 10 | < 10 | < 10 | < 10 |
| Zn | 160 | 250 | 50 | 50 | < 30 | < 30 | < 30 | 30 |
| Ga | 16 | 20 | 13 | 17 | 19 | 15 | 15 | 15 |
| Ge | 5 | 7 | 5 | 3 | 3 | 4 | 3 | 5 |
| As | < 5 | < 5 | < 5 | < 5 | < 5 | < 5 | < 5 | < 5 |
| Rb | 86 | 97 | 372 | 222 | 177 | 192 | 142 | 217 |
| Nb | 14 | 8 | 1 | 8 | 9 | < 1 | 7 | 4 |
| Mo | 2 | < 2 | < 2 | < 2 | < 2 | < 2 | < 2 | < 2 |
| Ag | < 0.5 | 0,5 | < 0.5 | < 0.5 | < 0.5 | < 0.5 | < 0.5 | < 0.5 |
| In | < 0.2 | < 0.2 | < 0.2 | < 0.2 | < 0.2 | < 0.2 | < 0.2 | < 0.2 |
| Sn | 9 | 18 | 6 | 15 | 15 | 6 | 15 | 17 |
| Sb | < 0.5 | < 0.5 | < 0.5 | < 0.5 | < 0.5 | < 0.5 | < 0.5 | < 0.5 |
| Cs | 13 | 20 | 43,3 | 10,5 | 14,4 | 10,8 | 8,4 | 6,7 |
| La | 2,4 | 14 | 2,6 | 7,1 | 4,4 | 2,5 | 26,6 | 0,8 |
| Ce | 4,8 | 32,1 | 5,5 | 14 | 9,3 | 5,2 | 56,3 | 1,7 |
| Pr | 0,5 | 3,78 | 0,6 | 1,7 | 0,94 | 0,55 | 6,27 | 0,19 |
| Nd | 1,5 | 12,3 | 2 | 5,8 | 3 | 1,8 | 21,8 | 0,7 |
| Sm | 0,8 | 5,9 | 1 | 2,4 | 1,3 | 0,6 | 6,9 | 0,3 |
| Eu | < 0.05 | 0,06 | 0,08 | 0,1 | 0,09 | < 0.05 | 0,54 | < 0.05 |
| Gd | 1,8 | 6,2 | 2,3 | 3,1 | 1,5 | 0,8 | 7,6 | 0,3 |
| Tb | 0,8 | 2,5 | 0,9 | 0,7 | 0,4 | 0,2 | 1,9 | < 0.1 |
| Dy | 6,4 | 18,4 | 7,1 | 5 | 2,5 | 1,2 | 13,9 | 0,6 |
| Ho | 1,3 | 3,4 | 1,2 | 0,9 | 0,4 | 0,2 | 2,7 | 0,1 |
| Er | 3,7 | 10,2 | 2,9 | 2,3 | 1,1 | 0,7 | 7,4 | 0,3 |
| Tm | 0,63 | 2,02 | 0,49 | 0,32 | 0,17 | 0,13 | 1,03 | 0,06 |
| Yb | 4,4 | 14 | 3,3 | 1,8 | 1,3 | 0,9 | 6,3 | 0,5 |
| Lu | 0,62 | 1,96 | 0,44 | 0,27 | 0,18 | 0,13 | 0,89 | 0,08 |
| Hf | 6,9 | 7,8 | 1,8 | 1,9 | 1,7 | 1,3 | 2,6 | 1,1 |
| Ta | 9,9 | 5 | 0,7 | 1,6 | 1,9 | 0,6 | 1,4 | 1 |
| W | < 1 | < 1 | < 1 | 1 | 1 | < 1 | 3 | 7 |
| Tl | 0,4 | 0,4 | 2,1 | 1 | 0,6 | 0,9 | 0,7 | 1,1 |
| Pb | 49 | 57 | 87 | 41 | 35 | 74 | 101 | 22 |
| Bi | 1 | 0,7 | 2,8 | 5,9 | 3,4 | 1,9 | 34,3 | 0,5 |
| Th | 1,7 | 6,6 | 1,3 | 2,1 | 1,2 | 0,4 | 9,8 | 0,4 |
| U | 8,1 | 6,9 | 1,7 | 5,8 | 27,6 | 28,9 | 12,4 | 12,1 |
| Li | 655 | 183 | 174 | 83 | 119 | 87 | 83 | 96 |

TABLE 5A. SELECTED MAJOR ELEMENT COMPOSITIONS OF GARNET FROM DATED SPODUMENE PEGMATITE AND LEUCOGRANITE SAMPLES (MEASURED BY EPMA)

| | 04R45 | | 14R16 | | 15R42 | | 15R69 | | RS32/01 | | RS33/01 | | PEG25-1 | | PEG57-1 | |
|---|---|---|---|---|---|---|---|---|---|---|---|---|---|---|---|---|
| | [core] | [rim] | [core] | [rim] | [core] | [rim] | [core] | [rim] | [core] | [rim] | [core] | [rim] | [core] | [rim] | [core] | [rim] |
| [wt.%] | | | | | | | | | | | | | | | | |
| $SiO_2$ | 35,74 | 36,96 | 35,86 | 36,91 | 36,02 | 36,88 | 35,93 | 37,01 | 35,95 | 37,45 | 37,64 | 35,97 | 36,10 | 36,89 | 35,98 | 35,75 |
| $TiO_2$ | 0,04 | 0,02 | 0,03 | 0,00 | 0,04 | 0,03 | 0,04 | 0,01 | 0,00 | 0,00 | 0,03 | 0,00 | 0,02 | 0,01 | 0,00 | 0,00 |
| $Al_2O_3$ | 20,78 | 21,40 | 20,98 | 21,05 | 21,00 | 21,37 | 21,02 | 21,50 | 21,08 | 21,52 | 21,48 | 21,67 | 21,26 | 21,40 | 21,07 | 20,94 |
| $Cr_2O_3$ | 0,00 | 0,02 | 0,01 | 0,00 | 0,00 | 0,01 | 0,01 | 0,00 | 0,00 | 0,00 | 0,00 | 0,00 | 0,02 | 0,02 | 0,01 | 0,00 |
| FeO | 19,93 | 11,39 | 19,22 | 20,83 | 18,59 | 11,95 | 34,46 | 22,15 | 30,02 | 14,70 | 14,38 | 35,20 | 33,50 | 22,93 | 28,02 | 28,10 |
| MnO | 21,59 | 18,73 | 22,28 | 13,93 | 22,99 | 19,89 | 7,55 | 5,82 | 12,20 | 10,29 | 10,43 | 6,67 | 7,50 | 7,06 | 14,81 | 14,91 |
| MgO | 0,10 | 0,07 | 0,03 | 0,27 | 0,08 | 0,05 | 0,30 | 0,13 | 0,36 | 0,00 | 0,26 | 0,59 | 0,73 | 0,25 | 0,24 | 0,24 |
| CaO | 1,08 | 10,95 | 0,78 | 7,36 | 1,28 | 9,71 | 0,84 | 13,26 | 0,60 | 15,95 | 15,77 | 0,53 | 0,99 | 11,14 | 0,21 | 0,17 |
| Total | 99,26 | 99,58 | 99,19 | 100,36 | 99,99 | 99,90 | 100,17 | 99,88 | 100,21 | 99,90 | 100,25 | 100,62 | 100,11 | 99,70 | 100,34 | 100,13 |
| *apfu* | | | | | | | | | | | | | | | | |
| Si | 2,97 | 2,98 | 2,97 | 2,98 | 2,97 | 2,97 | 2,96 | 2,96 | 2,96 | 2,98 | 2,97 | 2,98 | 2,96 | 2,97 | 2,96 | 2,95 |
| Ti | 0,00 | 0,00 | 0,00 | 0,00 | 0,00 | 0,00 | 0,00 | 0,00 | 0,00 | 0,00 | 0,00 | 0,00 | 0,00 | 0,00 | 0,00 | 0,00 |
| Al | 2,03 | 2,03 | 2,05 | 2,00 | 2,04 | 2,03 | 2,04 | 2,03 | 2,05 | 2,01 | 2,04 | 2,01 | 2,05 | 2,03 | 2,04 | 2,04 |
| Cr | 0,00 | 0,00 | 0,00 | 0,00 | 0,00 | 0,00 | 0,00 | 0,00 | 0,00 | 0,00 | 0,00 | 0,00 | 0,00 | 0,00 | 0,00 | 0,00 |
| $Fe_{tot}$ | 1,38 | 0,77 | 1,33 | 1,41 | 1,28 | 0,81 | 2,37 | 1,48 | 2,07 | 0,98 | 2,13 | 0,95 | 2,30 | 1,54 | 1,93 | 1,94 |
| Mn | 1,52 | 1,28 | 1,57 | 0,95 | 1,60 | 1,36 | 0,53 | 0,39 | 0,85 | 0,69 | 0,74 | 0,70 | 0,52 | 0,48 | 1,03 | 1,04 |
| Mg | 0,01 | 0,01 | 0,00 | 0,03 | 0,01 | 0,01 | 0,04 | 0,02 | 0,04 | 0,00 | 0,06 | 0,03 | 0,09 | 0,03 | 0,03 | 0,03 |
| Ca | 0,10 | 0,94 | 0,07 | 0,64 | 0,11 | 0,84 | 0,07 | 1,14 | 0,05 | 1,36 | 0,06 | 1,34 | 0,09 | 0,96 | 0,02 | 0,02 |
| endmember composition | | | | | | | | | | | | | | | | |
| XAlm | 45,2 | 25,1 | 45 | 45,6 | 41,9 | 26,0 | 78,5 | 47,8 | 68,0 | 31,1 | 71,1 | 30,6 | 76,5 | 50,4 | 63,5 | 63,1 |
| XSps | 51,1 | 42,9 | 52,6 | 32,0 | 54 | 45,6 | 17,8 | 13,3 | 28,8 | 23,3 | 24,8 | 23,5 | 17,6 | 16,2 | 34,9 | 35,3 |
| XPrp | 0,42 | 0,30 | 0,12 | 1,10 | 0,31 | 0,19 | 1,24 | 0,54 | 1,47 | 0,00 | 2,18 | 1,04 | 3,00 | 1,02 | 0,99 | 1,02 |
| XGrs | 3,16 | 31,4 | 2,33 | 20,86 | 3,73 | 27,73 | 2,43 | 37,1 | 1,73 | 44,5 | 1,89 | 44,03 | 2,9 | 31,6 | 0,61 | 0,49 |
| XAdr | 0,06 | 0,30 | 0,00 | 0,50 | 0,07 | 0,44 | 0,06 | 1,23 | 0,05 | 1,14 | 0,01 | 0,84 | 0,05 | 0,71 | 0,01 | 0,02 |

TABLE 5B. SELECTED MAJOR ELEMENT COMPOSITIONS OF PLAGIOCLASE FROM DATED SPODUMENE PEGMATITE AND LEUCOGRANITE SAMPLES (MEASURED BY EPMA)

| | 04R45 | | 14R16 | | 15R42 | | 15R69 | | RS32/01 | | RS33/01 | | PEG25-1 | | PEG57-1 | |
|---|---|---|---|---|---|---|---|---|---|---|---|---|---|---|---|---|
| | [core] | [rim] | [core] | [rim] | [core] | [rim] | [core] | [rim] | [core] | [rim] | [core] | [rim] | [core] | [rim] | [core] | [rim] |
| [wt.%] | | | | | | | | | | | | | | | | |
| $SiO_2$ | 68,19 | 68,47 | 68,26 | 68,43 | 66,97 | 66,73 | 66,70 | 66,48 | 68,42 | 68,25 | 66,94 | 67,12 | 66,03 | 66,02 | 68,96 | 68,99 |
| $TiO_2$ | 0,01 | 0,00 | 0,00 | 0,03 | 0,01 | 0,03 | 0,00 | 0,01 | 0,00 | 0,00 | 0,00 | 0,02 | 0,00 | 0,00 | 0,00 | 0,01 |
| $Al_2O_3$ | 19,80 | 20,17 | 20,10 | 20,08 | 21,15 | 21,25 | 21,08 | 21,29 | 20,49 | 20,53 | 21,14 | 21,08 | 21,61 | 21,56 | 19,82 | 19,82 |
| FeO | 0,01 | 0,01 | 0,00 | 0,01 | 0,00 | 0,00 | 0,00 | 0,00 | 0,00 | 0,00 | 0,01 | 0,00 | 0,00 | 0,02 | 0,00 | 0,00 |
| MnO | 0,01 | 0,00 | 0,00 | 0,00 | 0,00 | 0,00 | 0,00 | 0,00 | 0,00 | 0,00 | 0,00 | 0,00 | 0,01 | 0,01 | 0,01 | 0,00 |
| MgO | 0,01 | 0,00 | 0,00 | 0,00 | 0,01 | 0,00 | 0,01 | 0,00 | 0,00 | 0,00 | 0,02 | 0,00 | 0,01 | 0,00 | 0,01 | 0,01 |
| CaO | 0,46 | 0,69 | 0,37 | 0,33 | 1,77 | 1,82 | 2,01 | 2,06 | 0,70 | 0,69 | 1,72 | 1,59 | 2,35 | 2,28 | 0,09 | 0,09 |
| $Na_2O$ | 11,25 | 11,37 | 11,21 | 11,26 | 10,72 | 10,48 | 10,69 | 10,43 | 11,04 | 11,19 | 10,68 | 10,84 | 10,14 | 10,16 | 11,72 | 11,64 |
| $K_2O$ | 0,16 | 0,15 | 0,18 | 0,19 | 0,16 | 0,20 | 0,08 | 0,10 | 0,08 | 0,09 | 0,11 | 0,09 | 0,33 | 0,32 | 0,17 | 0,10 |
| BaO | 0,01 | 0,00 | 0,00 | 0,03 | 0,00 | 0,04 | 0,00 | 0,00 | 0,08 | 0,00 | 0,03 | 0,00 | 0,02 | 0,01 | 0,00 | 0,00 |
| Total | 99,91 | 100,87 | 100,13 | 100,34 | 100,79 | 100,54 | 100,57 | 100,37 | 100,81 | 100,75 | 100,65 | 100,75 | 100,48 | 100,38 | 100,78 | 100,65 |
| *apfu* | | | | | | | | | | | | | | | | |
| Si | 2,98 | 2,97 | 2,98 | 2,98 | 2,92 | 2,91 | 2,91 | 2,91 | 2,97 | 2,96 | 2,92 | 2,92 | 2,89 | 2,89 | 2,99 | 2,99 |
| Ti | 0,00 | 0,00 | 0,00 | 0,00 | 0,00 | 0,00 | 0,00 | 0,00 | 0,00 | 0,00 | 0,00 | 0,00 | 0,00 | 0,00 | 0,00 | 0,00 |
| Al | 1,02 | 1,03 | 1,03 | 1,03 | 1,09 | 1,09 | 1,08 | 1,10 | 1,05 | 1,05 | 1,09 | 1,08 | 1,11 | 1,11 | 1,01 | 1,01 |
| Fe | 0,00 | 0,00 | 0,00 | 0,00 | 0,00 | 0,00 | 0,00 | 0,00 | 0,00 | 0,00 | 0,00 | 0,00 | 0,00 | 0,00 | 0,00 | 0,00 |
| Mn | 0,00 | 0,00 | 0,00 | 0,00 | 0,00 | 0,00 | 0,00 | 0,00 | 0,00 | 0,00 | 0,00 | 0,00 | 0,00 | 0,00 | 0,00 | 0,00 |
| Mg | 0,00 | 0,00 | 0,00 | 0,00 | 0,00 | 0,00 | 0,00 | 0,00 | 0,00 | 0,00 | 0,00 | 0,00 | 0,00 | 0,00 | 0,00 | 0,00 |
| Ca | 0,02 | 0,03 | 0,02 | 0,02 | 0,08 | 0,08 | 0,09 | 0,10 | 0,03 | 0,03 | 0,08 | 0,07 | 0,11 | 0,11 | 0,00 | 0,00 |
| Na | 0,95 | 0,96 | 0,95 | 0,95 | 0,91 | 0,89 | 0,90 | 0,88 | 0,93 | 0,94 | 0,90 | 0,91 | 0,86 | 0,86 | 0,98 | 0,98 |
| K | 0,01 | 0,01 | 0,01 | 0,01 | 0,01 | 0,01 | 0,00 | 0,01 | 0,00 | 0,01 | 0,01 | 0,00 | 0,02 | 0,02 | 0,01 | 0,01 |
| Ba | 0,00 | 0,00 | 0,00 | 0,00 | 0,00 | 0,00 | 0,00 | 0,00 | 0,00 | 0,00 | 0,00 | 0,00 | 0,00 | 0,00 | 0,00 | 0,00 |
| endmember composition | | | | | | | | | | | | | | | | |
| XAn | 2,17 | 3,22 | 1,79 | 1,56 | 8,28 | 8,64 | 9,38 | 9,80 | 3,35 | 3,29 | 8,14 | 7,48 | 11,1 | 10,8 | 0,42 | 0,41 |
| XAb | 96,9 | 95,9 | 97,2 | 97,4 | 90,8 | 90,3 | 90,2 | 89,6 | 96,2 | 96,2 | 91,3 | 92,0 | 87 | 87,3 | 98,7 | 99 |
| XOr | 0,92 | 0,84 | 1,03 | 1,08 | 0,89 | 1,10 | 0,46 | 0,55 | 0,45 | 0,52 | 0,60 | 0,50 | 1,85 | 1,83 | 0,92 | 0,56 |

TABLE 5C. SELECTED MAJOR ELEMENT COMPOSITIONS OF K-FELDSPAR FROM DATED SPODUMENE PEGMATITE AND LEUCOGRANITE SAMPLES (MEASURED BY EPMA)

| | 04R45 | | 14R16 | | 15R42 | | 15R69 | | RS32/01 | | RS33/01 | | PEG25-1 | | PEG57-1 | |
|---|---|---|---|---|---|---|---|---|---|---|---|---|---|---|---|---|
| | [core] | [rim] | [core] | [rim] | [core] | [rim] | [core] | [rim] | [core] | [rim] | [core] | [rim] | [core] | [rim] | [core] | [rim] |
| [wt.%] | | | | | | | | | | | | | | | | |
| $SiO_2$ | 64,95 | 64,93 | 64,83 | 64,94 | 64,96 | 64,97 | 64,94 | 64,85 | 64,97 | 64,89 | 65,08 | 64,72 | 64,79 | 65,13 | 64,90 | 64,89 |
| $TiO_2$ | 0,00 | 0,00 | 0,01 | 0,00 | 0,04 | 0,00 | 0,01 | 0,01 | 0,00 | 0,00 | 0,00 | 0,00 | 0,01 | 0,00 | 0,02 | 0,01 |
| $Al_2O_3$ | 18,44 | 18,45 | 18,67 | 18,68 | 18,64 | 18,56 | 18,57 | 18,56 | 18,72 | 18,67 | 18,38 | 18,42 | 18,45 | 18,48 | 18,67 | 18,52 |
| FeO | 0,00 | 0,02 | 0,00 | 0,03 | 0,01 | 0,02 | 0,01 | 0,00 | 0,00 | 0,00 | 0,04 | 0,00 | 0,03 | 0,02 | 0,00 | 0,00 |
| MnO | 0,00 | 0,00 | 0,00 | 0,01 | 0,00 | 0,00 | 0,00 | 0,00 | 0,00 | 0,00 | 0,00 | 0,00 | 0,00 | 0,01 | 0,02 | 0,00 |
| MgO | 0,00 | 0,00 | 0,00 | 0,00 | 0,00 | 0,00 | 0,00 | 0,02 | 0,00 | 0,00 | 0,00 | 0,00 | 0,00 | 0,01 | 0,00 | 0,01 |
| CaO | 0,01 | 0,00 | 0,04 | 0,03 | 0,01 | 0,00 | 0,02 | 0,01 | 0,00 | 0,01 | 0,00 | 0,01 | 0,00 | 0,00 | 0,00 | 0,00 |
| $Na_2O$ | 0,73 | 0,76 | 0,79 | 0,53 | 1,07 | 0,98 | 0,50 | 0,39 | 0,54 | 0,49 | 0,37 | 0,27 | 0,56 | 0,55 | 0,60 | 0,59 |
| $K_2O$ | 15,46 | 15,48 | 15,70 | 16,02 | 15,11 | 15,04 | 15,73 | 16,06 | 15,87 | 15,96 | 16,02 | 16,09 | 15,95 | 15,95 | 15,90 | 15,79 |
| BaO | 0,00 | 0,03 | 0,00 | 0,01 | 0,00 | 0,00 | 0,00 | 0,05 | 0,01 | 0,00 | 0,00 | 0,01 | 0,00 | 0,06 | 0,04 | 0,02 |
| Total | 99,59 | 99,67 | 100,02 | 100,24 | 99,85 | 99,57 | 99,78 | 99,94 | 100,11 | 100,02 | 99,89 | 99,52 | 99,80 | 100,22 | 100,14 | 99,82 |
| *apfu* | | | | | | | | | | | | | | | | |
| Si | 3,00 | 3,00 | 2,99 | 2,99 | 2,99 | 3,00 | 3,00 | 3,00 | 2,99 | 2,99 | 3,00 | 3,00 | 3,00 | 3,00 | 2,99 | 3,00 |
| Ti | 0,00 | 0,00 | 0,00 | 0,00 | 0,00 | 0,00 | 0,00 | 0,00 | 1,02 | 1,02 | 0,00 | 0,00 | 0,00 | 0,00 | 0,00 | 0,00 |
| Al | 1,00 | 1,01 | 1,01 | 1,01 | 1,01 | 1,01 | 1,01 | 1,01 | 0,00 | 0,00 | 1,00 | 1,01 | 1,01 | 1,00 | 1,01 | 1,01 |
| Fe | 0,00 | 0,00 | 0,00 | 0,00 | 0,00 | 0,00 | 0,00 | 0,00 | 0,00 | 0,00 | 0,00 | 0,00 | 0,00 | 0,00 | 0,00 | 0,00 |
| Mn | 0,00 | 0,00 | 0,00 | 0,00 | 0,00 | 0,00 | 0,00 | 0,00 | 0,00 | 0,00 | 0,00 | 0,00 | 0,00 | 0,00 | 0,00 | 0,00 |
| Mg | 0,00 | 0,00 | 0,00 | 0,00 | 0,00 | 0,00 | 0,00 | 0,00 | 0,00 | 0,00 | 0,00 | 0,00 | 0,00 | 0,00 | 0,00 | 0,00 |
| Ca | 0,00 | 0,00 | 0,00 | 0,00 | 0,00 | 0,00 | 0,00 | 0,00 | 0,00 | 0,00 | 0,00 | 0,00 | 0,00 | 0,00 | 0,00 | 0,00 |
| Na | 0,07 | 0,07 | 0,07 | 0,05 | 0,10 | 0,09 | 0,05 | 0,03 | 0,05 | 0,04 | 0,03 | 0,02 | 0,05 | 0,05 | 0,05 | 0,05 |
| K | 0,91 | 0,91 | 0,92 | 0,94 | 0,89 | 0,89 | 0,93 | 0,95 | 0,93 | 0,94 | 0,94 | 0,95 | 0,94 | 0,94 | 0,93 | 0,93 |
| Ba | 0,00 | 0,00 | 0,00 | 0,00 | 0,00 | 0,00 | 0,00 | 0,00 | 0,00 | 0,00 | 0,00 | 0,00 | 0,00 | 0,00 | 0,00 | 0,00 |
| endmember composition | | | | | | | | | | | | | | | | |
| XAn | 0,05 | 0,00 | 0,18 | 0,13 | 0,07 | 0,00 | 0,11 | 0,04 | 0,00 | 0,03 | 0,00 | 0,03 | 0,00 | 0,00 | 0,00 | 0,00 |
| XAb | 6,73 | 6,92 | 7,05 | 4,81 | 9,72 | 9,03 | 4,64 | 3,55 | 4,90 | 4,44 | 3,40 | 2,49 | 5,10 | 4,98 | 5,44 | 5,38 |
| XOr | 93,2 | 93,1 | 92,8 | 95,1 | 90,2 | 91,0 | 95,3 | 96,4 | 95,1 | 95,5 | 96,6 | 97,5 | 94,9 | 95,0 | 94,6 | 94,6 |

TABLE 6A. SELECTED TRACE ELEMENT DATA FOR REPRESENTATIVE COMPOSITIONS OF GARNETS FROM SPODUMENE PEGMATITE AND LEUCOGARNITE SAMPLES (MEASURED BY LA ICP-MS, FORMULA DETERMINED WITH SINGLE-CRYSTAL STRUCTURE REFINEMENT)

| sample | 04R45 | 04R45 | 14R16 | 14R16 | 15R42 | 15R42 | 15R69 | 15R69 |
|---|---|---|---|---|---|---|---|---|
| mineral | Grt | Grt | Grt | Grt | Grt | Grt | Grt | Grt |
| domain | core | rim | core | rim | core | rim | core | rim |
| Li [ppm] | 638 | 746 | 774 | 658 | 712 | 233 | 660 | 457,6 |
| Be | 1,2 | 2,54 | 0,66 | 1,0 | 0,49 | 0,68 | bdl | 0,29 |
| B | 11 | 51 | 66 | 38 | 21 | 21 | 2,47 | 3,50 |
| P | 78 | 340 | 2112 | 2222 | 439 | 191 | 249 | 168 |
| V | 3,07 | 1,34 | 0,12 | 1,25 | 0,28 | 0,69 | 0,22 | 0,07 |
| Cr | 2,1 | 2,5 | 2,8 | 3,2 | 2,7 | 2,2 | 2,5 | 1,9 |
| Co | 0,12 | 0,10 | bdl | 0,02 | 0,29 | 0,51 | 0,29 | 0,33 |
| Ni | 0,13 | 0,47 | 0,52 | bdl | 0,11 | 0,08 | 0,01 | 4,93 |
| Cu | 0,08 | 0,08 | 0,68 | 1,28 | 0,31 | 0,48 | bdl | 1,87 |
| Zn | 274 | 369 | 439 | 514 | 460 | 509 | 728 | 724 |
| Ga | 37 | 39 | 55 | 55 | 53 | 27 | 41 | 38 |
| Ge | 176 | 160 | 217 | 217 | 174 | 94 | 90 | 92 |
| Rb | 0,92 | 111 | 5,3 | 0,3 | 8,3 | 9,4 | 0,99 | 0,64 |
| Sr | 0,45 | 0,39 | 1,15 | 0,37 | 0,35 | 0,30 | 0,41 | 0,26 |
| Zr | 4,28 | 16 | 173 | 150 | 36 | 29 | 45 | 21 |
| Nb | 2,2 | 11 | 213 | 148 | 8,9 | 1 | 3 | 1 |
| Mo | 20 | 24 | 19 | 18 | 21 | 15 | 8,6 | 7,4 |
| Sn | 71 | 116 | 755 | 734 | 445 | 36 | 36 | 24 |
| Cs | 0,42 | 9,4 | 1,80 | 0,06 | 0,80 | 1,07 | 0,03 | 0,03 |
| Ba | 0,29 | 0,41 | 7,3 | 4,3 | 0,25 | 0,58 | 0,05 | 0,40 |
| Hf | 0,36 | 0,93 | 13 | 9,7 | 2,52 | 1,29 | 1,84 | 0,76 |
| Ta | 2,5 | 2,7 | 91 | 60 | 32 | 1,3 | 2,3 | 0,77 |
| W | 0,4 | 0,87 | 1,36 | 0,17 | 0,11 | 0,02 | 0,12 | 0,23 |
| Tl | bdl | 0,39 | 0,04 | bdl | 0,04 | 0,05 | 0,01 | 0,00 |
| Pb | 2,4 | 5,2 | 0,78 | 15 | 7,2 | 7,2 | bdl | 2,6 |
| U | 0,14 | 0,22 | 20 | 9,9 | 0,54 | 0,21 | 0,76 | 1,46 |

TABLE 6B. SELECTED TRACE ELEMENT COMPOSITIONS OF PLAGIOCLASE FROM SPODUMENE PEGMATITE AND LEUCOGRANITE SAMPLES (MEASURED BY LA ICP-MS)

| sample | 04R45 | 04R45 | 14R16 | 14R16 | 15R42 | 15R42 | 15R69 | 15R69 |
|---|---|---|---|---|---|---|---|---|
| mineral | Fsp | Fsp | Fsp | Fsp | Fsp | Fsp | Fsp | Fsp |
| domain | core | rim | core | rim | core | rim | core | rim |
| Li | 10,8 | 19,8 | 8,2 | 7,5 | 6,4 | 6,2 | 7,8 | 9,2 |
| Be | 10,9 | 14,9 | 0,94 | 1,01 | 0,06 | 0,08 | 1,73 | 4,5 |
| B | 14 | 10,1 | 60 | 31 | 7,8 | 7,3 | 3,03 | 3,62 |
| P | 78 | 91 | 52 | 49 | 44 | 44 | 42 | 46 |
| Ti | 120 | 94 | 99 | 98 | 134 | 131 | 142 | 124 |
| V | 1,04 | 0,87 | 0,72 | 0,75 | 1,31 | 1,30 | 1,29 | 1,17 |
| Cr | 2,9 | 2,3 | 2,3 | 2,3 | 3,9 | 4,6 | 3,7 | 4,5 |
| Mn | 30 | 94 | 25 | 24 | 33 | 33 | 359 | 162 |
| Fe | 383 | 351 | 378 | 247 | 417 | 414 | 1490 | 860 |
| Co | 0,28 | 0,29 | 0,07 | 0,12 | 0,34 | 0,30 | 0,38 | 0,32 |
| Ni | 1 | 0,81 | 0,43 | 0,38 | 0,89 | 0,83 | 1,2 | 1,02 |
| Cu | 6,4 | 6 | 8,2 | 8,4 | 5,7 | 5,6 | 7,1 | 6,5 |
| Zn | 4,5 | 6,5 | 10,7 | 6,7 | 2,8 | 4,7 | 3,1 | 2,9 |
| Ga | 5,7 | 8,5 | 2,07 | 2,21 | 0,60 | 0,45 | 2,35 | 3,8 |
| Ge | 1,44 | 2,12 | 0,85 | 0,94 | 0,64 | 0,74 | 1,03 | 1,05 |
| Rb | 12 | 14 | 29 | 29 | 8,2 | 8,1 | 8,9 | 8 |
| Sr | 24 | 21 | 29 | 28 | 24 | 24 | 28 | 27 |
| Zr | 61 | 51 | 98 | 95 | 71 | 71 | 75 | 64 |
| Nb | 0,67 | 0,71 | 0,33 | 0,34 | 0,47 | 0,53 | 0,54 | 0,47 |
| Mo | 0,03 | 0,01 | 0,07 | 0,02 | 0,04 | 0,05 | 0,07 | 0,03 |
| Sn | 6,96 | 7,11 | 0,66 | 0,66 | 8,35 | 6,82 | 13 | 6,71 |
| Cs | 0,8 | 1,0 | 0,9 | 0,9 | 0,2 | 0,2 | 0,3 | 0,2 |
| Ba | 74 | 61 | 195 | 190 | 80 | 77 | 82 | 71 |
| Hf | 1,59 | 1,3 | 2,33 | 2,11 | 1,64 | 1,65 | 1,68 | 1,41 |
| Ta | 0,10 | 0,13 | 0,06 | 0,05 | 0,05 | 0,04 | 0,05 | 0,07 |
| W | 0,07 | 0,10 | 0,02 | 0,08 | 0,04 | 0,11 | 0,08 | 0,03 |
| Tl | 0,04 | 0,07 | 0,11 | 0,10 | bdl | 0,05 | 0,03 | 0,03 |
| Pb | 7,5 | 50 | 7,2 | 7,1 | 3,2 | 3,1 | 5,2 | 7 |
| U | 0,27 | 0,54 | 0,21 | 0,17 | 0,27 | 0,31 | 0,32 | 0,27 |

TABLE 6C. SELECTED LIGHT AND TRACE ELEMENT COMPOSITIONS OF TOURMALINES FROM DATED SPODUMENE PEGMATITE AND LEUCOGRANITE SAMPLES (MEASURED BY LA ICP-MS)

| sample | 04R45 | 04R45 | 14R16 | 14R16 | 15R42 | 15R42 | 15R69 | 15R69 |
|---|---|---|---|---|---|---|---|---|
| mineral | Tur | Tur | Tur | Tur | Tur | Tur | Tur | Tur |
| domain | core | rim | core | rim | core | rim | core | rim |
| Li [ppm] | 3652 | 4270 | 1332 | 2840 | 1348 | 713 | 354 | 570 |
| Be | 10,4 | 10,1 | 9 | 20,8 | 11 | 10,4 | 8 | 6,2 |
| B | 31260 | 31330 | 32640 | 36080 | 30830 | 30500 | nd | nd |
| P | 9 | bdl | 40 | 48 | 33 | 23 | 44 | 15 |
| K | 806 | 697 | 1190 | 1480 | 993 | 775 | 1010 | 1316 |
| Ca | 3714 | 3210 | 5920 | 4500 | 4540 | 1634 | 3900 | 6220 |
| Ti | 4059 | 895 | 2270 | 1345 | 2308 | 564 | 3030 | 1206 |
| V | 6,01 | 0,81 | 0,9 | 0,76 | 2,42 | 0,86 | 1,17 | 1,05 |
| Cr | 2,73 | 2,26 | 1,41 | 1,45 | 2,8 | 2,3 | 2,92 | 2,94 |
| Mn | 5356 | 6080 | 2790 | 5240 | 5560 | 4910 | 8800 | 4080 |
| Co | 1,04 | 1,67 | 0,53 | 0,04 | 0,3 | 0,34 | 1,29 | 0,67 |
| Ni | 0,02 | 0,16 | 0,07 | 0,69 | 0,1 | bdl | 0,09 | 0,04 |
| Cu | 2,16 | 2,47 | 3,42 | 3,51 | 2,29 | 1,84 | 1,91 | 2,02 |
| Zn | 4250 | 5300 | 3610 | 5540 | 4950 | 4430 | 4320 | 4270 |
| Ga | 137 | 134 | 117 | 146 | 153 | 128 | 133 | 170 |
| Ge | 4,4 | 6,2 | 5,5 | 11 | 6,7 | 4,0 | 7,2 | 6,4 |
| Rb | 0,02 | 0,26 | 0,77 | 2,28 | 0,04 | 0,12 | 2,28 | 5,2 |
| Sr | 6 | 4,63 | 16,2 | 3,8 | 9,2 | 3,08 | 5 | 7,5 |
| Zr | 0,36 | 0,66 | 0,79 | 2,97 | 0,36 | 0,78 | 0,89 | 1,16 |
| Nb | 2,22 | 2,81 | 2 | 7,2 | 2,93 | 0,97 | 3,72 | 4,11 |
| Mo | 0,30 | 0,34 | 0,29 | 0,44 | 0,42 | 0,25 | 0,51 | 0,22 |
| Sn | 80 | 62 | 54 | 102 | 78 | 44 | 36 | 52 |
| Cs | 0,01 | 0,06 | 0,08 | 0,02 | 0,01 | 0,02 | 0,23 | 0,19 |
| Ba | bdl | 1,27 | 3 | 15 | 0,17 | 0,54 | 0,5 | 1,41 |
| Hf | 0,07 | 0,02 | 0,03 | 0,09 | 0,07 | 0,10 | 0,04 | 0,03 |
| Ta | 0,55 | 1,08 | 0,36 | 2,10 | 0,55 | 0,42 | 1,24 | 0,62 |
| W | bdl | bdl | bdl | bdl | bdl | bdl | 0,02 | 0,05 |
| Tl | bdl | 0,02 | 0,01 | bdl | 0,01 | 0,04 | 0,01 | 0,05 |
| Pb | 28 | 18 | 46 | 41 | 46 | 13 | 10 | 21 |
| U | 0,06 | 0,01 | bdl | 0,02 | bdl | bdl | 0,07 | 0,05 |

nd: not detected, bdl: below detection limit

TABLE 7A. SELECTED MAIN AND TRACE ELEMENT COMPOSITIONS OF MUSCOVITE FROM LEUCOGRANITES (MEASURED BY LA ICP-MS WITH SI AS A STANDARD; SI MEASURED WITH SEM)

| sample numbe | MAR1 | | MAR4 | | 16R13 | | PEG25-1 | | PEG57-1 | | UTT1 | | UTT7 | |
|---|---|---|---|---|---|---|---|---|---|---|---|---|---|---|
| dike or body | Martell leucogranite | | Martell leucogranite | | Geißrücken leucogranite | | Geißrücken leucogranite | | Trahütten leucogranite | | Schlösselberg leucogranite | | Schlösselberg leucogranite | |
| core/rim | core | rim | core | rim | core | rim | core | rim | core | rim | core | rim | core | rim |
| $SiO_2$ [wt.%] | 43,34 | 42,63 | 43,60 | 43,19 | 44,00 | 43,87 | 44,07 | 43,45 | 43,36 | 43,00 | 43,36 | 43,79 | 43,15 | 43,15 |
| $TiO_2$ | 0,05 | 0,05 | 0,03 | 0,02 | 0,32 | 0,34 | 0,08 | 0,09 | 0,11 | 0,13 | 0,03 | 0,03 | 0,05 | 0,06 |
| $Al_2O_3$ | 37,15 | 36,94 | 37,36 | 37,28 | 37,11 | 36,52 | 34,11 | 32,82 | 38,47 | 37,68 | 37,56 | 36,64 | 37,60 | 38,04 |
| FeO | 1,88 | 1,66 | 1,90 | 1,58 | 1,26 | 1,71 | 3,92 | 3,60 | 1,08 | 1,03 | 1,69 | 1,49 | 1,69 | 1,53 |
| MnO | 0,03 | 0,03 | 0,02 | 0,02 | 0,01 | 0,02 | 0,02 | 0,02 | 0,01 | 0,01 | 0,01 | 0,01 | 0,01 | 0,01 |
| MgO | 0,30 | 0,60 | 0,53 | 0,63 | 0,66 | 0,78 | 0,91 | 0,95 | 0,48 | 0,38 | 0,55 | 0,56 | 0,51 | 0,51 |
| CaO | 0,03 | 0,06 | 0,03 | 0,07 | 0,00 | 0,00 | 0,00 | 0,01 | 0,01 | 0,00 | 0,08 | 0,27 | 0,14 | 0,15 |
| $Na_2O$ | 0,94 | 0,97 | 0,86 | 0,90 | 0,96 | 0,74 | 0,36 | 0,47 | 0,74 | 0,63 | 1,13 | 0,80 | 0,59 | 0,98 |
| $K_2O$ | 10,12 | 10,20 | 10,24 | 10,36 | 10,71 | 10,88 | 11,09 | 10,85 | 10,76 | 10,34 | 9,90 | 9,88 | 10,72 | 10,09 |
| Total | 93,84 | 93,14 | 94,56 | 94,05 | 95,04 | 94,87 | 94,57 | 92,27 | 95,03 | 93,19 | 94,32 | 93,45 | 94,46 | 94,53 |
| Li [ppm] | 575 | 449 | 358 | 403 | 53 | 32 | 398 | 415 | 305 | 315 | 70 | 62 | 176 | 179 |
| Be | 23 | 16 | 30 | 17 | 10 | 10 | 7 | 6 | 19 | 19 | 19 | 22 | 20 | 17 |
| Mg | 1235 | 1510 | 1458 | 2345 | 2667 | 3221 | 5071 | 5761 | 1595 | 1674 | 2960 | 1946 | 1970 | 2139 |
| P | 119 | 78 | 44 | 53 | 91 | 84 | 11 | 8 | 208 | 204 | 72 | 121 | 298 | 210 |
| Ca | 46 | 29 | 28 | 40 | 33 | 70 | 163 | 143 | 149 | 179 | 28 | 34 | 25 | 27 |
| Ti | 318 | 308 | 159 | 124 | 1936 | 2044 | 509 | 558 | 668 | 753 | 196 | 158 | 298 | 344 |
| V | 0,03 | 0,01 | 0,00 | 0,01 | 0,12 | 0,06 | 0,03 | 0,03 | 0,11 | 0,08 | 0,07 | 0,18 | 0,02 | 0,02 |
| Cr | 1,52 | 1,15 | 0,86 | 1,23 | 1,12 | 4,9 | 0,21 | 0,23 | 0,42 | 0,38 | 1,27 | 2,08 | 0,80 | 0,94 |
| Mn | 237 | 222 | 142 | 136 | 116 | 158 | 170 | 174 | 92 | 97 | 91 | 51 | 80 | 84 |
| Co | 0,27 | 0,05 | 0,07 | 0,12 | 0,17 | 0,46 | 0,30 | 0,32 | 0,04 | 0,04 | 0,15 | 0,42 | 0,08 | 0,08 |
| Ni | 2,02 | 0,28 | 0,05 | 0,08 | 0,00 | 0,15 | 1,96 | 0,14 | 1,75 | 0,34 | 0,01 | 0,19 | 0,04 | 0,08 |
| Cu | 0,41 | 0,12 | 0,12 | 0,16 | 0,12 | 0 | 0,31 | 0,18 | 0,25 | 0,24 | 0,18 | 1,17 | 0,09 | 0,09 |
| Zn | 86 | 94 | 126 | 52 | 16 | 11 | 184 | 209 | 85 | 88 | 89 | 28 | 80 | 84 |
| Ga | 118 | 106 | 93 | 98 | 75 | 73 | 43 | 38 | 109 | 107 | 102 | 111 | 121 | 120 |
| Ge | 3,6 | 2,8 | 2,3 | 2,5 | 3,1 | 3,0 | 2,3 | 1,6 | 3,5 | 3,2 | 2,2 | 2,6 | 3,9 | 3,8 |
| Rb | 1104 | 957 | 777 | 798 | 790 | 647 | 598 | 598 | 1371 | 1291 | 1073 | 1044 | 1090 | 1043 |
| Sr | 0,32 | 0,38 | 0,33 | 0,41 | 0,56 | 1,85 | 12,39 | 10,90 | 0,22 | 0,20 | 0,16 | 1,09 | 0,16 | 0,13 |
| Zr | 1,65 | 1,30 | 1,05 | 1,08 | 2,1 | 2,47 | 0,32 | 0,39 | 0,70 | 0,60 | 1,46 | 1,50 | 2,70 | 2,18 |
| Nb | 167 | 140 | 232 | 322 | 91 | 71 | 32 | 4 | 264 | 255 | 139 | 114 | 181 | 233 |
| Sn | 217 | 160 | 172 | 187 | 176 | 201 | 57 | 20 | 319 | 284 | 165 | 203 | 240 | 218 |
| Cs | 39 | 24 | 63 | 52 | 16 | 13 | 55 | 27 | 84 | 55 | 27 | 24 | 27 | 25 |
| Ba | 0,59 | 0,80 | 0,24 | 0,36 | 15 | 40 | 152 | 150 | 0,47 | 0,52 | 0,15 | 1,49 | 0,64 | 0,37 |
| Hf | 0,28 | 0,22 | 0,62 | 0,48 | 0,17 | 0,24 | 0,03 | 0,03 | 0,12 | 0,10 | 0,24 | 0,24 | 0,37 | 0,34 |
| Ta | 11 | 8 | 221 | 58 | 6 | 4 | 3 | bdl | 30 | 24 | 12 | 10 | 18 | 33 |
| W | 16 | 20 | 19 | 17 | 52 | 47 | 10 | 2 | bdl | bdl | 18 | 14 | 73 | 76 |
| Tl | 6 | 5 | 4 | 4 | 3 | 2 | 3 | 3 | 4 | 4 | 5 | 5 | 6 | 5 |
| Pb | 10 | 6 | 5 | 5 | 4 | 11 | 19 | 14 | 3 | 3 | 3 | 6 | 6 | 6 |
| K/Rb | 76 | 89 | 109 | 108 | 112 | 140 | 154 | 151 | 65 | 66 | 77 | 79 | 82 | 80 |
| K/Tl | 14757 | 17743 | 21842 | 23054 | 31188 | 36258 | 32487 | 31720 | 20931 | 21758 | 16930 | 16658 | 15894 | 16400 |
| K/Cs | 2158 | 3507 | 1343 | 1647 | 5507 | 7090 | 1671 | 3313 | 1067 | 1551 | 3067 | 3459 | 3251 | 3336 |
| K/Ba | 141574 | 106247 | 350343 | 236016 | 5770 | 2272 | 604 | 601 | 191545 | 166003 | 556603 | 54982 | 138302 | 223714 |

TABLE 7B. SELECTED MAIN AND TRACE ELEMENT COMPOSITIONS OF MUSCOVITE FROM SPODUMENE PEGMATITES (MEASURED BY LA ICP-MS WITH SI AS A STANDARD; SI MEASURED WITH SEM)

| sample numbe | 15R50 | | GM22 | | PEG200 | | PEG51 | | PEG73 | | RADZ1 | | SW1 | |
|---|---|---|---|---|---|---|---|---|---|---|---|---|---|---|
| locality | Weinebene spodumene pegmatite | | Schöcklkreuz spodumene pegmatite | | Garrach spodumene pegmatite | | Mitterberg spodumene pegmatite | | spodumene pegmatite (Wölzer Tauern pegmatite field) | | Rotes Kögele spodumene pegmatite | | spodumene pegmatite (Falkenberg pegmatite field) | |
| core/rim | core | rim | core | rim | core | rim | core | rim | core | rim | core | rim | core | rim |
| $SiO_2$ [wt.%] | 43,21 | 44,26 | 43,60 | 43,96 | 42,83 | 44,24 | 43,04 | 43,34 | 44,35 | 45,07 | 42,98 | 43,34 | 45,84 | 45,97 |
| $TiO_2$ | 0,27 | 0,26 | 0,07 | 0,06 | 0,05 | 0,05 | 0,04 | 0,04 | 0,12 | 0,12 | 0,57 | 0,60 | 0,27 | 0,26 |
| $Al_2O_3$ | 37,28 | 36,88 | 37,03 | 37,22 | 37,17 | 38,05 | 36,56 | 37,47 | 34,67 | 34,54 | 37,11 | 36,37 | 28,78 | 27,85 |
| FeO | 1,99 | 1,75 | 2,10 | 1,36 | 2,69 | 1,85 | 1,93 | 2,16 | 2,33 | 1,61 | 1,65 | 1,62 | 0,41 | 0,41 |
| MnO | 0,06 | 0,07 | 0,02 | 0,02 | 0,04 | 0,04 | 0,07 | 0,09 | 0,03 | 0,02 | 0,03 | 0,04 | bdl | bdl |
| MgO | 0,23 | 0,40 | 0,53 | 0,43 | 0,20 | 0,23 | 0,18 | 0,27 | 0,78 | 1,03 | 0,35 | 0,58 | 4,63 | 4,16 |
| CaO | 0,06 | 0,03 | 0,04 | 0,10 | 0,11 | 0,04 | bdl | 0,01 | 0,14 | bdl | 0,14 | 0,15 | 0,03 | bdl |
| $Na_2O$ | 0,70 | 0,70 | 0,78 | 0,71 | 0,32 | 0,73 | 0,63 | 0,23 | 0,89 | 1,09 | 0,75 | 0,78 | 0,42 | 0,16 |
| $K_2O$ | 10,22 | 9,95 | 10,24 | 10,49 | 10,61 | 10,55 | 10,96 | 11,01 | 10,62 | 10,02 | 10,59 | 10,29 | 11,11 | 10,56 |
| Total | 94,02 | 94,30 | 94,41 | 94,36 | 94,01 | 95,79 | 93,42 | 94,61 | 93,93 | 93,50 | 94,17 | 93,78 | 91,48 | 89,39 |
| Li [ppm] | 395 | 470 | 361 | 332 | 372 | 424 | 888 | 841 | 1316 | 891 | 1101 | 1582 | 1780 | 1736 |
| Be | 104 | 75 | 21 | 22 | 27 | 33 | 31 | 32 | 13 | 7 | 44 | 31 | 40 | 42 |
| Mg | 1533 | 1393 | 1278 | 1278 | 65 | 79 | 321 | 321 | 6436 | 5133 | 1795 | 2374 | 32574 | 31038 |
| P | 176 | 177 | 42 | 40 | 28 | 43 | 58 | 66 | 19 | 15 | 117 | 105 | bdl | bdl |
| Ca | 396 | 261 | 450 | 509 | 34 | 61 | 272 | 213 | 129 | 142 | 1061 | 916 | 50 | 91 |
| Ti | 1604 | 1546 | 430 | 332 | 277 | 282 | 249 | 232 | 711 | 691 | 3436 | 3625 | 1636 | 1575 |
| V | 1,86 | 2,39 | 0,39 | 0,36 | 0,38 | 0,46 | 0,05 | 0,03 | 0,43 | 0,42 | 0,09 | 0,09 | 46 | 46 |
| Cr | 1,10 | 0,61 | 0,44 | 0,50 | 1,4 | 1,4 | 0,5 | 0,5 | 0,4 | 0,4 | 5,7 | 4,3 | 16,9 | 29,7 |
| Mn | 484 | 563 | 147 | 141 | 296 | 336 | 545 | 678 | 251 | 179 | 232 | 293 | 16 | 17 |
| Co | 1,11 | 1,43 | 0,33 | 0,44 | 0,04 | 0,09 | 0,16 | 0,17 | 0,13 | 0,24 | 0,29 | 0,43 | 0,05 | 0,04 |
| Ni | 2,43 | 0,61 | 0,10 | 0,16 | 0,09 | 0,25 | 0,51 | 0,18 | 0,04 | bdl | 0,22 | 0,13 | 0,42 | 0,26 |
| Cu | 1,18 | 1,01 | 0,00 | 0,03 | 0,08 | 0,19 | 0,36 | 0,23 | 0,15 | 0,13 | 0,09 | 0,02 | 0,21 | 0,16 |
| Zn | 331 | 386 | 136 | 142 | 101 | 100 | 246 | 234 | 262 | 124 | 154 | 179 | 36 | 41 |
| Ga | 117 | 106 | 75 | 94 | 101 | 110 | 115 | 112 | 65 | 70 | 130 | 125 | 44 | 44 |
| Ge | 3,81 | 3,64 | 4,92 | 6,04 | 3,10 | 3,94 | 5,69 | 5,86 | 2,66 | 2,43 | 9,33 | 8,34 | 3,75 | 3,72 |
| Rb | 4678 | 4919 | 1031 | 2200 | 1892 | 1983 | 1748 | 1667 | 582 | 577 | 2341 | 2350 | 985 | 966 |
| Sr | 1,68 | 1,52 | 1,64 | 1,03 | 0,30 | 0,74 | 1,54 | 1,23 | 8,37 | 7,49 | 0,68 | 0,59 | 14,88 | 14,14 |
| Zr | 0,41 | 0,53 | 0,49 | 0,44 | 0,30 | 0,91 | 0,30 | 0,88 | 1,24 | 1,53 | 1,36 | 1,71 | 0,59 | 0,53 |
| Nb | 512 | 507 | 116 | 218 | 242 | 263 | 295 | 292 | 66 | 64 | 316 | 348 | 36 | 36 |
| Sn | 582 | 609 | 99 | 234 | 308 | 407 | 436 | 467 | 111 | 80 | 475 | 389 | 31 | 32 |
| Cs | 161 | 171 | 21 | 72 | 31 | 49 | 292 | 302 | 15 | 12 | 45 | 45 | 97 | 92 |
| Ba | 5,47 | 5,29 | 53,58 | 16,13 | 0,65 | 1,28 | 1,99 | 1,66 | 76,31 | 79,06 | 19,54 | 18,18 | 49,46 | 48,75 |
| Hf | 0,02 | 0,05 | 0,08 | 0,08 | 0,11 | 0,18 | 0,20 | 0,30 | 0,16 | 0,17 | 0,15 | 0,16 | 0,08 | 0,06 |
| Ta | 42 | 48 | 7,63 | 18 | 79 | 73 | 52 | 64 | 3,9 | 3,5 | 37 | 40 | 24 | 19 |
| W | bdl | bdl | bdl | bdl | 5,88 | 8,82 | bdl | bdl | bdl | bdl | bdl | bdl | bdl | bdl |
| Tl | 22 | 21 | 5,1 | 11 | 18 | 18 | 9,4 | 8,5 | 2,1 | 2,0 | 17 | 15 | 4,9 | 4,8 |
| Pb | 4,8 | 3,9 | 30 | 32 | 53 | 72 | 33 | 23 | 20 | 13 | 9,2 | 7,9 | 2,6 | 2,2 |
| K/Rb | 18 | 17 | 82 | 40 | 47 | 44 | 52 | 55 | 151 | 144 | 38 | 36 | 94 | 91 |
| K/Tl | 3924 | 3847 | 16770 | 8127 | 4910 | 4928 | 9687 | 10746 | 42205 | 42547 | 5264 | 5882 | 18823 | 18351 |
| K/Cs | 527 | 483 | 3995 | 1218 | 2799 | 1803 | 312 | 303 | 5977 | 7204 | 1940 | 1904 | 948 | 953 |
| K/Ba | 15505 | 15616 | 1587 | 5400 | 135901 | 68427 | 45685 | 55107 | 1156 | 1052 | 4499 | 4698 | 1864 | 1799 |

TABLE 8A. CHEMICAL FORMULAS OF TOURMALINE FROM SPODUMENE PEGMATITES

04R45 (core): Mg-bearing schorl - elbaite

$^{X}(Na_{0.70}Ca_{0.08}\square_{0.22})\ ^{Y}(Fe^{2+}_{1.51}Al_{0.69}Li_{0.45}Mg_{0.21}Mn^{2+}_{0.05}Ti^{4+}_{0.05}Zn^{2+}_{0.04})_{\Sigma 3.00}\ ^{Z}(Al_{5.74}Mg_{0.15}Fe^{3+}_{0.11})_{\Sigma 6.00}\ (BO_3)_3\ ^{T}[Si_{6.00}O_{18}]\ ^{V}(OH)_{3.00}\ ^{W}[(OH)_{0.84}F_{0.10}O_{0.06}]$

04R45 (rim): Mg-bearing schorl - elbaite

$^{X}(Na_{0.71}Ca_{0.05}\square_{0.24})\ ^{Y}(Fe^{2+}_{1.59}Al_{0.70}Li_{0.44}Mg_{0.16}Mn^{2+}_{0.05}Ti^{4+}_{0.04}Zn^{2+}_{0.03})_{\Sigma 3.01}\ ^{Z}(Al_{5.74}Mg_{0.15}Fe^{3+}_{0.11})_{\Sigma 6.00}\ (BO_3)_3\ ^{T}[Si_{6.00}O_{18}]\ ^{V}(OH)_{3.00}\ ^{W}[(OH)_{0.87}F_{0.09}O_{0.04}]$

14R16 (core): Li-bearing oxy-schorl

$^{X}(Na_{0.71}Ca_{0.03}\square_{0.26})\ ^{Y}(Fe^{2+}_{1.76}Al_{0.94}Li_{0.14}Mg_{0.05}Zn^{2+}_{0.05}Mn^{2+}_{0.04}Ti^{4+}_{0.02})_{\Sigma 3.00}\ ^{Z}(Al_{5.73}Fe^{3+}_{0.27})_{\Sigma 6.00}\ (BO_3)_3\ ^{T}[Si_{5.99}Al_{0.01}O_{18}]\ ^{V}(OH)_{3.00}\ ^{W}[O_{0.63}(OH)_{0.31}F_{0.06}]$

14R16 (rim): Mg-bearing oxy-schorl - elbaite

$^{X}(Na_{0.80}Ca_{0.06}\square_{0.14})\ ^{Y}(Fe^{2+}_{1.58}Al_{0.85}Li_{0.28}Mg_{0.20}Mn^{2+}_{0.03}Zn^{2+}_{0.03}Ti^{4+}_{0.03})_{\Sigma 3.00}\ ^{Z}(Al_{5.73}Fe^{3+}_{0.27})_{\Sigma 6.00}\ (BO_3)_3\ ^{T}[Si_{6.00}O_{18}]\ ^{V}(OH)_{3.00}\ ^{W}[O_{0.53}(OH)_{0.41}F_{0.06}]$

15R42 (core): Mg-bearing schorl - elbaite

$^{X}(Na_{0.74}Ca_{0.04}\square_{0.22})\ ^{Y}(Fe^{2+}_{1.73}Al_{0.73}Li_{0.28}Mg_{0.17}Mn^{2+}_{0.04}Ti^{4+}_{0.03}Zn^{2+}_{0.03})_{\Sigma 3.01}\ ^{Z}(Al_{5.66}Fe^{3+}_{0.24}Mg_{0.10})_{\Sigma 6.00}\ (BO_3)_3\ ^{T}[Si_{5.97}Al_{0.03}O_{18}]\ ^{V}(OH)_{3.00}\ ^{W}[(OH)_{0.72}O_{0.24}F_{0.04}]$

15R42 (rim): Mg-bearing schorl - elbaite

$^{X}(Na_{0.66}Ca_{0.06}\square_{0.28})\ ^{Y}(Fe^{2+}_{1.55}Al_{0.63}Li_{0.36}Mg_{0.28}Fe^{3+}_{0.10}Zn^{2+}_{0.04}Ti^{4+}_{0.03}Mn^{2+}_{0.03})_{\Sigma 3.02}\ ^{Z}(Al_{5.53}Fe^{3+}_{0.27}Mg_{0.20})_{\Sigma 6.00}\ (BO_3)_3\ ^{T}[Si_{5.99}Al_{0.01}O_{18}]\ ^{V}(OH)_{3.00}\ ^{W}[(OH)_{0.97}F_{0.03}]$

TABLE 8B. CRYSTAL DATA AND SELECTED INTERATOMIC DISTANCES IN TOURMALINE CRYSTALS FROM SPODUMENE PEGMATITES (STANDARD DEVIATION IN BRACKETS)

| sample no. | 04R45 (rim) | 14R16 (core) | 15R42 (core) |
|---|---|---|---|
| *a* (Å) | 15.958(1) | 15.954(1) | 15.956(1) |
| *c* (Å) | 7.157(1) | 7.154(1) | 7.167(1) |
| *R*1 (%) | 1,44 | 1,23 | 1,3 |
| <*X*-O> (Å) | 2.692(1) | 2.703(1) | 2.692(1) |
| <*Y*-O> (Å) | 2.042(1) | 2.037(1) | 2.039(1) |
| <*Z*-O> (Å) | 1.916(1) | 1.916(1) | 1.919(1) |
| <*T*-O> (Å) | 1.620(1) | 1.619(1) | 1.619(1) |

TABLE 9. Sm-Nd ISOTOPIC DATA FROM SPODUMENE PEGMATITE AND LEUCOGRANITE SAMPLES

| sample no. | rock type | material | Sm [ppm] | Nd [ppm] | $^{147}Sm/^{144}Nd$ | $^{143}Nd/^{144}Nd$ | 2σd(m) | age [Ma] | ε(*t*)Nd |
|---|---|---|---|---|---|---|---|---|---|
| 04R45 | Spd pegmatite | WR | 0,899 | 1,771 | 0,3067 | 0,512429 | 0,000003 | 261±13 | -7,8 |
| | | Grt2 | 11,56 | 0,966 | 7,2527 | 0,524446 | 0,000004 | | |
| | | Grt3 | 0,930 | 11,16 | 7,2723 | 0,524195 | 0,000012 | | |
| | | Trm | 0,459 | 1,577 | 0,1758 | 0,512182 | 0,000006 | | |
| 14R16 | Spd pegmatite | WR | 5,564 | 12,34 | 0,2726 | 0,512355 | 0,000004 | 263.4±8.6 | -8,1 |
| | | Grt1 | 7,382 | 0,785 | 5,6982 | 0,521819 | 0,000006 | | |
| | | Grt2 | 7,534 | 0,606 | 7,5412 | 0,524813 | 0,000010 | | |
| | | Trm | 0,447 | 1,365 | 0,1979 | 0,512236 | 0,000004 | | |
| 15R42 | Spd pegmatite | WR | 0,839 | 1,510 | 0,3359 | 0,512464 | 0,000004 | 267.5±2.0 | -8,0 |
| | | Grt1 | 11,08 | 0,873 | 7,6983 | 0,525410 | 0,000034 | | |
| | | Grt2 | 10,64 | 1,028 | 6,2728 | 0,522820 | 0,000006 | | |
| 15R69 | leucogranite | WR | 2,234 | 5,587 | 0,2417 | 0,512267 | 0,000004 | 270.1±2.1 | -8,8 |
| | | Grt1 | 15,05 | 2,730 | 3,3377 | 0,517723 | 0,000010 | | |
| | | Grt2 | 5,933 | 1,227 | 2,9263 | 0,517028 | 0,000016 | | |
| RS32/01 | leucogranite* | WR | 0,479 | 1,377 | 0,2102 | 0,512285 | 0,000005 | 276.8±2.8 | -7,4 |
| | | Grt1 | 1,501 | 0,386 | 2,3554 | 0,516374 | 0,000010 | | |
| | | Grt2 | 1,674 | 0,152 | 6,6917 | 0,524031 | 0,000004 | | |
| | | Qtz+Fsp | 0,171 | 0,228 | 0,4542 | 0,512552 | 0,000007 | | |
| RS33/01 | pegmatitic layer | WR | 0,757 | 2,026 | 0,2260 | 0,512477 | 0,000001 | 273.2±3.1 | -4,4 |
| | in granite* | Grt | 1,053 | 0,156 | 4,0795 | 0,519364 | 0,000018 | | |
| | | Qtz+Fsp | 0,157 | 0,151 | 0,6264 | 0,512257 | 0,000009 | | |
| PEG25-1 | leucogranite | WR | 6,710 | 21,92 | 0,1850 | 0,512204 | 0,000004 | 259.0±2.3 | -8,1 |
| | | Grt1 | 4,179 | 1,123 | 2,2506 | 0,515698 | 0,000004 | | |
| | | Grt2 | 4,789 | 3,486 | 0,8306 | 0,513302 | 0,000005 | | |
| PEG57-1 | leucogranite | WR | 0,333 | 0,850 | 0,1850 | 0,512310 | 0,000009 | 250.4±5.3 | -7,7 |
| | | Grt1 | 0,303 | 0,129 | 2,2506 | 0,514245 | 0,000071 | | |
| | | Grt2 | 0,252 | 0,103 | 0,1979 | 0,514347 | 0,000050 | | |
| | | Trm | 0,167 | 0,514 | 0,8306 | 0,512239 | 0,000005 | | |

* sample from Mair & Schuster (2003)

ε(t)Nd is calculated with individual sample age.

TABLE 10. Rb-Sr ISOTOPIC DATA FROM SPODUMENE PEGMATITE AND LEUCOGRANITE SAMPLES

| sample no. | rock type | material | Rb [ppm] | Sr [ppm] | $^{87}Rb/^{86}Sr$ | $^{87}Sr/^{86}Sr$ | 2σd(m) | age [Ma] | Io |
|---|---|---|---|---|---|---|---|---|---|
| 14R23a | Spd pegmatite | Spd | 20,74 | 0,818 | 74,89 | 0,91934 | 0,000078 | 272.2±3.0 | 0,629 |
| 14R23f | Spd pegmatite | KFs | 1561 | 7,625 | 758,3 | 3,56590 | 0,000046 | | |
| 14R24a | Spd pegmatite | KFs | 994,8 | 8,193 | 403,8 | 2,23377 | 0,000006 | 247.2±2.5 | 0,81 |
| 14R24c | Spd pegmatite | Ms | 1517 | 2,055 | 8130 | 29,3994 | 0,000708 | | |
| 04R45 | Spd pegmatite | WR | 86** | 14** | 17,92 | 0,79392 | 0,000004 | | 0,72660 |
| 14R16 | Spd pegmatite | WR | 97** | 13** | 21,77 | 0,79512 | 0,000002 | | 0,71335 |
| 15R42 | Spd pegmatite | WR | 373** | 21** | 52,42 | 0,91347 | 0,000002 | | 0,71881 |
| 15R69 | leucogranite | WR | 222** | 16** | 40,82 | 0,87996 | 0,000002 | | 0,72316 |
| RS32/01 | leucogranite* | WR | 167,7 | 19,58 | 25,02 | 0,80809 | 0,000006 | | 0,70982 |
| RS33/01 | peg. layer in granite* | WR | 192** | 11** | 51,45 | 0,90058 | 0,000004 | | 0,70073 |
| PEG25-1 | leucogranite | WR | 142** | 75** | 5,492 | 0,73412 | 0,000002 | | 0,71420 |
| PEG57-1 | leucogranite | WR | 217** | 4** | 333,0 | 1,32731 | 0,000006 | | 0,73528 |

* sample from Mair & Schuster (2003), ** concentrations measured by ICP-MS.
Io (initial $^{87}Sr/^{86}Sr$ isotopic ratio) for whole rocks is calculated with individual sample age given in Table 9.

## REFERENCES


Ahrer, S. (2014) Geowissenschaftliche und aufbereitungstechnische Untersuchungen an ausgewählten Pegmatiten und deren Nb-Ta-Vererzungen in den Ostalpen, Steiermark, Österreich. Unpublished Master Thesis, Montanuniversität Leoben, Leoben, Austria (105 pp.).

Angel, F. (1933) Spodumen und Beryll aus den Pegmatiten von St. Radegund bei Graz. Zeitschrift für Kristallographie, Mineralogie und Petrographie 43/6, 441–446.

Angel, F. & Meixner, H. (1953) Die Pegmatite bei Spittal an der Drau. Carinthia II 143, 165–168.

Beck-Managetta, P., Eisenhut, M., Ertl, V., & Homann, O. (1991) Geologische Karte der Republik Österreich 1:50000 Blatt 189 Deutschlandsberg. Geologische Bundesanstalt, Wien, Austria.

Bockemühl, C. (1988) Der Marteller Granit (Südtirol Italien). Unpublished Dissertation, University of Basel, Basel, Switzerland (143 pp.).

Cerny, I., Moser, P., & Nedeff, P. (1989) Das Projekt "Lithium Koralpe". Berg- und Hüttenmännische Monatshefte 134, 151–165.

Černý, P. (1991) Rare-element Granitic Pegmatites. Part II: Regional to Global Environments and Petrogenesis. Geoscience Canada 18(2), 68–81.

Černý, P. & Burt, D.M. (1984): Paragenesis, crystallochemical characteristics, and geochemical evolution of micas in granite pegmatites. In Micas, Reviews in Mineralogy 13 (S.W. Bailey, ed.). Mineralogical Society of America, Blacksburg, Virginia (257–297).

Černý, P. & Ercit, T.S. (2005) The classification of granitic pegmatites revisited. The Canadian Mineralogist 43/6, 2005–2026.

Černý , P., Halden, N.M., Ferreira, K., Meintzer, R.E., Brisbin, W.C., Chackowsky, L.E., Corkery, M.T., Longstaffe, F.J., & Trueman, D.L. (2012) Extreme fractionation and deformation of the leucogranite-pegmatite suite at red cross lake, Manitoba, Canada. II. Petrology of the leucogranites and pegmatites. The Canadian Mineralogist 50, 1807–1822.

Dickin, A.P. (1995) Radiogenetic isotope geology. Cambridge University Press, Cambridge, UK.

Ertl, A., Mali, H., Schuster, R., Körner, W., Hughes, J.M., Brandstätter, F., & Tillmanns, E. (2009) Li-bearing, disordered Mg-rich tourmalines from the pegmatite-marble contact from the Austroalpine basement units (Styria, Austria). Mineralogy and Petrology 99/1–2, 89–104.

Ertl, A., Kolitsch, U., Dyar, M.D., Meyer, H.-P., Henry, D.J., Rossman, G.R., Prem, M., Ludwig, T., Nasdala, L., Lengauer, C.L., Tillmanns, E., & Niedermayr, G. (2016) Fluor-schorl, a new member of the tourmaline supergroup, and new data on schorl from the cotype localities. European Journal of Mineralogy 28, 163–177.

Esterlus, M. (1983) Kurzer Überblick über die Pegmatite im Angerkristallin der Oststeiermark. Archiv für Lagerstättenforschung Geologische Bundesanstalt 3, 31–34.

Froitzheim, N., Plašienka, D., & Schuster, R. (2008) Alpine tectonics of the Alps and Western Carpathians. In The Geology of Central Europe Volume 2 Mesozoic and Cenozoic (T. McCann, ed.). Geological Society of London, London, UK (1141–1232).

Fuertes-Fuente, M. & Martin-Izard, A. (1998) The Forcarei Sur rare-element granitic pegmatite field and associated mineralization, Galicia, Spain. Canadian Mineralogist 36, 303–325.

Gaidies, F., Abart, R., DeCapitani, C., Schuster, R., Connolly, J.A.D., & Reusser, E. (2006) Characterisation of polymetamorphism in the Austroalpine basement east of the Tauern Window using garnet isopleth thermobarometry. Journal of metamorphic Geology 24, 451–475.

Gaidies, F., DeCapitani, C., Abart, R., & Schuster, R. (2008) Prograde garnet growth along complex P-T-t paths: results from numerical experiments on polyphaser garnet from the Wölz Complex (Austroalpine basement). Contribution to Mineralogy and Petrology 155, 674–688.

Göd, R. (1989) The spodumene deposit at “Weinebene”, Koralpe, Austria. Mineralium Deposita 24, 270–278.

Gotthardt, C. (2015) Pegmatitgenese des Rappold- Komplex um St. Radegund, des Millstatt- Komplex und des Prijakt-Polinik-Komplex. Unpublished Master Thesis, University of Graz, Graz, Austria (155 pp.).

Griffith, T.A., Habler, G. Rhede, D., Wirth, R., & Abart, R. (2014) Localization of submicron inclusion re-equilibration at healed fractures in host garnet. Contributions in Mineralogy and Petrology 168(6), doi.org/10.1007/s00410-014-1077-4.

Groat, L.A., Mulja, T., Mauthner, M.H.F., Ercit, T.S., Raudsepp, M., Gault, R.A., & Rollo, H.A. (2003) Geology and mineralogy of the Little Nahanni rare-element granitic pegmatites, Northwest Territories. Canadian Mineralogist 41, 139–160.

Habler, G. & Thöni, M. (2001) Preservation of Permo–Triassic low-pressure assemblages in the Cretaceous high-pressure metamorphic Saualpe crystalline basement (Eastern Alps, Austria). Journal of metamorphic Geology 19, 679–697.

Habler, G., Thöni, M., & Miller, C. (2007) Major and trace element chemistry and Sm-Nd age correlation of magmatic pegmatite garnet overprinted by eclogite-facies metamorphism. Chemical Geology 241/1, 4–22.

Handler, R., Neubauer, F. Hermann, S., & Dallmeyer, R.D. (1999) Silurian–Devonian $^{40}Ar/^{39}Ar$ mineral ages from the Kaintaleck nappe: evidence for Mid-Paleozoic tectonothermal activity in upper Austroalpine basement of the Eastern Alps (Austria). Geologica Carpathica 50/3, 229–239.

Heede, H.-U. (1997) Isolopengeologische Untersuchungen an Gesteinen des ostalpinen Saualpenkristallins. Kärnten-Österreich. Münstersche Forschungen zur Geologie und Paläontologie 81, 4–134.

Heilbronner, R. & Barrett, S. (2013) Image analysis in Earth sciences: microstructures and textures of earth materials (Vol. 129). Springer Science & Business Media, Berlin- Heidelberg, Germany.

Heritsch, H. (1984) Die Bildungsbedingungen des Spodumenpegmatites vom Steinbruch Gupper, Koralpe, bei Deutschlandsberg, Weststeiermark. Mitteilungen des Naturwissenschaftlichen Vereines für Steiermark 114, 47–56.

Höller H. (1959) Ein Spodumen-Beryll-Pegmatit und ein mineralreicher Marmor im Wildbachgraben bei Deutschlandsberg. Mineralogisches Mitteilungsblatt, Joanneum Graz 1959(1), 19.

Irvine, T.N. & Baragar, W.R.A. (1971) A guide to the chemical classification of the common volcanic rocks. Canadian Journal of Geosciences 8, 523–548.

Kesler, T.L. & Vine, J.D. (1976) Occurence, development and long-range outlook of lithium-pegmatite ore in the Carolinas. U.S. Geological Survey Professional Paper 1005, 45–50.

Kesler, S.E., Gruber, P.W., Medina, P.A., Keoleian, G.A., Everson, M.P., & Wallington, T.J. (2012) Global lithium resources: Relative importance of pegmatite, brine and other deposits. Ore Geology Reviews 48, 55–69.

Koller, F., Götzinger, M.A., Neumayer, R., & Niedermayr, G. (1983) Beiträge zur Mineralogie und Geochemie der Pegmatite des St. Radegunder Kristallins und der Gleinalpe. Archiv für Lagerstättenforschung Geologische Bundesanstalt 3, 47–65.

Kruger,F.J., Kamber, B.S., & Harris, P.D. (1998) Isotopic peculiarities of an Archaean pegmatite (Union Mine, Mica, South Africa) Geochemical and geochronological implications. Precambrian Research 91, 253–267.

London, D. (1984) Experimental phase equilibria in the system $LiAlSiO_4$-$SiO_2$-H2O: a petrogenetic grid for lithium-rich pegmatites. American Mineralogist 69, 995–1005.

London, D. (2008) Pegmatites. The Canadian Mineralogist Special Publication 10. Mineralogical Association of Canada, Québec, Canada.

Ludwig, K.R. (2003) Isoplot/Ex version 3.0. A geochronological toolkit for Microsoft Excel. Berkeley Geochronological Centre Special Publication, Berkeley, USA.

Mair, V. & Schuster, R. (2003) The metamorphic evolution of the Ortler Crystalline. Mitteilungen der Österreichischen Mineralogischen Gesellschaft 148, 215–217.

Mair, V., Nocker, C., & Tropper, P. (2007) Das Ortler-Campo Kristallin in Südtirol. Mitteilungen der Österreichisch Mineralogischen Gesellschaft, 153, 219–240.

Mali, H. (2004) Die Spodumenpegmatite von Brettstein und Pusterwald (Wölzer Tauern, Steiermark, Österreich). Joannea - Mineralogie 2, 5–53.

Marsch, F. (1983) Spodumenkristalle in einem Pegmatit der Kreuzeckgruppe. Mitteilungen der Österreichischen Mineralogischen Gesellschaft 129, 13-18.

Meixner, H. (1966) Neue Mineralfunde in den österreichischen Ostalpen XXI. Carinthia II 156/76, 97–108.

Moser, B., Postl, W., & Walter, F. (1987) Spodumen vom Klementkogel, Hebalpe (Steiermark). Mitteilungen der Österreichischen Mineralogischen Gesellschaft 132, 163–165.

Middlemost, E.A. (1994) Naming materials in the magma/igneous rock system. Earth-Science Reviews 37(3–4), 215–224.

Miller, C. & Thöni, M. (1997) Eo-Alpine eclogitisation of Permian MORB-type gabbros in the Koralpe (Eastern Alps, Austria): New geochronological, geochemical and petrological data. Chemical Geology 137, 283–310.

Miller, C., Zanetti, A., Thöni, M., & Konzett, J. (2007) Eclogitisation of gabbroic rocks: Redistribution of trace elements and Zr in rutile thermometry in an Eo-Alpine subduction zone (Eastern Alps). Chemical Geology 239, 96–123.

Nabelek, P.I. & Liu, M. (2004) Petrologic and thermal constraints on the origin of leucogranites in collisional orogens. Transactions of the Royal Society of Edinburgh, Earth Sciences 95, 73–85.

Niedermayr, G. & Göd, R. (1992) Das Spodumenvorkommen auf der Weinebene und seine Mineralien. Carinthia II 182/102, 21–35.

North American Commission on Stratigraphic Nomenclature (2005) North American Stratigraphic Code. American Association of Petroleum Geologists Bulletin 89, 1547–1591.

Ntaflos, T., Bizimis, M., & Abart, R. (2017) Mantle xenoliths from Szentbekalla, Balaton, Geochemical and petrological constrains on the evolution of the lithospheric mantle underneath Pannonian Basin, Hungary. Lithos 276, 30–44.

Passchier, C.W. & Trouw R.A.J. (2005) Microtectonics. 2nd Edition, Springer, Berlin Heidelberg, Germany.

Pestal, G., Rataj, J., Reitner, J.M., & Schuster, R. (2006) Geologische Karte der Republik Österreich 1:50000 Blatt 182 Spittal an der Drau. Geologische Bundesanstalt, Wien, Austria.

Philpotts, A. & Ague, J. (2009) Principles of Igneous and Metamorphic Petrology. Cambridge University Press, Cambridge, UK.

Pouchou, J.L. & Pichoir, F. (1991) Quantitative analysis of homogenous or stratified microvolumes applied the model "PAP". In: Electron Probe Quantification (K.F.J. Heinrich & D.E. Newbury, eds.). Springer, Boston, Massachusetts/USA (31–75).

Prince, C.I., Kosler, J., Vance, D., & Günther, D. (2003) Comparison of laser ablation ICPMS and isotope dilution REE analyses - implications for Sm-Nd garnet geochronology. Chemical Geology 168, 255–274.

Roda-Robles, E., Pesquera, A., Gil-Crespo, P.P., Vieira, R., Lima, A., Garante-Olave, I., Martins, T., & Torres-Ruiz, J. (2016) Geology and mineralogy of Li mineralization in the Central Iberian Zone (Spain and Portugal). Mineralogical Magazine 80, 103–126.

Proyer, A. (2003) The preservation of high-pressure rocks during exhumation: metagranites and metapelites. Lithos 70, 183–194.

Rubbo, M., Borghi, A., & Compagnoni, R. (1999) Thermodynamic analysis of garnet growth zoning in eclogite facies granodiorite from M. Mucrone, Sesia Zone, Western Italian Alps. Contributions to Mineralogy and Petrology 137, 289–303.

Rudnick, R.L. & Gao, S. (2003) Composition of the Continental Crust. In The Crust (R.L. Rudnick, ed.). Springer, Elsevier-Pergamon, Oxford, UK (1–64).

Schmid, S.M., Fügenschuh, B., Kissling, E., & Schuster, R. (2004) Tectonic map and overall architecture of the Alpine orogen. Eclogae Geologicae Helvetiae 97/1, 93–117.

Schulz, B. (1994) Geologische Karte des Altkristallins östlich des Tauferer Tales (Südtirol). Erlanger geologische Abhandlungen 124, 1–28.

Schulz, B. (2000) Bericht 1999 über geologische Aufnahmen im Ostalpinen Altkristallin auf Blatt 178 Hopfgarten in Defereggen. Jahrbuch der Geologischen Bundesanstalt 142/3, 366–368.

Schuster, R. & Stüwe, K. (2008) The Permian Metamorphic Event in the Alps. Geology 36/8, 303–306.

Schuster, R., Scharbert, S., Abart, R., & Frank, W. (2001) Permo-Triassic extension and related HT/LP metamorphism in the Austroalpine-Southalpine realm. Mitteilungen der Gesellschaft der Geologie und Bergbaustudenten Österreichs 45, 111–141.

Searle, M.P. & Fryer, B.J. (1986) Garnet, tourmaline and muscovite-bearing leucogranites, gneisses and migmatites of the Higher Himalayas from Zanskar, Kulu, Lahoul and Kashmir. In Collision Tectonics (M.P. Coward & A.C. Ries, eds.). Geological Society Special Publication 19, London, UK (185–201).

Selway, J.B., Breaks, F.W., & Tindle, A.G. (2005) A Review of Rare-Element (Li-Cs-Ta) Pegmatite Exploration Techniques for the Superior Province, Canada, and Large Worldwide Tantalum Deposits. Exploration and Mining Geology 14, 1–30.

Senzenberger, D. (2001) Zonarbau und geochemische Charakteristik von Pegmatiten des Hohenwart (Wölzer Tauern, Steiermark). Unpublished Diploma Thesis, Montanuniversität Leoben, Leoben, Austia (176 pp.).

Sheldrick, G.M. (1998) SHELXL97, Release 97-2. Program for crystal structure refinement. University of Göttingen, Göttingen, Germany.

Simmons, W., Falster, A., Webber, K., Roda-Robles, E., Boudreaux, A.P., Grassi, L.R., & Freeman, G. (2014) Bulk composition of Mt. Mica pegmatite, Maine, USA: Implications for the origin of an LCT type pegmatite by anatexis. The Canadian Mineralogist 54, 1053–1070.

Sölva, H., Grasemann, B., Thöni, M., Thiede, R., & Habler, G. (2005) The Schneeberg Normal Fault Zone: Normal faulting associated with Cretaceous SE-directed extrusion in the Eastern Alps (Italy/Austria). Tectonophysics 401, 143–166.

Sölva, H., Thöni, M., & Habler, G. (2003) Dating a single garnet crystal with very high Sm/Nd ratios (Campo basement unit, Eastern Alps). European Journal of Mineralogy 15, 35–42

Steiner, R. (2017) Differentiation der Pegmatite des Millstätter See-Rückens. Unpublished Master Thesis, Montanuniversität Leoben, Leoben, Austia (189 pp.).

Stöckhert, B. (1987) Das Uttenheimer Pegmatitfeld (Ostalpines Altkristallin, Südtirol) Genese und alpine Überprägung. Erlanger geologische Abhandlungen 114, 83–106.

Thöni, M. (2002) Sm-Nd isotope systematics in garnet from different lithologies (Eastern Alps): age results, and an evaluation of potential problems for garnet Sm-Nd chronometry. Chemical Geology 185, 255–281.

Thöni, M. & Miller, C. (2000) Permo-Triassic pegmatites in the eo-Alpine eclogite-facies Koralpe complex, Austria: age and magma source constraints from mineral chemical, Rb-Sr and Sm-Nd isotopic data. Schweizerische Mineralogische und Petrologische Mitteilungen 80, 169–186.

Thöni, M. & Miller, C. (2004) Ordovician meta-pegmatite garnet (N–W Ötztal basement, Tyrol, Eastern Alps): preservation of magmatic garnet chemistry and Sm-Nd age during mylonitization. Chemical Geology 209, 1–26.

Thöni, M. & Miller, C. (2010) Andalusite formation in a fast exhuming high-P wedge: Textural, microchemical and Sm-Nd and Rb-Sr age constraints for a Cretaceous P-T-t Path at Kienberg, Saualpe (Eastern Alps). Austrian Journal of Earth Sciences 103/2, 118–131.

Thöni, M., Miller, C., Zanetti, A., Habler, G., & Goessler, W. (2008) Sm-Nd isotope systematics of high-REE accessory minerals and major phases: ID-TIMS, LA-ICP-MS and EPMA data constrain multiple Permian–Triassic pegmatite emplacement in the Koralpe, Eastern Alps. Chemical Geology 254, 216–237.

Walter, F. (1998) Die Pegmatite des Millstätter See-Rückens. Mitteilungen der Österreichischen Mineralogischen Gesellschaft 143, 437–458.

Whitney, D.L. & Evans, B.W. (2010) Abbrevations for names of rock-forming minerals. American Mineralogist 95, 185–187.

Wenger, M. & Armbruster, T. (1990) Der Lithiumpyroxen Spodumen $LiAlSi_2O_6$: Mineralogie und Kristallchemie der Vorkommen in der Steiermark. Mitteilungen der Abteilung für Mineralogie am Landesmuseum Joanneum 58, 3–10.

Whitworth, M.P. & Feely, M. (1994) The compositional range of magmatic Mn-garnets in the Galway Granite, Connemara, Ireland. Mineralogical Magazine 58(1), 163–168.

Zeitlhofer, H., Schneider, D., Grasemann, B., Petrakakis, K., & Thöni, M. (2013) Polyphase tectonics and later Variscan extension in Austria (Moldanubian Zone, Strugenau Area). International Journal of Earth Science 103/1, 83–102.

## 4. LITHIUM PEGMATITE OF ANATECTIC ORIGIN - A CASE STUDY FROM THE AUSTROALPINE UNIT PEGMATITE PROVINCE (EASTERN EUROPEAN ALPS): GEOLOGICAL DATA AND GEOCHEMICAL MODEL

*Tanja Knoll[1], Benjamin Huet[2], Ralf Schuster[1], Heinrich Mali[3], Theodoros Ntaflos[4], Christoph Hauzenberger[5]*

*[1]Department of Mineral Resources, Geological Survey of Austria, Neulinggasse 38, 1030 Vienna, Austria*

*[2]Department of Hard Rock Geology, Geological Survey of Austria, Neulinggasse 38, 1030 Vienna, Austria*

*[3]Department of Applied Geosciences and Geophysics, Montanuniversität Leoben, Peter-Tunnerstraße 5, 8700 Leoben, Austria*

*[4]Department of Lithospheric Research, University of Vienna, Althanstraße 14, 1090 Vienna, Austria*

*[5]Institute of Earth Sciences - NAWI Graz Geocenter, Karl-Franzens-Universität Graz, 28010 Graz, Austria*

*Corresponding author: tanja.knoll@geologie.ac.at*

---

➔ *Manuscript status: open access publication*
➔ *Ore Geology Reviews, Volume 154, March 2023, 105298.; https://doi.org/10.3749/canmin.1700092*
➔ *Published: 12.01.2023*

---

ABSTRACT

There is an ongoing debate as to whether rare element pegmatite is always related to fractional crystallization of huge fertile granite bodies or whether it can also form directly from limited portions of enriched anatectic melt. In this contribution, we present a case study from the Eastern European Alps, showing the continuous evolution from melt generation in staurolite bearing micaschist to spodumene (LiAlSi2O6) bearing pegmatite. The investigated Austroalpine Unit Pegmatite Province formed during Permian lithospheric extension and all levels of the Permian crust are now accessible in a Cretaceous nappe stack. This nappe stack is mapped in detail, subdivided lithostratigraphically and the internal tectonic structure is well understood. It is clear that the described pegmatites are neither spatially nor genetically related to large fertile granite bodies. A review of geochronological data proofs that emplacement of pegmatite and leucogranite is broadly contemporaneous with high temperature-low pressure metamorphism of the country rocks. Field observations give clear evidence of a genetic link between simple pegmatite, leucogranite, evolved pegmatite and albite-spodumene pegmatite, on the one hand, and the subsolidus or suprasolidus metasediment hosting them on the other hand. These relations are underpinned by geochemical major and trace element investigations on all types of rock and the minerals therein. As source rock an Al-rich metapelite enriched in Li (70-270 ppm) with respect to the average upper continental crust is identified. The main Li-carrier is staurolite with up to 3000 ppm Li. The pegmatite and leucogranite originate in anatectic melts that formed between 0.6-0.8 GPa and 650-750°C, corresponding 18-26 km depth. During melt formation staurolite was consumed by sillimanite forming reactions. Subsequently, the melts were enriched in Li by fractional crystallization of quartz and feldspar during their ascent to higher crustal levels. While simple pegmatite and inhomogeneous leucogranite formed in lower and intermediate levels, evolved and albite-spodumene pegmatite crystallised at high levels at conditions between 0.3-0.4 GPa and 500-570°C, corresponding to about 12 km depth. Based on these data we develop a geochemical model for showing that Li can be transferred from a metasediment into an anatectic melt if staurolite is stable or metastable at the onset of melting. Such a melt can contain between 200 and 1000 ppm Li and the melt can be further enriched with up to 5000 to 10000 ppm Li through fractional crystallization of quartz and feldspar, allowing crystallization of spodumene. Estimated fractionation degrees vary between 81 and

99%, depending on the protolith composition, the melting scenario and the partitioning coefficients. Li-Al-rich metasediments are therefore a rich source of certain rare elements when they first melt. However, the spectrum of elements contained in the melt depends on a wide variety of conditions. This anatectic model provides an alternative explanation for the formation of Li-rich pegmatite if no fertile parent granite can be identified.

## INTRODUCTION

The long-term increasing demand of lithium (Li) for producing batteries (Tabelin et al., 2021) implies that even small Li deposits hosted in rare element pegmatite might become economically viable in the near future (Kesler et al., 2012; Ambrose & Kendall, 2020). The genesis of such deposits must, however, be understood in order to orient exploration and provide constraints on resource assessment. This question is also part of ongoing research on the source of pegmatite-forming melts (London, 2005; Černý et al., 2012b; Müller et al., 2021).

Two competing models are currently in use for explaining the genesis of Li-rich pegmatite often classified as LCT-pegmatite (lithium-cesium-tantalum-pegmatites). In the widely accepted model, rare element pegmatite bodies with economic concentrations of Li and additional Cs, Be, Ta and Nb are thought to derive from large fertile parent granite intrusions through fractionation, melt immiscibility and enrichment in volatiles (Černý, 1991a; b; Černý et al. 2012a; London 2008). In this model, pegmatite swarms ideally occur concentrically around the parent intrusion with increasing degrees of fractionation, concentration of volatile elements and zoning complexity towards higher structural levels (Černý, 1991a). This classical genetic model is challenged by a model in which anatexis plays a major role. Low percentage melting of Li-rich metasediments can produce Li-rich melts, presumably at lower temperatures than those of the solidus in Li-absent systems (Stewart, 1978). This alternative model can explain the formation of Li-bearing pegmatite bodies that (1) are not contemporaneous or genetically linked to a neighboring fertile granite, (2) occur in close time and space relationship with anatectic metasediments and (3) share major geochemical patterns with anatectic melts.

So far, the granite model has been favored in the pegmatite community because, on the one hand, pegmatite fields supporting the classical model have been well documented in the last few decades (Černý, 1991a; b; Sweetapple & Collins, 2002; London, 2008) and, on the other hand, the theoretical feasibility of the anatectic model was strongly contested (Černý, 1991b). Nevertheless, an anatectic origin has been postulated for several LCT-pegmatite bodies, fields or provinces. This includes, for example, the Oxford County field (Maine, USA, Simmons et al., 2016), bodies in the Chinese Altai (Lv et al. 2020) and the Songpan-Garze Fold Belt (China, Fei et al., 2020), the Laxfordian bodies (Scotland, Shaw et al. 2016), several bodies in the Moldanubian domain (Czech Republic, Melleton et al. 2012; Dill, 2016; Dill, 2018; Dill 2019) and the Sveconorwegian Province (Norway, Müller et al. 2017). The pegmatite bodies investigated in most of these studies formed during the terminal stages of the last tectonothermal event in their country rocks, and thus only a minor part of the crustal section is accessible for geological investigation. Hence, potential Li transfer from the anatectic source to the pegmatite sink is still poorly documented. To access all relevant crustal levels affected by melt generation, migration and crystallization, pegmatite fields have to be investigated in orogens within which tectonic activity occurred after the emplacement of the magmatic rocks.

The present study focuses on the Austroalpine Unit, which is a Cretaceous nappe stack exposed in the European Eastern Alps. It contains a large pegmatite province, the Austroalpine Unit Pegmatite Province (AUPP), which formed in Permian times, with thousands of pegmatite bodies emplaced in the Permian crust at a structural level and under a thermal regime compatible with granulite to greenschist-facies conditions, and now occurring within various nappes (Knoll et al., 2018). The AUPP hosts the most significant Li-bearing pegmatite deposit of central Europe, located at Weinebene (Koralpe, Austria), with spodumene ($LiAlSi_2O_6$) forming the economic Li-bearing phase. The $Li_2O$-concentration in the pegmatite averages 1.6 wt% and indicated

resources are expected to be larger than 200,000 t Li2O (Göd 1989). This deposit is not isolated, since albite-spodumene pegmatite dikes occur sporadically in the AUPP over an E-W distance of more than 400 km (Knoll et al., 2018). These dikes were interpreted to have been derived from fertile granite intrusions, following the classical genetic model (Göd, 1989; Mali, 2004). The lack of a Permian fertile parent granite in the field was explained by assuming that Alpine tectonics has removed the crustal level hosting such intrusions. In contrast, systematic field work shows that albite-spodumene pegmatites in the AUPP are always spatially associated with simple pegmatite and leucogranite bodies (Thöni & Miller, 2000; Knoll et al., 2018), all of which formed during the Permian (Habler & Thöni, 2001; Schuster et al., 2001; Schuster & Stüwe, 2008; Knoll et al, 2018). Additionally, patches and dikes of simple pegmatite frequently occur within migmatitic metasediments, suggesting that the former are a product of anatexis (Stöckert, 1987; Thöni & Miller, 2000). The AUPP therefore provides an excellent natural laboratory to study the relationships between the country rock, simple pegmatite, leucogranite and albite-spodumene pegmatite at different levels of the Permian crust.

In this contribution, we combine a wide range of petrological and geochronological data from the literature together with new field observations, geochemical analyses and an original geochemical modelling approach to establish that the albite-spodumene pegmatite of the AUPP derives from anatectic metasediments. Our case study also provides for the first time essential constrains on the chemical and mechanical processes active during melt generation, migration and crystallization from the migmatite source to the albite-spodumene pegmatite sink. These results are integrated into a genetic model, which is tested for LCT-pegmatites for which an antectic orgin has been suggested.

## Geological framework of the Austroalpine Unit Pegmatite Province

This chapter provides a geological overview of the Austroalpine Unit, which hosts the Austroalpine Unit Pegmatite Province (AUPP), as well as a synthesis of literature data constraining the timing of the pegmatite-forming event and the conditions of Permian metamorphism. Other Adria-derived continental units of the Alps are mentioned, because they give additional information on the geodynamic setting during pegmatite formation. For example, the Southalpine Unit represents a section down to the Permian uppermost mantle and rocks of the Permian lower crust are preserved in the Margna-Sesia Unit. Note that these units do not host Li-bearing pegmatite (Figure 1).

### The Austroalpine Unit and other relevant Adria-derived units

The Austroalpine Unit represents a nappe stack exposed in the Eastern Alps (Figure 1), formed of partly polymetamorphic basement rocks with Cambrian to early Carboniferous protolith ages as well as unmetamorphosed to low grade metamorphic Ordovician to Paleogene successions (Neubauer, 2002; Froitzheim et al., 2008; references therein). Four major tectono-metamorphic events are recorded in the Austroalpine Unit and the other Adria-derived continental units of the Alps:

(1) In the Cambrian and Ordovician large masses of greywackes and metapelites were deposited along the northern active margin of Gondwana. Together with slices of island arcs and oceanic crust from the surrounding oceanic realms (e.g. Servais et al., 2008; Siegismund et al., 2021) they were affected by ‘cratonisation’ in the sense of Zurbriggen (2017), meaning they formed juvenile continental crust. This process is indicated by migmatisation of sediments and intense magmatic activity, including basaltic and peraluminous felsic intrusions and volcanic rocks (Neubauer, 2002; Neubauer et al., 2022; Tropper et al., 2016; and references therein).

(2) Variscan continental collision in the Late Devonian and Carboniferous (375-300 Ma) resulted from the convergence between Gondwana and Laurussia during the closure of the Rheic ocean and the formation of the Pangea supercontinent (McCann et al., 2008, Spalla et al., 2014). Variscan parageneses indicate up to amphibolite- and eclogite-facies metamorphic conditions,

but only a few contemporaneous intrusions occur in the Austroalpine Unit (e.g. Mandl et al., 2018).

(3) After the collapse of the Variscan orogen, lithospheric extension in the Permian and Early to Middle Triassic (290-240 Ma) along the westernmost embayment of the Neotethys Ocean affected the rocks that form today the Austroalpine Unit. This was accompanied by basaltic underplating, high temperature-low pressure metamorphism up to granulite-facies, intense igneous activity as well as basin formation (e.g. Schuster & Stüwe, 2008; Sinigoi et al., 2016; Marotta et al., 2018; Roda et al., 2019). Further extension in Jurassic time triggered the breakup of Pangea, finally forming Africa and Europe, together with the Neotethys and Penninic (Alpine Tethys) oceanic realms and the Adriatic and Briançonnais microcontinents in between (Handy et al., 2010).

(4) The Alpine continental collision was the result of convergence between Africa and Europe since the Late Jurassic. The Austroalpine Unit formed during this event, between Late Jurassic to middle Late Cretaceous times (150-85 Ma) by accretion of Adria-derived material within a complex nappe stack (Froitzheim et al., 2008). The Alpine imprint within the Austroalpine Unit is variable, with peak metamorphic conditions reaching up to eclogite-facies and ultrahigh-pressure conditions (Vrabec et al., 2012). Ongoing convergence induced the subduction of the Penninic Ocean and finally the continental collision of Adria and Europe starting in the Eocene, whereby the Penninic, Subpenninic and Helvetic units developed (Schmid et al., 2004).

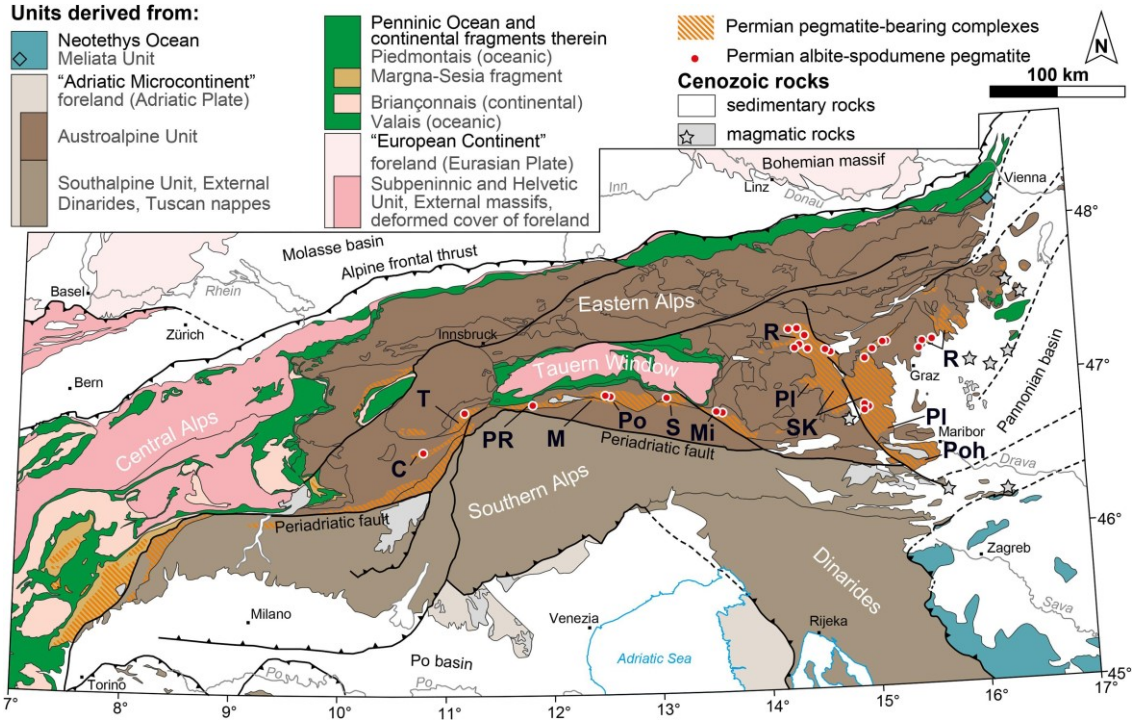


*Figure 1. The Austroalpine Unit pegmatite province with pegmatite-bearing lithostratigraphic complexes and albite-spodumene pegmatite occurrences shown on a simplified tectonic map of the Eastern Alps (modified after Knoll et al., 2018). The lithostratigraphic complexes mentioned in the text and figures are located on the map: C (Campo Complex), M (Michelbach Complex), Mi (Millstatt Complex), Pl (Plankogel Complex), Po (Polinik Complex), Poh (Pohorje area), PR (Petzeck-Rothenkogel Complex), R (Rappold Complex), S (Strieden Complex), SK (Saualpe-Koralpe Complex) and T (Texel Complex). Notice that a few complexes occur in different geographic localities as part of different nappes due to the complex alpine tectonics.*

## THE AUSTROALPINE STRATIGRAPHIC COMPLEXES HOSTING ALBITE-SPODUMENE PEGMATITE

About two dozen individual albite-spodumene pegmatite occurrences with more than 80 single albite-spodumene pegmatite bodies have been identified so far in the AUPP (Figure 1; Mali, 2004; Knoll et al., 2018). Together with simple pegmatite, evolved pegmatite and leucogranite,

they appear in pegmatite fields hosted by several lithostratigraphic complexes (in the sense of the North American Commission on Stratigraphic Nomenclature, 2005), such as, for example the Rappold, Saualpe-Koralpe and Plankogel complexes (Figure 1, Knoll et al., 2018). These complexes are mainly composed of micaschist and paragneiss with intercalations of amphibolite, marble and quartzite and in the case of the Saualpe-Koralpe additional eclogite. Detrital zircon geochronology (Frank et al., 2019) and Sr-isotopic data of marble layers (Puhr et al., 2010) indicate late Cambrian to Pennsylvanian depositional ages for these rocks. In most of these complexes, the first documented metamorphic imprint and associated magmatism is Permian, even though Variscan metamorphism has also been documented in some cases (e.g. Schuster et al., 2004; Gaidies et al., 2008b; Schulz & Krause, 2021). Other complexes exhibit an additional Ordovician imprint with peraluminous granitic intrusions (e.g. Silvretta Complex, Gruber et al., 2010; Polinik Complex, Hauke et al., 2019) and bear Permian simple pegmatite and evolved pegmatite but lack albite-spodumene pegmatite. During Alpine nappe stacking in Cretaceous time, these complexes were disrupted into different nappes and experienced additional metamorphism at lower greenschist- to eclogite-facies conditions. The associated Alpine deformation is significant in some areas and, there, the Permian magmatic rocks described in this contribution are mostly gneiss, sometimes highly mylonitic (Thöni & Miller, 2000; Knoll et al., 2018).

### Permian granitic intrusions

Beside the leucogranite bodies described in Knoll et al. (2018), several other types of Permian granitic intrusions occur in the Austroalpine Unit. Commonly they are deformed with a gneissic texture, contain biotite and intruded at greenschist- to upper-amphibolite-facies Permian crustal levels. They are frequent in lithostratigraphic complexes that may contain a few simple pegmatite dikes related to the granitic intrusions, but albite-spodumene pegmatite was never found therein (e.g. Strallegg Complex, Schuster & Nowotny, 2016).

The most important occurrences of such Permian and Triassic orthogneiss bodies are briefly described here. In the eastern part of the Austroalpine Unit, orthogneiss bodies derived from Permian granite intrusions are very frequent. The most common type is the high-K calc-alkaline to shoshonitic S-type Pretul orthogneiss ("Grobgneiss") with crystallization ages in the range of 280-250 Ma (Schuster & Nowotny, 2016; Yuan et al., 2020). The Permian (c. 260 Ma) Wolfsberg granitic orthogneiss (Thöni & Miller, 2000) and the alkaline, metaluminous Middle Triassic (c. 240 Ma) Eisenkappl granite (Miller et al., 2011) occur further west. Both show initial isotopic signatures different from the investigated pegmatite types, with significantly higher εNd values (-7.9 to 1.4 and -2.7 to -2.6 respectively). Additionally, published trace element concentrations of the described orthogneiss and granite occurences do not correspond to typical fertile granite (Černý, 1991b).

In summary, for spatial and geochemical reasons, the granites described above cannot be the parent intrusions of the investigated pegmatite types. The lithium present in the albite-spodumene pegmatite of the AUPP has, therefore, another origin. Permian granitic intrusions also occur in many other Adriatic-derived units in the Alps (Petri et al., 2017; Roda et al., 2019), but none of them is rich in Li or associated with spodumene pegmatite.

### Timing of magmatism and metamorphism

Pegmatite and leucogranite of the AUPP have been investigated with several geochronological methods. Rare occurrences of simple pegmatite are related to the Ordovician (Thöni & Miller, 2004), Variscan (Handler et al., 1999) and Alpine (Thöni & Miller, 2010) events. However, the large majority of pegmatite bodies and all albite-spodumene pegmatite dikes analysed yielded Permian to Middle Triassic ages (Figure 2a, b). In the Permian to Middle Triassic rocks, Sm-Nd garnet ages fall in the range 247-288 Ma for simple and fractionated pegmatite (Habler et al., 2007; Pestal et al., 2009; Schuster & Frank, 1999; Schuster et al., 2001; Sölva et al., 2003; Thöni & Miller, 2000; Thöni et al., 2008), 259-277 Ma for leucogranite and 263-267 Ma for albite-

spodumene pegmatite (Knoll et al., 2018). These ages are interpreted as crystallization ages of magmatic garnet, in agreement with all previous studies, as the closure temperature of the Sm-Nd system in garnet is higher than the temperature of the Alpine overprint (Thöni, 2002, and references therein). Consequently, these ages are considered to represent the time of pegmatite and leucogranite emplacement. A U-Pb zircon age of 240±1.5 Ma from an albite-spodumene pegmatite out of the Weinebene deposit (Heede, 1997) and a U-Pb cassiterite age of 289±5 Ma (Konzett et al., 2018) also date the crystallization of these rocks. A large number of Rb-Sr muscovite ages determined from all types of pegmatite yielded ages ranging between 65 to 292 Ma (e.g. Thöni & Miller, 2000; Schuster et al., 2001; Knoll et al., 2018). These ages strongly vary and are generally younger than those determined with the above-mentioned methods. The younging correlates with the intensity of deformation and recrystallization rather than with the metamorphic grade reached during the Alpine overprint (Eberlei et al., 2015). The results of Rb-Sr muscovite geochronology are therefore not considered here for defining emplacement ages of the Permian magmatic rocks.

Permian metamorphism in gneiss and micaschist of the pegmatite-bearing complexes has also been dated by different methods (Figure 2a, b). Sm-Nd garnet ages are in the range 254-286 Ma (Schuster et al., 2001; Thöni, 2002; Thöni & Miller, 2009). Owing to the high closure temperature of the isotopic systems (Thöni, 2002; and references therein), these data are considered as garnet formation ages close to the Permian metamorphic peak. Additional microprobe U-Th-Pb ages of monazite and xenotime included in garnet, staurolite or in the matrix fall in the similar range (Gaidies et al., 2008a; Krenn et al., 2012; Li et al., 2021; Schulz et al., 2005; Schulz, 2017; Schulz & Krause, 2021).

Note that a Permian extensional regime and pegmatite formation is also documented from Adria-derived units of the Western and Central Alps (see Dal Piaz et al., 1977; Diella et al., 1992; Henk et al.,1997; Müntener et al., 2000; Hansmann et al., 2001; Monjoie, 2004; Monjoie et al., 2005; Zucali et al., 2011; Marotta et al., 2018; Roda et al., 2019). Especially, the Permian crust-mantle transition is preserved in the Sesia Unit, which allows the characterization of processes active during basaltic underplating (Lardeaux & Spalla, 1991; Rebay & Spalla, 2001). Geochronological data determined on metapelites and magmatic rocks from this area indicate metamorphism in the same time range of 240-290 Ma (Hermann & Rubatto, 2003; Ewing et al., 2013; Kunz et al., 2018; Marotta et al., 2018 and references therein).

### The Permian metamorphic record

Based on the observed mineral assemblages and metamorphic reactions, the Permian metamorphic record in the Austroalpine Unit and other Adria-derived units of the Alps covers greenschist- to granulite-facies conditions with local to generalized anatexis (Figure 2c, Lardeaux & Spalla, 1991; Diella et al., 1992; Schuster & Stüwe, 2008; Kunz et al., 2018). Three levels of the Permian crust are distinguished in the AUPP.

Metapelites affected by a prograde greenschist-facies imprint in the upper part of the Permian middle crust are characterized by the occurrence of andalusite and/or garnet porphyroblasts. Chiastolitic andalusite up to 1 m in length developed in the Saualpe-Koralpe Complex (Schuster & Stüwe, 2008) and incipient garnet growth at 0.4±0.05 GPa and 535±20°C is documented in the Wölz Complex (W2 on Fig 2c, Gaidies et al., 2006). The range of P-T conditions for this crustal level spreads between 0.2-0.4 GPa at 440-520°C in the Wölz Complex (W1 on Fig 2c, Schuster & Frank, 1999), 0.25-0.4 GPa at 500-570°C in the Strieden Complex (S1 on Fig 2c, Hoke, 1990), ~0.46 GPa at 540°C in the Plankogel Complex (Pl1 on Fig 2c, Thöni & Miller, 2009) and 0.3-0.5 GPa at 540°C in the Campo Complex (C1 on Fig 2c, Petri et al., 2019). By comparison, at similar conditions of 0.375±0.075 GPa and 500±50°C andalusite, garnet and staurolite developed in Al-rich metapelite of the Jenig Complex, which does not host pegmatite (Schuster et al., 2015).

Andalusite formation by breakdown of Variscan or Permian staurolite (staurolite + muscovite + quartz = andalusite + biotite + $H_2O$) is a frequently observed reaction at amphibolite-facies

conditions in the lower part of the Permian middle crust (e.g. in the Strieden or Strallegg complexes, Hoke, 1990; Draganits, 1998; Schuster at al., 2001). With increasing temperature, sillimanite formed after andalusite and at somewhat higher pressures it developed by the reactions plagioclase + quartz = sillimanite + albite + H2O, garnet + muscovite = sillimanite + biotite + quartz and muscovite + quartz = sillimanite + K-feldspar + H2O (Hoke, 1990; Török, 1999). P-T conditions of 0.4±0.05 GPa and 600±20°C are reported for such sillimanite-bearing lithologies (SK1 on Fig 2c, Habler & Thöni, 2001).

The lower part of the Permian crust is characterized by upper amphibolite- and granulite-facies conditions with local anatexis. In the Austroalpine Unit this crustal level is mostly strongly overprinted by the Alpine event and, hence, reliable P-T data on the Permian imprint are scarce. Nevertheless, conditions of 0.6-0.8 GPa at 650°C (SK2 on Fig 2c, Schulz 2017) and 0.75-1.03 GPa at 600-650 ºC (Poh on Fig 2c, Li et al. 2021) were recently reported for the Saualpe-Koralpe Complex and the Pohorje area. In the Plankogel Complex, peak conditions of 0.4-0.7 GPa at 620°C were deduced from coexistence of staurolite and sillimanite at peak conditions (Pl2 on Fig2c, Thöni & Miller, 2009). This is consistent with the upper limit of the conditions of 0.5-0.7 GPa at 620-680°C determined in the Petzeck-Rothenkogel Complex (PR on Fig 2c, Stöckhert, 1987) and 0.5-0.7 GPa at 600-750°C determined for sillimanite-bearing partially molten metapelites from the Strieden Complex (S2 on Fig2c, Hoke, 1990). There, sillimanite developed partly out of progressive prograde destabilization of staurolite. The highest recorded temperature was determined in a xenolith and the contact aureole of a gabbro intrusion from the Campo Complex (C2 on Fig2c, 725-930°C at 0.4-0.6 GPa, Petri et al., 2019; see also Roda et al., 2018). Additional data exist from Adria-derived units in the Central and Western Alps. For example, granulite-facies metamorphism in partially molten metapelite is well constrained to 0.6-0.8 GPa and 770-850°C in the Valpelline Unit (Zucali et al., 2011; Manzotti & Zucali, 2013) and to 1.0 GPa and 800-850°C in the Malenco Unit (Hermann & Rubatto, 2003).

During the Alpine overprint, Permian andalusite and sillimanite were frequently transformed into typical fine-grained kyanite aggregates but remained stable in some units (e.g. Strieden Complex, Schuster et al., 2001). For example, decimeter-sized pseudomorphs after chiastolitic andalusite are present in the so called “Paramorphosenschiefer” and millimeters large kyanite aggregates after staurolite form large amounts of the rock-volume of biotite-rich paragneiss (“Disthenflasergneis”). Both lithologies frequently occur in the Saualpe-Koralpe Complex.

## Result

This chapter presents field and petrographical observations as well as geochemical data and modeling constraining the relationships between anatectic metasediments, the different types of pegmatite and the leucogranite of the AUPP.

### Field relationships

Field work was carried out in the Campo (Martell valley, Italy, abbreviation C on Figure 1), Petzeck-Rotenkogel (Uttenheim valley, Austria, PR), Strieden (Kreuzeck Mountains, Austria, S), Millstatt (Millstätter Seenrücken area, Austria, Mi), Saualpe-Koralpe (Krakaberg area, Austria, SK) and Rappold (Wölzer Tauern Mountains and St. Radegund area, R, see also figure 4) complexes. Despite the Alpine structural overprint, which varies from minor brittle deformation to intense ductile deformation (Knoll et al., 2018), distinctive pegmatite-bearing domains representing the three crustal levels of the Permian crust can be distinguished in all investigated areas (Figure 3). The migmatite descriptions follow the nomenclature of Maxeiner et al. (2017).

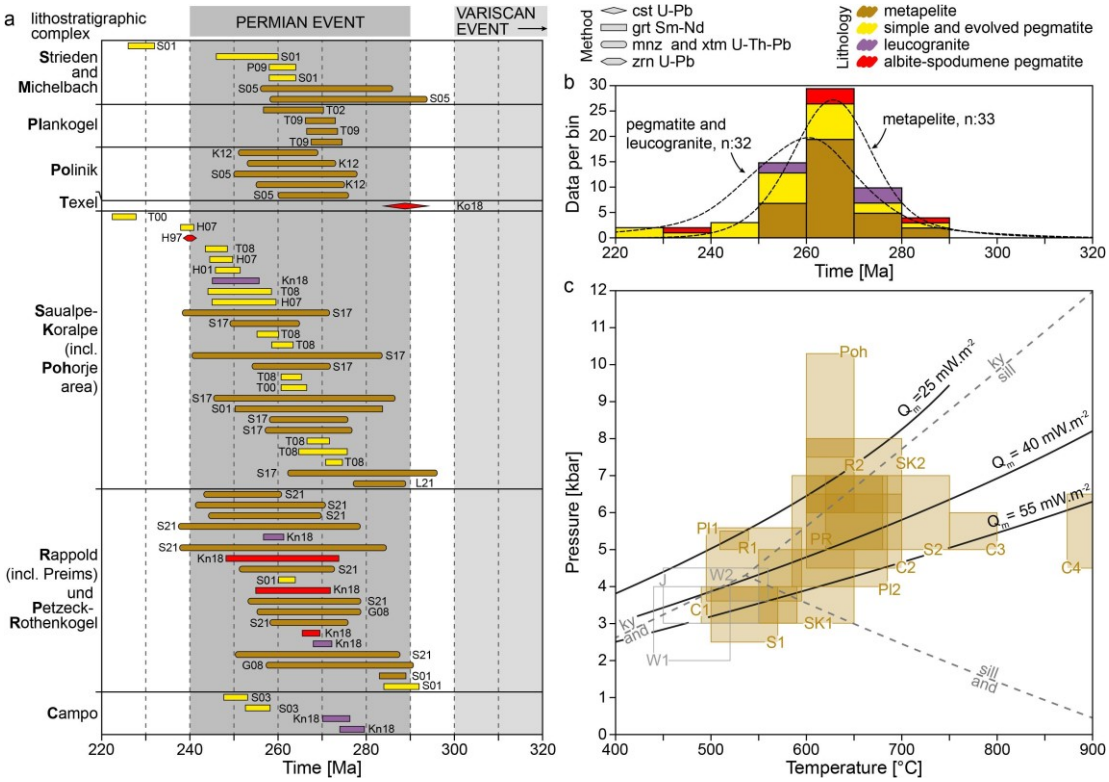


*Figure 2. a. Compilation of geochronological constraints for the Permian event in the Austroalpine Unit pegmatite province (see location of the lithostratigraphic complexes on figure 1). Age uncertainties are given at 2σ level. Notice that the monazite and xenotime U-Th-Pb ages are chemical ages affected by a large uncertainty. Mineral abbreviations after Whitney and Evans (2010): cassiterite (cst), garnet (grt), monazite (mnz), xenotime (xtm), zircon (zrn). References of the age data: Heede, 1997 (H97); Thöni and Miller, 2000 (T00); Habler and Thöni, 2001 (H01); Schuster et al., 2001 (S01); Thöni, 2002 (T02); Sölva et al., 2003 (S03); Schulz et al., 2005 (S05); Habler et al., 2007 (H07); Gaidies et al., 2008 (G08); Thöni et al., 2008 (T08); Pestal et al., 2009 (P09); Thöni and Miller, 2009 (T09); Krenn et al., 2012 (K12); Schulz, 2017 (S17); Knoll et al., 2018 (Kn18); Konzett et al., 2018 (Ko18); Li et al., 2021 (L21); Schulz & Krause, 2021 (S21). Based on tectonic and lithostratigraphic correlations, the age data from the Pohorje area, on the one hand, as well as Preims and Petzeck-Rothenkogel complexes, on the other hand, are grouped together with the Saualpe-Koralpe and Rappold complexes, respectively. b. Histogram plot showing the distribution of ages plotted in panel a. The curves show the kernel density estimates (KDE) for the pegmatite and leucogranite group as well as the metapelite group. The KDE are calculated with IsoplotR (Vermeesch, 2018). c. Compilation of pressure-temperature (P-T) constraints for the Permian event in the Austroalpine Unit pegmatite province (see location of the lithostratigraphic complexes on figure 1). Additional low P-T conditions determined in the Jenig and Wölz complexes, which do not host pegmatite, are presented by grey rectangles without background. If no P-T range or uncertainty is provided in the original reference, a pressure uncertainty of 0.1 GPa and a temperature uncertainty of 50°C is applied. The grey dashed lines indicate the aluminosilicate fields calculated with the database of Holland & Powell (2011). The black lines indicate crustal steady-state geotherms calculated for different mantle heat flux (Qm) following Turcotte & Schubert (2008). The following values were used in the calculation; crustal density: 2750 kg.m-3, crustal thickness: 35 km, thermal conductivity: 2.25 W.m-1.K-1, heat production rate: 1.5 µW.m-3. References of the P-T data: Strieden Complex: Hoke, 1990 (S1: andalusite zone, S2: sillimanite zone, including migmatite zone); Jenig Complex: Schuster et al., 2015 (J: andalusite zone); Plankogel Complex: Thöni & Miller, 2009 (Pl1: onset of garnet growth, Pl2: sillimanite-staurolite stability field), Saualpe-Koralpe Complex: Habler & Thöni, 2001 (SK1: peak of metamorphism), Schulz, 2017 (SK2: peak metamorphism); Pohorje area: Li et al., 2021 (Poh: peak of metamorphism); Rappold Complex: Gaidies et al., 2006 (R1: onset of garnet growth), Schulz & Krause (R2: peak of metamorphism); Petzeck-Rothenkogel Complex: Stöckhert, 1987 (PR: sillimanite zone, including migmatite zone); Wölz Complex: Schuster & Frank, 2000 (W1: andalusite zone), Gaidies et al., 2006 (W2: onset of garnet growth); Campo Complex: Petri et al., 2016 (C1: prograde regional metamorphism, C2: peak of regional metamorphism, C3: contact metamorphism in aureole, C4: contact metamorphism in xenolith).*

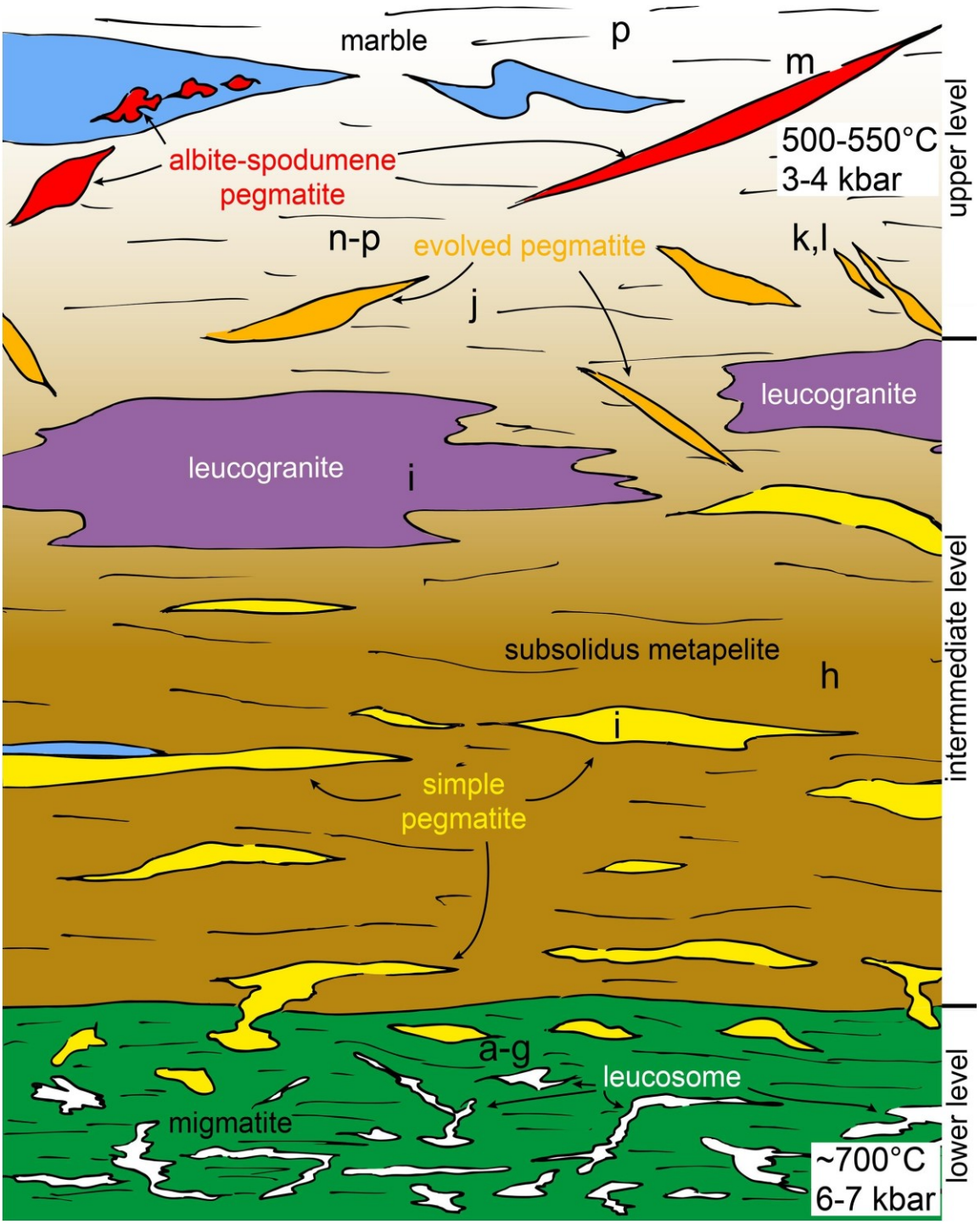


*Figure 3. Synthetic sketch of the field relationships between subsolidus metapelite, migmatite, different types of pegmatite and leucogranite in the three investigated structural levels. The pressure-temperature conditions are crude estimates for both ends of the profile (see sections 2.4 and 5.1.3). Note that the size of the individual bodies is not scaled.*

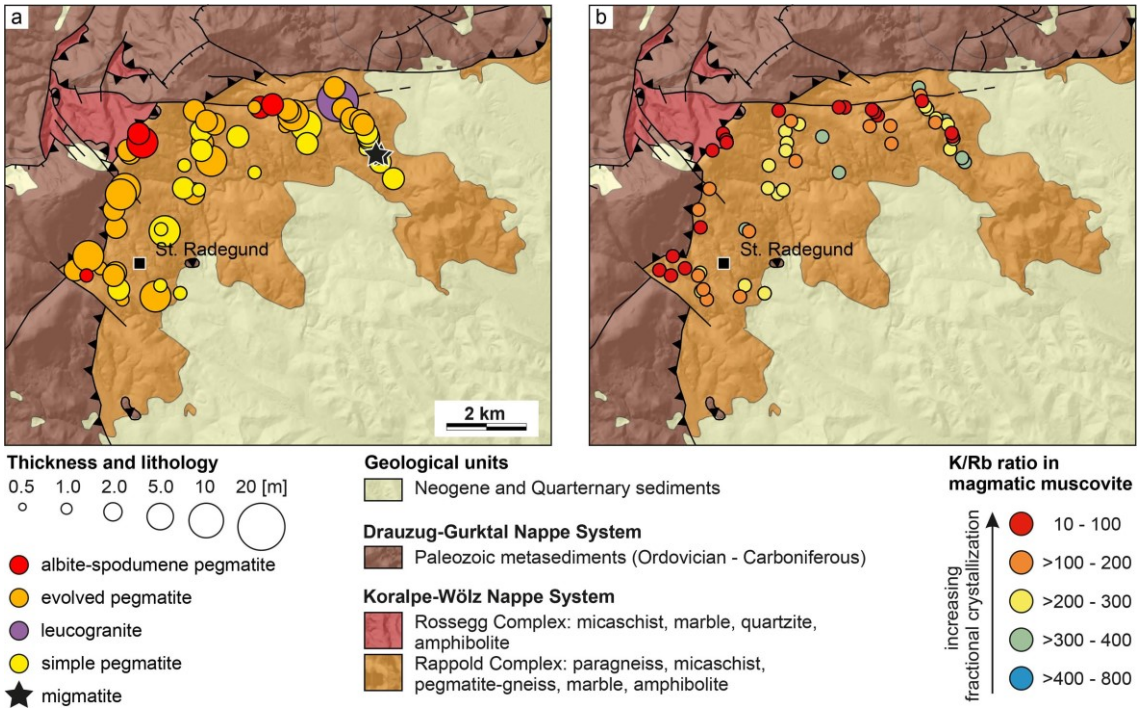


*Figure 4. Overview geological map of the St. Radegund area. a. Information on the lithology and thickness of the investigated magmatic rocks. b. K/Rb ratio of magmatic muscovite. Due to bad outcrop conditions and alteration, data was not acquired in the southern part of the Rappold Complex. Stars however indicate the occurrence of well preserved migmatites. Spodumene pegmatite dikes occur within partly staurolite-rich micaschist close to the top of the unit (for details see Schuster et al., 2019). In general, the K/Rb ratio of magmatic muscovite decreases and therefore the grade of fractionation increases towards the top of the unit. High K/Rb ratios (400-800) which are known from other areas of the AUPP are here missing. These maps show a small part of a database containing more than 1400 datapoints in the AUPP.*

### THE LOWER STRUCTURAL LEVEL

The lower structural level (Figure 3) is characterized by muscovite-rich migmatitic micaschist and paragneiss (Figure 5a-g). The paleosome contains biotite + quartz + plagioclase + muscovite + garnet ± sillimanite, the leucosome consists of coarse-grained quartz + alkali-feldspar ± plagioclase ± muscovite ± small garnet and the melanosome contains biotite + garnet + muscovite + plagioclase ± quartz ± sillimanite (often replaced by fine-grained kyanite during Alpine overprinting). The paleosome and melanosome are differentiated by the grain size, which is finer in the melanosome, and the relative amount of quartz, muscovite and plagioclase, which is lower in the melanosome (Figure 5b, c, d, f).

Three types of migmatitic textures are observed:

(1) Migmatite occuring at the base has a dominant stromatic to subordinate nebulitic texture (Figure 5b, f, 5a). It is mostly layered metatexite formed by millimeter- to centimeter-thick in-situ leucosome and melanosome (Figure 5a, e). Differentiation of paleosome and melanosome is sometimes difficult since those parts are finely layered and strongly nebulitic.

(2) Patchy migmatite is formed of lensoidal leucosome, elongated parallel to the schistosity (up to 10×20 cm) and rimed by a less than 1 cm thick melanosome within paleosome (Figure 5c, 5b). The patches can also consist of a few centimeter-sized alkali-feldspar crystals surrounded by quartz (Figure 5f). Anomalously large muscovite crystals (0.5-2 cm) occur parallel to the migmatite schistosity (Figure 5d).

(3) Net-textured migmatite, where the leucosome is either concordant or discordant to the schistosity of the paleosome with up to 90° obliquity (Figure 5g). The leucosome is a few centimeters thick and contains large alkali-feldspar phenocrysts (up to 2 cm). The contact

between the leucosome and paleosome is sharp and lacks melanosome. Associated simple pegmatite is sometimes present as concordant dikes up to a few meters thick and without zoning (Figure 5a, e). Their major components are alkali-feldspar + quartz ± plagioclase ± muscovite ± tourmaline.

The three migmatite types do not always occur together, likewise simple pegmatite is not present everywhere and tends to be more frequent in higher structural levels. Notably, the described rock association differs from typical pegmatite-hosting migmatite (Müller et al., 2017) mainly because of the local richness in muscovite porphyroblasts and the fine interlayering of melanosome and leucosome.

THE INTERMEDIATE STRUCTURAL LEVEL

The intermediate structural level (Figure 3) is characterized by simple pegmatite (Figure 6c) and in some places by leucogranite hosted by garnet-micaschist and paragneiss, often containing andalusite or sillimanite (Figure 6d) and staurolite (Figures 4h, 5e). At the basis of this level, metapelite also contains anomalously large muscovite parallel to the schistosity. Simple pegmatite occurs as several meters thick dikes or boudins with mineral assemblages of quartz + alkali-feldspar + muscovite + plagioclase ± garnet ± tourmaline (Figure 6c). It is mostly concordant to the schistosity and has a sharp contact to the host-rock. Simple pegmatite bodies are devoid of zoning. Additional biotite seldom occurs and can be overgrown by syntaxial muscovite. Associated leucogranite with quartz + alkali-feldspar + muscovite + plagioclase ± garnet ± tourmaline is present at a few localities (Figure 5i), forming less than hundred to several hundred meter-thick bodies, which may extend over some kilometers (Knoll et al., 2018). Leucogranite is texturally and mineralogically inhomogeneous. Domains with homogeneous, fine- to medium-grained granitic texture as well as interlayered coarse-grained pegmatitic and fine-grained aplitic domains, sometimes separated by garnet-rich or tourmaline-rich streaks, can be observed.

THE UPPER STRUCTURAL LEVEL

The upper structural level (Figure 3) is characterized by evolved pegmatite and albite-spodumene pegmatite hosted in garnet-micaschist and paragneiss, frequently also containing andalusite (typically pseudomorphosed by fine-grained kyanite aggregates; Figures 4j, 5f) and/or staurolite. Both types of pegmatite occur as up to a several meters thick, sometimes discordant, dikes (Figure 5k, n). Evolved pegmatite (defined by the Li concentration in muscovite, see section 3.2.2) is often zoned and characterized by domains dominated by alkali feldspar, quartz or tourmaline, sometimes showing comb structures growing from the rim towards the core. Alkali-feldspar + quartz ± muscovite + plagioclase ± garnet ± tourmaline ± beryl forms the common assemblage (Figure 6g). Centimeter-sized idiomorphic andalusite (preserved or replaced by fine-grained kyanite during the Alpine overprint) hosted in quartz veins or pegmatite bodies has been described from few localities (Figure 5l, Hoke, 1990; Habler et al., 2007). Small grains of cassiterite, columbite and REE-minerals have been found rarely (Konzett et al., 2018; see monazite on Figure 6g). Albite-spodumene pegmatite is found in about 80 bodies, in comparison to evolved pegmatite, it contains additional spodumene (Figures 4m, 5h, Knoll et al., 2018). Some dikes can be discontinuously followed for more than one kilometer (Göd, 1989; Mali, 2004, Knoll et al., 2018). Albite-spodumene pegmatite dikes are not systematically zoned (Knoll et al., 2018). Contacts with the surrounding micaschist, paragneiss and quartzite are mostly sharp, whereas at contact to marble, the boundaries have an intricate geometry with scattering thicknesses and boudinaged structures (Knoll et al., 2018).

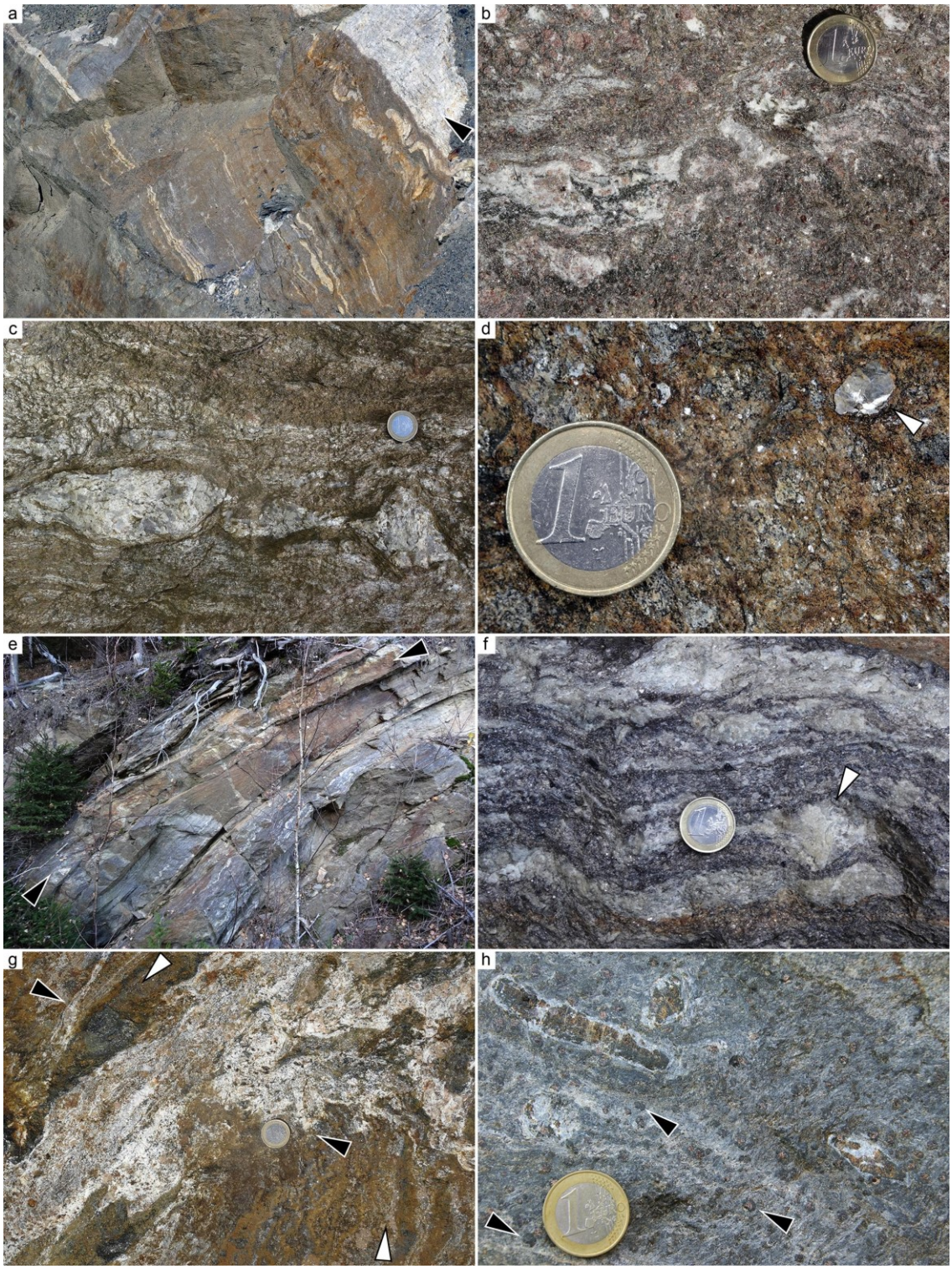
a
b
c
d
e
f
g
h


*(The subtitle to Figure 5 is on the following page)*

*Figure 5. Field photographs (Coordinates given in WGS 84). a. Layered metatexite formed by centimeter- to decimeter-thick in-situ leucosome and melanosome (stromatic texture), associated with patchy migmatite and a simple pegmatite (arrow). Width of the picture: ~4 meters. Rappold Complex, 14.147688°E, 47.212031°N. b. Migmatite with nebulitic texture. Rappold Complex, 14.147688°E, 47.212031°N. c. Patchy migmatite formed of lensoidal leucosome elongated parallel to the schistosity and surrounded by a dark biotite-rich seam. Rappold Complex, 14.147688°E, 47.212031°N. d. Paragneiss with coarse-grained magmatic muscovite porphyroblasts (arrow). Rappold Complex, 14.147688°E, 47.212031°N. e. Layered metatexite formed by millimeter- to decimeter-thick in-situ leucosome and melanosome (stromatic texture), associated with a simple pegmatite (arrows). Width of the picture ~5 meters. Rappold Complex, 14.5934248°E, 47.15802186°N. f. Patchy migmatite with nebulitic texture and large feldspar crystal (arrow) within the lensoidal leucosome rimed by a melanosome. Rappold Complex, 14.5934248°E, 47.15802186°N. g. Net-textured migmatite with leucosome (black arrows) discordant with respect to the planar fabric of the paleosome (white arrows). Rappold Complex, Rappold Complex, 14.147688°E, 47.212031°N. h. Staurolite-garnet micaschist with up to 3 cm long staurolite crystals and millimeter-sized garnet (arrows) within a muscovite-biotite rich matrix. Rappold Complex, 14.29556°E, 47.22953°N. i. Layered tourmaline and garnet bearing leucogranite interlayered with coarse-grained pegmatitic and fine-grained aplitic domains. Rappold Complex, 14.580712°E, 47.167473°N. j. Chiastolitic andalusite transformed into fine-grained kyanite aggregates within a garnet-micaschist. Saualpe-Koralpe Complex, 14.946966°E, 46.790038°N. k. Discordant evolved pegmatite dike with a fine-grained/coarse-grained zonation. Size of the boulder: ~2 m. Saualpe-Koralpe Complex, the block is not in situ and is presented as part of a geological exhibition. l. Centimeter-sized idiomorphic andalusite (arrows) within a tourmaline-bearing evolved pegmatite. Saualpe-Koralpe Complex, 14.96222508°E, 46.8081826°N. m. Centimeter-sized spodumene crystals with a strong cleavage (arrows) in an albite-spodumene pegmatite. Saualpe-Koralpe Complex, 15.20310077°E, 47.23348342°N. n. Evolved pegmatite with sharp upper and lower contacts parallel to the schistosity of the host-rock and xenolith and jagged lateral contacts (both indicated by arrows). Saualpe-Koralpe Complex, 15.01390812°E, 47.00100063°N. o. Unusually large K-feldspar crystals (arrows) in the schistosity of paragneiss. Petzeck-Rothenkogel Complex, 12.580203°E, 46.922204°N. p. 5-15 cm wide folded pegmatite dike discordant to the host-rock schistosity in the vicinity of an evolved pegmatite and below an albite-spodumene pegmatite. Petzeck-Rothenkogel Complex, 12.580203°E, 46.922204°N.*

Rare structures preserved from the Alpine overprint provide information on the contact between the pegmatite bodies of the upper structural level and the host-rock:

(1) A tabular pegmatite body has sharp contacts parallel to the schistosity of the host-rock at the upper and lower boundaries and jagged and discordant contacts indenting the host-rock at the sides (Figure 5n). Additionally, the pegmatite includes xenoliths of the host-rock up to 0.5 m in size. The schistosity in the xenolith has the same orientation as in the host-rock and the xenolith displays sharp contacts at its upper and lower boundary and jagged contact at its sides (Figure 5n).

(2) Large alkali-feldspar crystals (up to 2 cm) together with thin quartz veins parallel to the schistosity of the host-rock have been found in the vicinity of pegmatite (Figure 5o). These are considered as exceptional, since alkali-feldspar does not usually belong to the paragenesis of the metapelite in the pegmatite-hosting complexes.

(3) A 5 to 15 cm wide pegmatite dike discordant to the host-rock schistosity is present in the vicinity of an evolved pegmatite and below an albite-spodumene pegmatite, both being orientated within the schistosity (Figure 5p). It is remarkably thin and elongated in comparison to the surrounding pegmatite bodies, which do not show any folding.

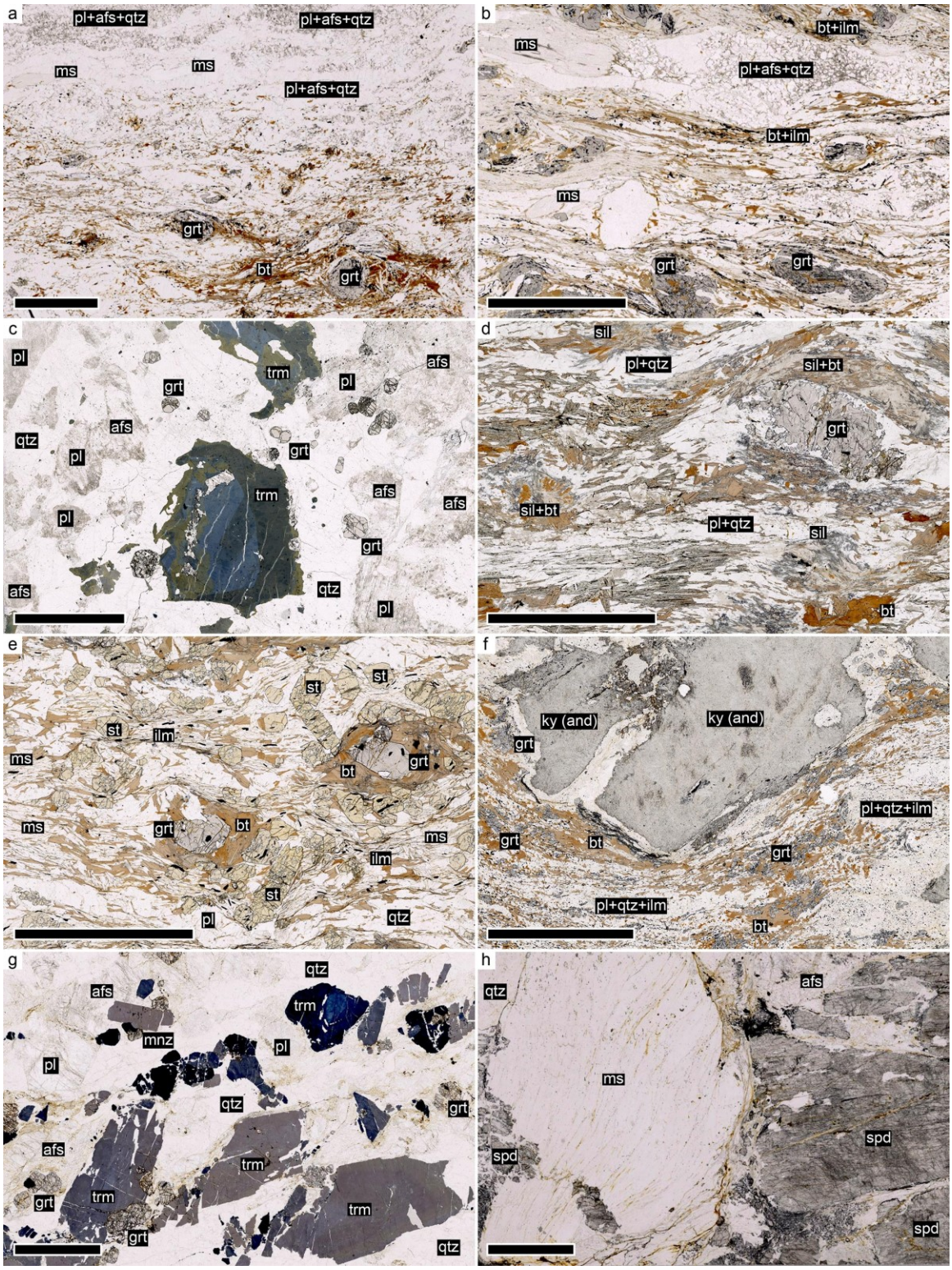


*(The subtitle to Figure 6 is on the following page)*

*Figure 6. Representative photomicrographs (Coordinates given in WGS 84). All scale bars represent 5 mm. Mineral abbreviations after Whitney & Evans (2010): afs (alkali-feldspar), andalusite (and), biotite (bt), garnet (grt), ilmenite (ilm), kyanite (ky), monazite (mnz), muscovite (ms), plagioclase (pl), quartz (qtz), sillimanite (sil), spodumene (spd), staurolite (st), tourmaline (trm). a. Nebulitic migmatite with leucosome containing coarser grained muscovite, plagioclase, alkali-feldspar and quartz as well as melanosome containing biotite, garnet and ilmenite. Rappold Complex, 14.5934248°E, 47.15802186°N. b. Patchy migmatite with large muscovite crystals in the lensoidal leucosome, partly rimed by a biotite- and ilmenite-rich melanosome. Garnet occurs in the paleosome. Rappold Complex, 14.5934248°E, 47.15802186°N. c. Simple pegmatite with large optically zoned tourmaline crystals and small garnet rounded crystals within a plagioclase, alkali-feldspar and quartz matrix. Strieden Complex, 12.587751°E, 46.873187°N. d. Sillimanite bearing micaschist with garnet porphyroblast. Strieden Complex, 12.587751°E, 46.873187°N. e. Staurolite-garnet micaschist with garnet porphyroblasts surrounded by a biotite rim and staurolite idiomorphic crystals. Strieden Complex, 13.10972°E, 46.88028°N. f. Andalusite porphyroblasts transformed into fine-grained kyanite aggregate within a fine-grained paragneiss matrix of garnet, plagioclase, quartz and ilmenite. Saualpe-Koralpe Complex, 14.971243°E, 46.779901°N. g. Evolved pegmatite with large and partly broken tourmaline crystals within a plagioclase, alkali-feldspar and quartz matrix. Note the small broken garnet crystals and the monazite crystal in the upper left quadrant of the picture. Rappold Complex, 15.204079°E, 47.233911°N. h. Albite-spodumene pegmatite with strongly cleaved spodumene crystals and large muscovite single crystal. Rappold Complex, 15.204079°E, 47.233911°N.*

### GEOCHEMICAL CHARACTERIZATION OF MAGMATIC AND METAMORPHIC ROCKS

Description of the analytical methods (SM1) and the geographic coordinates of sampling locations (SM2) are provided as supplementary material.

### WHOLE ROCK COMPOSITION

Whole-rock major and trace element compositions were determined for staurolite-garnet micaschist (13 samples), different parts of migmatitic micaschist (3 samples), simple pegmatite (6 samples), leucogranite (9 samples), evolved pegmatite (6 samples) and albite-spodumene pegmatite (4 samples). The results are plotted on figures 6 and 7. Selected analyses are presented in Table 1 and all analyses are provided as supplementary material (SM3). All studied metasedimentary and magmatic rocks are relatively Al-rich (Table 1, Figure 7). Most micaschist analyses plot in the shale domain of the classification scheme for clastic sediments and one analysis plots in the Fe-shale domain (Figure 7a, Herron, 1988). In contrast, migmatite analyses plot either in the shale domain or in the wake domain. All simple pegmatite, leucogranite, evolved pegmatite and albite-spodumene pegmatite samples have a peraluminous composition (Figure 7b). With one exception, they are also subalkaline (Figure 7c). Both diagrams however do not show a particular correlation between lithology and major element chemistry; notice, however, that leucogranite tends to cluster whereas pegmatite shows a large spread. This difference is probably induced by the inhomogeneity and the large grain size of pegmatite in comparison to leucogranite, making collecting a representative sample difficult.

Trace element analyses are normalized to average upper continental crust (Figure 8, Rudnick & Gao, 2003). If not specified, comparisons are done with respect to this reference. Note that element enrichments or depletions have mostly small magnitudes. In both micaschist and migmatite, the elements Li, Th, U, Be, Ge, Cs, Nb, Ta and Pb are slightly enriched, whereas the elements Sr and Tl show lower concentrations (Figure 8a). Micaschist is characterized by remarkably flat rare earth elements (REE) spectra and an enrichment compared to the average upper continental crust (Figure 8b). In contrast, the migmatite tends to be slightly depleted in light REEs and enriched in heavy REEs (Figure 8b). Both simple pegmatite and leucogranite are enriched in Li, Be, Bi, Pb and Sn, whereas Sc, Ba, Sr, Zr, Nb, Hf and Th are depleted (Figure 8c). Simple pegmatite and leucogranite are mostly depleted in REEs, with a large variation in the absolute numbers (Figure 8d). The concentrations slightly increase from light REEs to heavy REEs. Eu follows this trend for only one sample. For the others, it presents an anomaly that is positive for one sample and negative for all others. Similar, but more pronounced trends as those of simple pegmatite and leucogranite can be seen in the analyses of evolved pegmatite and albite-spodumene pegmatite (Figure 8e, f). Li, Be, Bi, Sn and Ta are even more abundant whereas Ba and Sr show the opposite pattern. Futhermore in most cases there is a negative Eu anomaly.

Whole-rock Li concentrations are crucial for the geochemical model developed in this paper and are given in tables 1 and 2. In micaschist, the Li concentration ranges from 68 to 269 ppm with an average content of 122 ppm. In migmatite, it is slightly lower (37-108 ppm Li, 81 ppm in average). Simple pegmatite shows values in the range 19-97 ppm Li with an average of 50 ppm, similarly to leucogranite (7-119 ppm Li

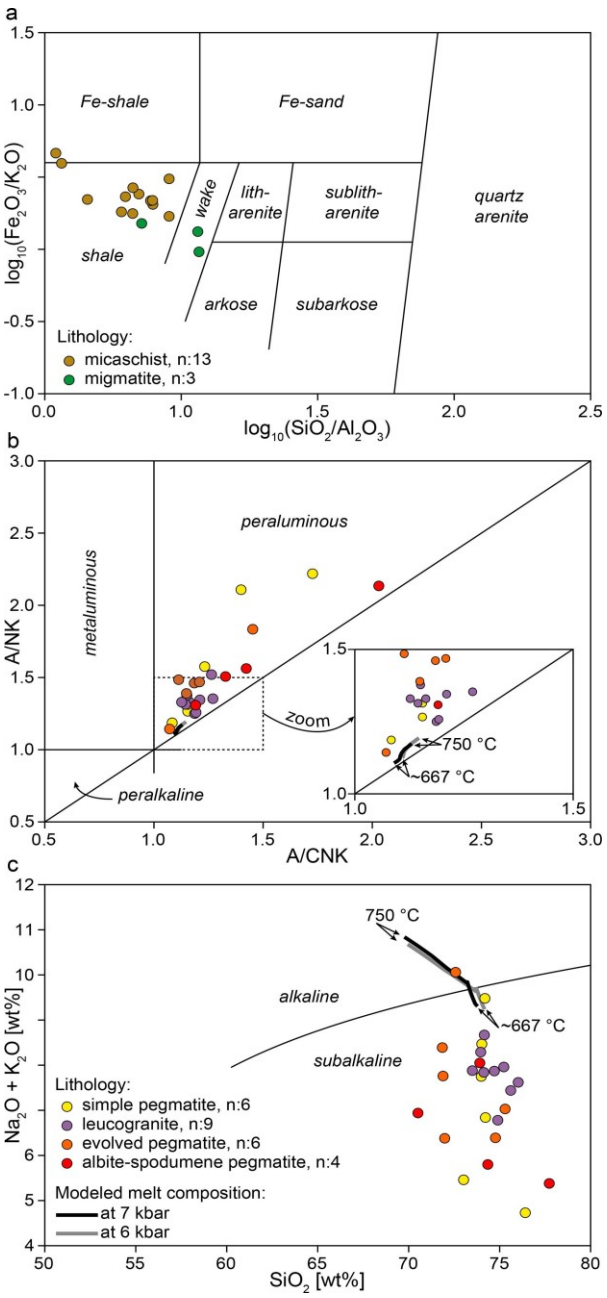


*Figure 7. Compositional diagrams for subsolidus and suprasolidus metapelite, different pegmatite types and leucogranite. a. Micaschist and migmatite analyses plotted in the classification diagram of clastic sediments (Herron, 1988). b. Simple pegmatite, leucogranite, evolved pegmatite and albite-spodumene pegmatite analyses plotted in the A/NK vs. A/CNK diagram. The thick grey and black lines show the evolution of the modeled melt composition with temperature. See panel c for legend. A/NK: molar Al2O3/(Na2O+K2O), A/CNK: molar Al2O3/(CaO+Na2O+K2O). c. Simple pegmatite, leucogranite, evolved pegmatite and albite-spodumene pegmatite analyses plotted in the alkali vs. silica diagram (Irvine and Baragar, 1971). The thick grey and black lines show the evolution of the modeled melt composition with temperature.*

range and 71 ppm in average) and evolved pegmatite (40-112 ppm Li range and 53 ppm in average). Albite-spodumene pegmatite shows the highest values and largest range: 174 to 7420 ppm Li. Note that the low minimum Li value is due to the substantial heterogeneity of the analyzed samples, including spodumene-free domains. This is why no average Li content is given for albite-spodumene pegmatite in Table 2.

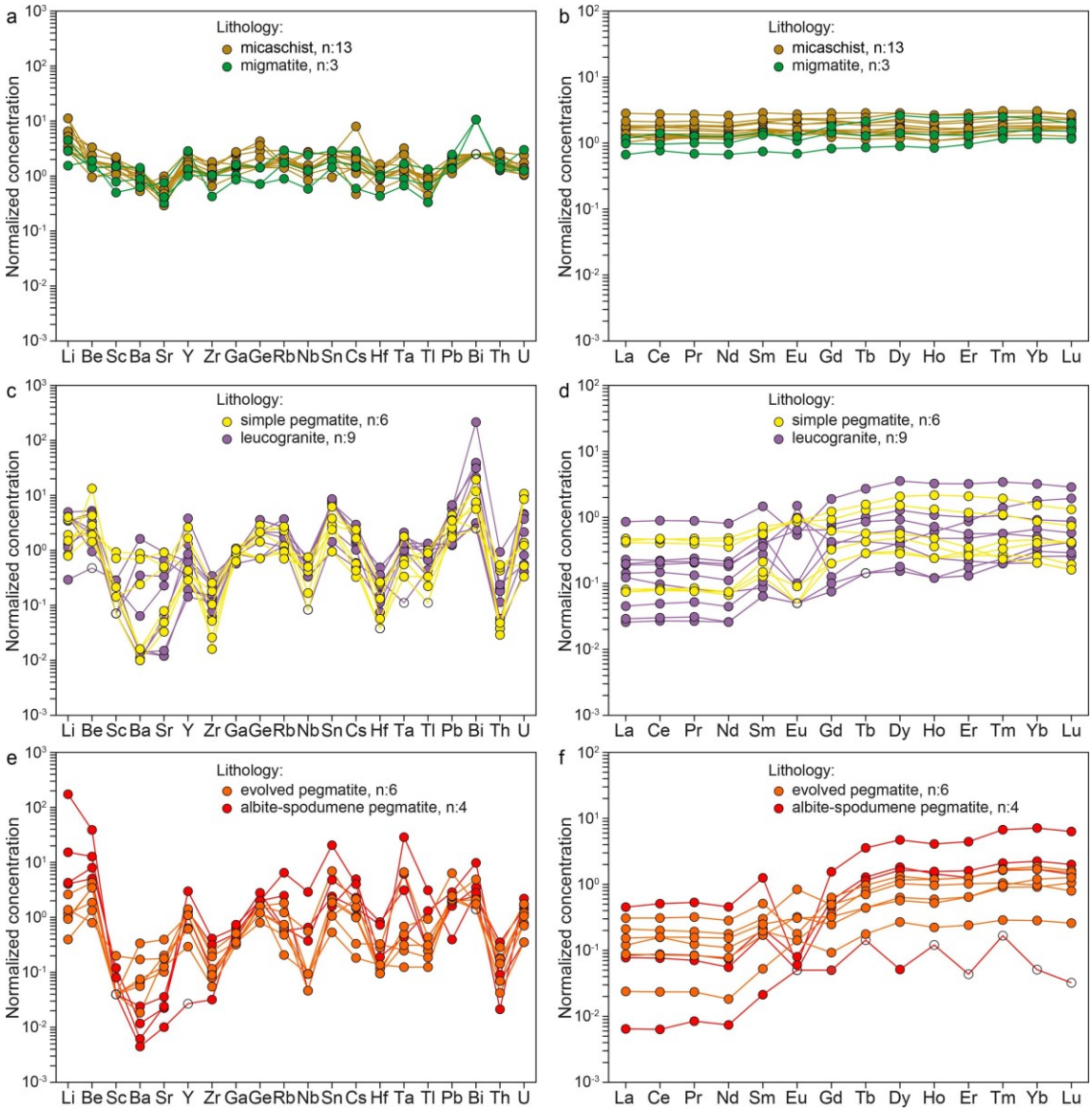


*Figure 8. Trace elements composition of subsolidus and suprasolidus metapelite (a, b), simple pegmatite and leucogranite (c, d) as well as evolved pegmatite and albite-spodumene pegmatite (e, f). Elemental concentrations are normalized over the upper continental crust averages (Rudnick & Gao, 2003). Analyses below detection limit are represented by open symbols.*

MUSCOVITE TRACE ELEMENT SYSTEMATICS

In order to decipher fractionation trends (Černý & Burt, 1984), trace elements analyses of muscovite were carried out with LA ICPS-MS. Undeformed or weakly deformed muscovite crystals larger than 0.5 cm were extracted from migmatite (12 analyses), simple pegmatite (73 analyses), leucogranite (44 analyses), evolved pegmatite (116 analyses) and albite-spodumene pegmatite (29 analyses). Note that the muscovite crystals extracted from migmatite are the anomalously large crystals described in section 3.1.1 (Figure 5d). Representative analyses are presented in Table 3. All analyses are provided as supplementary material (SM4). Evolved pegmatite is here defined by a Li concentration in muscovite higher than 100 ppm.

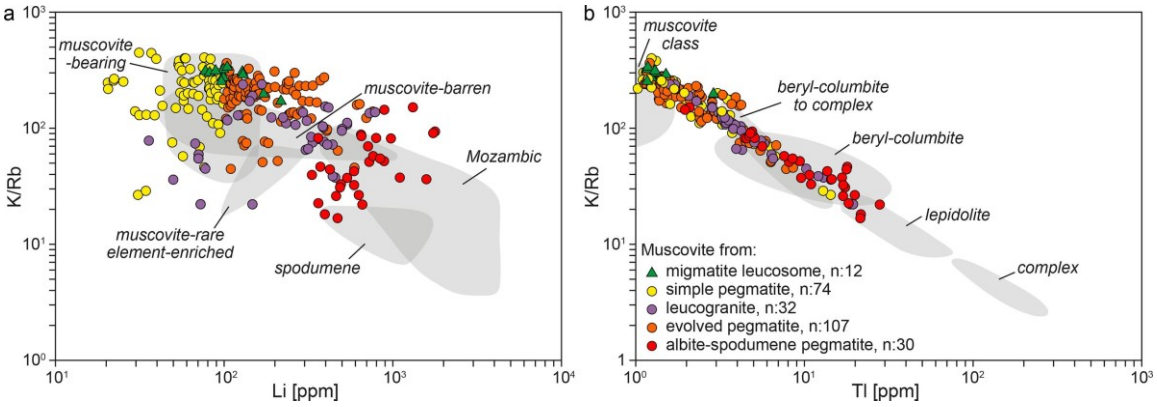


*Figure 9. Trace element composition of muscovite from migmatite leucosome, simple pegmatite, leucogranite, evolved pegmatite and albite-spodumene pegmatite. a. K/Rb ratio vs. lithium concentration. See panel b for legend. b. K/Rb ratio vs. thallium concentration. The grey backgrounds refer to pegmatite class defined in Černý & Burt (1984).*

The analyses show that the K/Rb ratio of muscovite progressively decreases from migmatite (254 to 337), simple pegmatite (27 to 448), leucogranite (22 to 193), evolved pegmatite (22 to 364) to albite-spodumene pegmatite (15 to 151, Figure 9, see also Figure 4b). The K/Rb ratio shows a negative correlation with the Li concentration (77-217 ppm in migmatite, 10-99 ppm in simple pegmatite, 36-785 ppm in leucogranite, 100-760 ppm in evolved pegmatite and 361-1780 ppm in albite-spodumene pegmatite, Figure 9a) as well as with the Tl concentration (1-3 ppm in migmatite, 1-19 ppm in simple pegmatite, 2-19 ppm in leucogranite, 1-19 ppm in fractionated pegmatite and 2-28 ppm in albite-spodumene pegmatite, Figure 9b). In contrast Ba is positively correlated to the K/Rb ratio and the Ba content in muscovite is always higher than in the corresponding whole-rock. Note that the correlation between the K/Rb ratio and Tl content is linear (with a logarithmic scale) and presents very little dispersion in comparison to the correlation between the K/Rb ratio and Li and Ba content respectively.

Our dataset shows a good (K/Rb vs Li, Figure 9a) to excellent (K/Rb vs Tl, Figure 9b) agreement with the trend defined by Černý & Burt (1984). However, in comparison to this pegmatite classification, muscovite from migmatite, simple pegmatite and leucogranite plot in the fields of muscovite-barren and muscovite-bearing pegmatite classes, whereas evolved pegmatite and albite-spodumene pegmatite only reach the fields of moderately fractionated pegmatite types (Figure 9a). Noticeably, most analyses from albite-spodumene pegmatite do not fall in the spodumene class (Knoll et al., 2018).

LITHIUM DISTRIBUTION IN THE METAPELITE

The subsolidus Al-rich metapelite hosting the AUPP contains between ~70 and ~270 ppm Li. In situ LA ICP-MS analyses were carried out on representative samples of staurolite- and/or garnet-bearing micaschist in order to identify the Li carriers and to quantify the Li partitioning between the main rock forming minerals. Six samples were selected for their limited degree of Alpine structural and metamorphic overprint. Selected analyses are presented in table 4 and all

analyses are provided as supplementary material (SM5). A summary of the Li concentration of each phase in each sample is provided in table 2.

Staurolite, biotite, muscovite and garnet are the main Li carriers (Table 2). Staurolite is by far the Li-richest phase with Li concentrations between 367 and 2973 ppm. The Li concentration is relatively homogeneous in most samples and individual crystals. Low Li concentrations occur in samples with abundant staurolite (>20 vol%) whereas higher Li concentrations occur in samples with less staurolite (<5 vol%). In biotite, the Li concentrations range between 115 and 907 ppm and are relatively homogeneous within each sample. Note that in some samples biotite crystals are too small for reliable analysis (RS36/99 and 16R42, table 2). In muscovite, the Li concentration spreads over two orders of magnitude (6 to 209 ppm), with samples containing Li-rich muscovite and others Li-poor muscovite. This does not correlate with the degree of Alpine overprint in the sample or with the lithostratigraphic complex from which the sample was collected. Garnet contains between 15 and 110 ppm Li and is relatively homogeneous with respect to the Li concentration.

Quartz was analyzed from two samples and yielded very low concentrations, just above the detection limit (3-5 ppm Li). Li partitioning coefficients were calculated using the average Li concentration in each phase and each sample (Table 5). They are expressed using the concentration in biotite as reference using $D_i=C_{bt}/_{Ci}$, where $D_i$ is the Li partitioning coefficient of phase i with respect to biotite, $C_{bt}$ is the concentration in biotite and $C_i$ is the concentration in phase i (see supplementary material SM1). The partitioning of Li between biotite and staurolite determined in three samples does not vary with the Li concentration in these phases and lies between 0.21 and 0.31, with an average of 0.27. For muscovite, garnet and quartz the range of partitioning coefficients is significantly wider lying between 4.8-13.8, 3.3-17.8 and 60-217 respectively.

### GEOCHEMICAL MODELING

We here present a geochemical model in an attempt to quantify how much lithium could be transferred from an Al-rich metapelite to an anatectic melt. The modeling procedures are presented in the supplementary material (SM1).

### THERMODYNAMIC FORWARD MODELING OF PARTIAL MELTING

The first stage of the model involves calculating a pseudosection with the composition of a Al-rich metapelite representative of the AUPP as input. This procedure ensures that partial melting is modeled in a thermodynamically consistent way. The pseudosection calculated in the P-T range 650-750˚C and 0.2-1.0 GPa (Figure 10a) shows several important features. Along the solidus, silicate melt is produced by a set of water-present (below 0.645 GPa) and water-absent (above 0.645 GPa) reactions, with the melt fraction increasing with decreasing pressure. The largest production of melt is linked to the muscovite dehydration melting reaction, which has a positive slope. Staurolite is stable in a narrow pressure (0.6-0.9 GPa) and temperature (up to 680˚C maximum) range, partly together with melt. It breaks down in reactions involving the formation of aluminosilicate, biotite and garnet at higher and lower pressures. The staurolite-dehydration melting reaction bounds the staurolite stability field at high temperature and leads to the formation of peritectic garnet, biotite and aluminosilicate.

The pseudosection reproduces the sequence of reactions involving staurolite, sillimanite and melt (Figure 10a) described in the Strieden Complex by Hoke (1990). It also displays typical features of Al-rich metapelite (White et al., 2014) and especially the coexistence of staurolite and melt in a narrow temperature range (0.645-0.87 GPa and 660-680 ˚C, Figure 10a). Note that the stability of staurolite and melt has been confirmed by $H_2O$-present melting experiments of metapelite at 0.6-1.4 GPa between 700-775°C (García-Casco et al., 2003). Equilibrium of anatectic melt and staurolite is therefore not an artifact caused by a special or simplified bulk-rock composition. Two factors might also promote the coexistence of staurolite and melt in nature. First, the analyzed staurolite crystals are rich in Li (up to 2970 ppm Li, table 2) and Zn (up to 0.82 wt% ZnO, table 4, supplementary material SM5). Such compositions tend to stabilizes staurolite, especially at high temperatures (Dutrow, 1991). Second, Li lowers the experimental melting point in the LiNASH system by almost 100°C (Stewart, 1978) and has a similar effect in the LiKASH system (Munoz, 1971). This implies that Li-rich metasediments could melt at temperatures 75°C lower than typical Li-free metasediments (Stewart, 1978). Hence, Li induces a shift of the staurolite-out reaction to higher temperatures and a shift of the solidus to lower temperatures. Since lithium is not considered in the thermodynamic calculation, the narrow temperature range of stability between staurolite and melt predicted by the model is likely to be an underestimate.

The pseudosection demonstrates that Li might be directly transferred from staurolite, the main Li carrier in the metapelite, to anatectic melt. To illustrate the different scenarios associated with destabilization of staurolite and the formation of melt, the volumetric fraction of solid and melt phases have been calculated between 650 and 750˚C along two isobaric paths, at 0.6 and 0.7 GPa (Figure 10b, c). These conditions fall within the P-T range of regional metamorphism in the Permian lower crust in the AUPP (Figure 2c), especially at the upper pressure limit of the conditions of melting determined for the Strieden (Hoke, 1990) and Petzeck-Rothenkogel complexes (Stöckhert, 1987). These isobaric paths are simple proxies for regional heating associated to lithospheric extension. They are consistent with reconstructed paths that indicate that a temperature increase coincided with almost constant pressure in the AUPP (Thöni & Miller, 2009; Roda et al., 2018; Petri et al., 2019).

At 0.6 GPa, staurolite first breaks down at 658˚C by the reaction staurolite + muscovite = sillimanite + biotite + $H_2O$, before melt forms at 666°C and reaches up to 10 vol% (Figure 10b). A sequence of reactions involving muscovite dehydration melting followed by destabilization of quartz and plagioclase yields large fractions of melt (up to 25 vol%) with the peritectic phases

biotite, garnet, alkali-feldspar and sillimanite. In contrast, at 0.7 GPa and 668˚C, melt appears in minor amounts (less than 2 vol%) while staurolite is still stable (Figure 10c). Destabilization of staurolite at 676˚C induces an increase of the melt fraction to 4 vol%. The higher temperature evolution is then similar to the one at 0.6 GPa, with a different order for the muscovite-, plagioclase- and quartz-out reactions. For both prograde paths, the modeled melt chemistry is peraluminous (Figure 7b) and gets richer in alkaline elements with increasing temperature, especially above the muscovite dehydration melting reaction (Figure 7c). The calculated melt chemistry is compatible with our analyses of pegmatite and leucogranite, even though it tends to be significantly richer in alkaline elements at high temperature.

### Equilibrium and disequilibrium partitioning

In the first stage of the model, Li is actually not considered as reactive. Its distribution between the solid phases and melt is calculated in a second stage, with trace element partitioning calculations. Two end-member models are tested. “Equilibrium partitioning” assumes that, at all conditions, the distribution of Li in all phases is in equilibrium, which corresponds to a batch melting model (Wilson, 2007). This implies that inward and outward intracrystalline diffusion of Li in the solid phases is fast in comparison to the heating rate along the prograde path. However, it can be argued that potentially the core of solid phases could be isolated due to low Li diffusion rate and not participate to partitioning (Bea, 1996). Furthermore, processes such as disequilibrium and overstepping of metamorphic reactions have been suggested to be active in amphibolite-facies metapelite (e.g. Waters & Lovegrove, 2002; Pattison & Spear, 2018). Figure 10a shows that for the considered bulk-rock composition there is a difference of 8°C between the staurolite to sillimanite breakdown reaction and the solidus. Since the staurolite to sillimanite reaction has a low Gibbs free energy difference and dissolution of staurolite is considered to be slow (Pattison & Spear, 2018), a modest overstepping of 8°C for staurolite is not unrealistic (Pattison et al., 2011; Carlson et al., 2015). This would imply that staurolite could remain metastable until solidus temperature along the 0.6 GPa prograde path.

It is challenging to model phase assemblages out of equilibrium (Gaidies et al., 2008b; Spear & Pattison, 2017). In this perspective, a second model, termed “disequilibrium partitioning”, is introduced for testing the effects of metastability by considering the following hypotheses at each step of the prograde path (Bea, 1996): (1) Only the solid phases that destabilize deliver Li in proportion of their lost mass. (2) Li from the melt always participates to partitioning. (3) Li is distributed only in phases of increasing mode. (4) Staurolite is metastable up to solidus conditions, which only applies to the 0.6 GPa path. The “disequilibrium partitioning” model can therefore be considered as a pragmatic approach that accounts for disequilibrium in the Li distribution, even though the phase assemblages are controlled by equilibrium.

In terms of calculation, the only difference between the two models is the set of volumetric fractions given as input. In the “equilibrium partitioning” model, the fractions are those calculated for equilibrium at the given P-T conditions (Figure 10b, c). In the “disequilibrium partitioning” model, no changes are considered in subsolidus conditions and fractions in suprasolidus conditions are modified so that only volumes modified during reactions participate in partitioning. A fundamental consequence of the model hypotheses is that the “equilibrium partitioning” model is instantaneous (or reversible), whereas the “disequilibrium partitioning” model keeps a memory of the metamorphic reaction sequence and is therefore irreversible.

### Two sets of lithium partitioning coefficients

Ideally, a consistent set of Li partitioning coefficients should be established by experiments on subsolidus and suprasolidus metapelite in a well-constrained environment. In the absence of such a set, we have used several sources to produce a set for further calculations. We have also considered two sets of partitioning coefficients owing to the uncertainties on muscovite-biotite and garnet-biotite partitioning (Table 5). In the following, biotite is used as the reference phase, since it is stable over the whole P-T range of interest. The “partitioning coefficient of muscovite”

therefore means “partitioning coefficient of muscovite with respect to biotite”. The same notation as in section 3.2.3 is used here.

To our knowledge, Icenhower & London (1995) is the only experimental study that characterized the partitioning of Li between biotite and peraluminous melt, yielding $D_{melt}$=1.64 at 650°C and $D_{melt}$~1 at 750°C. Even though the experiments were carried out at 0.2 GPa (at least 0.4 GPa lower than the pressure considered in our model) and the partitioning coefficient decreases with increasing temperature, we use the value 1.64 and not the unity value or a variable coefficient in order to provide conservative estimates. This choice has a strong impact on the results since all partitioning coefficients use biotite as reference. It implies that the Li concentration in the melt might be underestimated by the model, especially at high temperatures.

The distribution of Li between biotite, muscovite, staurolite, garnet and quartz is constrained by the analyses of six subsolidus metapelite samples from the AUPP (Campo, Rappold, Gailtal, Plankogel and Strieden complexes) presented in section 3.2.3. The conditions of Permian peak metamorphism that these samples experienced are above 600°C and 0.4 GPa (see figure 2c) and we consider that the analyses represent an equilibrated Li distribution at temperatures slightly below the solidus. The partitioning coefficients of staurolite, muscovite, garnet and quartz are calculated as the rounded average of the values determined in section 3.2.3 (Table 5).

The range and average of partitioning coefficients of staurolite (0.21-0.31 and 0.27, respectively) are in very good agreement with values determined in upper greenschist to amphibolite facies metapelite (0.22-0.48, Dutrow et al., 1986). This coefficient has a reduced variability and its value seems well constrained. The partitioning coefficient used for quartz (calculated as the average from two samples), sillimanite (same as for quartz) and the two feldspar phases (Bea et al., 1994) are most likely poorly constrained but are consistent with the notion that these phases are not major Li hosts. Tests showed that the exact value of these coefficients has little impact on the calculated Li concentration in the melt, as long as the coefficients remain high.

The partitioning coefficients of muscovite and garnet show a large scatter (Table 5). Nevertheless, the average values imply muscovite and garnet have lower Li concentrations than biotite, with more Li in muscovite than in garnet. This is consistent with the results of Dutrow et al. (1986). Our average coefficient for muscovite, $D_{ms}$=9.7, is however, significantly larger than the values measured for amphibolite-facies metapelite reported in the literature (4.57, Dutrow et al., 1986; 5.31, Dahl et al., 1993; 4.49, Yang & Rivers, 2000). A similar discrepancy appears when comparing our average coefficient for garnet, $D_{grt}$=11, to the only one in the literature (5.15, Dutrow et al., 1986). Hence, even though the relative partitioning of Li between garnet and muscovite is compatible with the measurements published in the literature, the partitioning coefficients calculated with our data are larger than those of the literature by a factor ~2.15. To account for the uncertainty on the partitioning coefficients of muscovite and garnet, two sets of partitioning coefficients are tested. In both sets, the coefficients of melt, staurolite, quartz, sillimanite, plagioclase and alkali-feldspar remain the same. In the “preferred set”, values of $D_{ms}$=9.7 and $D_{grt}$=11 are used. In the “alternative set” the Li distribution is modeled using $D_{ms}$=4.50 and $D_{grt}$=5.15, in agreement with the values found in the literature (Dutrow et al., 1986; Dahl et al., 1993; Yang & Rivers, 2000).

#### Modeling of the lithium concentration in anatectic melt

The results of the two partitioning models using the two sets of partitioning coefficients calculated for the two prograde melting paths are presented in Figure 11a, b. The curves represent the concentration of Li in the melt normalized over the concentration in the protolith before melting. Solid and dashed curves correspond to “equilibrium partitioning” and “disequilibrium partitioning”, respectively. Black and grey curves correspond to the “preferred set” and “alternative set” of partitioning coefficients. The evolution of these curves is described and interpreted in the light of the modal diagrams (Figure 10b, c). All curves show values well above 1 implying that the lithium concentration in the melt is always larger than the initial

protolith concentration. This contradicts with the notion that the effective partitioning coefficient between rock and melt should be close to unity (Bea, 1996). This apparent contradiction can be explained the following way. Staurolite strongly fractionates Li in subsolidus conditions and rapidly destabilizes at the onset of melting. The shape of the curves therefore reflects that the distribution of Li during melting is partly controlled by the subsolidus Li distribution.

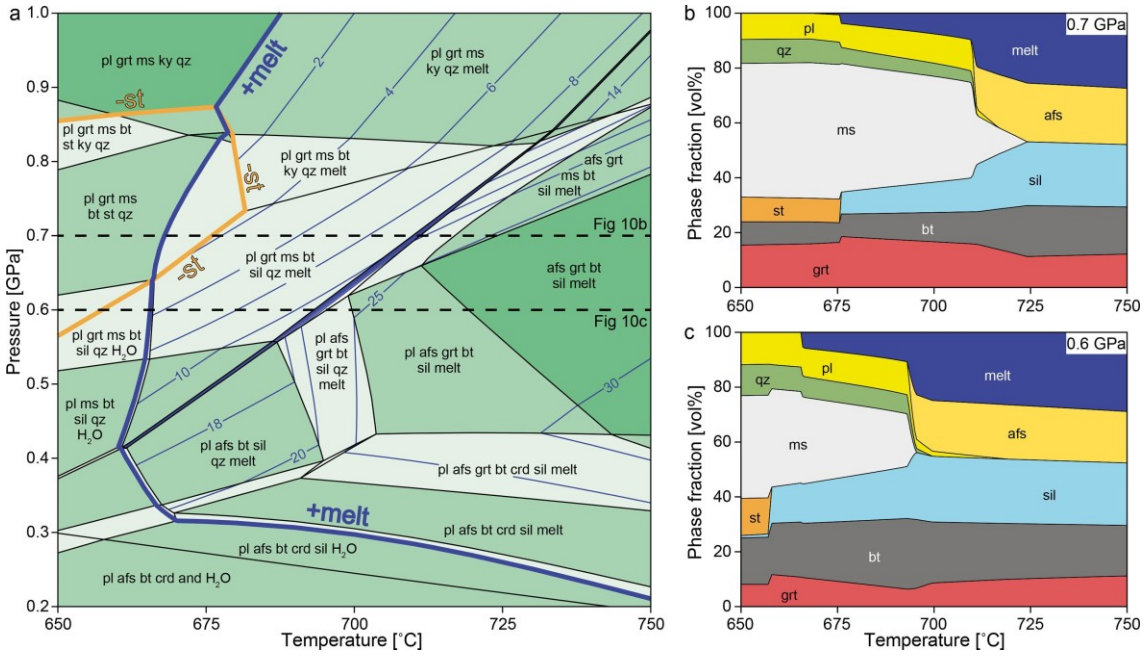


*Figure 10. a. Pseudosection calculated for a representative Al-rich metapelite (see section 3.2.1). The thick orange line indicates the set of staurolite breakdown reactions. The thick blue line indicates the solidus. The isolines of melt mode are represented by thin blue lines labeled by melt vol%. The black thick dashed lines correspond to the two considered prograde isobaric paths. b. Phase modes calculated along a prograde isobaric path at 0.7 GPa. c. Phase modes calculated along a prograde isobaric path at 0.6 GPa. Mineral abbreviations after Whitney and Evans (2010): alkali feldspar (afs), and (andalusite), biotite (bt), cordierite (crd), garnet (grt), ky (kyanite), ms (muscovite), plagioclase (pl), qz (quartz), sil (sillimanite), st (staurolite).*

The "preferred set" of partitioning coefficients is considered first. For "equilibrium partitioning" at 0.6 GPa, staurolite is unstable at the onset of melting and at that stage Li is mostly partitioned between biotite, muscovite and garnet. The Li concentration in the incipient melt shows relatively constant values around 2. It then progressively decreases to 1.6 for a melt fraction between 5 and 11 vol% (Figure 11a), which is controlled by the progressive increase of biotite fraction (the main Li carrier in absence of staurolite) before muscovite dehydration melting (Figure 10c). This is followed by a down sloping plateau for 11 to 23 vol% melt, actually corresponding to the narrow temperature range of muscovite dehydration melting (690-695°C). The following modest increase in Li concentration to 1.6-1.7 is driven by the progressive destabilization of biotite.

If staurolite is metastable until the solidus temperature is reached ("disequilibrium partitioning" model), the Li concentration in the incipient melt has a relatively high value of 7.6 and progressively decreases to 1.9 until a melt fraction of 23 vol% is reached (Figure 11a). This peak is the result of transfer of Li from rapidly destabilizing staurolite mostly into the melt. The following decrease is linked to the dilution of Li in the melt with ongoing melt production and to the increase of biotite fraction that additionally sequestrates Li in the solid fraction (Figure 10c). The final slight increase in Li concentration to 2.1 for a melt fraction larger than 23 vol% has the same origin as for "equilibrium partitioning".

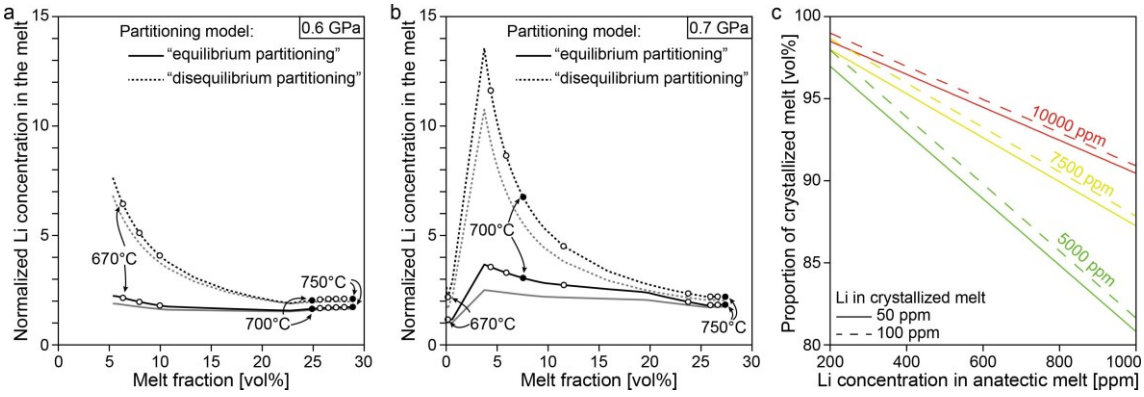


*Figure 11. Li concentration in the melt produced by partial melting of a Al-rich metapelite as a function of melt mode, calculated at 0.6 GPa (a) and 0.7 GPa (b). The concentration of lithium in the melt is normalized over the concentration in the protolith before melting. Two partitioning models are tested: "equilibrium partitioning" and "disequilibrium partitioning" (see section 5.2 for details). The black and grey curves correspond to calculations with the "preferred set" and "alternative set" of partitioning coefficients (see section 5.3 for details). Dots are placed every 10°C on the curves. c. Li concentration in the residual melt after fractional crystallization as a function of Li concentration in the anatectic melt at escape, proportion of melt crystallized as Li-poor product (simple and evolved pegmatite, leucogranite). Two values for the Li concentration in the crystallized melt are tested: 50 and 100 ppm (see text for details).*

For "equilibrium partitioning" at 0.7 GPa, the curve of normalized Li concentration in the melt first increases up to a peak reaching 3.7 for a melt fraction equal to 4 vol% (Figure 11b), associated with the progressive breakdown of staurolite combined with the increase of melt fraction (Figure 10b). The following slight decrease to values of 2-3 is associated with Li dilution and an increase of biotite fraction (see above), until a final value of 1.8 is reached after muscovite dehydration melting. For "disequilibrium partitioning" at 0.7 GPa, the curve displays a similar evolution compared to model "equilibrium partitioning" with a peak reaching a large value of 13.6 and a final value of 2.2. The difference is due to the assumptions (1) and (3) of the "disequilibrium partitioning" model. It reflects that when staurolite, the main Li carrier, destabilizes, it mostly delivers its Li to the melt, the phase with the largest fraction change at this stage of the prograde path (Figure 10b).

Results calculated with the "alternative set" of partitioning coefficients indicate trends very similar to those calculated with the "preferred set". The Li concentration in the melt is, however, always lower. This is in agreement with the smaller values for the partitioning coefficients of muscovite and garnet, implying that those solid phases fractionate more Li. The difference is, however, significant only for the "equilibrium partitioning" model at 0.7 GPa.

## DISCUSSION

This chapter focuses on an interpretation of the literature data, new data and modelling presented above and establishes the link between partial melting of metasediments and formation of albite-spodumene pegmatite. The new findings are integrated in a comprehensive genetic model of albite-spodumene pegmatite out of anatectic melt. Potential limitations and further applications of this model are presented in the light of recent research on LCT-pegmatite.

### INTERPRETATION OF THE LITERATURE P-T-T DATA

#### TEMPORAL RELATION OF PEGMATITE EMPLACEMENT AND METAMORPHISM

The ages presented in our review (Figure 2a) are directly related to the timing of emplacement of pegmatite and leucogranite or regional metamorphism of metapelite. The compilation shows that most ages cluster between 240 and 290 Ma, which corresponds to most of the Permian together with the Early and Middle Triassic (Figure 2a, b). All considered types of lithologies cover more or less the whole age range at the scale of the AUPP and also at the scale of individual complexes (e.g. Saualpe-Koralpe and Rappold complexes). The age distribution shows a

noticeable symmetric pattern with a strong concentration in the range 270-260 Ma (Figure 2b). The moderate negative skewness is due to four ages younger than 240 Ma.

A closer inspection of the compilation suggests that the majority of metamorphic ages clusters in the upper part of the age range (290-250 Ma), whereas magmatic crystallization ages scatter over the whole age range. This difference is illustrated by the kernel density estimate (KDE) curves of the two groups (Figure 2b): the metapelite curve has a narrow and slightly early peak in comparison to the pegmatite and leucogranite curve. This pattern could suggest that regional metamorphism occurred mostly at the beginning of the Permian event while pegmatite and leucogranite emplacement spread over the whole event. This would be in line with observations from the Campo Complex showing that widespread regional metamorphism was followed by focused contact metamorphism associated to intrusion of mafic bodies (Roda et al., 2018; Petri et al., 2019). An alternative interpretation of the difference in age pattern is that metamorphic garnet and monazite could have grown during initial stages of the prograde metamorphism (Gaidies et al., 2006; 2008b; Schulz, 2017) before partial melting close to peak conditions would have produced the source of pegmatite and leucogranite. The two explanations do not exclude each other.

We conclude that the Permian metamorphism and the emplacement of pegmatite and leucogranite was broadly contemporaneous, in the age range 290-240 Ma at the scale of lithostratigraphic complexes and the AUPP. Note that age of anatexis has not been directly recorded in the Austroalpine Unit yet, but migmatite formation in Adria-derived units in the Western Alps occured in the same age range (Kunz et al., 2018 and references therein). This age range (290-240 Ma) is distinguishable from the Variscan event even within error on the compiled ages but correlates with the age of gabbro intrusions that originated in the melting of the uplifting mantle (Thöni, 2002; and references therein). All these processes (metamorphism, pegmatite and leucogranite emplacement, mantle uplift), with additional volcanism and basin formation in the upper crust, relate to the same event of lithospheric extension (Lardeaux & Spalla, 1991; Rebay & Spalla, 2001; Schuster & Stüwe, 2008).

### THE PERMIAN METAMORPHIC RECORD

The considerable number of P-T estimates from the Austroalpine Unit documents an almost continuous metamorphic record between 450°C and 750°C covering, the middle and lower parts of the Permian crust (Figure 2c). This record clearly indicates that metamorphism occurred along high temperature-low pressure gradients and is for large parts similar to the one documented in Adria-derived units of the Western Alps (Marotta and Spalla, 2007; Roda et al., 2019, Kunz et al., 2018). The crustal geotherms plotted on figure 2c show that most P-T estimates fall between steady state conductive geotherms calculated for a normal mantle heat flux (25 $mW.m^{-2}$) and a more than doubled mantle heat flux (55 $mW.m^{-2}$). The P-T conditions related to contact metamorphism in the Campo Complex (C4 on figure 2c, Petri et al., 2019) provide a noticeable exception to this trend and relate most likely to heat advection. Hence, the thermal regime of the Permian crust associated with an increased mantle heat flow are therefore consistent with the context of lithospheric extension and are not directly related to the late stages of the Variscan orogeny (Marotta & Spalla, 2007; Schuster & Stüwe, 2008).

More details on the thermal structure can be gained from a close examination of the different crustal levels. A strongly elevated field gradient of 55 to 70°C/km was modeled for the Permian sedimentary successions in the north-westernmost part of the Austroalpine Unit (Mählmann & Petschick, 1996). It is consistent with the high heat flux in the Permian and Triassic required for explaining organic metamorphism in the southeastern parts of the Austroalpine Unit (Rantitsch et al., 2020). Most data from the middle crust indicate moderate pressures of 0.2 to 0.6 GPa (Figure 2c), in agreement with the occurrence of andalusite and sillimanite. Additionally, the andalusite bearing greenschist to lower amphibolite-facies assemblages consistently indicate a high geothermal field gradient of 40°C to 50°C (Hoke, 1990; Draganits, 1998; Török, 1999; Habler

& Thöni, 2001; Schuster et al., 2001; Thöni & Miller, 2009) because of the restriction to the andalusite stability field with pressure of less than 0.43 GPa at 534°C (value of the aluminosilicate triple point calculated with the database of Holland & Powell, 2011, consistent with Pattison et al., 2002). The Permian lower crustal record indicates pressures between 0.4 and 1.0 GPa for temperatures of 600°C to almost 900°C (Stöckhert, 1987; Hoke, 1990; Petri et al., 2019; Schulz, 2016; Li et al., 2021). The absence of cordierite in Austroalpine Unit (except in the Campo Complex, see Petri et al. 2017) provides a lower bound of 0.4 GPa for suprasolidus conditions (Pattison et al., 2002). The rather high pressure conditions at temperatures consistent with partial melting are consistent with the P-T data determined for Permian migmatite and granulite in Adria-derived units of the Western Alps (e.g. Hermann & Rubatto, 2003; Luvizotto & Zack, 2009; Redler et al. 2012).

This data indicates a thermal structure with a slightly decreasing thermal gradient with increasing depth. There are several ways to interpret this gradient: (1) Modern methods used for estimating the P-T conditions in the upper-amphibolite- to granulite facies tend to better constrain pressure than the petrogenetic grids used for greenschist- to amphibolite-facies conditions. Additionally, old papers used a lower pressure value than modern ones for the aluminosilicate triple point. The decrease of the thermal gradient could therefore be artificially exaggerated. (2) The different gradients characterize different stages, with a steeper gradient at the onset of metamorphism and a shallower gradient for peak metamorphic conditions. This would be consistent with the Permian prograde transformation of staurolite to andalusite and sillimanite, and of andalusite to sillimanite observed in several complexes (Hoke, 1990; Draganits, 1998; Török, 1999; Schuster at al., 2001). This is also consistent with the distribution of most P-T estimates between steady state conductive geotherms calculated for a normal and a more than doubled mantle heat flux (Figure 2c). (3) Variations might be explained by both horizontally and vertically heterogeneous crustal thinning (Petri et al., 2019) as well as a complex timing of extension and intrusion of mafic bodies in the lower crust. In that respect, the Campo Complex, which is the deepest exposed Permian crust in the Austroalpine Unit, reveals large P-T variations and complex P-T evolutions within a relatively small area (Petri et al., 2019). These three explanations do not exclude each other.

## Interpretation of the field observations

### Depth of pegmatite and leucogranite emplacement

The metamorphic framework described here constrains the conditions of pegmatite and leucogranite emplacement. Evolved and albite-spodumene pegmatite types occur in the upper structural level within country rocks partly showing Permian upper greenschist-facies metamorphism. This implies that the upper level of the profile (Figure 3) corresponds to the upper part of the middle crust. This is consistent with the occurrence of andalusite in evolved pegmatite (Figure 5l) and in the host-rock of evolved and albite-spodumene pegmatite (Figure 5j) in the Saualpe-Koralpe Complex. Metamorphic conditions of 0.53±0.03 GPa and 525±15°C have been determined by Gaidies et al. (2008b) for the initial growth of Permian garnet in micaschist of the Rappold Complex at Mount Hohenwart, which is one of the largest albite-spodumene pegmatite occurrence in the AUPP. These conditions also apply for the emplacement of pegmatite, if we assume that they intruded the country rocks close to peak metamorphic conditions. Finally, elevated pressures (Figure 2c) are in agreement with the fact that no petalite (London, 1984; 2008) or miarolitic cavities have been found in the albite-spodumene pegmatite bodies (Knoll et al., 2018). All constraints taken together indicate pressures of 0.3 to 0.5 GPa and temperatures of 500-550°C for the emplacement of evolved and albite-spodumene pegmatite (Figures 2c, 3). Assuming lithostatic pressure and a constant crustal density of 2750 kg.m-3, this corresponds to an intrusion depth of 11 to 15 km.

The intermediate level of the profile, where simple pegmatite and leucogranite occur (Figure 3), corresponds to the lower part of the middle crust. The P-T conditions in metamorphic rocks and

widespread staurolite stability indicates pressures between 0.4 and 0.6 GPa and temperatures of 550°C to 650°C (Figures 2c, 3). This translates to an intrusion depth of 14 to 22 km for the simple pegmatite and leucogranite. The lowest level of the profile, which is characterized by partial melting, corresponds to lower crustal sections with temperatures greater than 650°C, and pressures between 0.5 and 0.8 GPa (Figures 2c, 3). This constrains the depth at which metapelite started to melt to 18-30 km.

Hence, a systematic zonation can be observed in the AUPP, representing the structure of the crust during Permian lithospheric extension (Figure 12 a, b). This spans over vertical sections of 11±8 kilometers of the Permian crust (minimum: 3 km, average: 12 km, maximum: 19 km). The lower structural level (~18-30 km depth, upper part of the lower crust) is occupied by migmatitic metapelite with dominant metatexite texture and simple pegmatite. The intermediate structural level (~14-22 km depth, lower part of the middle crust) corresponds to amphibolite-facies metapelite intruded by simple pegmatite and leucogranite. In the upper structural level (~11-15 km depth depth, upper part of the middle crust), evolved pegmatite and albite-spodumene pegmatite emplaced into upper greenschist-facies metapelite. Owing to the Permian and Alpine deformation as well as the large uncertainty on the thickness of the investigated Permian profiles, any comparison to present day thicknesses is most likely irrelevant.

### Mechanisms of melt segregation, migration and emplacement

The spatial relationships between magmatic rocks and metasediments as well as the systematic vertical sequence across the Permian crust observed in this study are in good agreement with previous investigations (Schuster et al., 2001; Manzotti & Zucali, 2013). The observed structures constrain the melt related processes, which are presented here from the lower to the upper crustal levels.

In patchy migmatite, the large leucosomes that are parallel to the schistosity and rimed by melanosome (Figure 5c) are indicative of melt collection at inscipient melting (Sawyer, 2008). Such leucosomes are dominantly parallel to the Permian schistosity (Figure 5a, c, e, f) and can be interpreted as compaction melt bands forming at large pressure under modest differential stress (Weinberg et al., 2015). This would be compatible with pure shear deformation during extension and attest that melt segregation was assisted by deformation. In contrast, in the net-textured migmatite, the discordant leucosome has sharp contacts to the paleosome and lacks melanosome rim (Figure 5g), which indicates further melting (Oliver & Barr, 1997). This also suggests that the leucosome was injected from a short distance, probably through porous flow into shear bands formed during layer-parallel extension (Brown, 2004).

The locally observed exceptional large alkali-feldspar and muscovite porphyroblasts crystallized in the migmatite schistosity (Figure 5d, f) are interpreted as leftovers of melt impregnating the paleosome. This interpretation is underpinned by processes described in Sawyer (2001): removal of the melt from the drainage network is possible since the viscosity of the melt is much lower than the residual solid matrix. Then, once the channel network at grain scale closes, any remaining melt that had dispersed into the matrix crystallizes as overgrowths on matrix minerals. The exceptional large alkali-feldspar and muscovite porphyroblasts therefore suggest pervasive melt migration along distributed channels that are now closed. This interpretation also applies to the occurrences of exceptionally large muscovite and feldspar (Figure 5o) found in rather fine-grained micaschist and paragneiss at the basis of the intermediate level and within the upper level, respectively. Evidence of pervasive flow through porous matrix justifies the two phase flow modeling approach of Plunder et al. (2022), which showed that pegmatite can form as a result of upward migrating anatectic melt pulses.

The leucogranite bodies, with their textural and mineralogical inhomogeneities (Figure 5i), reflect the accumulation of distinct melt pulses of different composition. The structures of these accumulations argue against homogenization of the whole melt volume. The different melt compositions are interpreted as an effect of individual melt injections and their fractional

crystallization (Knoll et al., 2018; see sections 4.3 and 4.4 below). The leucogranite bodies are therefore important witnesses of fractional crystallization as they are much larger than other types of pegmatite bodies and are always found at mid crustal levels (Knoll et al., 2018).

Overall, two mechanisms of pegmatite emplacement have been identified. The discordant dikes in the upper part of the middle crust (Figure 5k) likely formed as injections into brittle fractures (Černý, 1991b) with orientations probably controlled by the tectonic stress regime (Delaney et al., 1981; Vanderhaeghe, 1999). The similarities between the geometry of the contact between a well-preserved pegmatite and its host-rock as well as its xenolith (sharp upper and lower contact parallel to the schistosity and jagged lateral contacts, Figure 5n) suggests another mode of emplacement by injection in several sheets parallel to the schistosity. This geometry could be compared with sheet intrusions (Marinoni, 2001). Additionally, we argue that discordant pegmatite dikes do not only record melt emplacement but can also be interpreted as frozen melt channels (e.g. Tibaldi, 2015; Varga et al., 1998). Especially the thin and folded discordant dikes shown on Figure 5p is interpreted as a partly closed channel connecting the different larger pegmatite bodies in its surrounding.

Even though we could not observe a profile without outcrop interruption between the partially molten metasediments and the albite-spodumene pegmatite, the observations presented here and the related mechanisms suggest a coherent picture. In the upper part of the lower crust anatectic melt segregated in migmatite and subsequently migrated upward through it and through the middle crust. Two modes of migration have been identified: channelized flow through fractures and pervasive flow through porous matrix. We consider that melt ascent was driven by buoyancy (Brown, 2010 and references therein). Melt migrated trought rarely preserved fractures oblique to the main fabric in the metasediments and was emplaced in sheets parallel to it. We postulate that all these mechanisms were most likely assisted by deformation during extension.

### Interpretation of the geochemical data

#### Al-rich metapelite as lithium source

The whole-rock composition of the metapelites from the AUPP suggests that most of these rocks derive from Al-rich sediments such as shales, despite possible chemical modifications during metamorphism and partial melting (Figure 7a). This is consistent with the occurrence of metamorphic Al-rich phases such as staurolite, sillimanite, andalusite and kyanite. The very flat REE pattern of the non-migmatitic metasediments (Figure 7b) additionally implies that the Al-rich sediments could be direct products of upper continental crust erosion, without significant chemical modification. However, the Li concentrations of the analyzed metapelite samples (~50-250 ppm) are clearly higher than the average values determined for the upper (24 ppm), middle (12 ppm) and lower continental crust (13 ppm, Rudnick & Gao, 2003) and are also higher than the upper crustal concentration of 35 ppm proposed by Teng et al. (2004). The enrichment in Li in metasediments derived from clay minerals is not surprising, since Li is concentrated in the clay fraction of shales through uptake of isotopically heavy Li from the hydrosphere (Teng et al., 2004). Hence, Li concentrations between 50 and 100 ppm are not untypical for shales deposited in continental and oceanic basins (Teng et al., 2004; Chan et al., 2006). Likewise, hectorite clay deriving from altered volcanic deposits can be enriched in lithium (Bowell et al., 2020). The highest Li concentrations measured in crustal materials come from in pore brines with 200-300 ppm Li in marginal zones, 500-1600 ppm Li in intermediate zones and 1510-6400 ppm in salt nucleuses (Warren, 2010 and references therein). This implies that an evaporite component may contribute to the Li concentration of a metasediment. However, a role for evaporite as significant Li source for the AUPP is unlikely since the REE patterns shown on Figure 8b are flat and do not correspond to those characteristic for halite crystallization and fractionation, which tend to have a positive Eu anomaly and higher enrichment in REEs (e.g. Censi et al. 2017; Sohrabi et al. 2017).

In general, Li concentration decreases during prograde metamorphism. In metamorphic rocks, the depletion of Li ranges between 20 to 50 %, depending on the conditions of peak metamorphism dehydration (Zack et al., 2003; Marschall et al., 2007; Teng et al., 2007; Qiu et al., 2011) and is particularly severe during melting at upper amphibolite- and granulite-facies conditions (Qiu et al., 2011). This is consistent with the average difference of 40 ppm Li between the analyzed subsolidus and suprasolidus metasediments investigated in this study (Table 2). Our analyses indicate however uncommonly high Li concentrations in amphibolite-facies metasediments, raising the question of the stability of the Li host minerals in metapelite of the AUPP during prograde metamorphism below the solidus temperature.

Our LA ICP-MS data shows that staurolite is by far the Li-richest phase, with concentrations between 367-2973 ppm Li, which is considerable since Li is substituting for ions such as Mg, Fe or Zn in the staurolite cystal structure (Dutrow et al., 1986; Hawthorne et al., 1993). In fact, data for synthetic and natural staurolite demonstrate maximum Li concentrations of 1850 ppm (Wunder et al., 2007) and 5900 ppm (Dutrow et al., 1986; Chopin et al., 2003) respectively. The sequence of relative Li concentration in the analyzed porphyroblasts is staurolite > biotite > muscovite > garnet, which is in agreement with the sequence staurolite > cordierite > biotite > muscovite > garnet – tourmaline – chloritoid reported by Dutrow et al. (1986). The Li concentrations determined for the metapelite of the AUPP indicate that metamorphic Li loss due to dehydration was avoided by a particular set of successive mineral reactions during prograde metamorphism. At low temperatures Li was most probably assimilated in newly grown cookeite, probably out of a Li-bearing clay mineral or zeolite (Vidal & Goffé, 1991; Verlaguet et al., 2011; 2016). Li-rich staurolite then grew at the expense of cookeite (Feenstra et al., 2003) and was stabilized up to solidus conditions (Dutrow, 1991). All these reactions are strongly favoured by Al-rich chemistry as they have been inferred mostly in metabauxite and Al-rich metapelite.

In this sense, the Al-rich metapelites of the AUPP, especially those containing staurolite, represent fertile metasediments that could have released a significant amount of Li during their first anatectic event involving staurolite break down. This release of Li into a melt is attested by the difference in Li concentrations between the subsolidus and suprasolidus metasediments.

### GEOCHEMICAL EVIDENCE FOR FRACTIONAL CRYSTALLIZATION OF ANATECTIC MELT

The leucosome in migmatite, simple pegmatite, leucogranite, evolved pegmatite and albite-spodumene pegmatite are characterized by a similar magmatic mineral assemblage of K-feldspar, quartz, plagioclase, muscovite, garnet and tourmaline with spodumene only being present in albite-spodumene pegmatite. Such an assemblage is typical for hydrous melts derived from metapelites and at temperatures lower than biotite dehydration melting (Patiño Douce & Harris, 1998; Solar et al., 2016). In addition, the occurrence of K-feldspar in leucosome is an indicator for muscovite dehydration melting (Spear et al., 1999). Garnet from the investigated pegmatite and leucogranite is characterized by an elevated Mn content (Thöni & Miller, 2000; Habler et al., 2007; Knoll et al., 2018) typical for crystallization of a peraluminous melt derived from metasediment in general (Whitworth & Feely, 1994) and for fractionated pegmatitic melt in particular (Selway et al. 2005). The occurrence of muscovite and tourmaline and the very rare occurrence of biotite indicate crystallization from Ti-poor and B-rich melts (Nabelek & Liu, 2004). According to Nabelek & Liu (2004), biotite usually crystallizes in melts and fluids with more than 0.06 wt.% $TiO_2$, otherwise tourmaline develops dominantly. Additional “exotic” phases such as beryl, andalusite, Nb-, Ta-, Sn-bearing ore minerals and spodumene found in evolved pegmatite and albite-spodumene pegmatite respectively are typical for high degrees of fractionation in pegmatite (Ercit et al. 2005). Note that the albite-spodumene pegmatite of the AUPP does not contain the full spectrum of rare elements. Especially, it is commonly very poor in REE, Ti, U, Th, Sn, Ta, Nb, Rb, Cs, Be, B and/or F that are considered as typical for the different types of Li-rich pegmatite (Ercit et al., 2005).

The peraluminous granitic composition of the investigated pegmatite samples generalizes the results from albite-spodumene pegmatite and leucogranite presented in Knoll et al. (2018). All magmatic rocks show an enrichment in Li, Be, Bi, Pb, wherby the signals are more pronounced in evolved pegmatite and albite-spodumene pegmatite. This signature is typical for leucogranite and pegmatite derived from molten metasediments (Patiño Douce & Harris, 1998; McKechnie et al., 2013; Sola et al., 2013). The further enrichment in evolved pegmatite and albite-spodumene pegmatite would indicate that these are products of advanced differentiation. However, it is necessary to evaluate if these features are due to fractionated crystallization in a huge granitic intrusion or alternatively in limited volumes of anatectic melt. In the following, the signals of several elements are discussed.

Several elements are indicative of a metasedimentary source. The depletion in Ti, Fe and Mg may indicate fractionation of mafic minerals and biotite in particular, whereas a depletion in Zr and Hf might be due to zircon fractionation. Alternatively, these signals might be explained by anatexis at conditions below biotite dehydration melting, possibly during peritectic growth of biotite. In this case the primary melt would not only be depleted in Ti, Fe and Mg, but also accessory phases like monazite, zircon or apatite, commonly included in biotite, would tend to remain in the melanosome. The effect is a depletion in Zr and Hf but also in Th and LREE (McKechnie et al., 2015). In fact these signals are observed in the investigated magmatic rocks. The general depletion of Ba and Sr in the investigated rocks might be due to feldspar fractionation in a parental granitic melt. However, such a process seems not necessary for the following reasons: on the one hand, Sr is depleted in the available metasedimentary source rock and on the other hand, muscovite was identified as one of the main carrier of Ba. The highest Ba concentrations of up to 2000 ppm were measured in muscovite porphyroblasts in the migmatite and they might have prevented Ba transfer to the melt. In the available metasedimentary source-rocks Nb and Ta appear in concentrations fitting to those of the upper continental crust (Rudnik & Gao, 2003). However, in the magmatic rocks Nb is slightly depleted with respect to Ta. This effect may be explained if rutile, a main Nb carrier, remains stable in the paleosome.

Other elements indicate fractional crystallization. Li, Be, Bi, Sn and Ta are successively enriched from simple pegmatite and leucogranite to evolved pegmatite and albite-spodumene pegmatite. This is due to the fractional crystallization of quartz and feldspar out of the pegmatitic melt that enriches in incompatible elements (Ercit et al., 2005) and typical for albite-spodumene pegmatite (Černý, 1991a). What is more, since Eu is strongly compatible in feldspar and is progressively extracted by this phase during fractional crystallization, the products of early crystallization tend to show a positive Eu anomaly, whereas the products of late crystallization have a negative one (Bea, 1996). Our analyses show that the three pegmatite types, as well as leucogranite, can display both a positive and a negative anomaly. This contradicts the conclusion presented in Knoll et al. (2018), which was based on fewer samples. We argue that the variation in Eu anomalies is an effect of the heterogeneous metasedimentary source composition, a low anorthite component of feldspar, variations in both the degree of partial melting and subsequent fractionation as well as apatite crystallization.

A very strong argument for the petrogenetic link between metapelite, leucogranite and pegmatites is represented by the systematics of muscovite composition. Rb, Li, Cs, Tl and Ba contents measured in muscovite display continuous trends (Fig. 8) that can be interpreted as fractionation trends (Černý & Burt, 1984). They are particulary notable for K/Rb versus Li and K/Rb versus Tl diagrams of Figure 9. New data from Keyser at al. (submitted) show a similar Li trend for quartz in metapelite, leucogranite and pegmatites of the AUPP. The trace element signatures of muscovite from migmatite and simple pegmatite indicate crystallization from a primitive melt, whereas muscovite from albite-spodumene pegmatite developed from a highly fractionated melt. Leucogranite and evolved pegmatite are intermediate fractionation products. The scattering of the data in the K/Rb versus Li diagram for a given lithology may be related to

the following two factors: (1) The heterogeneity of the source. As Permian high temperature metamorphism extended over time and space, different metapelites with different geochemical compositions might have partially melted, with different melting degrees. (2) The Alpine amphibolite- to eclogite-facies overprint might have perturbed the initial concentration of mobile elements (Knoll et al., 2018).

Finally, published initial isotopic ratios (Thöni & Miller, 2000; Schuster et al., 2001; Knoll et al., 2018) calculated with the age of the individual sample, yield εNdt = -6.5 to -8.8 (mean value -7.7) and Sr Io = 0.7073 to 0.9686 (mean value = 0.73117). In spite of the scattering of some Sr ratios most probably induced by an Alpine overprint, these isotopic data point to a crustal source (Allègre, 2008).

Hence, mineralogy and whole-rock geochemistry suggests that the melt source of simple pegmatite, evolved pegmatite, albite-spodumene pegmatite and leucogranite is a metasediment. As there are no fertile granites present in the AUPP and all geochemical features of the investigated magmatic rocks can be explained by alternative processes we argue that pegmatite and leucogranite of the AUPP derived from small portions of anatectic melts formed at temperatures below the biotite dehydration melting temperature. Whole-rock geochemistry together with muscovite trace element chemistry show that there is a continuous fractionation trend between the anatectic melt, simple pegmatite, leucogranite, evolved pegmatite and albite-spodumene pegmatite. These results are consistent with the published radiogenic isotope data.

## INTERPRETATION OF THE GEOCHEMICAL MODEL

### QUANTIFICATION OF LITHIUM TRANSFER IN ANATECTIC MELT

Comparing the results of the two melting models shows that the Li concentration in the melt is always higher for “disequilibrium partitioning” than for “equilibrium partitioning”, all other parameters remaining the same. This directly reflects the hypotheses of the “disequilibrium partitioning” model where Li is concentrated in the melt, the phase having the largest fraction increase in suprasolidus conditions. In contrast, “equilibrium partitioning” tends to distribute Li, even into phases that do not react. The two models can therefore be considered as endmembers, providing limits to the Li concentration in the anatectic melt. Since the processes related to melting are irreversible (London, 2018 and references therein) and disequilibrium melting is likely to be the rule in nature, rather than an exception (Bea, 1996), we consider that the upper bound provided by the “disequilibrium partitioning” model is the most likely scenario.

Realistic limits of Li concentration in the anatectic melt can be deduced from the normalized curves in Figure 11a, b and values of Li concentration in metapelite (Table 2). Inspection of Figure 11a, b and table 6 shows that the Li concentration in the melt varies between a minimum of ~100 ppm and a maximum of ~3660 ppm, depending on the initial metapelite concentration, the pressure, the partitioning model and the set of partitioning coefficients. Importantly, the Li concentration also depends strongly on the melt fraction. The relevant Li concentration determining how much Li can be transferred into an anatectic melt is therefore primarily dependant on the question when melt escape from the migmatitic metapelite becomes feasible and upward melt migration in the crust is initiated.

A segregated melt can escape the solid network if its fraction reaches a certain threshold that depends chiefly on the migmatite structure, deformation and melt viscosity. Modeling and field observations constrain the melt escape threshold to 20-25 vol% of melt (Vigneresse et al., 1996). For the considered Al-rich metapelite, this fraction is achieved immediately after a dramatic increase from 10 to 20 vol%, which occurs within a temperature range of ~5°C due to muscovite dehydration melting (Figure 10). This reaction is associated with a large and positive volumetric change and promotes melt segregation and the development of melt pathways by increasing the pore pressure (Rushmer, 2001; Holyoke & Rushmer, 2002). Rock experiments on metapelite

have shown that rates and amounts of melting are strongly enhanced by deformation, suggesting that melt segregation and extraction are much more efficient in dynamic environments (Misra et al., 2009; Tumarkina et al., 2011). Hence, melt may escape at fractions of 7-10 vol% in cases where deformation is active (Brown, 2007; 2010), which corresponds to melt fractions just above the liquid percolation threshold at 7-8% (Vigneresse et al., 1996; Rosenberg & Handy, 2005). Modeling suggests that pure shear, that can be inferred from observed structured (see section 4.2.2) plays an additional role in segregating melt efficiently, potentially allowing melt to concentrate locally and then to escape (Vigneresse & Burg, 2000). Finally, Li- and H2O-rich melts have low viscosity (Bartels, et al., 2011; Bartels et al., 2015) promoting their mobility and facilitating their extraction through gravity driven compaction (Rutter, 1997; Baker & Vaillancourt, 1995). These considerations of segregation and extraction processes indicates that the investigated anatectic metapelite provides a favorable environment for extracting melt from its solid-state network at low values of melt fraction. In the following, we therefore consider critical melt fractions allowing melt escape of 7 vol% (dynamic case) and 20 vol% (static case).

Table 6 provides minimal, average and maximal Li concentrations in melt for 7 and 20 vol% in several scenarios (prograde path at 0.6 or 0.7 GPa, “equilibrium partitioning” or “disequilibrium partitioning”, “preferred set” and “alternative set” of partitioning coefficients). The minimal, average and maximal concentrations directly reflect the minimal (~70 ppm), average (~120 ppm) and maximal (~270 ppm) Li concentration in the analyzed subsolidus metapelite samples (Table 2). As argued in the previous section, the uncertainty in the partitioning coefficients of muscovite and garnet is of minor importance in this regard. A high Li concentration in the metapelite and a low melt fraction at escape are favorable for high Li concentrations in escaping melt. Another important factor is the stability (at 0.7 GPa) or the metastability (at 0.6 GPa) of staurolite at the onset of melting. As explained above, this permits a direct transfer of Li from staurolite into the melt. In such favorable cases, and considering a Li-rich protolith (270 ppm Li), the concentration in an escaping melt reaches 931-2755 ppm Li (dynamic case) and 572-739 ppm Li (static case). Under less favorable assumptions, Li concentrations at melt escape comprising between 200 and 500 ppm are readily achieved for average metapelite Li concentration. In the least favorable case, the range of Li concentrations at melt escape is larger than 100 ppm. Note that a metapelite with an average concentration corresponding to the average upper crust (24 ppm; Rudnick & Gao, 2003) would produce melt with more than 200 ppm Li only in the most favorable cases.

Migrating melt can progressively enrich in Li by assimilating immobile Li-richer low fraction melt stored along its pathway. This effect is a direct consequence of the inverse correlation between Li concentration and melt fraction above 4-5 vol% (Figure 11a, b). Calculation of integrated Li concentrations between extraction at 20 vol% melt and solidus level (see supplementary material SM1 for the derivation) indicates that this process is mostly relevant in cases of “disequilibrium partitioning” (Table 6), where the peak of Li concentration is the highest (Figure 11a, b). This process contributes to an increase in the Li concentration in melt by a factor larger than 2, yielding a concentration of almost 2000 ppm Li in the most favorable case.

Considering the large muscovite flakes occurring in migmatite to be a witness of the most primitive melts, the largest Li concentration of ~200 ppm (Figure 9a) indicates Li concentrations in melts of 500 ppm to 1000 ppm, depending on the partition coefficient used (Table 5). Lower muscovite concentrations of 100 ppm Li yields melt concentrations of between 250 and 500 ppm. This calculation provides an independent constraint on the range of Li concentration in the anatectic melt before fractional crystallization.

In conclusion, it can be demonstrated that the Li concentration in the melt extracted from migmatitc Al-rich metapelite can reach up to 1000 to 3000 ppm. Several conditions have to be fulfilled: (1) staurolite is stable or metastable at the onset of melting, (2) the Li concentration in

the protolith is high, (3) Li only partitions between the phases that react and (4) melt escapes at small fractions or the ascending melt assimilates Li-rich melt. All these assumptions are likely to apply to the investigated Permian lower crust exposed in the AUPP implying that Li concentrations of several 1000 ppm in a migrating anatectic melt was locally possible. In less favorable cases, the Li concentration in the melt at escape can reach 200 to 500 ppm Li. This range corresponds to a realistic lower bound corresponding to conservative hypotheses. 200 ppm Li is actually a minimum if the metapelite contains the average value of 120 ppm Li.

### Quantification of Li-enrichement through fractional crystallization

The geochemical evidence suggests that the albite-spodumene pegmatite of the AUPP crystallized from residual melts derived from anatectic melts. These have then been enriched in Li through fractional crystallization, generating relatively low-Li products along the way (i.e., simple pegmatite, leucogranite and evolved pegmatite). The calculated minimal value of 200 ppm Li in the migrating melt at escape is twice the maxium value measured in simple pegmatite and leucogranite (Tables 1, 2). It is also twice the average concentration of evolved pegmatite. This difference indicates that fractional crystallization indeed contributed to increasing Li concentrations in the remaining melt.

For quantifying Li enrichment through fractional crystallization we use a simple mass balance calculation that does not account explicitely for partitioning between melt and solid phases (see supplementary material SM1). Note that more complex Rayleigh-type fractionation models can also be employed for modeling trace element evolution of a pegmatite forming melt through fractionation (e.g. Hulsbosch et al., 2014; Maner et al., 2019; Chakraborty & Upadhyay, 2020). Usage of such a simplified model is justified by the relatively low Li concentration in simple pegmatite, leucogranite and evolved pegmatite, which is a consequence of the low Li concentration in the principle rock forming minerals (quartz, plagioclase and K-feldspar). Importantly, muscovite (the only phase containing significant amount of Li) is only a minor phase even in evolved pegmatite.

The minimum Li concentration of a granitic melt required for crystalizing spodumene can be estimated by several approaches. The average Li concentration in albite-spodumene pegmatite from the AUPP ranges between 5000 and 10000 ppm (Göd, 1989; Mali, 2004 and references therein), in good agreement with the relatively homogeneous concentration of ~7000 ppm Li proposed for several occurrences of Li-bearing pegmatite (Stewart, 1978). Our largest measured concentration (7420 ppm; Table 2) is compatible with these estimates. Laboratory experiments yield similar results. The eutectic composition in the system albite-orthoclase-quartz-spodumene-$H_2O$ corresponds to ~10000 ppm Li, constraining the minimum Li concentration needed for crystallizing albite-spodumene pegmatite to this value (London, 2008). In contrast, the solubility of Li in a granitic melt decreases slightly with increasing temperature and ranges between 5000 and 8000 ppm for a temperature of 500-550°C (Maneta et al., 2015 and references therein). Note, however, that crystallization experiments also proved that Li-bearing melts can be supersaturated with Li concentrations reaching more almost 2200 ppm at 500°C (Maneta et al., 2015). Such a supersaturation could explain the local occurrence of spodumene-bearing pegmatite with an unusually high Li concentration (e.g. Potter et al., 2009). Without evidence for Li supersaturation in the AUPP pegmatite bodies, we consider that the minimum concentration required for crystalizing spodumene ranges between 5000-10000 ppm Li.

Figure 11c shows the proportion of crystalized melt (or degree of fractionation) required for attaining concentrations of 5000, 7500 and 10000 ppm Li in the residual melt as a function of the Li concentration in the anatectic melt. Two values of Li concentration in the solid fraction (50 and 100 ppm) are tested, corresponding to the range of average concentration in simple pegmatite, leucogranite and evolved pegmatite. For modest concentrations of 200 to 500 ppm Li in the anatectic melt, a fractionation degree of 91 to 99% is needed to allow spodumene to

crystallize in the residual melt. In contrast, for an anatectic melt containing 1000 ppm Li, the required fractionation degree is comprised between 81 and 91%.

In the AUPP the proportion of simple pegmatite, leucogranite and evolved pegmatite in comparison to albite-spodumene pegmatite is in any case larger than 100 to 1 (Figure 4a). This fact is evidenced by the maps in scale 1:50000 of the Geological Survey of Austria (e.g. Beck-Mannagetta, 1980; Weißenbach & Pistotnik, 2000; Pestal et al., 2009). Even if in these maps only larger pegmatite dikes are indicated, albite-spodumene pegmatite dikes are extremely scarce in comparison to simple pegmatite occurences.

In order to verify the consistency of these estimates, we present a calculation based on the Weinebene deposit (Saualpe-Koralpe Complex) that hosts the largest albite-spodumene pegmatite swarm of the AUPP (Göd, 1989; Knoll et al., 2018). There, 7 dikes with economic potential have an average thickness of 2 m and have been identified over a maximum distance along strike of 1.5 km and a maximum down dip distance of 450 m. This corresponds to total area of 4500 $m^2$ per section perpendicular to the strike direction. Assuming a fractionation degree of 90% or 99% and an extracted melt fraction of 20 vol%, this implies an area of molten metapelite of approximately 0.23 to 2.3 km2. The lower and upper bounds represent melt collection and extraction from an area of 1 km width over a thickness of 270 m and 2.7 km, respectively. Both bounds appear realistic owing to the thermal state of the crust during the Permian event. Notice that this calculation considers the largest albite-spodumene pegmatite deposit of the AUPP and maximum values for the dike down dip depth. This implies that the smaller albite-spodumene pegmatite deposits correspond to smaller estimates of molten area.

### LITHIUM PEGMATITE OF ANATECTIC ORIGIN

#### FROM THE MIGMATITE SOURCE TO THE ALBITE-SPODUMENE PEGMATITE SINK

The interpretation of P-T and geochronological data, the field observations, the geochemical analyses and the quantification from geochemical modeling forms the building stone of a new genetic model for albite-spodumene pegmatite. This model is based on constraints from the AUPP but we postulate that it applies to other Li-bearing pegmatite deposits (see section 4.5.2). The chain of processes involved from the anatectic metasedimentary source to the albite-spodumene pegmatite sink is illustrated on a pressure/depth-temperature diagram (Figure 12b) and a depth-lithium concentration diagram (Figure 12c) and summarized in the following.

The source of lithium is a Li-Al-rich metapelite deriving from a shale. The lithium concentration is larger than 100 ppm, which is three to four times average upper crustal values (Figure 12c). Li concentration is unlikely to be homogeneous at the scale of a metasedimentary unit, which is the consequence of three superimposing factors: the regional distribution of Li-rich shale, local variations of Li concentration in the shale and heterogeneous Li-loss during diagenesis and metamorphism. The Li-Al-rich metapelite is first metamorphosed in the amphibolite facies, allowing the crystallization of staurolite that concentrates Li. The metapelite then experiences partial melting induced by prograde heating up to muscovite dehydration melting, resulting into breakdown of staurolite (Figure 12b). Favourable conditions occur in the upper amphibolite-facies to the granulite facies at temperatures between 660 and 750 °C and 0.6 to 0.9 GPa. Note that staurolite formation and destabilization do not need to occur during the same geodynamic event.

At the onset of melting, staurolite is either stable or metastable. This allows direct and efficient transfer of Li into the melt while staurolite breaks down. In this case, geochemical calculations show that local peaks of Li concentration of a few 1000 ppm in the melt phase can be reached at the onset of anatectic melting. Lithium becomes diluted with ongoing melt production once it is transferred from staurolite to the anatectic melt. The threshold fraction at which the melt phase escapes its solid matrix is therefore a key parameter determining the Li concentration of melt that forms pegmatite. Several processes contribute to the escape of melts containing

between 100 and more than 1000 ppm Li (Figure 12c). In absence of deformation, melt escapes at ~20 vol% and carries ~600 ppm Li if it derives from a very Li-rich protolith and at least 100 ppm in less favorable cases. If melt extraction is assisted by deformation it occurs at about 7 vol%. In the most favorable case, the escaping melt contains up to several thousand ppm Li while under less favorable assumptions with minimal Li values in the protolith, the Li concentration at melt escape reaches 500 ppm Li. We consider escape of less than 3 vol% fraction melt as proposed by Stewart (1978) as mechanically impossible even if it can contain a few 1000 ppm Li. However, the addition of immobile low-fraction Li-rich melt into a melt that already escaped is possible since ascending melts can react with the rocks they flow through. Depending on the Li concentration in the protolith, melt integration could yield enriched melts with between 120 and 2000 ppm Li.

We suggest that melt escape occurs as ascending pulses (see Plunder et al., 2022) with variable Li concentrations depending on the melt extraction processes. For example, escape of melt at 7 vol% shortly after the staurolite-breakdown reaction yields a first pulse of Li-rich melt. Once the migmatite is depleted in Li, the following pulses forms after further melt production are most likely Li-poor. Alternatively, once low-fraction Li-rich melt are integrating in the first ascending melt pulse, the next pulses cannot incorporate much Li anymore. This process together with the heterogeneity of the Li concentration in the protolith might be part of the explanation why albite-spodumene pegmatite do not occur in every field of the AUPP. Once melt migration initiates, the ascend through the crust is most likely buoyancy driven. We suggest that upward migration happens through a combination of channelized flow through fractures and pervasive flow through a porous matrix.

Peraluminous simple pegmatite, leucogranite, evolved pegmatite and albite-spodumene pegmatite crystallize from those melt (Figure 12b, c). Fractional crystallization occurs concurrently with melt ascend and is controlled by the crystallization of quartz and feldspar. This enriches the ascending residual melt in Li and other incompatible elements (Be, Sn, Nb and Ta) that enventually crystallizes as evolved pegmatite and albite-spodumene pegmatite. Locally the most residual melts reach a threshold Li concentration of 5000 to 10000 ppm, allowing the crystallization of spodumene. Mass-balance calculations show that for initial concentrations of 200 to 500 ppm Li in the anatectic melt, a fractionation degree of 91 to 99% is needed in order to reach concentrations suitable for crystallizing to albite-spodumene pegmatite. For an initial concentration of 1000 ppm Li in the anatectic melt, the fractionation degree lies between 81 and 91%.

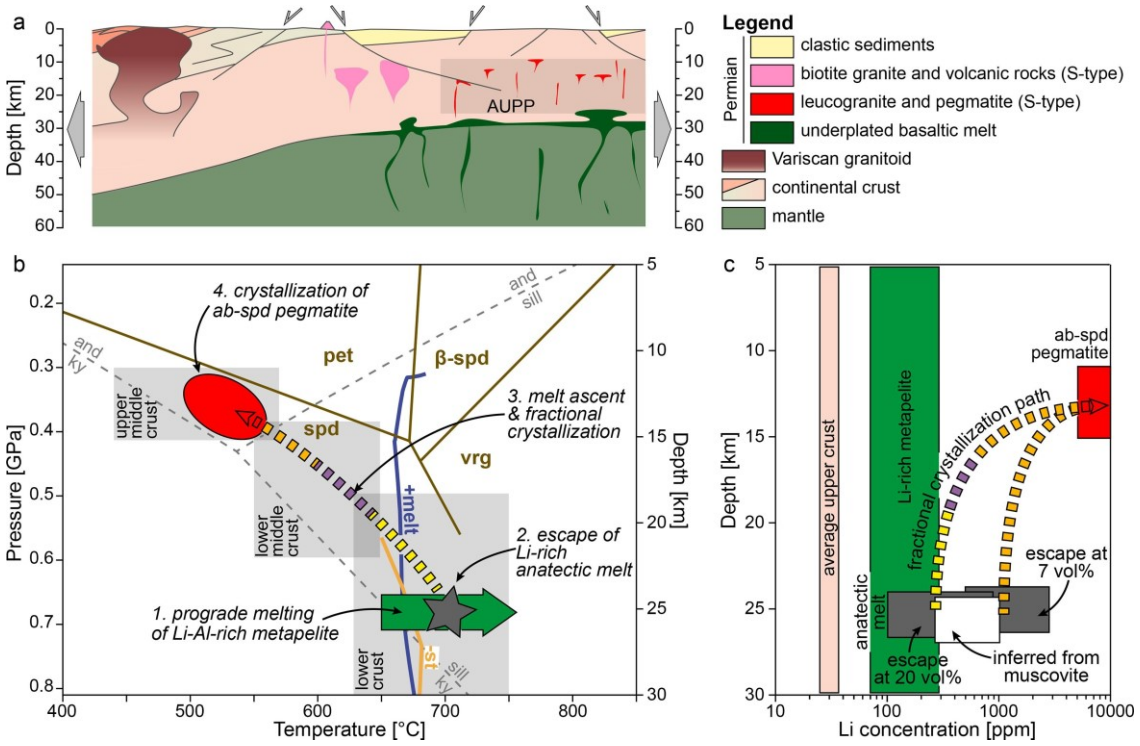


*Figure 12. a. Position of the Austroalpine Unit Pegmatite Province (AUPP) within the Adria continental crust during Permian lithospheric extension. Note that the Permian Event and the formation of the AUPP unambiguously postdates the Variscan Orogeny and related granite emplacement. b. The main processes of the genetic model placed on a pressure-temperature diagram: 1. Prograde melting of Li-Al-rich metapelite in the lower crust. 2. Escape of Li-rich anatectic melt from the migmatite of the lower crust. 3. Ascent of the melt through the lower middle crust and progressive fractional crystallization. 4. Crystallization of residual melt as albite-spodumene pegmatite in the upper middle crust. The star and the ellipse respectively represent the estimated conditions of melt escape and crystallization of albite-spodumene pegmatite. The colored dashed line represents the inferred range of melt crystallization conditions and is not the P-T path of ascending melt. Yellow, violet and orange represent simple pegmatite, leucogranite and evolved pegmatite respectively. The brown lines indicate the reactions between the main Li-aluminosilicates of pegmatite (London, 1984, spd: spodumene, β-spd: β-spodumene, vrg: virgilite, pet: petalite). The grey dashed lines indicate the aluminosilicate fields calculated with the database of Holland & Powell (2011). The blue and orange lines respectively indicate the position of the solidus and staurolite-out reactions represented on Figure 10. The three investigated crustal levels are indicated by grey rectangles. Depth is calculated assuming lithostatic pressure and a constant crustal density of 2750 kg/m$^3$. c. Postulated evolution of anatectic melt concentration during ascent. The light rose and green rectangles indicate concentrations of the protolith. Average upper crustal values are taken from Rudnick & Gao (2003) and Teng et al. (2004). The dark grey rectangles correspond to calculated concentrations for melt escape at 7 and 20 vol% respectively. The white rectangle corresponds to concentrations inferred from the magmatic muscovite in migmatite. The colored dashed line represents the inferred concentrations of melt during ascent. Yellow, violet and orange represent simple pegmatite, leucogranite and evolved pegmatite respectively. The red rectangle indicates concentration in albite-spodumene pegmatite.*

### COMPARISON WITH THE FERTILE GRANITE MODEL

Since melting of staurolite-bearing metapelite occurs at relatively low temperatures, at least below the biotite dehydration melting reaction, Li is the only rare element that is transfered in large amounts into the anatectic melt. The transfer mechanism where a solid phase of a metasediment naturally enriched in a rare element delivers this rare element to an anatectic melt while it breaks down has already been postulated for beryl-bearing pegmatite (London, 2018). In this case, the melt is enriched in Be due to breakdown of cordierite, leading to Be saturation of the granitic pegmatite magma (Evensen et al., 1999). It is likely that a similar process happens for Li in destabilizing cordierite or biotite since both theses minerals are important Li hosts, just after staurolite (Dutrow et al., 1986). Important side effects of the

proposed transfer mechanism must be emphasized. It can happen only once until total destabilization of the rare element-bearing mineral, probably in a rather narrow pressure and/or temperature window. This window corresponds to the conditions at which the host mineral and melt are in equilibrium together or the host phase is still metastable at the onset of melting. Since this transfer mechanism is only valid for one pair of rare element and host mineral, it is unlikely that transfer of a broad spectrum of rare elements occurs at the same time.

Pegmatite with a large spectrum of rare elements could derive from fertile granite intrusions or anatectic melts formed above the temperature of biotite dehydration melting while albite-spodumene pegmatite devoid of rare elements other than Li could derive from anatectic melts formed below the temperature of biotite dehydration melting. Thus, is the common mineralogy of most pegmatite types of the AUPP relatively simple, in contrast to pegmatite derived from fertile granite. Hence, the mineralogy of rare element pegmatite derived from anatectic melt is likely to reflect not only the chemistry and mineralogy of the source but also the conditions of melting and the melt forming reactions. In contrast to a homogeneous fertile granitic origin, the Li concentration in anatectic melt is affected by heterogeneities inherited from the protolith or induced by the variable P-T conditions at which melt can escape, by the pulse-like melt extraction and ascent and by variations in fractionation degree. These heterogeneities largely influence the formation of albite-spodumene pegmatite and explain why they do not occur in every lithostratigraphic complex hosting pegmatite.

In both genetic models, fractional crystallization during melt ascent over several km plays a major role. Buoyancy is also considered as the main migration driving force for melts derived from fertile granite (Černý, 1991b) as well as anatectic melts. Without fractional crystallization, it is unlikely that the Li concentration in melt, irrespective of its origin, reaches the threshold required for crystallization of spodumene. Estimations of the fractionation degree for the albite-spodumene pegmatite of the AUPP is however in the lower bound of the fractionation degrees determined for rare element pegmatite or even below it (London 2008; Hulsbosch et al., 2014; London, 2018; Chakraborty & Upadhyay, 2020). This is a direct consequence of the potentially high Li concentration in anatectic melt. It also implies that anatectic melts can be more fertile than granite-derived melts if their formation is associated to direct and efficient transfer of rare elements. The difference in fractionation degree also explains why the muscovite trace elements analyses from albite-spodumene pegmatite of the AUPP do not plot at the highly fractionated end of the classical classification plots (Černý & Burt, 1984; Figure 9) since those classifications were established from data of granite-derived pegmatites. This implies this classification may be therefore misleading for exploration of rare elements pegmatites deriving from anatectic melts.

### Comparison to other Li-rich pegmatite occurences with a proposed anatectic origin

As summarized in Bradley et al. (2017) spodumene bearing pegmatite of the LCT family have formed since the Mesoarchean but show some variations during the long-term geodynamic evolution of the Earth. While the Archean examples include large complex bodies (e.g. Tanco pegmatite, Stilling et al., 2006) derived from metaaluminous melts, the younger ones are mostly peraluminous. They frequently correlate with times of collisional orogeny and supercontinent assembly, especially for the Phanerozoic record where evidence regarding the geodynamic is better preserved. Generally, they appear in orogenic zones, but only a few are syn-collisional, whereas most are late- to post-collisional and are related to extensional processes or large strike-slip fault systems (e.g. Zagorsky et al., 2014). Even most syn-collisional examples are related to major extensional structures such as those in the Himalaya, which appear together with (leuco)-granite along the South Tibetan Detachment (e.g. Liu et al., 2020).

Many Li-rich pegmatite swarms show spatial and genetic relationships to contemporaneous large fertile granitic plutons (e.g. London, 2008; Liu et al., 2020). However, in several cases such plutons are not present in the surrounding geology (e.g. Lv et al., 2021), or do not match to the timing of pegmatite emplacement (Zagorsky et al., 2014 and references therein). In fact, recently

detailed geochronology revealed that in several cases there is an age gap of tens of millions of years between the young pegmatite dikes and spatially associated old plutons (Zagorsky, 2009; Fei et al., 2020). In the past, missing surface evidence has generally been interpreted to indicate that an unexposed pluton of the same age as the pegmatite must exist at depth.

In recent years, an alternative anatectic origin, compatible with the model presented in this study, has been suggested for the pegmatite-forming melt of several LCT pegmatite occurrences. This includes the Laxfordian bodies (Scotland, Shaw et al., 2016), several bodies of the Moldanubian domain (Czech Republic, Melleton et al., 2012; Dill, 2015; Dill, 2016), the Mt. Mica pegmatite of the Oxford County field (Maine, USA, Simmons, 1995; Simmons et al., 2016; Webber et al., 2019), Pegmatites of the Leinster region (Ireland, Barros & Menuge, 2016; Kaeter et al., 2018; Barros et al., 2020;), the Chinese Altai bodies (China, Lv et al., 2021) and bodies of the Songpan-Garze Fold Belt (China, Fei et al., 2020). Additionally, an anatectic source was proposed for the Sveconorwegian Pegmatite Province in Norway belonging to the NYF family (Müller et al., 2017). The main features of these Li-rich pegmatite examples are presented in table 7. Note that many studies that do not explicitly mention an anatectic origin are not provided in table 7.

LCT pegmatite dikes and fields for which an anatectic origin has been suggested show striking similarities. With the exception of two older occurrences (Laxfordian pegmatites and pegmatites from the Leinster region), LCT pegmatite swarms related to anatexis are Carboniferous to Triassic and formed in a late orogenic or extensional environment. This environment is compatible with greenschist facies to granulite facies metamorphism along MT-MP to HT-LP gradients, with partial melting located in the lower crust. All LCT pegmatites presented in table 7 are peraluminous but they do not show a large fertile cogenetic and/or contemporaneous granitic pluton. This point is evidenced by field observations, geochronology and various geochemical methods. In contrast, some of them (Chinese Altai bodies, bodies of the Lijiagou area and the AUPP) are associated with simple pegmatite or small leucogranite bodies and all of them are situated in metasediments, sometimes migmatitic. Beside in the AUPP, staurolite in the host rock has also been described for the Chinese Altai bodies (Lv et al., 2021). We however postulate that staurolite in the surrounding metapelite has not been reported in other cases because it is out of the focus for pegmatite studies. The mineralogical composition of all occurences corresponds to typical associations of the LCT-group (Černý & Ercit, 2005). Note that the albite-spodumene pegmatite of the AUPP is in comparison to the other cases mineralogically rather poor. This feature has to be explained by the special conditions of the AUPP. The parent melts formed during the first metamorphic and migmatitisation event in the Al-rich metasediments at comparatively low temperatures, below biotite dehydration melting and breakdown of oxide and phosphate minerals. Therefore, Li is more or less the only mobilized rare element, explaining why the albite-spodumene pegmatite mostly contains minor concentrations of Cs, Ta or Nb.

It could be argued that in the case of the Chinese Altai, Songpan-Garze Fold Belt and maybe in the Central Maine Belt melt formation and pegmatite emplacement also occurred during the first low pressure-high temperature metamorphic imprint, but the melting temperature might have been somewhat higher than in the AUPP, explaining the more complex mineralogy with more cassiterite and columbite-group minerals. In contrast, for the Moldanubian domain, melting of rocks that had already experienced granulite-facies or migmatization is proposed. This implies melting at high temperatures as well as the breakdown of biotite and ore minerals, resulting in an even more complex mineralogy of the individual pegmatite bodies.

Our Li partitioning model shows that after breakdown of staurolite biotite is the Li-richest solid phase in a migmatite derived from an Al-rich pelite. Its dehydration melting is, therefore, likely to produce a second pulse of Li-rich melt. A similar feature could apply to destabilization of cordierite that can also host large concentrations of Li (Dutrow et al., 1986) and Be (Evensen &

London, 2003). Generally, the breakdown of a solid phase enriched in rare elements into an anatectic melt (London, 2018) is a process that deserves more detailed investigation. Future research including modeling the transfer of elements such as F, Be, Cs, Ta, Nb or Sn into anatectic melts is needed for understanding the processes forming rare element pegmatite out of crustal sources. Our model should be a first step in validating the genesis of albite-spodumene pegmatites with an anatectic origin. However, more experimental work has to be carried out for measuring the Li and other rare elements distribution between the solid phases and melt at different pressures, temperatures and melt fractions in well-controlled environments.

## CONCLUSION

Our investigations in the Austroalpine Unit Pegmatite Province yield the following conclusions:

Field observations of Permian crustal profiles over more than 400 km, together with geochronological and geochemical investigations indicate that the migmatite, simple pegmatite, leucogranite, evolved pegmatite and albite-spodumene pegmatite are contemporaneous and cogenetic. They are all associated to Permian lithospheric extension.

The three pegmatite types and leucogranite derived from anatectic melt produced by melting of Al-rich metasediments at temperature conditions up to muscovite dehydration melting and below those of biotite dehydration melting.

Melt segregation in the migmatite and extraction from it was most likely assisted by deformation. Melt ascent through the crust occurred over several km.

Simple pegmatite, leucogranite, fractionated pegmatite and albite-spodumene pegmatite represent consecutive stages of crystallization of the anatectic melt, at progressively shallower crustal levels.

Geochemical investigation indicates continuous fractional crystallization during melt ascent, accompanied by progressive enrichment of Li in the melt.

The Li source for the albite-spodumene pegmatite was a Li-Al-rich metapelite with Li concentrations between 70-270 ppm Li, derived from a shale precursor.

Staurolite is by far the Li-richest phase within the metapelite with concentrations between 367-2973 ppm Li. The Li concentration sequence in the analyzed samples is staurolite > biotite > muscovite > garnet.

This fertile metasediment released significant amounts of Li while it experienced partial melting at upper amphibolite facies conditions for the first time.

The mechanism of Li transfer from the metapelite into the anatectic melt is strongly controlled by the breakdown of staurolite in the presence of melt. This indicates that partial melting initiated in the range between 650-750°C and 0.6-0.8 GPa, i.e. 18-26 km depth.

Efficient melt transfer yielded Li concentration in ascending melt comprised between 200 and 1000 ppm. This range is consistent with the composition of Li-rich large muscovite in migmatite.

For modest concentrations of 200 to 500 ppm Li in the anatectic melt, a fractionation degree of 91 to 99% is needed to allow spodumene to crystallize in the residual melt. For 1000 ppm Li, the required fractionation degree ranges between 81% and 91%.

Albite-spodumene pegmatite was emplaced as residual melt at upper greenschist facies conditions at 12-15 km depth.

Our case study provides the basis of an anatectic model of Li-pegmatite and an alternative explanation for the formation of Li-pegmatite if no fertile parent granite can be identified.

ACKNOWLEDGMENTS

This research was supported financially by the ‘‘Mineral und Rohstoffinitiative’’ of the Bundesministerium für Wissenschaft, Forschung und Wirtschaft (BMWFW). The authors would like to thank Hugh Rice, Jürgen Konzett and Holger Paulick for discussions and review of the manuscript, Peter Onuk for measuring the muscovite samples at the LA ICP-MS, Christian Auer for his support with the SEM, Gerald Schuberth-Hlavec for building the pegmatite database and Richard Göd for his critical and constructive input. The authors also thank Ibrahim Özcan for processing the samples and Ilka Wünsche and Andreas Wunderlich for preparing the thin sections. The authors are grateful for reviews of associate editor Harald Dill and two anonymous reviewers, which improved the quality of the manuscript. Last but not least, a big heartfelt thanks to Caro, Little L and Johann, for their continued support and acceptance, and to Sloba for her motivation and support in all situations, as well as her role as the greatest possible role model.

| Sample | RS014/97 | RS37/99 | RS008/00 | 15R107 b | 15R107 d | RS13/00 | PEG57-2 | 17R21 | 04R45 | |
|---|---|---|---|---|---|---|---|---|---|---|
| Lithologie | micaschist | micaschist | micaschist | migmatite | migmatite | pegmatite | leucogranite | pegmatite | | pegmatite |
| Type | staurolite-bearing | staurolite-bearing | | melanosome | leucosome | simple | | evolved | | albite-spodumene |
| $SiO_2$ | 45,39 | 54,92 | 66,11 | 69,33 | 73,72 | 73,99 | 73,96 | 71,85 | | 77,73 |
| $TiO_2$ | 1,48 | 1,03 | 0,77 | 0,58 | 0,27 | 0,02 | 0,01 | 0,04 | | 0,03 |
| $Al_2O_3$ | 28,94 | 23,46 | 15,91 | 13,81 | 14,50 | 15,37 | 14,93 | 16,10 | | 12,64 |
| $Fe_2O_3$ | 11,07 | 8,70 | 5,58 | 4,68 | 1,95 | 0,97 | 0,91 | 0,91 | | 1,42 |
| MnO | 0,18 | 0,19 | 0,05 | 0,08 | 0,05 | 0,09 | 0,20 | 0,15 | | 0,38 |
| MgO | 2,43 | 2,08 | 2,26 | 1,38 | 0,56 | 0,11 | 0,06 | 0,12 | | 0,13 |
| CaO | 0,49 | 1,28 | 0,50 | 1,12 | 1,57 | 0,82 | 0,37 | 1,41 | | 0,55 |
| $Na_2O$ | 1,46 | 1,54 | 2,52 | 1,86 | 3,83 | 5,97 | 5,06 | 4,35 | | 4,73 |
| $K_2O$ | 5,00 | 3,76 | 2,96 | 3,53 | 2,03 | 1,78 | 3,23 | 4,04 | | 0,65 |
| $P_2O_5$ | 0,22 | 0,16 | 0,21 | 0,15 | 0,04 | 0,16 | 0,34 | 0,13 | | 0,01 |
| LOI | 2,88 | 3,34 | 3,57 | 2,09 | 1,17 | 0,97 | 0,68 | 0,38 | | 0,57 |
| Total | 99,53 | 100,46 | 100,50 | 98,61 | 99,69 | 100,24 | 99,75 | 99,48 | | 98,84 |
| Li | 142 | 156 | 57 | 69 | 37 | 0 | 97 | 59 | | 655 |

*Table 1. Whole-rock geochemical composition measured by TD ICP-MS for selected staurolite-bearing micaschist, garnet micaschist, migmatite, simple pegmatite, leucogranite, evolved pegmatite and albite-spodumene pegmatite samples. Major elements in wt%, Li in ppm, all Fe as Fe2O3, LOI: loss on ignition. Geographic coordinates of sampling locations (SM2) and all whole-rock analyses used in this study (SM3) are provided as supplementary material.*

| Lithology | Sample | Analyzed fraction | Number of analyses | Li concentration (ppm) | | |
|---|---|---|---|---|---|---|
| | | | | minimum | maximum | average |
| staurolite-bearing micaschist | | whole rock | 13 | 68 | 269 | 122 |
| migmatite | | whole rock | 2 | 53 | 108 | 81 |
| simple pegmatite | | whole rock | 5 | 19 | 46 | 34 |
| leucogranite | | whole rock | 5 | 27 | 98 | 70 |
| highly evolved pegmatite | | whole rock | 8 | 40 | 183 | 97 |
| albite-spodumene pegmatite | | whole rock | 4 | 174 | 7420 | - |
| staurolite-bearing micaschist | RS34/01 | staurolite | 6 | 2842 | 2973 | 2938 |
| staurolite-bearing micaschist | RS34/01 | biotite | 3 | 830 | 907 | 868 |
| staurolite-bearing micaschist | RS34/01 | garnet | 4 | 44 | 110 | 64 |
| staurolite-bearing micaschist | RS34/01 | muscovite | 5 | 86 | 129 | 108 |
| staurolite-bearing micaschist | RS34/01 | quartz | 2 | 3 | 5 | 4 |
| staurolite-bearing micaschist | RS14/97 | staurolite | 30 | 571 | 839 | 722 |
| staurolite-bearing micaschist | RS14/97 | biotite | 12 | 115 | 169 | 149 |
| staurolite-bearing micaschist | RS14/97 | garnet | 17 | 20 | 47 | 31 |
| staurolite-bearing micaschist | RS36/99 | staurolite | 4 | 1219 | 1745 | 1486 |
| staurolite-bearing micaschist | RS36/99 | garnet | 4 | 24 | 47 | 36 |
| staurolite-bearing micaschist | RS36/99 | muscovite | 4 | 105 | 200 | 150 |
| staurolite-bearing micaschist | RS28/01 | staurolite | 8 | 367 | 540 | 456 |
| staurolite-bearing micaschist | RS28/01 | biotite | 8 | 128 | 148 | 140 |
| staurolite-bearing micaschist | RS28/01 | muscovite | 5 | 6 | 9 | 8 |
| staurolite-bearing micaschist | 16R42 | staurolite | 10 | 630 | 1389 | 922 |
| staurolite-bearing micaschist | 16R42 | garnet | 8 | 31 | 51 | 42 |
| staurolite-bearing micaschist | 16R42 | muscovite | 5 | 47 | 168 | 74 |
| garnet-bearing micaschist | 16R57 | biotite | 5 | 180 | 392 | 301 |
| garnet-bearing micaschist | 16R57 | garnet | 8 | 15 | 28 | 22 |
| garnet-bearing micaschist | 16R57 | muscovite | 6 | 71 | 106 | 92 |
| garnet-bearing micaschist | 16R57 | quartz | 2 | 4 | 5 | 5 |

*Table 2. Measured minimum (min.), maximum (max.) and average (avg.) Li concentrations in whole-rock and mineral analyses of staurolite-bearing micaschist, garnet micaschist, migmatite, simple pegmatite, leucogranite, evolved pegmatite and albite-spodumene pegmatite. Whole-rock concentrations measured by TD ICP-MS and mineral concentrations measured by LA ICP-MS. Geographic coordinates of sampling locations are provided as supplementary material (SM2).*

| Sample | 15R107d | | 15R107d | | 15R108 | | 15R108 | | PEG214 | | PEG214 | | Peg30 | | Peg30 | | UTT7 | | UTT7 | | UTT7 | |
|---|---|---|---|---|---|---|---|---|---|---|---|---|---|---|---|---|---|---|---|---|---|---|
| Lithologie | migmatite | | migmatite | | migmatite | | migmatite | | pegmatite | | pegmatite | | pegmatite | | pegmatite | | pegmatite | | leucogranite | | leucogranite | |
| Type | leucosome | | leucosome | | migmatite | | migmatite | | simple | | simple | | simple | | simple | | simple | | | | | |
| $K_2O$ | 8,77 | | 8,54 | | 8,15 | | 7,95 | | 8,17 | | 8,75 | | 8,82 | | 8,82 | | 8,62 | | 8,90 | | 8,38 | |
| Li | 98 | | 99 | | 99 | | 82 | | 10 | | 13 | | 31 | | 31 | | 35 | | 176 | | 179 | |
| Rb | 316 | | 312 | | 253 | | 263 | | 1117 | | 1154 | | 681 | | 681 | | 660 | | 1090 | | 1043 | |
| Tl | 1,3 | | 1,2 | | 1,2 | | 1,3 | | 5,0 | | 4,7 | | 3,5 | | 3,5 | | 3,3 | | 5,6 | | 5,1 | |
| K/Rb | 278 | | 273 | | 322 | | 302 | | 73 | | 76 | | 130 | | 130 | | 131 | | 82 | | 80 | |

| Sample | Peg53 | | Peg53 | | PEG36 | | PEG36 | | 15R14 | | 15R14 | | PEG200 | | PEG200 | | PEG73 | | PEG73 | | PEG73 | |
|---|---|---|---|---|---|---|---|---|---|---|---|---|---|---|---|---|---|---|---|---|---|---|
| Lithologie | leucogranite | | leucogranite | | pegmatite | | pegmatite | | pegmatite | | pegmatite | | pegmatite | | pegmatite | | pegmatite | | pegmatite | | pegmatite | |
| Type | | | | | evolved | | evolved | | evolved | | evolved | | albite-spodumene | | albite-spodumene | | albite-spodumene | | albite-spodumene | | albite-spodumene | |
| $K_2O$ | 8,55 | | 8,72 | | 8,67 | | 8,36 | | 8,50 | | 8,51 | | 8,81 | | 8,76 | | 8,82 | | 8,32 | | | |
| Li | 67 | | 36 | | 104 | | 107 | | 111 | | 118 | | 372 | | 424 | | 1316 | | 891 | | | |
| Rb | 1158 | | 1116 | | 309 | | 327 | | 518 | | 493 | | 1892 | | 1983 | | 582 | | 577 | | | |
| Tl | 5,8 | | 5,5 | | 1,4 | | 1,3 | | 1,5 | | 1,4 | | 17,9 | | 17,8 | | 2,1 | | 2,0 | | | |
| K/Rb | 74 | | 78 | | 281 | | 256 | | 164 | | 173 | | 47 | | 44 | | 151 | | 144 | | | |

*Table 3. Selected K2O, Li, Rb and Tl concentrations and K/Rb ratio of muscovite from migmatite, simple pegmatite, leucogranite, evolved pegmatite and albite-spodumene pegmatite samples measured by LA ICP-MS. Geographic coordinates of sampling locations (SM2) and all muscovite analyses used in this study (SM4) are provided as supplementary material.*

| | staurolite | | | | | | biotite | | | | | |
|---|---|---|---|---|---|---|---|---|---|---|---|---|
| Sample | 16R42 | 16R42 | RS28/01 | RS34/01 | RS34/01 | RS36/99 | 16R57 | 16R57 | RS28/01 | RS28/01 | RS34/01 | RS34/01 |
| Lithology | micaschist | micaschist | micaschist | micaschist | micaschist | micaschist | micaschist | micaschist | micaschist | micaschist | micaschist | micaschist |
| Type | staurolite-bearing | staurolite-bearing | staurolite-bearing | staurolite-bearing | staurolite-bearing | staurolite-bearing | | | staurolite-bearing | staurolite-bearing | staurolite-bearing | staurolite-bearing |
| $SiO_2$ | 27,81 | 27,78 | 27,07 | 26,97 | 27,26 | 27,99 | 37,45 | 37,78 | 34,67 | 34,67 | 34,47 | 34,75 |
| $TiO_2$ | 0,51 | 0,58 | 0,71 | 0,59 | 0,48 | 0,54 | 1,68 | 1,79 | 1,39 | 1,45 | 1,63 | 1,52 |
| $Al_2O_3$ | 55,21 | 54,76 | 54,74 | 55,25 | 55,60 | 55,23 | 17,72 | 17,61 | 19,78 | 19,30 | 19,12 | 19,06 |
| $Cr_2O_3$ | 0,00 | 0,00 | 0,00 | 0,00 | 0,00 | 0,00 | 0,04 | 0,04 | 0,02 | 0,03 | 0,02 | 0,02 |
| FeO | 12,51 | 13,33 | 14,20 | 12,42 | 12,25 | 12,07 | 16,27 | 15,74 | 21,60 | 22,17 | 21,01 | 21,28 |
| MnO | 0,01 | 0,03 | 0,24 | 0,18 | 0,19 | 0,05 | 0,06 | 0,03 | 0,07 | 0,09 | 0,07 | 0,05 |
| MgO | 1,36 | 1,66 | 1,15 | 0,98 | 0,99 | 1,50 | 11,63 | 11,52 | 8,25 | 8,15 | 9,32 | 9,12 |
| ZnO | 0,29 | 0,37 | 0,15 | 0,76 | 0,57 | 0,57 | na | na | na | na | na | na |
| CaO | 0,01 | 0,00 | 0,00 | 0,00 | 0,01 | 0,00 | 0,12 | 0,14 | 0,00 | 0,00 | 0,00 | 0,01 |
| $Na_2O$ | 0,01 | 0,00 | 0,00 | 0,02 | 0,01 | 0,00 | 0,14 | 0,14 | 0,36 | 0,32 | 0,24 | 0,18 |
| $K_2O$ | 0,00 | 0,00 | 0,01 | 0,00 | 0,00 | 0,00 | 7,85 | 7,71 | 8,31 | 8,26 | 8,29 | 8,52 |
| Total | 97,72 | 98,49 | 98,271 | 97,158 | 97,363 | 97,94 | 92,97 | 92,50 | 94,46 | 94,44 | 94,16 | 94,52 |
| Li | 1154 | 726 | 463 | 2842 | 3022 | 1741 | 352 | 180 | 144 | 132 | 866 | 907 |

| | muscovite | | | | | | garnet | | | | | |
|---|---|---|---|---|---|---|---|---|---|---|---|---|
| Sample | 16R42 | 16R57 | RS28/01 | RS34/01 | RS34/01 | RS36/99 | 16R42 | 16R42 | 16R57 | RS34/01 | RS36/99 | RS36/99 |
| Lithology | micaschist | micaschist | micaschist | micaschist | micaschist | micaschist | micaschist | micaschist | micaschist | micaschist | micaschist | micaschist |
| Type | staurolite-bearing | | staurolite-bearing | staurolite-bearing | staurolite-bearing | staurolite-bearing | staurolite-bearing | staurolite-bearing | | staurolite-bearing | staurolite-bearing | staurolite-bearing |
| $SiO_2$ | 45,03 | 45,68 | 47,52 | 45,17 | 45,65 | 46,89 | 37,14 | 36,98 | 37,10 | 36,41 | 36,79 | 37,64 |
| $TiO_2$ | 0,68 | 0,95 | 0,27 | 0,53 | 0,48 | 0,49 | 0,04 | 0,05 | 0,00 | 0,04 | 0,09 | 0,12 |
| $Al_2O_3$ | 36,33 | 33,63 | 34,40 | 36,04 | 36,12 | 33,50 | 21,37 | 21,05 | 21,16 | 20,84 | 20,98 | 21,49 |
| $Cr_2O_3$ | 0,01 | 0,01 | 0,02 | 0,02 | 0,03 | 0,01 | 0,04 | 0,03 | 0,02 | 0,01 | 0,02 | 0,04 |
| FeO | 0,89 | 1,52 | 1,00 | 0,87 | 0,90 | 1,23 | 32,65 | 35,72 | 31,76 | 31,11 | 30,74 | 31,08 |
| MnO | 0,01 | 0,00 | 0,00 | 0,00 | 0,00 | 0,01 | 0,21 | 1,95 | 4,80 | 3,05 | 4,47 | 0,44 |
| MgO | 0,53 | 1,48 | 0,96 | 0,52 | 0,53 | 1,75 | 2,95 | 1,90 | 3,25 | 1,52 | 1,11 | 4,49 |
| CaO | 0,00 | 0,00 | 0,00 | 0,00 | 0,00 | 0,00 | 5,98 | 3,21 | 2,43 | 6,51 | 6,33 | 5,20 |
| $Na_2O$ | 1,25 | 0,91 | 1,38 | 1,27 | 1,19 | 1,17 | na | na | na | na | na | na |
| $K_2O$ | 9,60 | 9,98 | 8,91 | 9,63 | 9,63 | 9,35 | na | na | na | na | na | na |
| Total | 94,33 | 94,17 | 94,46 | 94,04 | 94,52 | 94,39 | 100,51 | 100,98 | 100,65 | 99,68 | 100,69 | 100,60 |
| Li | 56 | 94 | 9 | 122 | 86 | 155 | 43 | 50 | 26 | 54 | 47 | 45 |

*Table 4. Selected major elements and Li analyses of staurolite, biotite, muscovite and garnet from metapelite. Major elements measured by EPMA, Li concentration measured by LA ICP-MS. Major elements in wt%, Li in ppm, all Fe as FeO. Geographic coordinates of sampling locations (SM2) and all mineral analyses from metapelite used in this study (SM5) are provided as supplementary material.*

| Mineral pair | | Partitioning coefficient | Reference |
|---|---|---|---|
| biotite/staurolite | RS04/01 | | 0,30 measured, this study |
| biotite/staurolite | RS14/97 | | 0,31 measured, this study |
| biotite/staurolite | RS28/01 | | 0,21 measured, this study |
| biotite/staurolite | model | | 0,27 average, this study |
| biotite/muscovite | RS34/01 | | 8,03 measured, this study |
| biotite/muscovite | RS28/01 | | 17,84 measured, this study |
| biotite/muscovite | 16R57 | | 3,26 measured, this study |
| biotite/muscovite | model, preferred set of partitioning coefficients | | 9,70 average, this study |
| biotite/muscovite | model, alternative set of partitioning coefficients | | 4,50 average of literature values |
| biotite/garnet | RS34/01 | | 13,52 measured, this study |
| biotite/garnet | RS14/97 | | 4,81 measured, this study |
| biotite/garnet | 16R57 | | 13,80 measured, this study |
| biotite/garnet | model, preferred set of partitioning coefficients | | 11,0 average, this study |
| biotite/garnet | model, alternative set of partitioning coefficients | | 5,15 Dutrow et al. (1987) |
| biotite/quartz | RS34/01 | | 217 measured, this study |
| biotite/quartz | 16R57 | | 60,16 measured, this study |
| biotite/quartz | model | | 140 average, this study |
| biotite/melt | model | | 1,64 Icenhower & London (1995) |
| biotite/alkali feldspar | model | | 25 Bea et al. (1994) |
| biotite/plagioclase | model | | 63 Bea et al. (1994) |
| biotite/sillimanite | model | | 140 estimated, this study |

*Table 5. Partitioning coefficients, with values calculated for each sample and values used in the model. Geographic coordinates of sampling locations are provided as supplementary material (SM2).*

| Melting model | Pressure (kbar) | (Meta)stability of staurolite at the onset of melting | peak | at escape (dynamic case) | at escape (static case) | integration of low fraction melt |
|---|---|---|---|---|---|---|
| | | | 4-5 melt vol% | 7 melt vol% | 20 melt vol% | 20 to min vol% |
| preferred set of partitioning coefficients | | | | | | |
| equilibrium partitioning | 6 | no | 157-269-605 | 145-248-559 | 112-192-432 | 135-231-520 |
| equilibrium partitioning | 7 | yes | 258-443-996 | 241-414-931 | 165-283-637 | 214-368-827 |
| disequilibrium partitioning | 6 | yes | 534-916-2062 | 407-698-1570 | 148-254-572 | 339-581-1308 |
| disequilibrium partitioning | 7 | yes | 949-1627-3660 | 714-1224-2755 | 192-329-739 | 508-870-1958 |
| alternative set of partitioning coefficients | | | | | | |
| equilibrium partitioning | 6 | no | 132-226-509 | 126-215-485 | 108-185-416 | 120-205-462 |
| equilibrium partitioning | 7 | yes | 175-301-676 | 170-292-657 | 142-244-549 | 160-275-618 |
| disequilibrium partitioning | 6 | yes | 477-818-1840 | 368-630-1418 | 145-249-560 | 309-530-1191 |
| disequilibrium partitioning | 7 | yes | 753-1290-2903 | 573-982-2210 | 172-296-665 | 414-710-1597 |

*Table 6. Li concentration in the melt calculated with the Li partitioning model.*

*(Continuation of Table 7 is on the following page)*

| Location | Occurence | Geological Unit | Geodynamic setting | Conditions of pegmatite formation/emplacement | Age of pegmatite |
|---|---|---|---|---|---|
| Scotland | Laxfordian pegmatites | Laxfordian terrane | Laxfordian orogeny, compression and crustal thickening | amphibolite-facies metamorphism | Paleoproterozoic |
| Ireland | Pegmatites of the Leinster region | Tullow Lowlands Unit, East Carlow Deformation Zone | | lower greenschist facies | Silurian to Devonian |
| Czech Republic | Variscan Pegmatite provinces | Moldanubian Domain | Variscan orogeny, orogenic collapse | granulite-facies metamorphism | Carboniferous (late Variscan) |
| Maine | Oxford County Pegmatite Field | Central Maine Belt, Appalachians | lithospheric extension | greenschist-upper amphibolite facies | Permian |
| China | Chinese Altai bodies | Central Asian Orogenic Belt | post-accretion extension | amphibolite to granulite-facies metamorphism | Permian |
| China | Bodies of the Lijiagou area | Songpan-Garze Fold Belt | lithospheric extension and decompression melting | M to LP-HT metamorphism | Triassic |
| Austria | Austroalpine Unit Pegmatite Province | Austroalpine Unit | Permian Event, lithospheric extension, magmatic underplating | LP-HT greenschist to granulite facies metamorphism; prograde metamorphism and migmatisation of Al-rich metasediments | Permian, Early Triassic |

*Table 7. Selected albite-spodumene pegmatite occurences with an assumed anatectic origin*

| Location | Main pegmatite index minerals | Host-rock | Anatectic origin inferred from | Comment | References |
|---|---|---|---|---|---|
| Scotland | biotite, pyrite, allanite | different types of metasedimentary rocks, metagabbro and amphibolite | missing contemporaneous potential parental pluton with a suitable geochemical signature; spatial relationship to Al-rich metasediments | | Goodenough et al., 2013; Shaw et al., 2016 |
| Ireland | muscovite, spodumene, spessartine, fluorapatite, beryl, columbite group minerals, cassiterite | partly metamorphosed sedimentary, volcanic rocks and igneous intrusions | missing contemporaneous potential parental pluton with a suitable geochemical signature | | Barros & Menuge, 2016; Kaeter et al., 2018; Barros et al., 2020; |
| Czech Republic | biotite, columbite-group minerals, cassiterite, amblygonite, petalite, lepidolite, minor (secondary) spodumene, elbaite | granitic, gneissic and metasedimentary rocks | no systematic geochemical and isotopic compatibility with the Central and South Bohemian batholiths | | Janoušek & Holub, 2007; Melleton et al., 2012; Ertl et al., 2012; Dill, 2016; Dill, 2018; Dill, 2019 |
| Maine | muscovite, garnet, schorl, beryl, hydroxylherderite, columbite-group minerals, cassiterite, elbaite, lepidolite, spodumene, pollucite | different types of metasedimentary rocks, migmatite | missing contemporaneous potential parental pluton with a suitable geochemical signature; geochemical and textural affinity to surrounding migmatite | | Simmons, 1995; Simmons et al., 2016; Webber et al., 2019 |
| China | muscovite, biotite, spodumene, beryl, monazite, xenotime, columbite-tantalite, apatite, lepidolite, titanite, monazite, spessartine, schorl, cassiterite, zircon | micaschist (partly staurolite bearing), gneiss, granite | missing contemporaneous potential parental pluton with a suitable geochemical signature; occurence of migmatites | genetically linked leucogranite bodies | Lv et al., 2021 |
| China | muscovite, biotite, spodumene, beryl, monazite, xenotime, columbite-tantalite, apatite, beryl, lepidolite, titanite, monazite, spinel, fergusonite, lepidolite, cassiterite, tourmaline | different types of metasedimentary rocks, gneiss, felsic plutons | Hf-isotopy argues against a cogenetic origin with nearby granitic bodies | genetically linked leucogranite and two-mica granites bodies; independent pegmatite-forming event, with melts deriving from staurolite-bearing assemblages formed in the contact aureole of the preexisting granite intrusions | Fei et al., 2020 |
| Austria | muscovite, tourmaline, spodumene, beryl; rare and small grains of cassiterite, columbite-group minerals | micaschist (partly staurolite bearing), paragneiss, amphibolite, marble, quartzite and eclogite | missing contemporaneous potential parental pluton with a suitable geochemical signature; spatial, temporal and geochemical relation to Li-Al-rich metasediments, partly migmatitic; staurolite as main Li-host in the metasediment | small genetically linked leucogranite bodies | Knoll et al., 2018; Konzett et al., 2018; Krenn et al., 2022; Keyser et al., submitted; this study |

## REFERENCES

Allègre, C. J., Schneider, S. H., 2008. The evolution of the Earth, in: Evolution, University of Chicago Press., Chicago. pp. 72-84. Ambrose, H., Kendall, A., 2020. Understanding the future of lithium: Part 1, resource model. Journal of Industrial Ecology. 24(1), 80-89.

Baker, D. R., Vaillancourt, J.,1995. The low viscosities of F+ H2O-bearing granitic melts and implications for melt extraction and transport. Earth and Planetary Science Letters. 132(1-4), 199-211.

Barros, R., & Menuge, J. F. (2016). The origin of spodumene pegmatites associated with the Leinster Granite in southeast Ireland. The Canadian Mineralogist, 54(4), 847-862.

Barros, R., Kaeter, D., Menuge, J. F., & Škoda, R. (2020). Controls on chemical evolution and rare element enrichment in crystallising albite-spodumene pegmatite and wallrocks: Constraints from mineral chemistry. Lithos, 352, 105289.

Bartels, A., Vetere, F., Holtz, F., Behrens, H., Linnen, R. L., 2011. Viscosity of flux-rich pegmatitic melts. Contributions to Mineralogy and Petrology. 162(1), 51-60.

Bartels, A., Behrens, H., Holtz, F., Schmidt, B. C., 2015. The effect of lithium on the viscosity of pegmatite forming liquids. Chemical Geology. 410, 1-11.

Bea, F., Pereira, M. D., Stroh, A., 1994. Mineral/leucosome trace-element partitioning in a peraluminous migmatite (a laser ablation-ICP-MS study). Chemical Geology. 117(1-4), 291-312.

Bea, F., 1996. Controls on the trace element composition of crustal melts. Transactions of the Royal Society of Edinburgh-Earth Sciences. 87(1), 33-42.

Beck-Mannagetta, P., 1980. Wolfsberg 1:50.000. Verlag der Geologischen Bundesanstalt (GBA). Wien, in: Geologische Karte der Republik Österreich 1:50.000. pp. 188.

Bowell, R. J., Lagos, L., de los Hoyos, C. R., Declercq, J., 2020. Classification and characteristics of natural lithium resources. Elements: An International Magazine of Mineralogy, Geochemistry, and Petrology. 16(4), 259-264.

Bradley, D. C., McCauley, A. D., & Stillings, L. L. (2017). Mineral-deposit model for lithium-cesium-tantalum pegmatites (No. 2010-5070-O). US Geological Survey.

Brown, M., 2004. The mechanism of melt extraction from lower continental crust of orogens. Earth and Environmental Science Transactions of the Royal Society of Edinburgh. 95(1-2), 35-48.

Brown, M., 2007. Crustal melting and melt extraction, ascent and emplacement in orogens: mechanisms and consequences. Journal of the Geological Society. 164(4), 709-730.

Brown, M., 2010. The spatial and temporal patterning of the deep crust and implications for the process of melt extraction. Philosophical Transactions of the Royal Society A: Mathematical, Physical and Engineering Sciences. 368(1910), 11-51.

Carlson, W.D., Pattison, D.R., Caddick, M.J., 2015. Beyond the equilibrium paradigm: How consideration of kinetics enhances metamorphic interpretation. American Mineralogist, 100(8-9), 1659-1667.

Censi, P., Inguaggiato, C., Chiavetta, S., Schembri, C., Sposito, F., Censi, V., Zuddas, P., 2017. The behaviour of zirconium, hafnium and rare earth elements during the crystallisation of halite and other salt minerals. Chemical Geology. 453, 80-91.

Černý, P., Burt, D.M., 1984. Paragenesis, crystallochemical characteristics, and geochemical evolution in micas in granite pegmatite, in: Bailey, S.W., (Eds.), Micas Reviews in Mineralogy 13, Mineralogical Society of America, Washington. pp. 257–297.

Černý, P., 1991a. Rare-element granitic pegmatites. Part I: Anatomy and internal evolution of pegmatite deposits. Geoscience Canada. 18(2), 49-67.

Černý, P., 1991b. Rare-element Granitic Pegmatites. Part II: Regional to Global evironments and Petrogenesis. Geoscience Canada. 18(2), 68–81.

Černý, P., & Ercit, T. S. (2005). The classification of granitic pegmatites revisited. The Canadian Mineralogist, 43(6).

Černý, P., Halden, N.M., Ferreira, K., Meintzer, R.E., Brisbin, W.C., Chackowsky, L.E., Corkery, M.T., Longstaffe, F.J., Trueman, D.L., 2012a. Extreme fractionation and deformation of the leucogranite-pegmatite suite at Red Cross Lake, Manitoba, Canada. II. Petrology of the leucogranite and pegmatite. Canadian Mineralogist. 50, 1807–1822.

Černý, P., London, D., & Novák, M.,2012b. Granitic pegmatites as reflections of their sources. Elements, 8(4), 289-294.

Chakraborty, T., Upadhyay, D., 2020. The geochemical differentiation of S-type pegmatites: constraints from major–trace element and Li–B isotopic composition of muscovite and tourmaline. Contributions to Mineralogy and Petrology. 175, 1-25.

Chan, L. H., Leeman, W. P., Plank, T., 2006. Lithium isotopic composition of marine sediments. Geochemistry, Geophysics, Geosystems. 7(6).

Chopin, C., Goffe, B., Ungaretti, L., Oberti, R., 2003. Magnesiostaurolite and zincostaurolite: mineral description with a petrogenetic and crystal-chemical update. European Journal of Mineralogy. 15(1), 167-176.

Dahl, P. S., Wehn, D. C., Feldmann, S. G., 1993. The systematics of trace-element partitioning between coexisting muscovite and biotite in metamorphic rocks from the Black Hills, South Dakota, USA. Geochimica et Cosmochimica Acta. 57(11), 2487-2505.

Dal Piaz, G.V., 2010. The Italian Alps: a journey across two centuries of Alpine geology (M. Beltrando, A. Peccerillo, M. Mattei, S. Conticelli, & C. Doglioni, Eds.): Journal of the Virtual Explorer, v. 36, doi: 10.3809/jvirtex.2010.00234

Delaney, P. T., Pollard, D. D., 1981. Deformation of host rocks and flow of magma during growth of minette dikes and breccia-bearing intrusions near Ship Rock, New Mexico. USGPO. 1202.

Diella, V., Spalla, M. I., & Tunesi, A., 1992. Contrasting thermomechanical evolutions in the Southalpine metamorphic basement of the Orobic Alps (Central Alps, Italy). Journal of Metamorphic Geology. 10(2), 203-219.

Dill, H.G., 2015. The Hagendorf-Pleystein Pegmatite Province, SE Germany: The center of pegmatites in an ensialic orogen (Modern Approaches in Solid Earth Sciences). Springer, Dortrecht, Heidelberg, London, New York, ISBN-978-3-319-18805-8, 343 pp.

Dill, H.G., 2016. The CMS classification scheme (Chemical composition-Mineral assemblage-Structural geology)-linking geology to mineralogy of pegmatitic and aplitic rocks. Neues Jahrbuch für Mineralogie-Abhandlungen. 193, 231–263.

Dill, H.G., 2018. Geology and chemistry of Variscan-type pegmatite systems (SE Germany) - With special reference to structural and chemical pattern recognition of felsic mobile components in the crust. Ore Geology Reviews. 92, 205-239.

Dill, H.G., 2019. Coupling restites and mobilizates – Geological and litho-chemical investigations of paired belts of calcsilicate fels and quartzite (SE German Basement) - Quo Vadis David London´s pegmatology ?. Ore Geology Reviews. 105, 636-662.

Draganits, E., 1998. Seriengliederung im Kristallin des südlichen Ödenburger Gebirges (Burgenland) und deren Stellung zum Unterostalpin am Alpenostrand. Jahrbuch der Geologischen Bundesanstalt. 141, 113-146.

Dutrow, B. L., Holdaway, M. J., Hinton, R. W., 1986. Lithium in staurolite and its petrologic significance. Contributions to Mineralogy and Petrology. 94(4), 496-506.

Dutrow, B., 1991. The effects of Al and vacancies on Li substitution in iron staurolite: a synthesis approach. American Mineralogist. 76, 42-48.

Eberlei, T., Habler, G., Wegner, W., Schuster, R., Körner, W., Abart, R., Thöni, M., 2015. Rb/Sr isotopic and compositional retentivity of muscovite during deformation. Lithos. 227, 161-178.

Ercit, T. S., Linnen, R. L., Samson, I. M., 2005. REE-enriched granitic pegmatites. Rare-element geochemistry and mineral deposits: Geological Association of Canada. GAC Short Course Notes. 17, 175-199.

Ertl, A., Schuster, R., Hughes, J.M., Ludwig, T. Meyer, H.-P., Finger, F., Dyar, M.D., Ruschel, K., Rossman, G.R., Klötzli, U., Brandstätter, F., Lengauer, Ch.L., Tillmanns, E., 2012. Li-bearing tourmalines in Variscan granitic pegmatites from the Moldanubian nappes, Lower Austria. European Journal of Mineralogy. 24, 695–715.

Evensen J. M., London D., and Wendlandt R. F., 1999. Solubility and stability of beryl in granitic melts. American Mineralogist. 84, 733–745.Evensen, J. M., London, D., 2003. Experimental partitioning of Be, Cs, and other trace elements between cordierite and felsic melt, and the chemical signature of S-type granite. Contributions to Mineralogy and Petrology. 144(6), 739-757.

Ewing, T. A., Hermann, J., Rubatto, D., 2013. The robustness of the Zr-in-rutile and Ti-in-zircon thermometers during high-temperature metamorphism (Ivrea-Verbano Zone, northern Italy). Contributions to Mineralogy and Petrology. 165(4), 757-779.

Feenstra, A., Ockenga, E., Rhede, D., Wiedenbeck, M., 2003. Li-rich zincostaurolite and its decompression-related breakdown products in a diaspore-bearing metabauxite from East Samos (Greece): An EMP and SIMS study. American Mineralogist. 88(5-6), 789-805.

Fei, G., Menuge, J. F., Li, Y., Yang, J., Deng, Y., Chen, C., Yang, Y., Yang, Z., Qin, L., Zheng, L., Tang, W., 2020. Petrogenesis of the Lijiagou spodumene pegmatites in Songpan-Garze Fold Belt, West Sichuan, China: Evidence from geochemistry, zircon, cassiterite and coltan U-Pb geochronology and Hf isotopic compositions. Lithos. 364, 105555.

Frank, N., Kurz, W., He, D., Schuster, R., Dong, Y., Hauzenberger, C., 2019: Detrital U/Pb zircon age distribution in metasedimentary units of the Eastern Alps. EGU General Assembly 2019. Geophysical Research Abstracts. 21: EGU2019-17014-1.

Froitzheim, N., Plašienka, D., Schuster, R., 2008. Alpine tectonics of the Alps and Western Carpathians, in: McCann, T., (Eds.), The Geology of Central Europe Volume 2: Mesozoic and Cenozoic. Geological Society of London, London. pp. 1141–1232.

Gaidies, F., Abart, R., De Capitani, C., Schuster, R., Connolly, J. A. D., Reusser, E., 2006. Characterization of polymetamorphism in the Austroalpine basement east of the Tauern Window using garnet isopleth thermobarometry. Journal of Metamorphic Geology. 24(6), 451-475.

Gaidies, F., Krenn, E., De Capitani, C., Abart, R., 2008a. Coupling forward modelling of garnet growth with monazite geochronology: an application to the Rappold Complex (Austroalpine crystalline basement). Journal of metamorphic Geology. 26(7), 775-793.

Gaidies, F., De Capitani, C., Abart, R., 2008b. THERIA_G: a software program to numerically model prograde garnet growth. Contributions to Mineralogy and Petrology. 155(5), 657-671.

García-Casco, A., Haissen, F., Castro, A., El-Hmidi, H., Torres-Roldan, R. L., Millán, G., 2003. Synthesis of staurolite in melting experiments of a natural metapelite: consequences for the phase relations in low-temperature pelitic migmatites. Journal of Petrology. 44(10), 1727-1757.

Goodenough, K. M., Crowley, Q. G., Krabbendam, M., Parry, S. F., 2013. New U-Pb age constraints for the Laxford Shear Zone, NW Scotland: Evidence for tectono-magmatic processes associated with the formation of a Paleoproterozoic supercontinent. Precambrian Research. 233, 1-19.

Göd, R., 1989. The spodumene deposit at “Weinebene”, Koralpe, Austria. Mineralium Deposita. 24(4), 270-278.

Gruber, A., Pestal, G., Nowotny, A., Schuster, R., 2010. Erläuterungen zur Geologischen Karte der Republik Österreich 1:50.000, Blatt 141 Landeck. 192 p, Geologische Bundesanstalt (Wien).

Habler, G., Thöni, M., 2001. Preservation of Permo–Triassic low-pressure assemblages in the Cretaceous high-pressure metamorphic Saualpe crystalline basement (Eastern Alps, Austria). Journal of metamorphic Geology. 19(6), 679-697.

Habler, G., Thöni, M., Miller, C., 2007. Major and trace element chemistry and Sm–Nd age correlation of magmatic pegmatite garnet overprinted by eclogite-facies metamorphism. Chemical Geology. 241(1-2), 4-22.

Handler, R., Neubauer, F., Hermann, S., Dallmeyer, R., 1999. Silurian-Devonian 40Ar/39Ar mineral ages from the Kaintaleck Nappe: Evidence for mid-Paleozoic tectonothermal activity in Upper Austroalpine basement units of the Eastern Alps (Austria). Geologica Carpatica. 50, 229-240.

Handy, M.R., Schmid, S. M., Bousquet, R., Kissling, E. Bernoulli, D., 2010. Reconciling plate-tectonic reconstructions of Alpine Tethys with the geological–geophysical record of spreading and subduction in the Alps. Earth-Science Reviews. 102(3-4), 121-158.

Lardeaux, J. M., & Spalla, M. I., 1991. From granulites to eclogites in the Sesia zone (Italian Western Alps): a record of the opening and closure of the Piedmont ocean. Journal of Metamorphic Geology, 9(1), 35-59.

Li, H., Hong, T., Yang, Z. Q., Chen, Ji. Z., Ke, Q., Wang, X. H., Niu, L., Xu, X. W., 2021. Comparative studying on zircon, cassiterite and coltan U-Pb dating and 40Ar/39Ar dating of muscovite rare-metal granitic pegmatites: A case study of the northern Tugeman lithium-beryllium deposit in the middle of Altyn Tagh. Acta Petrologica Sinica. 36(9), 2869-2892.

Hauke, M., Froitzheim, N., Nagel, T. J., Miladinova, I., Fassmer, K., Fonseca, R.O.C., Sprung, P., Münker, C., 2019. Two high-pressure metamorphic events, Variscan and Alpine, dated by Lu–Hf in an eclogite complex of the Austroalpine nappes (Schobergruppe, Austria). International Journal of Earth Sciences. 108(4), 1317-1331.

Heede, H.-U., 1997. Isotopengeologische Untersuchungen an Gesteinen des ostalpinen Saualpenkristallins, Kärnten, Österreich. Münstersche Forschungen zur Geologie und Palaeontologie. pp. 122.

Henk, A., Franz, L., Teufel, S., Oncken, O., 1997. Magmatic underplating, extension, and crustal reequilibration: Insights from a cross-section through the Ivrea Zone and Strona-Ceneri Zone, northern Italy. The Journal of Geology. 105(3), 367-378.

Herron, M.M., 1988. Geochemical classification of terrigenous sands and shales from core or log data. Journal of Sedimentary Research. 58(5), 820-829.

Hermann, J., Rubatto, D., 2003. Relating zircon and monazite domains to garnet growth zones: age and duration of granulite facies metamorphism in the Val Malenco lower crust. Journal of Metamorphic Geology. 21(9), 833-852.

Hoke, L., 1990. The Altkristallin of the Kreuzeck Mountains, SE Tauern Window, Eastern Alps; basement crust in a convergent plate boundary zone. Jahrbuch der Geologischen Bundesanstalt. 133(1), 5-87.

Holland, T.J.B., Powell, R., 2011. An improved and extended internally consistent thermodynamic dataset for phases of petrological interest, involving a new equation of state for solids. Journal of Metamorphic Geology. 29(3), 333-383.

Holyoke III, C. W., Rushmer, T., 2002. An experimental study of grain scale melt segregation mechanisms in two common crustal rock types. Journal of metamorphic Geology. 20(5), 493-512.

Hulsbosch, N., Hertogen, J., Dewaele, S., André, L., Muchez, P., 2014. Alkali metal and rare earth element evolution of rock-forming minerals from the Gatumba area pegmatites (Rwanda): Quantitative assessment of crystal-melt fractionation in the regional zonation of pegmatite groups. Geochimica et Cosmochimica Acta. 132, 349-374.

Icenhower, J., London, D., 1995. An experimental study of element partitioning among biotite, muscovite, and coexisting peraluminous silicic melt at 200 MPa (H2O). American Mineralogist. 80(11-12), 1229-1251.

Janoušek, V., Holub, F. V., 2007. The causal link between HP-HT metamorphism and ultrapotassic magmatism in collisional orogens: case study from the Moldanubian Zone of the Bohemian Massif. Proceedings of the Geologists Association. 118(1), 75-86.

Kaeter, D., Barros, R., Menuge, J.F., Chew, D.M., 2018, The magmatic-hydrothermal transition in rare-element pegmatites from southeast Ireland: LA-ICP-MS chemical mapping of muscovite and columbite-tantalite: Geochimica et Comochimica Acta, v. 240, p. 98–130.

Kesler, S.E., Gruber, P.W., Medina, P.A., Keoleian, G.A., Everson, M.P. Wallington, T.J., 2012. Global lithium resources: Relative importance of pegmatite, brine and other deposits. Ore Geology Reviews. 48, 55–69.

Keyser, W., Müller, A., Berndt, J., Steiner, R., Knoll, T., Menuge, J. F., Hart, E., Fegan, T., Harrop, J., submitted. Quartz chemistry of lithium pegmatites and its petrogenetic and economic implications: examples from the Wolfsberg (Austria) and Moylisha (Ireland) occurrences. Submitted to Economic Geology

Knoll, T., Schuster, R., Huet, B., Mali, H., Onuk, P., Horschinegg, M., Ertl, A., Giester, G., 2018. Spodumene Pegmatite and Related Leucogranite from the AustroAlpine Unit (Eastern Alps, Central Europe): Field Relations, Petrography, Geochemistry, and Geochronology. Canadian Mineralogist. 56(4), 489-528.

Konzett, J., Schneider, T., Nedyalkova, L., Hauzenberger, C., Melcher, F., Gerdes, A., Whitehouse, M., 2018. Anatectic Granitic Pegmatites from the Eastern Alps: A Case of Variable Rare-Metal Enrichment During High-Grade Regional Metamorphism–I: Mineral Assemblages, Geochemical Characteristics, and Emplacement Ages. Canadian Mineralogist. 56(4), 555-602.

Krenn, E., Schulz, B., Finger, F., 2012. Three generations of monazite in Austroalpine basement rocks to the south of the Tauern Window: evidence for Variscan, Permian and Eo-Alpine metamorphic events. Swiss Journal of Geosciences. 105(3), 343-360.

Krenn, K., Konzett, J., & Stalder, R., 2022. Anatectic granitic pegmatites from the eastern Alps: A case of variable rare metal enrichment during high-grade regional metamorphism. III: Fluid inclusions as potential indicators for anatectic pegmatite parent melt formation. The Canadian Mineralogist. 60(1), 155-169.

Kunz, B. E., Manzotti, P., von Niederhäusern, B., Engi, M., Darling, J. R., Giuntoli, F., Lanari, P., 2018. Permian high-temperature metamorphism in the Western Alps (NW Italy). International Journal of Earth Sciences. 107(1), 203-229.

Li, B., Massonne, H. J., Koller, F., Zhang, J., 2021. Metapelite from the high-ultrahigh pressure terrane of the Eastern Alps (Pohorje Mountains, Slovenia)–new pressure, temperature, and time constraints on a polymetamorphic rock. Journal of Metamorphic Geology. 39, 695-726.

Liu, C., Wang, R. C., Wu, F. Y., Xie, L., Liu, X. C., Li, X. K., Yang, L., Li, X. J., 2020. Spodumene pegmatites from the Pusila pluton in the higher Himalaya, South Tibet: Lithium mineralization in a highly fractionated leucogranite batholith. Lithos. 358-359, 105421.

London, D., 1984: Experimental phase equilibria in the system LiAlSiO4–SiO2–H2O: a petrogenetic grid for lithiumrich pegmatites. American Mineralogist. 69, 995-1004.

London, D., 2005. Granitic pegmatites: an assessment of current concepts and directions for the future. Lithos. 80(1-4), 281-303.

London, D., 2008. Pegmatites, in: Canadian Mineralogist Special Publication 10, Mineralogical Association of Canada, Quebec. pp. 347.

London, D., 2018. Ore-forming processes within granitic pegmatites. Ore Geology Reviews. 101, 349-383.

Luvizotto, G.L., Zack, T., 2009. Nb and Zr behavior in rutile during high-grade metamorphism and retrogression: an example from the Ivrea-Verbano Zone. Chemical Geology. 261(3–4), 303–317.

Lv, Z. H., Zhang, H., & Tang, Y., 2021. Anatexis origin of rare metal/earth pegmatites: Evidences from the Permian pegmatites in the Chinese Altai. Lithos, 380, 105865.

Mali, H., 2004. Die Spodumenpegmatite von Brettstein und Pusterwald (Wölzer Tauern, Steiermark, Österreich). Joannea Mineralogie. 2, 5–53.

Mandl, M., Kurz, W., Hauzenberger, C., Fritz, H., Klötzli, U., Schuster, R., 2018. Pre-Alpine evolution of the Seckau Complex (Austroalpine basement/Eastern Alps): Constraints from in-situ LA-ICP-MS UPb zircon geochronology. Lithos. 296, 412-430.

Maner IV, J. L., London, D., Icenhower, J. P., 2019. Enrichment of manganese to spessartine saturation in granite-pegmatite systems. American Mineralogist. 104(11), 1625-1637.

Maneta, V., Baker, D. R., Minarik, W., 2015. Evidence for lithium-aluminosilicate supersaturation of pegmatite-forming melts. Contributions to Mineralogy and Petrology. 170(1), 1-16.

Manzotti, P., Zucali, M., 2013. The pre-Alpine tectonic history of the Austroalpine continental basement in the Valpelline unit (Western Italian Alps). Geological Magazine. 150(1), 153-172.Marinoni, L. B., 2001. Crustal extension from exposed sheet intrusions: review and method proposal. Journal of Volcanology and Geothermal Research. 107(1-3), 27-46.

Marotta, A. M., Spalla, M. I., 2007. Permian-Triassic high thermal regime in the Alps: Result of late Variscan collapse or continental rifting? Validation by numerical modeling. Tectonics. 26(4), TC4016.

Marotta, A. M., Roda, M., Conte, K., & Spalla, M. I., 2018. Thermo-mechanical numerical model of the transition from continental rifting to oceanic spreading: the case study of the Alpine Tethys. Geological Magazine. 155(2), 250-279.

Marschall, H. R., von Strandmann, P. A. P., Seitz, H. M., Elliott, T., Niu, Y., 2007. The lithium isotopic composition of orogenic eclogites and deep subducted slabs. Earth and Planetary Science Letters. 262(3-4), 563-580.

Maxeiner, R. O., Ashton, K., Card, C. D., Morelli, R. M., Knox, B., 2017. A field guide to naming migmatites and their textures, with Saskatchewan examples. Summary of Investigations. 2, 2017-4.

McCann, T., Skompski, S., Poty, E., Dusar, M., Vozárová, A., Schneider, J., Wetzel, A., Krainer, K., Kornpihl, K., Schäfer, A., Krings, M., Oplustil, S., Tait, J., 2008. Carboniferous, in: McCann, T., (Eds.), The Geology of Central Europe Volum1: Precambrian and Palaeozoic. Geological Society of London, London. pp. 411-529.

McKechnie, C. L., Annesley, I. R., Ansdell, K. M. (2013). Geological setting, petrology, and geochemistry of granitic pegmatites and leucogranites hosting U-Th-REE mineralization at Fraser Lakes Zone B, Wollaston Domain, northern Saskatchewan, Canada. Exploration and Mining Geology. 21, 1-26.

Melleton, J., Gloaguen, E., Frei, D., Novak, M., Breiter, K., 2012. How are the emplacement of rare-element pegmatites, regional metamorphism and magmatism interrelated in the Moldanubian Domain of the Variscan Bohemian Massif, Czech Republic. Canadian Mineralogist. 50, 1751–1773.

Miller, C., Thöni, M., Goessler, W., Tessadri, R., 2011. Origin and age of the Eisenkappel gabbro to granite suite (Carinthia, SE Austrian Alps). Lithos. 125(1), 434-448.

Misra, S., Burlini, L., Burg, J. P., 2009. Strain localization and melt segregation in deforming metapelites. Physics of the Earth and Planetary Interiors. 177(3-4), 173-179.

Monjoie, P., Bussy, F., Lapierre, H., & Pfeifer, H. R., 2005. Modeling of in-situ crystallization processes in the Permian mafic layered intrusion of Mont Collon (Dent Blanche nappe, western Alps). Lithos. 83(3-4), 317-346.

Monjoie, P., Bussy, F., Schaltegger, U., Mulch, A., Lapierre, H., & Pfeifer, H. R., 2007. Contrasting magma types and timing of intrusion in the Permian layered mafic complex of Mont Collon (Western Alps, Valais, Switzerland): evidence from U/Pb zircon and 40 Ar/39 Ar amphibole dating. Swiss Journal of Geosciences. 100(1), 125-135.

Munoz, J. L., 1971. Hydrothermal stability relations of synthetic lepidolite. American Mineralogist. 56(11-12), 2069-2087.

Müller, A., Romer, R.L., Pedersen, R.-B., 2017. The Sveconorwegian Pegmatite Province -thousands of pegmatites without parental granites. Canadian Mineralogist. 55, 283–315.

Müller, A., Keyser, W., Simmons, W. B., Webber, K., Wise, M., Beurlen, H., ... & Galliski, M. Á. (2021). Quartz chemistry of granitic pegmatites: Implications for classification, genesis and exploration. Chemical Geology, 584, 120507.

Müntener, O., Hermann, J., & Trommsdorff, V., 2000. Cooling history and exhumation of lower-crustal granulite and upper mantle (Malenco, Eastern Central Alps). Journal of Petrology. 41(2), 175-200.

Nabelek, P. I., Liu, M., 2004. Petrologic and thermal constraints on the origin of leucogranites in collisional orogens. Earth and Environmental Science Transactions of the Royal Society of Edinburgh. 95(1-2), 73-85.

Neubauer, F., 2002. Evolution of late Neoproterozoic to early Paleozoic tectonic elements in Central and Southeast European Alpine mountain belts: review and synthesis. Tectonophysics. 352(1-2), 87-103.

Neubauer, F., Liu, Y., Dong, Y., Chang, R., Genser, J., & Yuan, S. (2022). Pre-Alpine tectonic evolution of the Eastern Alps: From Prototethys to Paleotethys. Earth-Science Reviews, 226, 103923.

Oliver, N. H. S., Barr, T. D., 1997. The geometry and evolution of magma pathways through migmatites of the Halls Creek Orogen, Western Australia. Mineralogical Magazine. 61(1), 3-14.

Patiño Douce, A. E., Harris, N., 1998. Experimental constraints on Himalayan anatexis. Journal of Petrology. 39(4), 689-710.

Pattison, D. R. M., Spear, F. S., Debuhr, C. L., Cheney, J. T., Guidotti, C. V., 2002. Thermodynamic modelling of the reaction muscovite+ cordierite→ Al2SiO5+ biotite+ quartz+ H2O: constraints from natural assemblages and implications for the metapelitic petrogenetic grid. Journal of metamorphic Geology. 20(1), 99-118.

Pattison, D. R., De Capitani, C., Gaidies, F., 2011. Petrological consequences of variations in metamorphic reaction affinity. Journal of Metamorphic Geology. 29(9), 953-977.

Pattison, D. R., Spear, F. S., 2018. Kinetic control of staurolite–Al2SiO5 mineral assemblages: Implications for Barrovian and Buchan metamorphism. Journal of Metamorphic Geology. 36(6), 667-690.

Pestal, G., Hejl, E., Braunstingl, R., Schuster, R., 2009. Erläuterungen Geologische Karte von Salzburg 1: 200000. Geologische Bundesanstalt. pp. 162.

Petri, B., Mohn, G., Skrzypek, E., Mateeva, T., Galster, F., & Manatschal, G., 2017. U–Pb geochronology of the Sondalo gabbroic complex (Central Alps) and its position within the Permian post-Variscan extension. International Journal of Earth Sciences. 106(8), 2873-2893.

Petri, B., Duretz, T., Mohn, G., Schmalholz, S. M., Karner, G. D., Müntener, O., 2019. Thinning mechanisms of heterogeneous continental lithosphere. Earth and Planetary Science Letters. 512, 147-162.

Plunder, A., Le Pourhiet, L., Räss, L., Gloaguen, E., Pichavant, M., & Gumiaux, C., 2022. Pegmatites as geological expressions of spontaneous crustal flow localisation. Lithos. 416, 106652.

Potter, E. G., Taylor, R. P., Jones, P. C., Lalonde, A. E., Pearse, G. H., Rowe, R., 2009. Sokolovaite and evolved lithian micas from the eastern Moblan granitic pegmatite, Opatica subprovince, Quebec, Canada. Canadian Mineralogist. 47(2), 337-349.

Puhr, B., Hoinkes, G., Schuster, R., 2010. Petrologic and isotopic characteristics of metacarbonate rocks of the Austroalpine Basement east of the Tauern Window (Eastern Alps). Journal of Alpine Geology. 52, 206.

Qiu, L., Rudnick, R. L., McDonough, W. F., Bea, F., 2011. The behavior of lithium in amphibolite-to granulite-facies rocks of the Ivrea–Verbano Zone, NW Italy. Chemical Geology. 289(1-2), 76-85.

Rantitsch, G., Iglseder, C., Schuster, R., Hollinetz, M. S., Huet, B., Werdenich, M., 2020. Organic metamorphism as a key for reconstructing tectonic processes: a case study from the Austroalpine unit (Eastern Alps). International Journal of Earth Sciences. 109(6), 2235-2253.

Rebay, G., & Spalla, M. I., 2001. Emplacement at granulite facies conditions of the Sesia–Lanzo metagabbros: an early record of Permian rifting?. Lithos. 58(3-4), 85-104.

Redler, C., Johnson, T. E., White, R. W., Kunz, B. E., 2012. Phase equilibrium constraints on a deep crustal metamorphic field gradient: metapelitic rocks from the Ivrea Zone (NW Italy). Journal of Metamorphic Geoogy. 30(3), 235–254.

Roda, M., Regorda, A., Spalla, M. I., & Marotta, A. M., 2019. What drives Alpine Tethys opening? Clues from the review of geological data and model predictions. Geological Journal. 54(4), 2646-2664.

Rosenberg, C. L., Handy, M. R., 2005. Experimental deformation of partially melted granite revisited: implications for the continental crust. Journal of Metamorphic Geology. 23(1), 19-28.

Rudnick, R.L., Gao, S., 2003. Composition of the Continental Crust, in: Rudnick, R.L., (Eds.), The Crust. Springer, Elsevier-Pergamon, Oxford. pp. 1–64.

Rushmer, T., 2001. Volume change during partial melting reactions: implications for melt extraction, melt geochemistry and crustal rheology. Tectonophysics. 342(3-4), 389-405.

Rutter, E. H., 1997. The influence of deformation on the extraction of crustal melts: a consideration of the role of melt-assisted granular flow. Mineralogical Society Series. 8, 82-110.

Sawyer, E. W., 2001. Melt segregation in the continental crust: distribution and movement of melt in anatectic rocks. Journal of metamorphic Geology. 19(3), 291-309.

Sawyer, E.W., 2008. Atlas of Migmatites, in: Canadian Mineralogist Special Publication 9. Mineralogical Association of Canada, Quebec. pp. 371.

Schmid, S.M., Fügenschuh, B., Kissling, E., Schuster, R., 2004. Tectonic map and overall architecture of the Alpine Orogen. Eclogae Geologicae Helvetiae. 97(1), 93-117.

Schulz, B., Finger, F., Krenn, E., 2005. Auflösung variskischer, permischer und alpidischer Ereignisse im polymetamorphen ostalpinen Kristallin südlich der Tauern mit EMS-Datierung von Monazit. Arbeitstagung der Geologischen Bundesanstalt Österreich. 141–153.

Schulz, B., 2017. Polymetamorphism in garnet micaschists of the Saualpe Eclogite Unit (Eastern Alps, Austria), resolved by automated SEM methods and EMP–Th–U–Pb monazite dating. Journal of Metamorphic Geology. 35(2), 141-163.

Schulz, B., Krause, J., 2021. Electron probe petrochronology of polymetamorphic garnet micaschists in the lower nappe units of the Austroalpine Saualpe basement (Carinthia, Austria). Zeitschrift der Deutschen Gesellschaft für Geowissenschaften. 19-46.

Schuster, R., Frank, W., 1999. Metamorphic evolution of the Austroalpine units east of the Tauern Window: indications for Jurassic strike slip tectonics. Mitteilung der Gesellschaft der Geologie- und Bergbaustudenten in Österreich. 42, 37-58.

Schuster, R., Scharbert, S., Abart, R., Frank, W., 2001. Permo-Triassic extension and related HT/LP metamorphism in the Austroalpine-Southalpine realm. Mitteilung der Gesellschaft der Geologie- und Bergbaustudenten in Österreich. 45, 111-141.

Schuster, R., Koller, F., Hoeck, V., Hoinkes, G., Bousquet, R., 2004: Explanatory notes to the map: Metamorphic structure of the Alps - Metamorphic evolution of the Eastern Alps. Mitteilungen der Österreichischen Mineralogischen Gesellschaft. 149, 175-199.

Schuster, R., Stüwe, K., 2008. Permian metamorphic event in the Alps. Geology. 36(8), 603-606.

Schuster, R., Tropper, P., Krenn, E., Finger, F., Frank, W., Philippitsch, R., 2015. Prograde Permo-Triassic metamorphic HT/LP assemblages from the Austroalpine Jenig Complex (Carinthia, Austria). Austrian Journal of Earth Sciences. 108(1), 73-90.

Schuster, R., Nowotny, A., 2016. Die Einheiten des Ostalpinen Kristallins auf den Kartenblättern GK50 Blatt 103 Kindberg und 135 Birkfeld. Arbeitstagung der Geologischen Bundesanstalt. 10-37.

Schuster, R., Knoll, T., Mali, H., Huet, B., Griesmeier, G.E.U., 2019. Field trip guide: a profile from migmatites to spodumene pegmatites (Styria, Austria). Berichte der Geologischen Bundesanstalt. 134.Selway, J. B., Breaks, F. W., Tindle, A. G., 2005. A review of rare-element (Li-Cs-Ta) pegmatite

exploration techniques for the Superior Province, Canada, and large worldwide tantalum deposits. Exploration and Mining Geology. 14(1-4), 1-30.

Servais, T., Dzik, J., Fatka, O., Heuse, T., Vecoli, M., Verniers, J., 2008. Ordovician, in: McCann, T., (Eds.), The Geology of Central Europe Volume 1: Precambrian and Palaeozoic, Geological Society of London, London. pp. 203-248.

Shaw, R.A., Goodenough, K.M., Roberts, N.M.W., Horstwood, M.S.A., Chenery, S.R., Gunn, A.G., 2016. Petrogenesis of rare-metal pegmatites in high-grade metamorphicterranes: A case study from the Lewisian Gneiss Complex of northwest Scotland. Precambrian Research. 281, 338–362.

Simmons, W.B., Foord, E.E., Falster, A.U., King, V.T., 1995. Evidence for an anatectic origin of granitic pegmatites, Western Maine, USA. Geological Society of America Annual Meeting, New Orleans, LA., Abstracts with Programs 27. 6, A411.

Sinigoi, S., Quick, J. E., Demarchi, G., & Klötzli, U. S., 2016. Production of hybrid granitic magma at the advancing front of basaltic underplating: Inferences from the Sesia Magmatic System (south-western Alps, Italy). Lithos. 252, 109-122.

Sohrabi, N., Kalantari, N., Amiri, V., Nakhaei, M., 2017. Assessing the chemical behavior and spatial distribution of yttrium and rare earth elements (YREEs) in a coastal aquifer adjacent to the Urmia Hypersaline Lake, NW Iran. Environmental Science and Pollution Research. 24(25), 20502-20520.

Sola, A. M., Becchio, R. A., Pimentel, M. M., 2013. Petrogenesis of migmatites and leucogranites from Sierra de Molinos, Salta, Northwest Argentina: A petrologic and geochemical study. Lithos. 177, 470-491.

Solar, G. S., & Tomascak, P. B., 2009. The Sebago pluton and the Sebago Migmatite Domain, Southern Maine: results from new studies. In: 2009 Annual Meeting of Northeastern Section, Geological Society of America, Field Trip. Vol. 2, pp. 1-24.

Solar, G. S., Tomascak, P. B., Berry, H. N., West, D. P., 2016. The Migmatite-Granite Complex of southern Maine: Its structure, petrology, geochemistry, geochronology, and relations to the Sebago Pluton. In Guidebook for field trips along the Maine coast from Maquoit Bay to Muscongus Bay: New England Intercollegiate Geological Conference. 19-42.

Sölva, H., Thöni, M., Habler, G., 2003. Dating a single garnet crystal with very high Sm/Nd ratios (Campo basement unit, Eastern Alps). European Journal of Mineralogy. 15(1), 35-42.

Rebay, G., & Spalla, M. I., 2001. Emplacement at granulite facies conditions of the Sesia–Lanzo metagabbros: an early record of Permian rifting?. Lithos. 58(3-4), 85-104.

Spear, F. S., Kohn, M. J., Cheney, J. T., 1999. P-T paths from anatectic pelites. Contributions to Mineralogy and Petrology. 134(1), 17-32.

Spear, F. S., & Pattison, D. R. (2017). The implications of overstepping for metamorphic assemblage diagrams (MADs). Chemical Geology, 457, 38-46.Stewart, D. B. (1978). Petrogenesis of lithium-rich pegmatites. American Mineralogist. 63(9-10), 970-980.

Stewart, D. B. (1978). Petrogenesis of lithium-rich pegmatites. American Mineralogist. 63(9-10), 970-980.

Stilling, A., Ćerný, P., Vanstone, P. J., 2006. The Tanco pegmatite at Bernic Lake, Manitoba. XVI. Zonal and bulk compositions and their petrogenetic significance. Canadian Mineralogist. 44(3), 599-623.

Stöckhert, B., 1987. Das Uttenheimer Pegmatitfeld (Ostalpines Altkristallin, Südtirol) Genese und alpine Überprägung. Erlanger geologische Abhandlungen. 114, 83-106.

Sweetapple, M.T., Collins, P.L.F., 2002. Genetic framework for the classification and distribution of Archean rare metal pegmatites in the North Pilbara Craton, Western Australia. Economic Geologist. 97, 873–895.

Tabelin, C. B., Dallas, J., Casanova, S., Pelech, T., Bournival, G., Saydam, S., Canbulat, I., 2021. Towards a low-carbon society: A review of lithium resource availability, challenges and innovations in mining, extraction and recycling, and future perspectives. Minerals Engineering. 163, 106743.

Teng, F. Z., McDonough, W. F., Rudnick, R. L., Dalpé, C., Tomascak, P. B., Chappell, B. W., Gao, S., 2004. Lithium isotopic composition and concentration of the upper continental crust. Geochimica et Cosmochimica Acta. 68(20), 4167-4178.

Teng, F. Z., McDonough, W. F., Rudnick, R. L., Wing, B. A., 2007. Limited lithium isotopic fractionation during progressive metamorphic dehydration in metapelites: a case study from the Onawa contact aureole, Maine. Chemical Geology. 239(1-2), 1-12.

Tibaldi, A., 2015. Structure of volcano plumbing systems: A review of multi-parametric effects. Journal of Volcanology and Geothermal Research. 298, 85-135.

Thöni, M., Miller, C., 2000. Permo-Triassic pegmatite in the eo-Alpine eclogite-facies Koralpe complex, Austria: age and magma source constraints from mineral chemical, Rb-Sr and Sm-Nd isotope data. Schweizerische Mineralogische und Petrographische

Thöni, M., 2002. Sm-Nd isotope systematics in garnet from different lithologies (Eastern Alps): Age results, and an evaluation of potential problems for garnet Sm-Nd chronometry. Chemical Geology. 185, 255–281.

Mitteilungen. 80(2), 169-86.

Thöni, M, Miller, C., 2004. Ordovician meta-pegmatite garnet (NW Ötztal basement, Tyrol, Eastern Alps): preservation of magmatic garnet chemistry and Sm–Nd age during mylonitization. Chemical Geology. 209(1-2), 1-26.

Thöni, M., Miller, C., Zanetti, A., Habler, G., Goessler, W., 2008. Sm–Nd isotope systematics of high-REE accessory minerals and major phases: ID-TIMS, LA-ICP-MS and EPMA data constrain multiple Permian–Triassic pegmatite emplacement in the Koralpe, Eastern Alps. Chemical Geology. 254(3-4), 216-237.

Thöni, M., Miller, C., 2009. The “Permian event” in the Eastern European Alps: Sm–Nd and P–T data recorded by multi-stage garnet from the Plankogel unit. Chemical Geology. 260(1-2), 20-36.

Thöni, M., Miller, C., 2010. Andalusite formation in a fast exhuming high-P wedge: textural, microchemical, and Sm-Nd and Rb-Sr age constraints for a Cretaceous P-T-t path at Kienberg, Saualpe (Eastern Alps). Austrian Journal of Earth Sciences. 103(2), 118-131.

Török, K., 1999. Pre-Alpine development of the andalusite-sillimanite-biotite-schist from the Sopron Mountains (Eastern Alps, Western Hungary). Acta Geologica Hungarica. 42(2), 127-160.

Tropper, P., Finger, F., Krenn, E., Kloetzli, U., Piber, A., Gangl, S., 2016. The Kellerjoch Gneiss (Tyrol, Eastern Alps): An Ordovician pluton with A-type affinity in the crystalline basement nappes north of the Tauern Window. Austrian Journal of Earth Sciences. 109(2), 178-188.

Tumarkina, E., Misra, S., Burlini, L., Connolly, J. A., 2011. An experimental study of the role of shear deformation on partial melting of a synthetic metapelite. Tectonophysics. 503(1-2), 92-99.

Vanderhaeghe, O., 1999. Pervasive melt migration from migmatites to leucogranite in the Shuswap metamorphic core complex, Canada: control of regional deformation. Tectonophysics. 312(1), 35-55.

Varga, R. J., Gee, J. S., Staudigel, H., Tauxe, L., 1998. Dike surface lineations as magma flow indicators within the sheeted dike complex of the Troodos Ophiolite, Cyprus. Journal of Geophysical Research: Solid Earth. 103(B3), 5241-5256.

Verlaguet, A., Goffé, B., Brunet, F., Poinssot, C., Vidal, O., Findling, N., Menut, D., 2011. Metamorphic veining and mass transfer in a chemically closed system: a case study in Alpine metabauxites (western Vanoise). Journal of Metamorphic Geology. 29(3), 275-300.

Verlaguet, A., Brunet, F., Goffé, B., Menut, D., Findling, N., Poinssot, C., Huet, B., 2016. Selective transfer of Li-Al-rich phyllosilicate to metamorphic veins (Western Alps): Laser Induced Breakdown Spectroscopy (LIBS) compositional profiles and microstructural characterization. Journal of Geodynamics. 101, 51-72.

Vidal, O., Goffé, B., 1991. Cookeite LiAl 4 (Si 3 Al) O 10 (OH) 8: Experimental study and thermodynamical analysis of its compatibility relations in the Li2O− Al2O3− SiO2− H2O system. Contributions to Mineralogy and Petrology. 108(1), 72-81.

Vigneresse, J. L., Barbey, P., Cuney, M., 1996. Rheological transitions during partial melting and crystallization with application to felsic magma segregation and transfer. Journal of Petrology. 37(6), 1579-1600.

Vigneresse, J. L., Burg, J. P., 2000. Continuous vs. discontinuous melt segregation in migmatites: insights from a cellular automaton model. Terra Nova. 12(4), 188-192.

Vrabec, M., Janák, M., Froitzheim, N., De Hoog, J. C., 2012. Phase relations during peak metamorphism and decompression of the UHP kyanite eclogites, Pohorje Mountains (Eastern Alps, Slovenia). Lithos. 144, 40-55.

Warren, J. K., 2010. Evaporites through time: Tectonic, climatic and eustatic controls in marine and nonmarine deposits. Earth-Science Reviews. 98(3-4), 217-268.

Waters, D. J., Lovegrove, D. P., 2002. Assessing the extent of disequilibrium and overstepping of prograde metamorphic reactions in metapelites from the Bushveld Complex aureole, South Africa. Journal of Metamorphic Geology. 20(1), 135-149.

Webber, K. L., Simmons, W. B., Falster, A. U., Hanson, S. L., 2019. Anatectic pegmatites of the Oxford County pegmatite field, Maine, USA. Canadian Mineralogist. 57(5), 811-815.

Weinberg, R. F., Veveakis, E., Regenauer-Lieb, K., 2015. Compaction-driven melt segregation in migmatites. Geology. 43(6), 471-474.

Weißenbach, N., Pistotnik, J., 2000: Bad Sankt Leonhard im Lavanttal 1:50.000, in: Geologische Karte der Republik Österreich 1:50.000. Verlag der Geologische Bundesanstalt. 187.

White, R. W., Powell, R., Holland, T. J. B., Johnson, T. E., Green, E. C. R., 2014. New mineral activity–composition relations for thermodynamic calculations in metapelitic systems. Journal of Metamorphic Geology. 32(3), 261-286.

Whitworth, M. P., Feely, M., 1994. The compositional range of magmatic Mn-garnets in the Galway Granite, Connemara, Ireland. Mineralogical Magazine. 58(390), 163-168.

Wilson, B. M., 2007. Igneous petrogenesis: A global tectonic approach. Springer Science & Business Media. pp. 457.

Yang, P., Rivers, T., 2000. Trace element partitioning between coexisting biotite and muscovite from metamorphic rocks, Western Labrador: Structural, compositional and thermal controls. Geochimica et Cosmochimica Acta. 64(8), 1451-1472.

Yuan, S., Neubauer, F., Liu, Y., Genser, J., Liu, B., Yu, S., Chang, R., Guan, Q., 2020. Widespread Permian granite magmatism in Lower Austroalpine units: significance for Permian rifting in the Eastern Alps. Swiss Journal of Geosciences. 113(1), 1-25.

Zack, T., Tomascak, P. B., Rudnick, R. L., Dalpé, C., McDonough, W. F., 2003. Extremely light Li in orogenic eclogites: the role of isotope fractionation during dehydration in subducted oceanic crust. Earth and Planetary Science Letters. 208(3-4), 279-290.

Zagorsky, V.Ye., 2009. On emplacement of compositionally heterogeneous pegmatite melts: petrogenetic implications. Estudos Geol. 19 (2), 365–369.Zagorsky, V. Y., Vladimirov, A. G., Makagon, V. M., Kuznetsova, L. G., Smirnov, S. Z., D'yachkov, B. A., Uvarov, A. N., 2014. Large fields of spodumene pegmatites in the settings of rifting and postcollisional shear–pull-apart dislocations of continental lithosphere. Russian Geology and Geophysics. 55(2), 237-251.

Zucali, M., Manzotti, P., Diella, V., Pesenti, C., Risplendente, A., Darling, J., Engi, M., 2011. Permian tectonometamorphic evolution of the Dent-Blanche Unit (Austroalpine domain, Western Italian Alps). Rendiconti online della Società Geologica Italiana. 15, 133-136.

Zurbriggen, R., 2017. The Cenerian orogeny (early Paleozoic) from the perspective of the Alpine region. International Journal of Earth Sciences. 106(2), 517-529.

## 5. FIELD TRIP GUIDE: A PROFILE FROM MIGMATITES TO SPODUMENE PEGMATITES (STYRIA, AUSTRIA)

*Ralf Schuster[1], Tanja Knoll[1], Heinrich Mali[2], Benjamin Huet[1] & Gerit E.U. Griesmeier[1]*

*[1]Geologische Bundesanstalt, Neulinggasse 38, 1030 Vienna, Austria.*

*[2]Montanuniversität Leoben, Department Applied Geosciences and Geophysics, Peter-Tunner-Straße 5, 8700 Leoben*

*Corresponding author: Ralf.Schuster@geologie.ac.at*

---

➔ *Manuscript status: open access book*
➔ *Geologische Bundesanstalt , 2019. - 29 pp.: Ill.. - In: Berichte der Geologischen Bundesanstalt ; Nr. 134 (2019),* https://www.zobodat.at/pdf/BerichteGeolBundesanstalt_134_0001-0029.pdf
➔ *Published: 2019*

---

PREFACE

Rare element pegmatite is an important host for critical elements crucial to the high-tech industry (Li, Nb, Ta …). All types are traditionally interpreted as products of highly fractionated granitic melts and thought to be genetically linked to large parental fertile granite bodies. Recent studies, however, suggest that some pegmatite fields including rare element pegmatite could have an anatectic origin. Since 2015, a series of joint projects lead by the Geological Survey of Austria (GBA) and the Montanuniversität Leoben (MUL) targeted spodumene ($LiAlSi_2O_6$) pegmatite occurrences within the Austroalpine Unit of the Eastern Alps. The results argue that the studied rare element pegmatite have an anatectic origin.

To present the spodumene pegmatite of the Austroalpine Unit and its field relation to its hostrocks, a one-day field trip to the St. Radegund area (Styria, Austria) was offered at the European Geosciences Union (EGU) 2019 conference in the frame of the session “Impacts of partial melting on the evolution of the continental crust: different views, one topic”. About 40 participants from ten countries visited key outcrops providing an exceptional insight into the genetic relationships between migmatite, simple pegmatite, leucogranite and spodumene pegmatite. Field observations were discussed in the light of geochemical and geochronological data acquired on the visited outcrops and the surrounding area.

We published this field trip guide to provide a basis for future excursions

## 1. Introduction

In the Austroalpine Unit of the Eastern Alps, spodumene pegmatites spread heterogeneously across an E–W distance of more than 400 km (Fig. 1). These pegmatites are classified as albite-spodumene pegmatites of the rare element (RE) class (Göd, 1989; Černý & Ercit, 2005). They are always spatially associated with simple pegmatite and leucogranite bodies lacking remarkable RE-mineralizations. Simple pegmatite and leucogranite bodies are considered to be the products of anatexis (Stöckert, 1987; Thöni & Miller, 2000) and formed during the Permian event, which is characterized by lithospheric extension, causing crustal basaltic underplating, high temperature-low pressure (HT/LP) metamorphism and intense magmatic activity within the crust (Schuster & Stüwe, 2008). In a recent study (Ilickovic et al., 2017; Knoll et al., 2018; Mali et al., 2019; Schuster et al., 2017), the genetic relationship of spodumene pegmatite with respect to simple pegmatite and leucogranite was worked out, based on field relations, Rb-Sr and Sm-Nd geochronology, bulk-rock geochemistry and mineral Laser Ablation-ICPMS analyses. The results indicate a formation of all of these magmatic rocks from anatectic melts generated during prograde HT/LP metamorphism of specific Al-rich metapelites and following fractionated crystallization of simple pegmatite, leucogranite, moderate fractionated pegmatite and spodumene pegmatite. Additionally, a quantitative model explaining the Li-transfer from metapelite into spodumene pegmatite was proposed (Schuster et al., 2019; Knoll et al., in prep.).

In the course of the excursion to the St. Radegund area (Styria/Austria), the field relations of the above-mentioned rocks are presented within a single nappe of the Austroalpine Unit. At the base of the Radegund Nappe, migmatic micaschist and paragneiss with aborted melt formation occur, whereas the top consists of staurolite-bearing micaschist with spodumene pegmatite bodies therein. This allows to study an upright section through the Permian middle crust, in spite of a pressure dominated amphibolite facies overprint and related deformation, which occurred during the Eoalpine event in the Cretaceous.

This field guide includes a short introduction to the regional geology of the Eastern Alps, some remarks on the route from Vienna to the St. Radegund area and a detailed description of the field stops.

## 2. Geological overview of the Eastern Alps

The Alpine orogen developed from two continental and two oceanic realms existing in Late Jurassic to Cretaceous times (Fig.1). Additionally, the lowermost tectonic units represented by the Allochthonous Molasse in the Eastern Alps, formed from parts of the northern foreland basin during post-Oligocene shortening. The former European continental margin was incooperated since the Eocene and comprises the Helvetic nappes appearing along the northern front and the Subpenninic nappes present in the more internal part of the orogenic belt. The overlying Penninic nappes are derived from the Penninic Ocean (Alpine Tethys) and continental fragments therein. Together with the Subpenninic nappes, they experienced Alpine tectonics and metamorphism, mainly in the Eocene to Miocene. The Austroalpine and the Southalpine Unit, separated by the Periadriatic fault, are both derived from the Adriatic Microcontinent and now occur on top of the previously described units. The Austroalpine nappes were sheared off during the Eoalpine event in the Cretaceous and the individual nappes experienced variegated tectonic and metamorphic overprints during subduction, nappe stacking and exhumation. All the above-mentioned units represent the northwest-verging pro-wedge of the Alpine orogen, whereas the Southalpine Unit formed as a south-verging retro-wedge mainly after the Oligocene. Tectonic slices derived from the Neotethys Ocean, referred to as the Meliata Unit, occur within the Austroalpine nappe pile. They were mobilized in the Jurassic and reached their present position by out-of-sequence thrusting in the Early Cretaceous (Froitzheim et al., 2008).

While Permian magmatic rocks occur in all major tectonic units composed of continental crust, Permian pegmatites are restricted to those derived from the Adriatic Microcontinent. The continental crust of this domain was affected by intense magmatism during a Cambro-

Ordovician event related to extension at the northern margin of Gondwana, the late Devonian to Carboniferous Variscan collisional event in the course of Pangea formation, a Permian extensional event within Pangea and finally the Alpine collisional event since the earliest Cretaceous. As pegmatite formation occurred during the Permian extensional event and they were overprinted during the Alpine event, these two events are described in more detail.

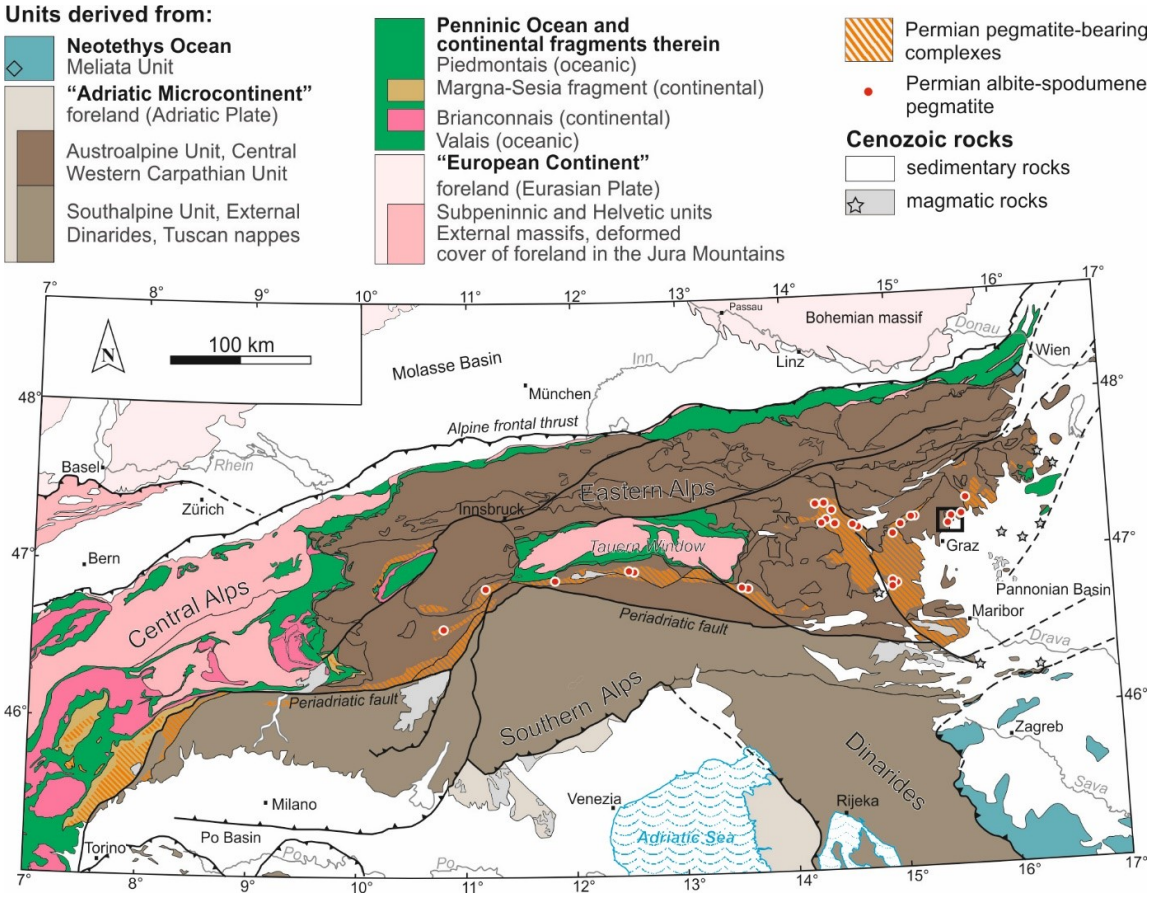


*Fig. 1: Tectonic map of the Alps showing the paleogeographic origin of the major tectonic units of the Alps (modified after Froitzheim et al., 2008). Additionally, the distribution of complexes containing Permian pegmatite and spodumene pegmatite is highlighted (modified after Mali, 2004 and Knoll et al., 2018). Black square indicates the area of St. Radegund shown in Figure 6.*

## 2.1. PERMIAN EXTENSIONAL EVENT

The Permian event in the Alps followed in the wake of the Variscan tectonic evolution. Lithospheric extension affected the Adria derived Austroalpine and Southalpine Unit, but also the Europe derived Brianconnais and Subpenninic Unit. The Permian event onset at about 290 Ma may be considered when crustal thickness decreased below normal and thus cannot be related to gravitational collapse of the Variscan orogen anymore. Basaltic melts rose up from the mantle to the base of the crust and caused intense magmatic activity and related HT/LP metamorphism. Peak metamorphic conditions were reached at about 280–260 Ma at a geothermal gradient of up to 45 C/km (Habler & Thöni, 2001; Schuster et al., 2001; Kunz et al., 2018). Subsequently, the metamorphosed rocks were not exhumed, but the lithosphere cooled down slowly to a steady state geotherm of c. 25 C/km at about 200 Ma. Slow cooling of the lithosphere caused continuous subsidence in late Permian and throughout Triassic time. This subsidence triggered the deposition of more than 3 km thick Permian clastic successions and Triassic carbonate platform sediments (Schuster & Stüwe, 2008). A map showing the distribution of the Permian metamorphic grade and related magmatic and sedimentary rocks is given in Figure 2. Numbers in the text refer to key areas indicated also therein. A section through the base of the Permian crust with gabbroic and dioritic intrusions as well as restitic kinzigites is

exposed in the Ivrea Zone (Quick et al., 1995) (1). Deep crustal levels are indicated by amphibolite to granulite facies rocks with sillimanite, andalusite and indications of anataxis (Kunz et al., 2018). Therein, gabbro, diorite and granite bodies as well as pegmatite dikes occur. Such sections are well preserved in the Kreuzeck-Gailtaler Alpen Nappe (2), at the base of the Silvretta Nappe (3) or within the Campo Nappe (4) (Schuster et al., 2001; Thöni, et al., 2008). From the Permian middle crust upper greenschist facies metamorphic units with garnet-bearing assemblages are known e.g. from the Donnersbach Nappe (5). Somewhat higher levels are characterized by large bodies of biotite-granite, which intruded within greenschist facies metapelite partly showing contact phenomena.

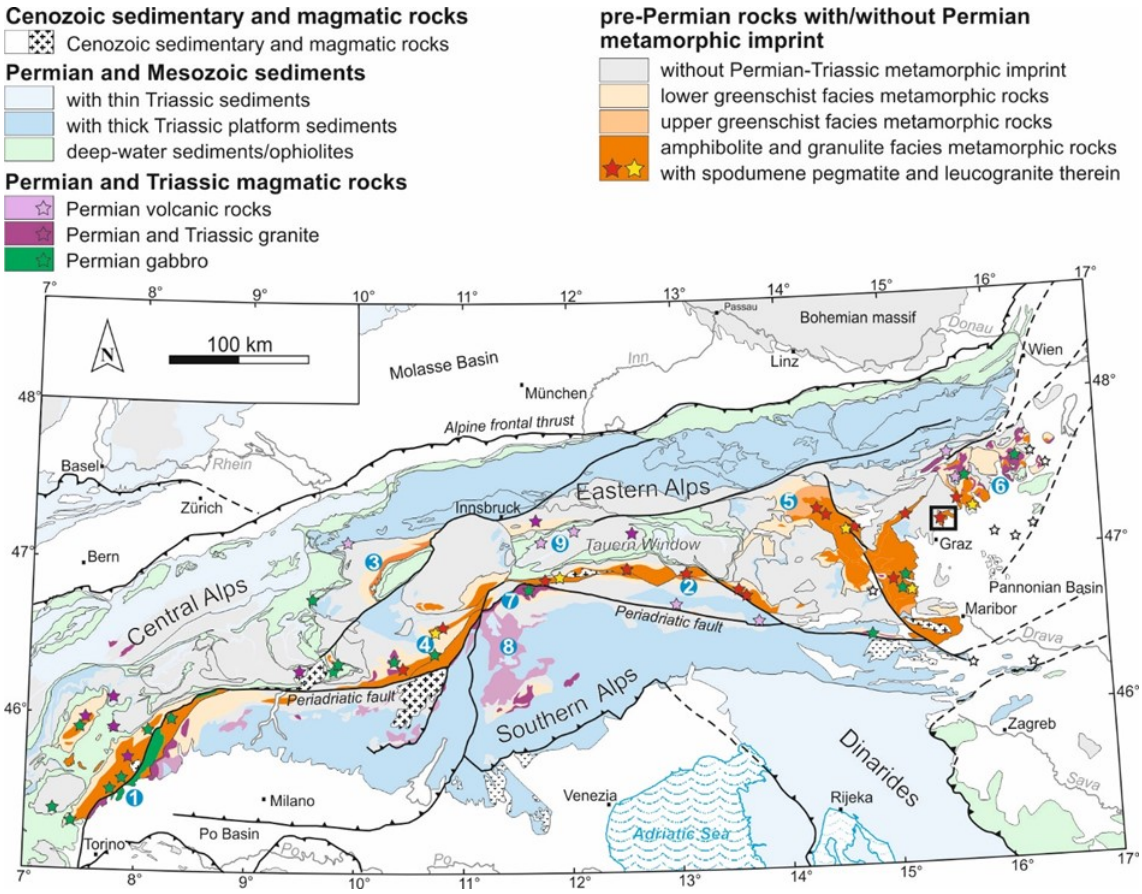


*Fig. 2: Map of the Alps showing the distribution of Permian metamorphism and related magmatic and sedimentary rocks. Pegmatite bodies are frequent in most of the amphibolite to granulite facies units. Numbers refer to the text and the black square indicates the area of St. Radegund shown in Figure 6. Map modified from SCHUSTER & STÜWE (2008).*

Such kind of basement can be studied in the easternmost part of the Eastern Alps (6), but also in the Southalpine Unit (7). Within the uppermost crust, subvolcanic dikes and intrusions occur and at the surface Permian grabens are filled with sedimentary piles typically containing volcanic layers (Cassinis et al., 2012). The most famous volcanic centre is represented by the Bozen quartzporphyry (8), but similar rocks are also known from the Subpenninic nappes of the Tauern Window (9).

Fieldwork and detailed mapping revealed that Permian pegmatite and leucogranite in the Eastern Alps are restricted to distinct complexes with typical lithological associations and petrological features (Knoll et al., 2018). These complexes stayed in lower to middle crustal levels during the Permian. Three different domains can be distinguished (Fig. 3).

(1) In structurally lower parts, pegmatitic patches, narrow pegmatite dikes and larger feldspar dominated pegmatite dikes occur in aluminosilicate-bearing, garnet-rich micaschist and paragneiss representing restites of initial anatexis. The pegmatitic patches have a thickness of a

few centimeters to decimeters. Associated pegmatite formed by accumulation of melts from the patches is present as networks of centimeter thick veins or up to a few meters thick dikes. They are concordant and mostly composed of feldspar and quartz. According to data from surrounding micaschist and paragneiss this level stayed in a depth of c. 20 km and experienced upper amphibolite to granulite facies metamorphic conditions (~0.65 GPa and 650 C; Knoll et al., in prep.) during the Permian event. (2) Structurally higher domains are characterized by frequent concordant, simple pegmatites of several meters thickness and mineral assemblages with feldspar, quartz, muscovite, garnet and tourmaline. In some places (e.g. Martell valley, Uttenheim valley, Geißrücken near Judenburg), associated inhomogeneous leucogranite bodies with pegmatitic and aplitic striae occur. They extend up to a few kilometers in size. (3) Moderate fractionated pegmatite is present as partly discordant dikes in structurally uppermost levels. Feldspar, quartz, muscovite, garnet and tourmaline form the common assemblage, but additionally spodumene and beryl may be present. Very rarely, tiny grains of cassiterite, columbite and REE-minerals have been found. Spodumene pegmatite occurs in about a dozen places forming up to a few meters thick dikes with lengths up to more than one kilometer (Göd, 1989; Mali, 2004; Knoll et al., 2018), but they also occur as several decimeter sized boudins. The occurrence of contemporaneously formed garnet in surrounding micaschist and paragneiss, these pegmatite dikes intruded in upper greenschist facies conditions (~0.45 GPa at 500 C) at crustal levels of c. 17 km depth.

Muscovites from simple pegmatite, leucogranite, moderate fractionated pegmatite and spodumene pegmatite plot on continuous fractionation trends in the diagrams by Černý & Ercit (2005). This trend is particularly notable for muscovite on the K/Rb versus Li and K/Rb versus Tl diagrams of Figure 4. The analyses show that the K/Rb ratio of muscovite progressively decreases from migmatite (254 to 337), simple pegmatite (27 to 448), leucogranite (22 to 193), moderate fractionated pegmatite (22 to 364) to spodumene pegmatite (15 to 151). Additionally, the K/Rb ratio shows a negative correlation with the Li concentration (77–217 ppm in migmatite, 10–99 ppm in simple pegmatite, 36–785 ppm in leucogranite, 100–760 ppm in moderate fractionated pegmatite and 361–1,780 ppm in spodumene pegmatite, Figure 4A) as well as with the Tl concentration (1–3 ppm in migmatite, 1–19 ppm in simple pegmatite, 2–19 ppm in leucogranite, 1–19 ppm in moderate fractionated pegmatite and 2–28 ppm in albite-spodumene pegmatite, Figure 4B).

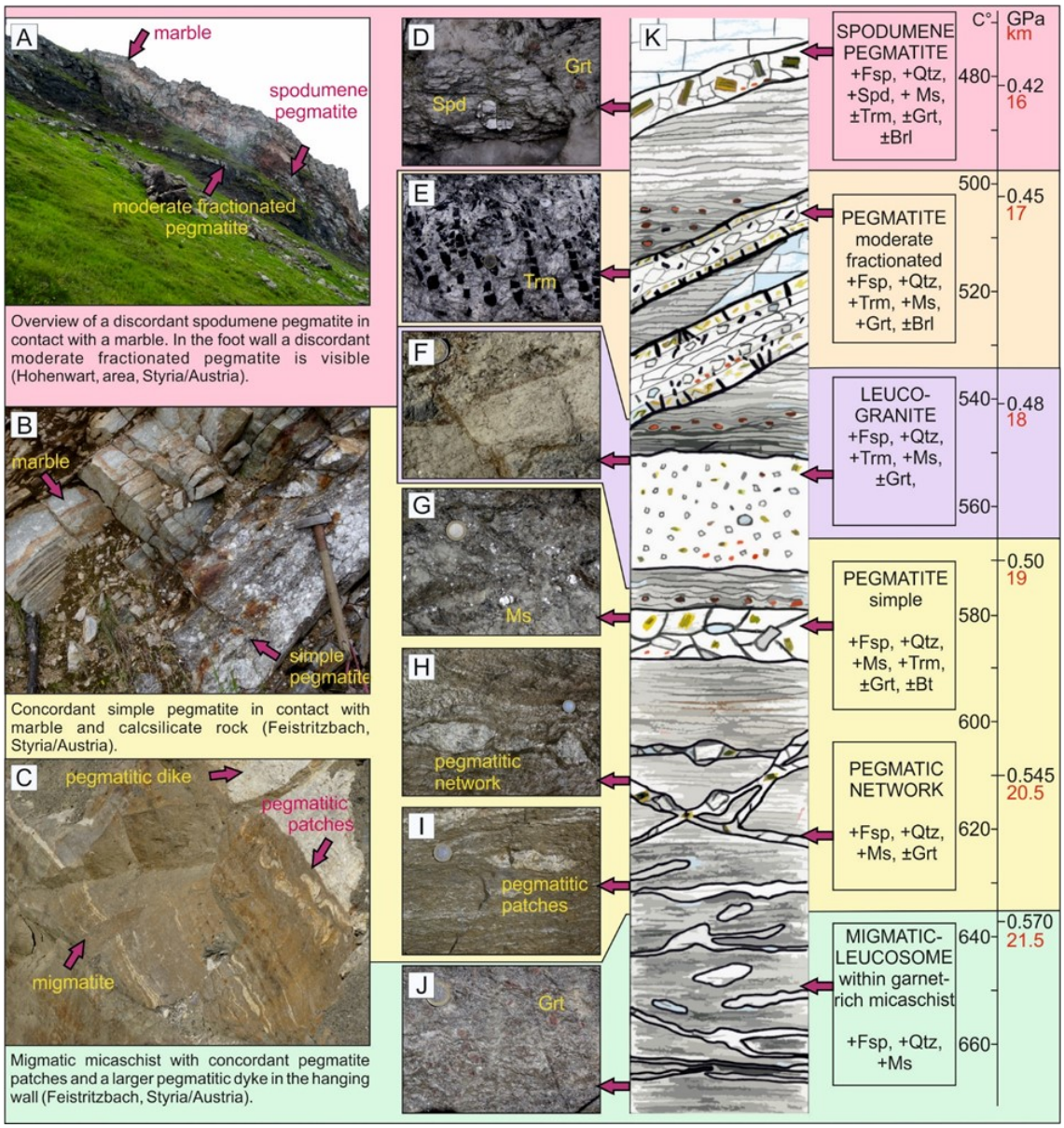


*Fig. 3: Synoptic diagram showing field relations for Permain pegmatites and leucogranites in the Austroalpine Unit of the Eastern Alps. As mentioned in the text a lower migmatic domain (green and yellow), a domain with evolved pegmatite and leucogranite (yellow and violet) and an upper domain with evolved pegmatite and spodumene pegmatite (orange and red) can be distinguished. Outcrop pictures of A) spodumene pegmatite, B) concordant simple pegmatite and C) migmatic micaschist with pegmatitic networks and dikes. Compilation of typical lithologies: D) spodumene pegmatite (width of image 7 cm), E) comb structures of deformed tourmaline (width of image 37 cm), F) inhomogeneous leucogranite (width of image 20 cm), G) muscovite pegmatite (width of image 25 cm), H) deformed pegmatitic network (width of image 40 cm), I) pegmatitic patches within deformed migmatic micaschist (width of image 30 cm), J) garnet-rich restitic paragneiss (width of image 20 cm). K) Schematic column shows the distribution of typical lithologies, magmatic assemblages and depth-pressure-temperature relations. Abbreviations: Spd = spodumene, Brl = beryl, Trm = tourmaline, Grt = garnet, Ms = muscovite, Fsp = alkali feldspar and plagioclase, Qtz = quartz.*

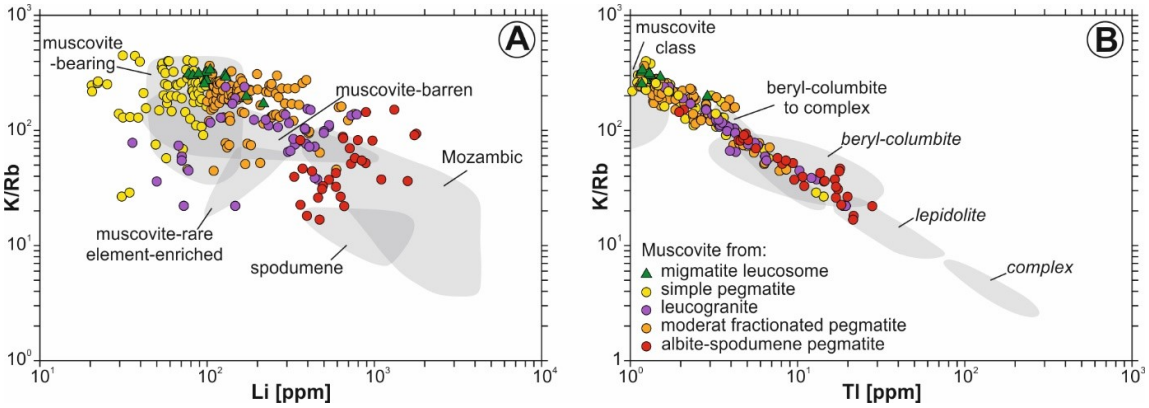


*Fig. 4: Trace element composition of muscovite from migmatite leucosome, simple pegmatite, moderate fractionated pegmatite, leucogranite and spodumene pegmatite. A) K/Rb ratio vs. Li. B) K/Rb ratio vs. Tl. The grey backgrounds refer to pegmatite groups defined in Černý & Burt (1984).*

## 2.2. Alpine collisional event

The Alpine collisional event is a consequence of the convergence between the African, Adriatic and Eurasian plates. Even though there is a general consensus about the paleogeographic framework, models with one or up to four suture zones have been proposed to explain the present day tectonic situation (Fig. 5) (e.g. Froitzheim et al., 1996; Neubauer et al., 2000; Kurz & Fritz, 2003; Janák et al., 2015).

Following Stüwe & Schuster (2010) collision initiated at an south(east) dipping intracontinental subduction zone within the Adriatic Microcontinent. The Austroalpine nappes formed during the consumption of the Adriatic continental crust from earliest Cretaceous until middle Late Cretaceous time (Eoalpine event). Some stayed at high crustal levels, whereas others were subducted and reached eclogite facies and even ultra-high pressure metamorphism. Peak conditions were reached at about 92 Ma in the early Late Cretaceous (Thöni, 2006) followed by a medium pressure overprint during exhumation of the high-pressure rocks. In the eastern part of the Eastern Alps exhumation of the deeply buried units occurred by N- or NW-directed thrusting and S- to SE-directed extensional tectonics, causing the formation of a metamorphic extrusion wedge. The latter shows a lower part with an inverted metamorphic field gradient and an upper part with an upright metamorphic field gradient. Cooling ages are in the range of 90 to 70 Ma (Hoinkes et al., 1999; Thöni, 1999).

Ongoing subduction of the lithospheric plate caused the entrance of the Penninic oceanic domain into the subduction zone at about 85 Ma. Parts of the sediments, oceanic crust and uppermost mantle were sheared off and incorporated into the orogenic wedge referred to as Penninic nappes. After the closure of the ocean, European continental lithosphere got into the subduction zone in the Eocene at about 45 Ma (Schmid et al., 2013). These processes referred to as the Mesoalpine and Neoalpine events are dominating in the Central and Western Alps. They resulted in the formation of the Subpenninic and Helvetic nappes. In the Eastern Alps, the Neoalpine event caused a LT/HP metamorphism in the Penninic and Subpenninic nappes at 35–40 Ma (Thöni, 1999). A subsequent medium pressure overprint at about 30–25 Ma is referred to as „Tauernkristallisation“ (Sander, 1921; Thöni, 1999). In Eocene to Oligocene times, the lithospheric slab formed since the Early Cretaceous teared below the Eastern Alps. Slab break-off induced uprise of hot asthenosphere and caused the Periadriatic magmatism (Davis & von Blankenburg, 1995).

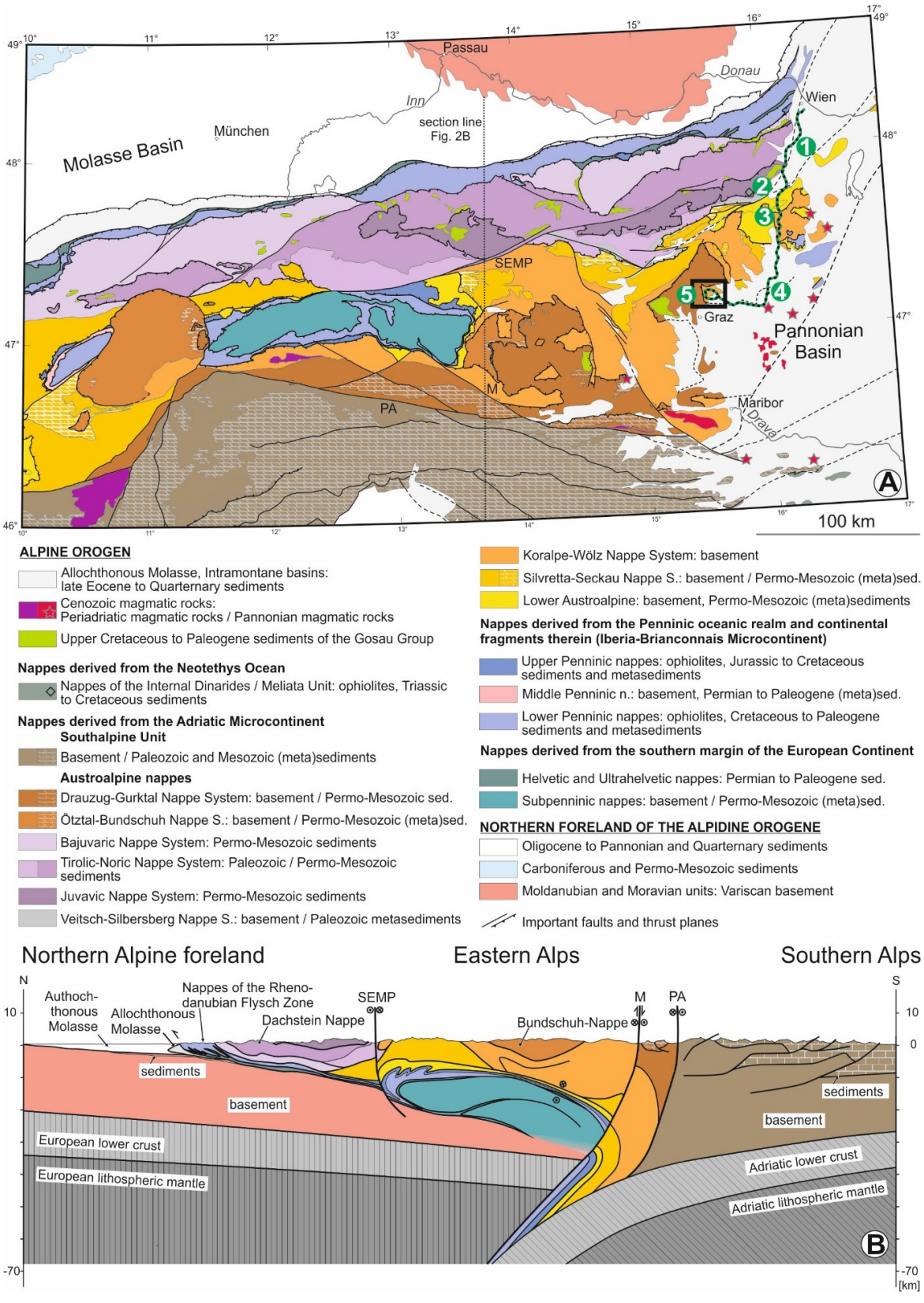


*Fig. 5: Tectonic map A) and section B) of the Eastern Alps according to the nomenclature in* FROITZHEIM *et al. (2008). SEMP = Salzach-Ennstal-Mariazell-Puchberg fault, M = Mölltal fault, PA = Periadriatic fault. The black square indicates the area of St. Radegund shown in Figure 6. Numbers refer to certain sections of the travelling route: 1 = Vienna Basin, 2 = Mt. Schneeberg area, 3 = Mt. Wechsel area, 4 = Styrian Basin (near Hartberg), 5 = Mt. Schöckl near to Graz.*

Indentation by the Adriatic microplate into the eastern part of the Alpine orogenic wedge since the beginning of the Miocene (23 Ma) caused further shortening of the northwest-vergent pro wedge. It reached about 50 % of the former width in the area of the western Tauern Window (SCHARF et al., 2013). Contemporaneous top-south-directed thrusting formed the retro wedge represented by the Southalpine Unit.

Also in the early Miocene, slab retreat in the course of the final closure of the Penninic Ocean in the Carpathian realm (Froitzheim et al., 2008) triggered thinning and eastward extrusion of the orogenic wedge. This process referred to as lateral extrusion (Ratschbacher et al., 1989) is responsible for the formation of a system of strike-slip and normal faults (Genser & Neubauer, 1989; Fügenschuh et al., 1997; Schmid et al., 2013). Along these faults the Lower Engadine Window, Tauern Window and Rechnitz Window Group formed, exposing Penninic and Subpenninic units at the surface. Typical cooling ages for the rocks from within the tectonic windows are in the range of 25 to 15 Ma (Dunkl et al., 1998; Luth& Willingsdorfer, 2008). Partly also the lowermost Austroalpine units (Lower Austroalpine nappes) adjacent to the windows experienced a structural and very-low to low grade Alpine metamorphic overprint (Hoinkes et al., 1999; Sschuster et al., 2004). Major strike-slip faults are the Periadriatic, Inntal, Salzach-Ennstal-Mariazell-Puchberg, Mur-Mürz and Vienna Basin transfer faults. They have a major influence on the recent morphology, because fault bounded blocks like the Saualpe, Koralpe or Niedere Tauern mountain ranges were lifted up and tilted, whereas nearby basins like the Vienna, Styrian or Pannonian Basin developed. Thinning of the lithosphere and mantle upwelling below the Styrian Basin and Pannonian Basin caused synsedimentary magmatic activity (Pannonian magmatism). The occurrence of weak fault rocks triggered intense erosion along the faults, especially during the Quaternary glaciations.

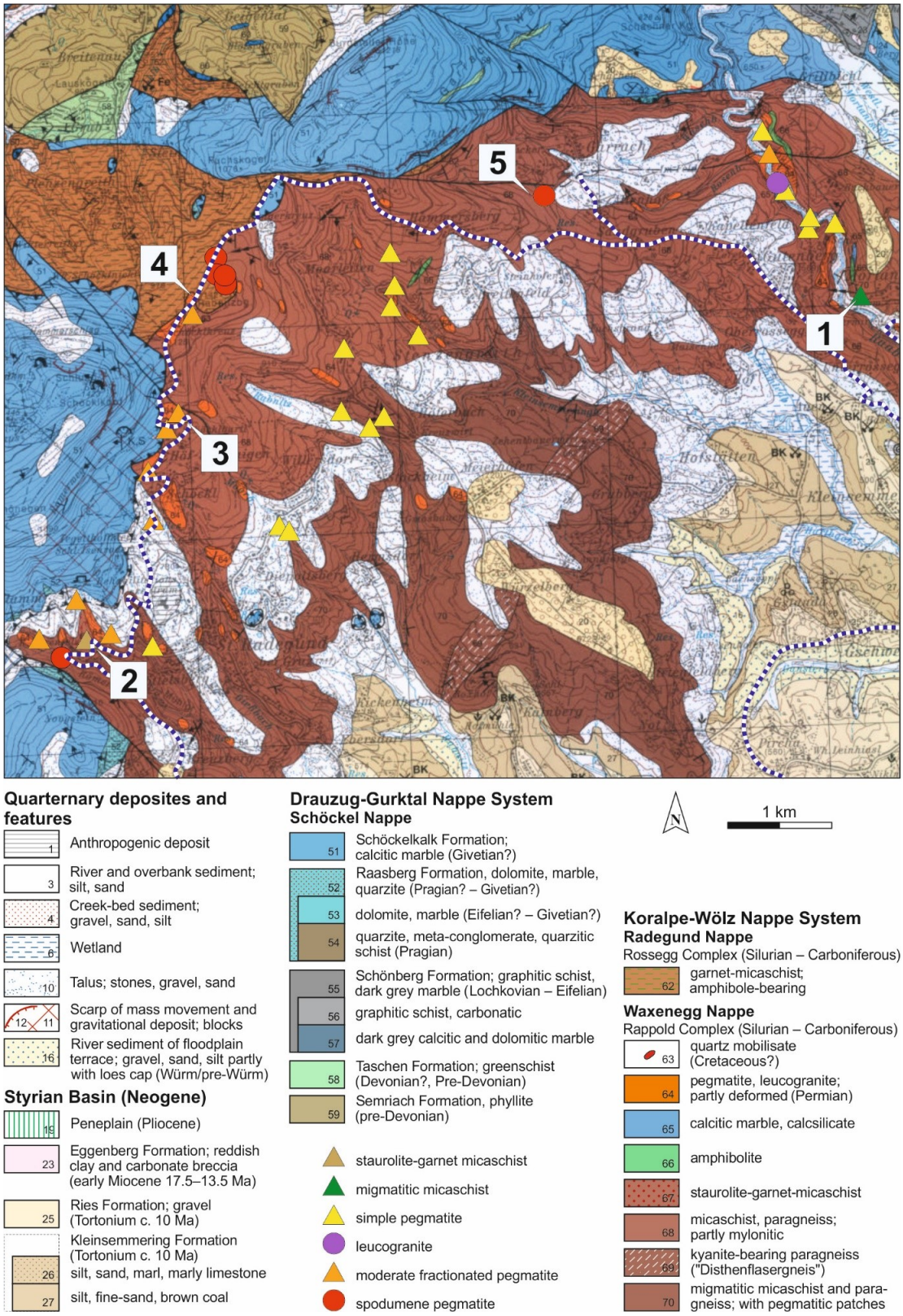


*Fig. 6: Location of the field trip stops plotted on map sheet Graz (FLÜGEL et al., 2011) in the scale 1:50.000 from the Austrian Geological Survey. The analysed samples from staurolite-garnet-micaschist, migmatic micaschist, simple pegmatite, leucogranite, moderate fractionated pegmatite and spodumene pegmatite are plotted on the map. Dotted lines indicate traveling route.*

## 3. Overview of the St. Radegund area

The area of interest around the village St. Radegund is shown in Figure 6 according to the geological map of Flügel et al. (2011). In the northwestern part, nappes of the Austroalpine Unit form the surface, whereas in the southeast they are covered by transgressive sediments of the Neogene Styrian Basin. The Austroalpine Unit comprises nappes of the Koralpe-Wölz Nappe System in the footwall and the Drauzug-Gurktal Nappe System in a hanging wall position. The boundary in between is a moderately west dipping normal fault in the west and a steeply north dipping normal fault in the north.

All visited outcrops will be in the Radegund Nappe of the Koralpe-Wölz Nappe System, as it contains the Permian pegmatite and leucogranite bodies. It is important to note that almost all of these bodies are deformed and characterized by a gneissic texture. This nappe is the lowermost tectonic element in the area and is built up by the Rappold Complex, consisting of paragneiss and micaschist with a few intercalations of amphibolite, marble and calcsilicate rock (Nowotny, 2007, 2008). Based on data from the same complex, but from other localities, the metasediments of the Rappold Complex were most probably deposited in a shelf and/or slope environment. From detrital zircons and Sr-isotopic data, a depositional age from the Silurian or Devonian to the Carboniferous can be inferred (Puhr et al., 2009; Frank et al., 2019). Based on the occurrence of two garnet generations a polyphase metamorphic history is indicated (Fig. 7a). The first metamorphic imprint is Permian in age and proofed by Sm-Nd garnet and U-Pb monazite ages of about 275–255 Ma (Gaidies et al., 2006; Hauzenberger et al., 2008). It reached up to upper amphibolite facies conditions with partial anatexis. The generated melts crystallized as pegmatitic patches, simple pegmatite, leucogranite, moderate fractionated pegmatite and spodumene pegmatite in different levels. A Sm-Nd garnet age of an moderate fractionated pegmatite from the locality Schöckelbartl (Stop 3) is 260 ± 3 Ma (Gotthardt, 2015), which perfectly fits to other Sm-Nd garnet and U-Th-Pb monazite ages from other pegmatite occurrences within the Rappold Complex (Schuster et al., 2001; Röggla, 2007). The Alpine overprint reached about 600  C and 0.1 GPa (Röggla, 2007) and caused deformation of variable intensity (Fig. 7b).

Within the Rappold Complex of the St. Radegund area, certain associations of metasediments and pegmatite types show a distinct distribution (Nowotny, 2008). In the southeast, anatectic micaschist and paragneiss with stromatic to subordinate nebulitic texture is typical (Stop 1a). The metapelites are medium-grained, biotite-rich and often contain eye-catching muscovite flakes up to 5 mm in size. In thin sections, a mineral assemblage with alkali-feldspar + plagioclase + biotite + muscovite + garnet ± kyanite is visible (Nowotny, 2007). Garnet porphyroblasts are characterized by Permian cores with few relatively large inclusions of biotite, quartz and plagioclase often with a roundish shape. In contrast, the Eoalpine rims are more inclusion-rich (Fig. 7c). Sometimes the rims consist of several idiomorphic subgrains with a similar orientation, causing a rough and irregular shape of the porphyroblast. Kyanite forms aggregates composed of tiny crystals, often embedded in fine-grained muscovite (Fig.7d) (Nowotny, 2007). These aggregates developed from Permian andalusite and/or sillimanite, which was transformed to kyanite during the Eoalpine overprint (Schuster et al., 2004). Therein, pegmatitic patches and pegmatite(-gneiss) bodies composed of feldspar, quartz, minor muscovite and extremely scarce garnet and tourmaline appear.

Towards the overlying units in the west and north and towards high structural levels, respectively, the grain size of the matrix in the metapelites is decreasing and the large mica flakes and pegmatitic patches disappear. Instead, the pegmatite bodies get thicker even though they are strongly deformed and boudinaged (Stop 1b, 1c). Partly, they are very coarse-grained with up to 20 cm large alkali feldspar clasts (Fig.7e). In the Raabklamm gorge, a body with a largely homogeneous medium-grained texture and a thickness of more than 100 m is present, which is referred to as leucogranite in here (Stop1d).

In the uppermost part, staurolite-bearing garnet-micaschist with a fine-grained matrix composed of biotite + muscovite + quartz ± plagioclase is characteristic (Fig.7f). Both staurolite and garnet show a dark grey colour due to inclusions of graphitic pigment and they may reach up to more than 1 cm in diameter. The textures can best be observed in the walls of the castle ruin Ehrenfels (Stop 2), because of the nicely weathered surfaces.

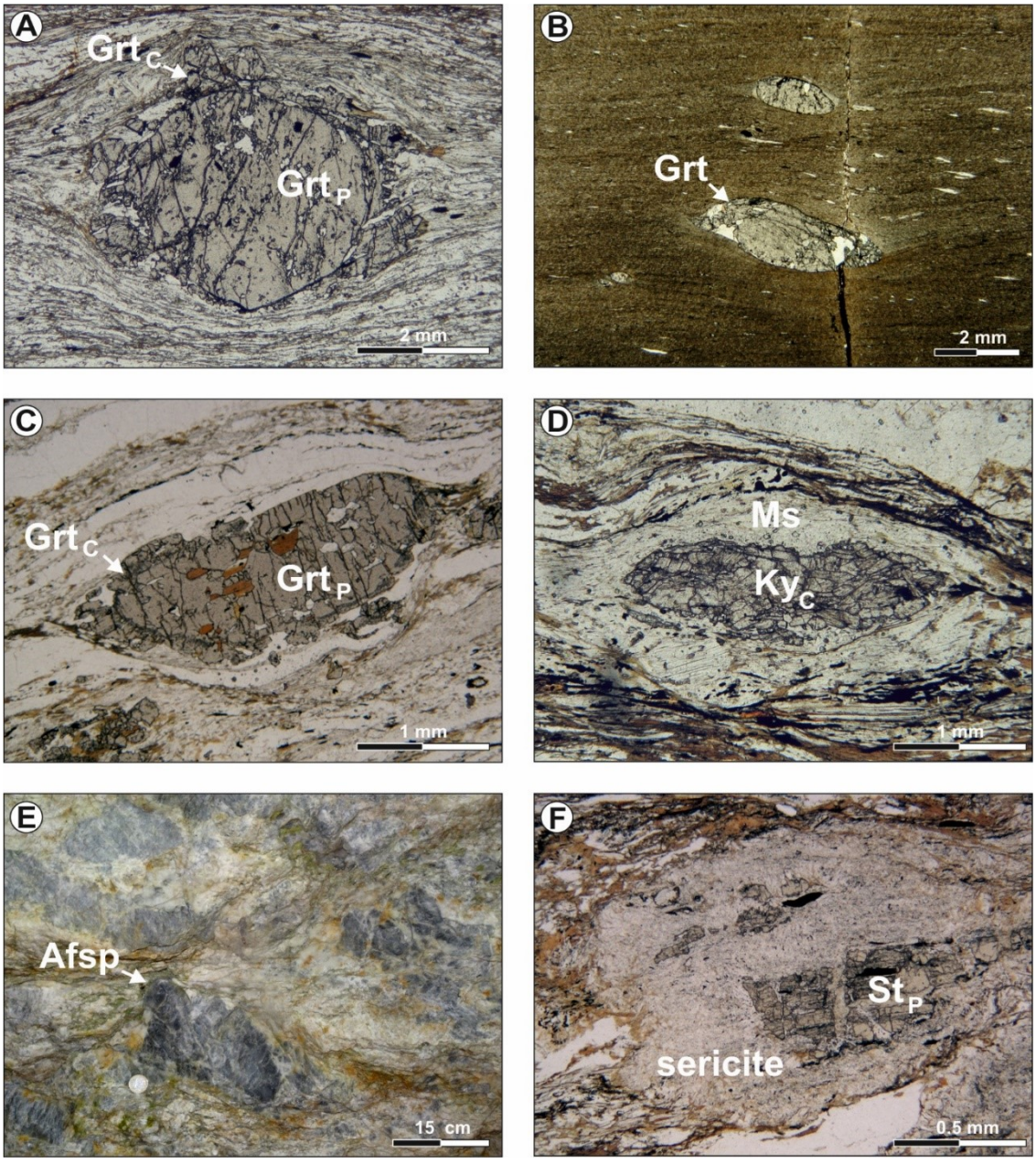


*Fig. 7: Lithologies of the Rappold Complex from the Radegund Nappe. A) Microphotograph of a micaschist with polyphase garnet with Permian core and Eoalpine (Cretaceous) rim (sample RO4-14). B) Microphotograph of an ultramylonitic micaschist (sample RA-4). C) Microphotograph of a mylonitisized migmatic micaschist with polyphase garnet. Within the garnet core larger inclusions of biotite and plagioclase are present (sample NO26-05). D) Microphotograph of a migmatic micaschist with a Cretaceous kyanite aggregate formed from Permian andalusite and/or sillimanite. Kyanite is partly replaced by muscovite (sample RK30). E) Moderate fractionated pegmatite with deformed alkali feldspar phenocrysts up to 25 cm in diameter. F) Staurolite-garnet-micaschist with Permian staurolite embedded in Cretaceous sericite (sample NO21-05). All microphotographs were taken with parallel polarizers. Abbreviations: Grt = garnet, Ms = muscovite, Ky = kyanite, Afsp = alkali feldspar, St = staurolite, P = Permian, C = Cretaceous.*

Based on textural observations the staurolites formed contemporaneously with the Permian cores of the garnets. As in the structural lower parts of the Rappold Complex, the garnet cores are relatively poor in inclusions, but in this position, they contain mostly quartz and ilmenite instead of biotite and plagioclase. The Eoalpine garnets are again rich in inclusions mostly represented by graphitic pigment and quartz. Their chemical zoning is characterized by a significantly lower grossular component with respect to the rims (see detailed descriptions e.g. in Eisenberg & Hauzenberger, 2001; Gaidies et al., 2006; Röggla, 2007). In this uppermost part, additionally spodumene and beryl occur in the pegmatite gneiss bodies. One spodumene pegmatite (Stop 4) is known from the locality Schöcklkreuz at Rabnitzberg hill (Angel, 1933; Koller et al., 1983; Gassner, 2001; Gotthardt, 2015) and a second one (Stop 5) forms an outcrop with a length of 12 m and a minimal thickness of 4 m in a valley close to the village of Garrach (Ahrer, 2014). 20 km further to the east, the Rappold Complex appears near to the village Anger. There, a spodumene pegmatite has been described by Esterlus (1983).

Spodumene is up to several centimeters in size and shows a white colour. Due to alterations, it may be slightly greenish or brownish (Ahrer, 2014). The $Li_2O$ content is in the range of 6.56–7.83 wt% (Koller et al., 1983). Beryl is very scarce and inconspicuous with a badly preserved idiomorphic shape and a pale greyish or bluish colour. Exceptionally, it reaches several centimeters in length. Chemical compositions (e.g. Li content, K/Rb ratio) of cm-sized magmatic muscovites from simple pegmatite, leucogranite, moderate fractionated pegmatite and spodumene pegmatite reveal a regional zoning (Fig. 8). Most peculiar is the upward decrease of the K/Rb ratio in the rock column, which reflects the upward migration of melts that get continuously fractionated. It also indicates an upright position of the Rappold Complex with respect to the Permian configuration.

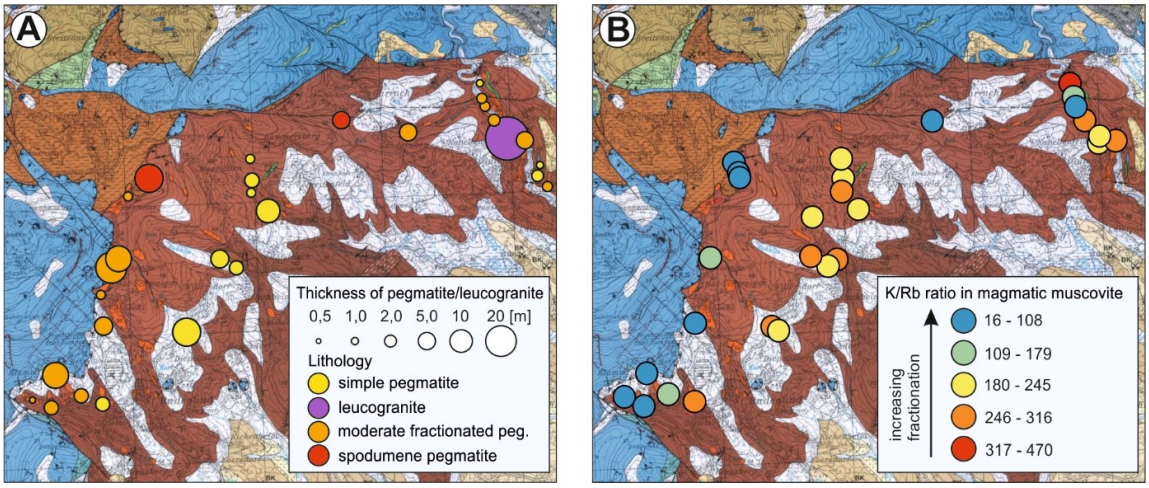


*Fig. 8: Cutout from a database dealing with Permian pegmatite and leucogranite in the Eastern Alps. Visible is the area around the village St. Radegund (Styria/Austria) based on maps in the scale 1:50,000 from the Geological Survey of Austria (legend see Fig. 6). In A) pegmatite bodies and their thickness are displayed. In B) the K/Rb ratio from magmatic muscovites is plotted. The data indicate a clear fractionation trend with decreasing ratios towards the top of the Rappold Complex. This implies an upward increasing fractionation trend and therefore an upright position of the Rappold Complex with respect to the Permian configuration.*

In a detailed study on pegmatite samples from the structurally uppermost part of the Rappold Complex, Koller et al. (1983) investigated the Li, Be and F content of 67 whole rock samples and corresponding muscovite and feldspar. In the whole rocks, they found less than 50 ppm Li in almost all samples, but in a few spodumene-bearing samples it reaches up to 8,500 ppm. The Li content is correlated to the modal amount of muscovite, as the latter contains a few hundred ppm Li in most cases. In the whole rocks Be is typically less than 5 ppm but reaches up to 159 ppm in the highest fractionated samples, whereas in the muscovites it is 1.0–9.7 ppm. F is 100–260 ppm in the whole rocks and 565–2,310 ppm in muscovites. The F content in the whole rock

is much less than in the upper continental crust (557 ppm, Rudnick & Gao, 2003) or granites (~850 ppm, Turekian & Wedepohl, 1961). This fits to the observation that topaz has not been found in any of the Permian pegmatite bodies.

## 4. Description of stops

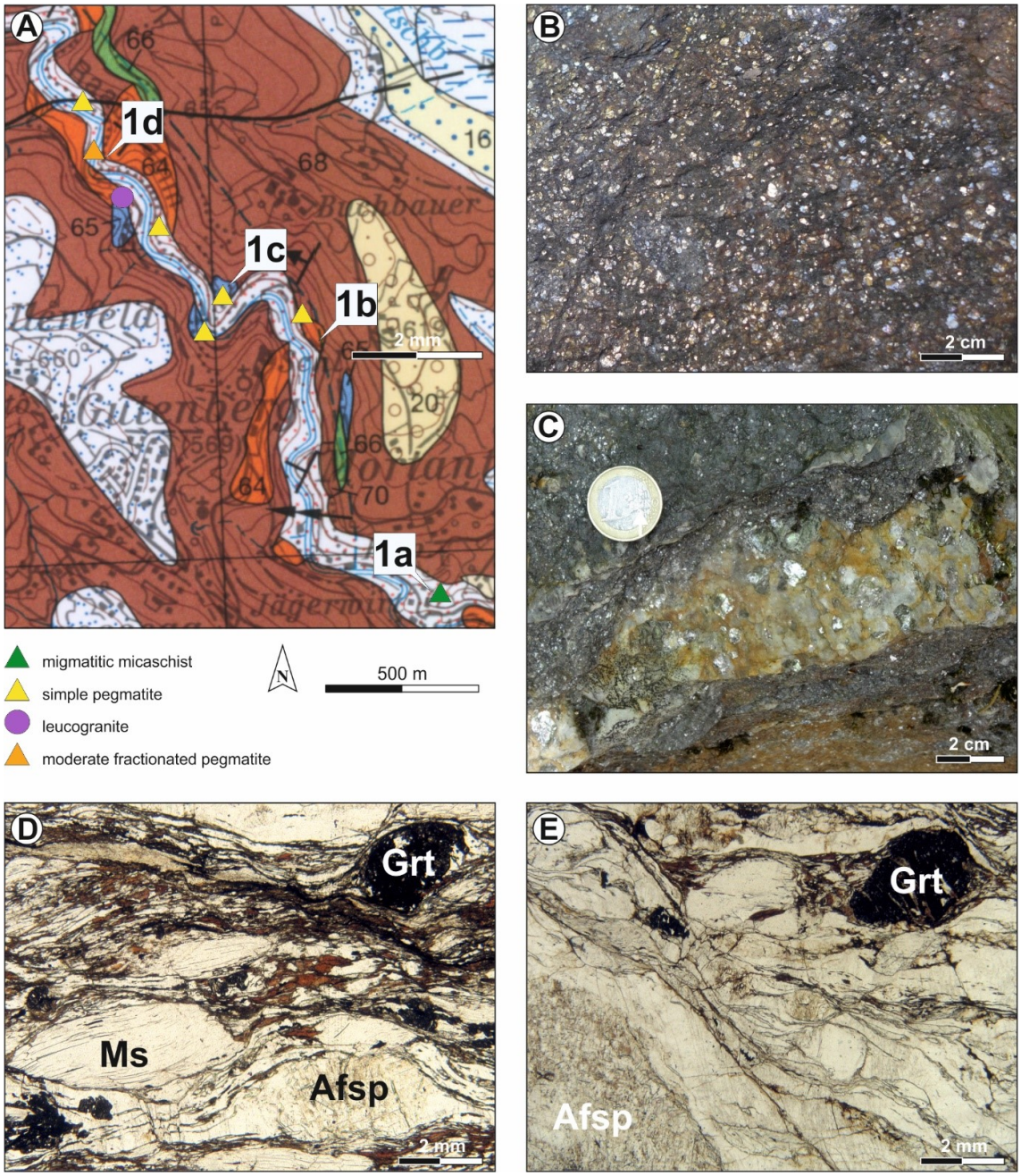


*Fig. 9: Outcrops of Stop 1 and lithologies of Stop 1a. A) Geological map (Flügel et al., 2011) showing a part of the Raabklamm gorge with the four outcrops described in the text. Additionally, the analysed samples from migmatic micaschist, simple pegmatite, leucogranite and moderate fractionated pegmatite are plotted. Legend for lithologies see Figure 6. B) Migmatic micaschist from Stop 1a with large muscovite flakes aligned to the schistosity. C) Pegmatitic patch within migmatic micaschist in Stop 1a. D) Microphotograph of a migmatic micaschist with large muscovite flakes, garnet and alkali feldspar (sample 17R16; parallel polarizers, Stop 1a). E) Microphotograph of a migmatic micaschist with the transition from the paragneiss to a pegmatitic patch with a large alkali feldspar (sample 17R16; parallel polarizers; Stop 1a). Abbreviations: Grt = garnet, Ms = muscovite, Afsp = alkali feldspar.*

STOP 1 RAABKLAMM GORGE: WALK FROM MIGMATITE TO LEUCOGRANITE (FIG.9)
Locality: ÖK50 sheet 164 Graz, outcrops along the hiking path in the Raabklamm gorge.

Parking: At the parking site beside the former restaurant Jägerwirt.

STOP 1A: MIGMATIC MICASCHIST
(WGS 84, 15°34'35.4"E / 47°12'18.9"N)

The outcrops of migmatic micaschist are situated directly along the road beside the former restaurant Jägerwirt. The rocks in the structurally lower part in the southeast have a dominant stromatic to subordinate nebulitic texture, but the differentiation of paleosome and melanosome in this outcrop is difficult. It is mostly layered metatexite formed by 0.5 cm thick in-situ leucosome and 0.5 cm thick melanosome. The leucosome contains quartz + alkali feldspar ± plagioclase ± muscovite ± small garnet and the melanosome is composed of biotite + garnet + muscovite + plagioclase ± quartz.

A few meters further to the northwest along the road, coarse-grained micaschist with partly migmatic texture and up to 0.5 cm large muscovite flakes, aligned within the foliation planes, occurs. Patchy migmatite formed by lensoidal leucosome elongated parallel to the schistosity and graphite-rich paleosome layers are common. The Eoalpine schistosity of the micaschist dips moderately towards SW (217/38).

On the way to Stop 1b several outcrops with smaller bodies of simple pegmatite-(gneiss) occur on both sides of the path.

STOP 1B: SIMPLE PEGMATITE
(WGS 84, 15°34'15.1"E / 47°12'50.3"N)

The simple pegmatite body in this outcrop is > 5 m wide and embedded in fine-grained, brownish to greyish coloured micaschist. The Eoalpine schistosity penetrates partly the pegmatite forming a gneissic texture. The main mineral assemblage is quartz + alkali feldspar ± plagioclase ± muscovite ± garnet (< 0.3 cm). Alkali feldspar can be identified by its greyish-blue colour, whereas plagioclase is white. Rarely some black tourmaline with a maximum size of 0.5 cm occurs. The Eoalpine schistosity dips shallowly towards SSW (202/15).

STOP 1C: SIMPLE PEGMATITE
(WGS 84, 15°34'3.7"E / 47°12'52.5"N


*Fig. 10: Lithologies of Stop 1c. A) Outcrop of layered marble and calcsilicate rock with pegmatite boudins marked by the white dotted line (size of hammer is 0.5 m). B) Microphotograph of a calcsilicate rock composed of calcite + quartz + plagioclase + phlogopite + (clino)zoisite + titanite ± tremolite + opaque ore minerals (sample 17R12, parallel polarizers). Abbreviations: Pl = plagioclase, Zoi = zoisite, Cc = calcite, Phl = phlogopite.*

In this outcrop, a simple pegmatite situated within folded marble, calcsilicate rock and micaschist can be observed (Fig. 10). The contact of the pegmatite with marble has an intricate geometry showing a “bubbly” boudinage like structure. The pegmatite boudins have a thickness of about 0.5 m and a length that is only a little bit larger. The boudins may have formed during the emplacement of the pegmatitic melt within the marble/calcsilicate rock, or during Eoalpine deformation. The pegmatite dike in contact to the micaschist has a maximum thickness of 2 m. The main mineral assemblage of the pegmatite is quartz + alkali feldspar ± plagioclase ± muscovite (< 2 cm) ± tourmaline (< 3 cm). Marble and calcsilicate rock have a white to greyish colour and they show diffuse transitions. While the marble is more coarse-grained and mostly consists of calcite, the calcsilicate rock is fine-grained, inhomogeneous and composed of calcite + quartz + plagioclase + phlogopite + (clino)zoisite + titanite ± tremolite + opaque ore minerals. The micaschist is dark brown, fine to medium-grained and relatively rich in biotite. The Eoalpine schistosity dips moderately towards N (350/32), the fold axis is approximately E–W oriented.

### STOP 1D: LEUCOGRANITE-GNEISS

(WGS 84, 15°33'50.5"E / 47°13'3.1"N)

The leucogranite-gneiss forms an about 100 m thick body, which is disclosed along both sides of the gorge, forming up to 20 m high cliffs. Mostly, it shows a homogeneous fine to medium-grained texture and a mineral assemblage of quartz + alkali feldspar ± plagioclase ± muscovite and additionally small amounts of garnet and tourmaline as ferromagnesian minerals. Locally, inhomogeneous parts with pegmatitic texture occur. Mostly, it shows a penetrative Eoalpine schistosity.

STOP 2 CASTLE RUIN EHRENFELS: STAUROLITE-GARNET-MICASCHIST (FIG. 11)
Locality: ÖK50 sheet 164 Graz, outcrops along the hiking path to and around the castle ruin.

Parking: Beside the main road underneath the castle ruin Ehrenfels.

(WGS 84, 15°28'28.322"E / 47°10'45.834"N)

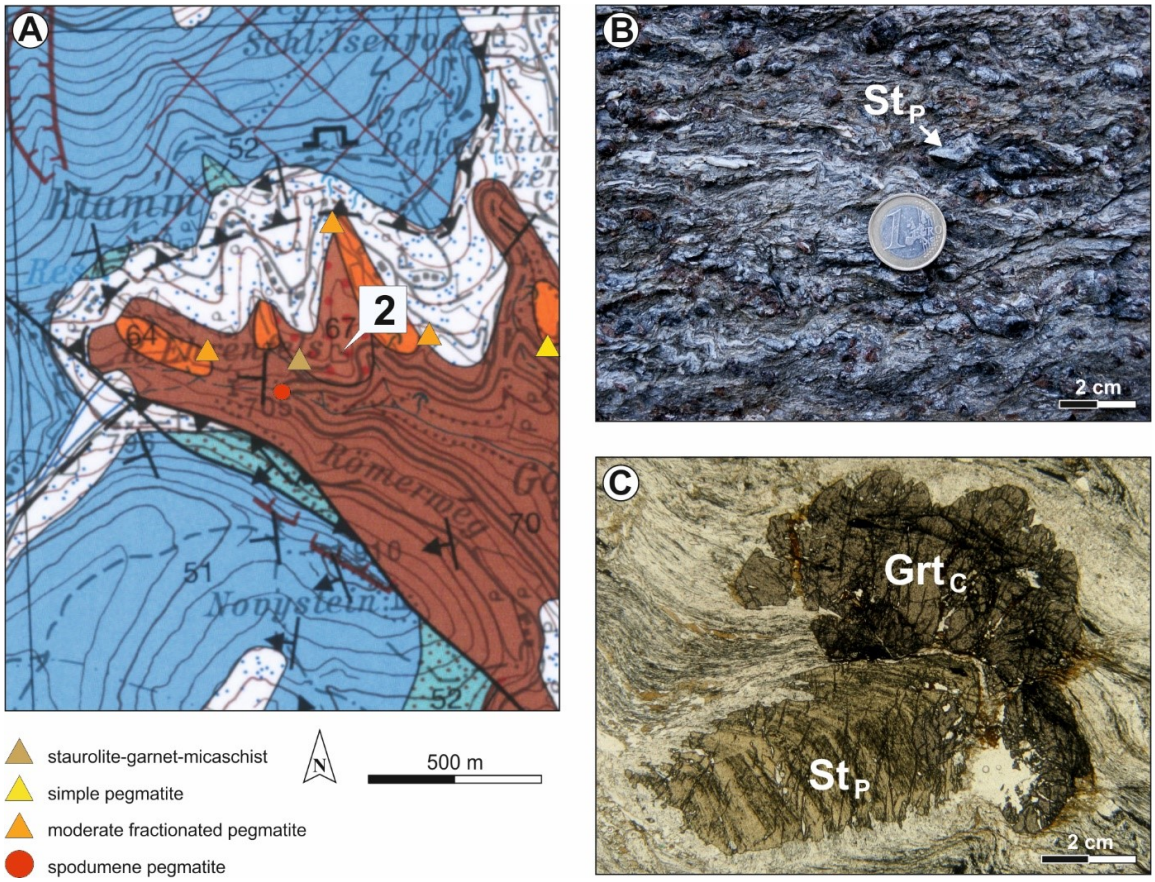


*Fig. 11: Location and lithologies of Stop 2. A) Geological map (Flügel et al., 2011) showing the area around the castle ruin Ehrenfels. Additionally, the analysed samples from simple pegmatite, moderate fractionated pegmatite, spodumene pegmatite and staurolite-garnet-micaschist are plotted. Legend for lithologies see Figure 6. B) Dark gray staurolite-garnet-micaschist in the wall of ruin Ehrenfels. The Permian garnet cores show a reddish color, whereas the staurolite (St) is black. C) Microphotograph of a staurolite-garnet-micaschist (sample 05R04, parallel polarizers). Abbreviations: Grt = garnet, St = staurolite, P = Permian, C = Cretaceous.*

In the tiny outcrops along the path, dark greyish staurolite-garnet-micaschist with a fine-grained matrix is present. Staurolite-rich garnet-micaschist is best exposed in the walls of the castle ruin Ehrenfels, because of the nicely weathered surfaces (Fig. 11B). These rocks were digged in the immediate surrounding. Both, staurolite and garnet are up to more than 1 cm in diameter and show a dark grey colour due to inclusions of graphitic pigment. Garnet is polyphase with a sometimes reddish Permian core and an irregular shaped Eoalpine rim. Based on textural relations, the staurolite formed together with the garnet cores. It shows nice graphite inclusion trails and is partly or fully transformed into sericite (Fig. 11C).

STOP 3: RESTAURANT SCHÖCKLBARTL: MODERATELY FRACTIONATED PEGMATITE (FIG. 12)
Outcrop: ÖK50 sheet 164 Graz, along a hiking path and at the road "Schöcklstraße" beside the restaurant "Schöcklbartl".

Parking: At parking ground directly beside the road "Schöcklstraße" in front of the outcrop.

(WGS 84, 15°29'14.3"E / 47°11'57.2"N)

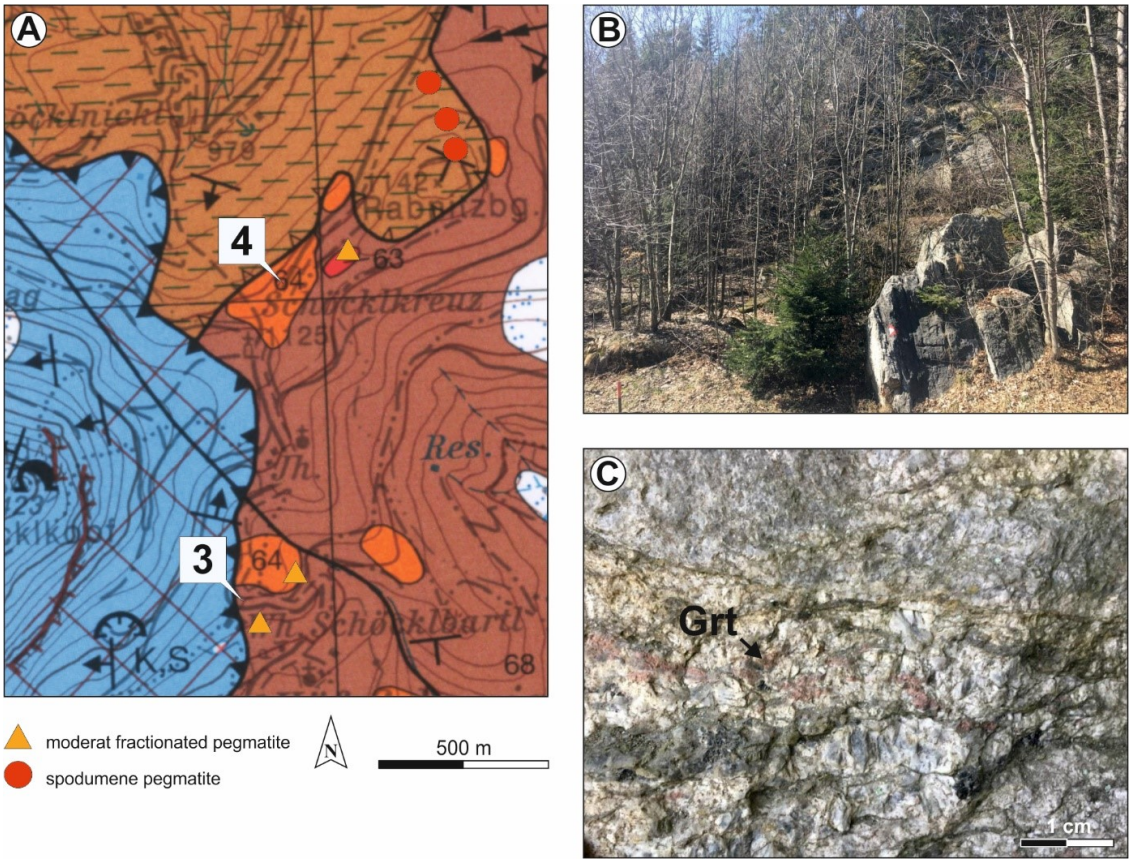


*Fig. 12: Locations of Stop 3 and 4 and lithologies of Stop 3. A) Geological map (Flügel et al., 2011) showing the area around Schöcklkreuz. Additionally, the analysed samples from moderate fractionated pegmatite and spodumene pegmatite are plotted. Legend for lithologies see Figure 6. B) Outcrop of moderate fractionated pegmatite within the forest. From this pegmatite body a Sm-Nd garnet age yields 260 ± 3 Ma (Gotthardt, 2015). C) Garnet-rich layer within the outcrop of Figure 12B.*

Along the hiking path, several meters high outcrops (Fig. 12B) of a moderate fractionated pegmatite dike are present in the forest. The rocks show the usual magmatic assemblage quartz + alkali feldspar + plagioclase ± muscovite, but layers with garnet (Fig. 12C) and/or tourmaline also occur. The rocks exhibit a strong Eoalpine foliation.

STOP 4: SCHÖCKLKREUZ: BERYL-BEARING PEGMATITE (FIG. 12)
Outcrop: ÖK50 sheet 164 Graz, boulders beside the road “Schöcklstraße” northwards of the “Schöcklkreuz”.

Parking: Directly beside the road “Schöcklstraße”.

(WGS 84, 15°29'18.1"E / 47°12'30.0"N

On both sides of the road and around the summit of Rabnitzberg (Altitude 1142 m), several pegmatite boulders with < 2 m in size and a main mineral assemblage of quartz + alkali feldspar ± plagioclase ± muscovite are scattered in the forest. Rarely, beryl with a tabular shape occurs as up to 25 mm large crystals with a badly preserved idiomorphic shape and a milky white to pale blue colour. Some bolders of spodumene pegmatite can be found along the hiking path from Schöcklkreuz to restaurant Schöcklnickl (Walter Postl, pers. com.).

STOP 5: GARRACH: SPODUMENE PEGMATITE (FIG. 13)
Locality: ÖK50 sheet 164 Graz, outcrop in the forest near the path “Schneidebertl Weg”

Parking: Beside the fire brigade at the beginning of the path “Schneidebertl Weg” in Garrach

(WGS 84, 15°32'1.0"E / 47°13'2.6"N)

From the parking ground, a forest road follows the northern side of a smooth valley towards the west. After about 700 m small outcrops are visible on the southern side of the valley (Fig. 13B). They mostly consist of a spodumene pegmatite body, which can be traced for about 10 m with a maximal width of 4 m. The contact to the surrounding micaschist and paragneiss is not visible. After Ahrer (2014), five zones can be distinguished within the pegmatite body: (1) The outer part is fine-grained, showing a penetrative Eoalpine schistosity. The main mineral assemblage consists of quartz + alkali feldspar + plagioclase ± garnet ± spodumene. (2) In a medium to coarse-grained zone the feldspar content is less than in zone (1), whereas the quartz, muscovite (< 0.5 cm) and spodumene (< 1 cm) contents raise. (3) A coarse-grained zone composed of quartz + alkali feldspar + plagioclase ± garnet with frequent spodumene crystals up to 3 cm in size (Fig. 13C, D, E). (4) A medium to coarse-grained zone rich in muscovite (< 3 cm) with additional quartz + alkali feldspar + plagioclase ± garnet. (5) The core zone contains up to decimeter sized albite crystals with medium to coarse-grained quartz and spodumene. Tourmaline occurs as accessory in some zones as < 4 cm long crystals. Around the spodumene pegmatite body, greyish-brown, fine-grained micaschist occurs. Biotite and muscovite form the foliation planes. In some parts, idiomorphic garnet (< 0.2 cm) occurs. The Eoalpine schistosity dips moderatly towards W (278/29).

ACKNOWLEDGEMENTS
The authors thank Walter Postl and Kurt Krenn (Karl-Franzens University of Graz) for providing additional information and photos from the field. Christine Hörfarter is acknowledged for her logistic assistance during the excursion.

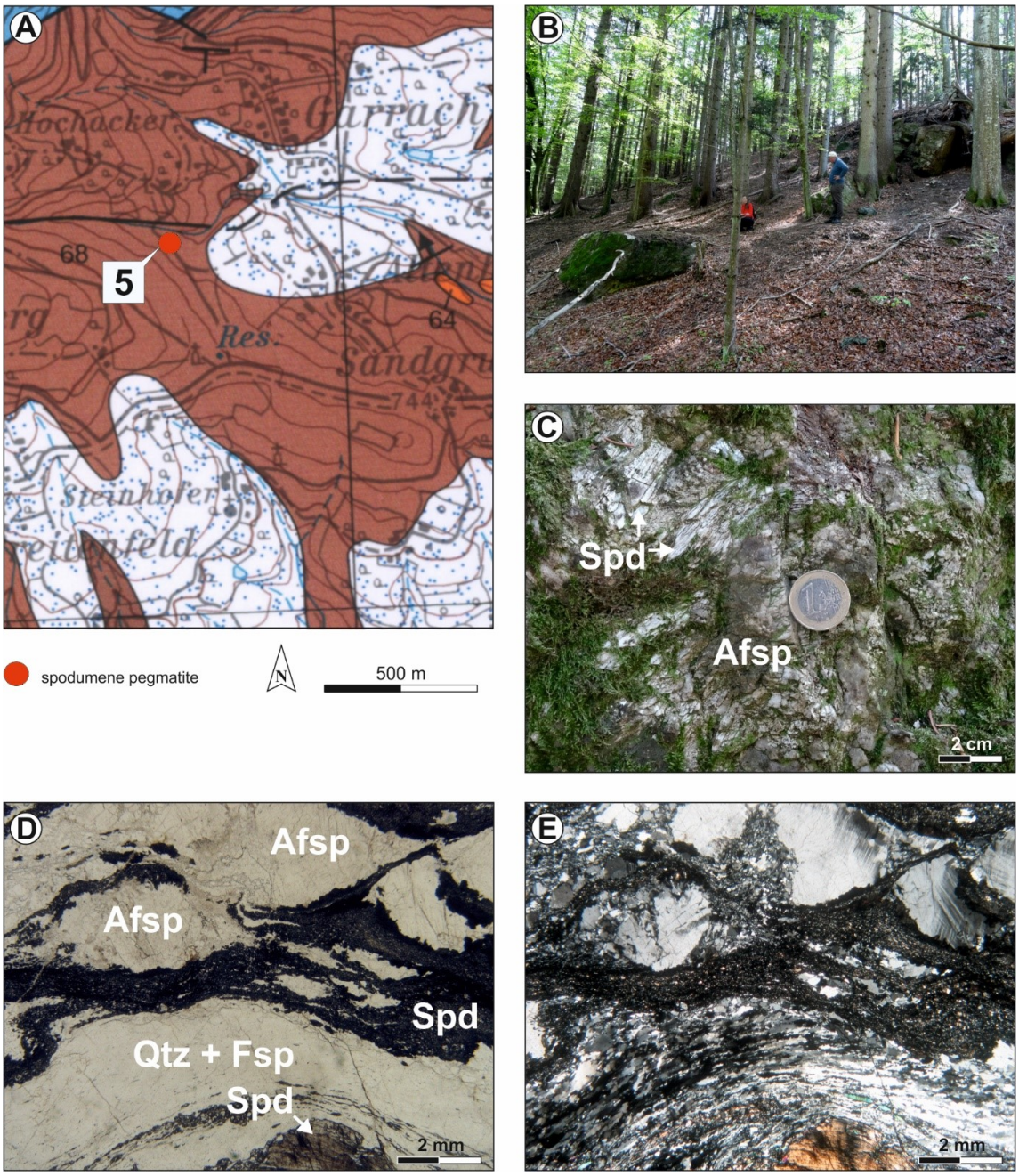


*Fig. 13: Location and lithologies of Stop 5. A) Geological map (Flügel et al., 2011) showing the area around Garrach with the investigated spodumene pegmatite. Legend for lithologies see Figure 6. B) Spodumene pegmatite outcrop described by Ahrer (2014) at the southern side of the valley. C) White spodumene crystals within a matrix with alkali feldspar, plagioclase and quartz. D + E) Microphotograph of mylonitized spodumene pegmatite (sample 17R11, parallel and crossed polarizers). Abbreviations: Spd = spodumene, Afsp = alkali feldspar, Fsp = alkali feldspar and plagioclase, Qtz = quartz.*

## REFERENCES


Ahrer, S. (2014): Geowissenschaftliche und aufbereitungstechnische Untersuchungen an ausgewählten Pegmatiten und deren Nb-Ta-Vererzungen in den Ostalpen, Steiermark, Österreich. – Unpublished Master Thesis, Montanuniversität Leoben, 105 pp., Leoben.

Angel, F. (1933) Spodumen und Beryll aus den Pegmatiten von St. Radegund bei Graz. – Zeitschrift für Kristallographie, Mineralogie und Petrographie, **43**/6, 441–446, Leipzig.

Cassinis, G., Perotti, C.R. & Ronchi, A. (2012): Permian continental basins in the Southern Alps (Italy) and peri-mediterranean correlations. – International Journal of Earth Sciences, **101**/1**,** 129–157, Berlin–Heidelberg.

Černý, P. & Burt, D.M. (1984): Paragenesis, crystallochemical characteristics, and geochemical evolution of micas in granite pegmatites. – In: Bailey, S.W. (Ed.): Micas. – Reviews in Mineralogy, **13**, 257–297, Washington, D.C.

Černý, P. & Ercit, T.S. (2005): The classification of granitic pegmatites revisited. – The Canadian Mineralogist, **43**/6, 2005–2026, Quebec.

Davis, H.J. & von Blankenburg, F. (1995): Slab breakoff: A model of lithosphere detachment and its test in the magmatism and deformation of collisional orogens. – Earth and Planetary Science Letters, **129**, 85–102, Amsterdam.

Dunkl, I., Grasemann, B. & Frisch, W. (1998): Thermal effects of exhumation of a metamorphic core complex on hanging wall syn-rift sediments: an example from the Rechnitz Window, Eastern Alps. – Tectonophysics, **297**, 31–50, Amsterdam.

Eisenberg, J. & Hauzenberger, C. (2001): Geologisch-petrologische Geländebeobachtungen des nordwestlichen Radegunder Kristallins. – Mitteilungen des naturwissenschaftlichen Vereins für Steiermark, **131**, 5–17, Graz.

Esterlius, M. (1983): Kurzer Überblick über die Pegmatite im Angerkristallin der Oststeiermark. – Archiv für Lagerstättenforschung der Geologischen Bundesanstalt, **3**, 31–34, Wien.

Flügel, H.W., Nowotny, A. & Gross, M. (2011): Geologische Karte der Republik Österreich 1:50,000, Blatt 164 Graz. – Geologische Bundesanstalt, Wien.

Frank, N., Kurz, W., He, D., Schuster, R., Dong, Y. & Hauzenberger, C. (2019): Detrital U/Pb zircon age distribution in metasedimentary units of the Eastern Alps. – EGU General Assembly 2019, Geophysical Research Abstracts, **21**, EGU2019-17014-1, Katlenburg-Lindau.

Froitzheim, N., Plašienka, D. & Schuster, R. (2008): Alpine tectonics of the Alps and Western Carpathians. – In: McCann, T. (Ed.): The Geology of Central Europe. Volume 2: Mesozoic and Cenozoic, Geological Society of London, 1141–1232, London.

Froitzheim, N., Schmid, S.M. & Frey, M. (1996): Mesozoic paleoegeography and the timing of eclogitefacies metamorphism in the Alps: A working hypothesis. – Eclogae Geologicae Helvetiae, **89**/1, 81–110, Basel.

Fügenschuh, B., Seward, D. & Mancktelow, N. (1997): Exhumation in a convergent orogen: the western Tauern window. – Terra Nova, **9**, 213–217, Oxford.

Gaidies, F., Abart, R., DeCapitani, C., Schuster, R., Connolly, J.A.D. & Reusser, E. (2006): Characterisation of polymetamorphism in the Austroalpine basement east of the Tauern Window using garnet isopleth thermobarometry. – Journal of metamorphic Geology, **24**, 451–475, Oxford.

Gassner, M. (2001): Geochemische und petrologische Untersuchungen an ausgewählten steirischen Pegmatiten (Koralpe, Stubalpe, Kristallin von St. Radegund, Anger-Kristallin). – Unpublished Master Thesis, Montanuniversität Leoben, 176 pp., Leoben.

Genser, J. & Neubauer, F. (1989): Low angle normal faults at the eastern margin of the Tauern window (Eastern Alps). – Mitteilungen der Österreichischen Geologischen Gesellschaft, **81**, 233–243, Wien.

Göd, R. (1989): The spodumene deposit at "Weinebene", Koralpe, Austria. – Mineralium Deposita, **24**, 270–278, Berlin.

Gotthardt, C. (2015): Pegmatitgenese des Radegunder Kristallins, des Millstätter Kristallins und der Kreuzeckgruppe. – Unpublished Master Thesis, Technische Universität Graz, 156 pp., Graz.

Habler, G. & Thöni, M. (2001): Preservation of Permo-Triassic low-pressure assemblages in the Cretaceous high-pressure metamorphic Saualpe crystalline basement (Eastern Alps, Austria). – Journal of Metamorphic Geology, **19**, 679–697, Oxford.

Hauzenberger, C., Roeggla, M., Schuster, R. & Nowotny, A. (2008): New petrological results from the "Anger" and "Radegund Crystalline", two polymetamorphic Austroalpine basement occurrences east of the Tauern window (Alps, Austria/Europe). – Abstract Volume "2nd Workshop and Summer School on Architecture of Collisional Orogens: Eastern Alps versus China Central Orogenic Belt", September 5–15, 2008, Department of Geology, Northwest University Xian (China), 20–22, Xian.

Hoinkes, G., Koller, F., Rantitsch, G., Dachs, E., Höck, V., Neubauer, F. & Schuster, R. (1999): Alpine metamorphism of the Eastern Alps. – Schweizerische Mineralogische und Petrographische Mitteilungen, **79**, 155–181, Basel.

Ilickovic, T., Schuster, R., Mali, H., Onuk, P. & Horschinegg, M. (2017): Genesis of spodumene pegmatites in the Austroalpine unit (Eastern Alps): isotopic and geochemical investigations. – Abstracts and proceedings of the Geological Society of Norway (8th International Symposion on Granitic Pegmatites, Kristiansand, 14.–19.06.2017), **2/2017**, 54–57, Oslo.

Janák, M., Froitzheim, N., Yoshida, K., Sasinková, V., Nosko, M., Kobayashi, T., Hirajima, T. & Vrabec, M. (2015): Diamond in metasedimentary crustal rocks from Pohorje, Eastern Alps: a window to deep continental subduction. – Journal of Metamorphic Geology, **33**, 495–512, Oxford.

Knoll, T., Schuster, R., Mali, H., Onuk, P., Huet, B., Horschinegg, M., Ertl, A. & Gister, G. (2018): Spodumene pegmatites and related leucogranites from the Austroalpine Unit (Eastern Alps): field relations, petrology, geochemistry and geochronology. – The Canadian Mineralogist, **56**, 489–528, Quebec. http://dx.doi.org/10.3749/canmin.1700092

Koller, F., Götzinger, M.A., Neumayer, R. & Niedermayr, G. (1983): Beiträge zur Mineralogie und Geochemie der Pegmatite des St. Radegunder Kristallins und der Gleinalpe. – Archiv für Lagerstättenforschung der Geologischen Bundesanstalt, **3**, 47–65, Wien.

Kunz, B.E., Manzotti, P., von Niederhäusern, B., Engi, M., Darling, J.R., Giuntoli, F. & Lanari, P. (2018): Permian high-temperature metamorphism in the Western Alps (NW Italy). – International Journal of Earth Sciences, **107**/1, 203–229, Berlin–Heidelberg.

Kurz, W. & Fritz, H. (2003): Tectonometamorphic evolution of the Austroalpine Nappe Complex in the central Eastern Alps – consequences for the Eo-Alpine evolution of the Eastern Alps. – International Geology Review, **45**, 100–127, Columbia.

Luth, S.W. & Willingshofer, E. (2008): Mapping of the post-collisional cooling history of the Eastern Alps. – Swiss Journal of Geoscience Supplements, **101**, 207–223, Heidelberg.

Mali, H. (2004): Die Spodumenpegmatite von Brettstein und Pusterwald (Wölzer Tauern, Steiermark, Österreich). – Joannea-Mineralogie, **2**, 5–53, Graz.

Mali, H., Schuster, R., Knoll, T. & Huet, B. (2019): Zoning of pegmatite fields as a key for unraveling the internal structure of basement nappes: examples from the Eastern Alps (Austria). – EGU General Assembly 2019, Geophysical Research Abstracts, **21**, EGU2019-14565, Katlenburg-Lindau.

Neubauer, F., Genser, J. & Handler, R. (2000): The Eastern Alps: Result of a two-stage collision process. – Mitteilungen der Österreichischen Geologischen Gesellschaft, **92**, 117–134, Wien.

Nowotny, A. (2007): Bericht 2006 über geologische Aufnahmen auf Blatt 164 Graz. – Jahrbuch der Geologischen Bundesanstalt, **147**/3–4, 664–665, Wien.

Nowotny, A. (2008): Bericht 2007 über geologische Aufnahmen auf Blatt 164 Graz. – Jahrbuch der Geologischen Bundesanstalt, **148**/2, 266–26, Wien.

Puhr, B., Schuster, R., Hoinkes, G. & Moshammer, B. (2009): $^{87}Sr/^{86}Sr$ isotope study of marbles. – Abstract Volume, 9th Workshop on Alpine Geological Studies (Cogne/Italy), 16.–18. September 2009, 83, Cogne.

Quick, J.E., Sinigoi, S. & Mayer, A. (1995): Emplacement of mantle peridotite in lower continental crust, Ivrea-Verbano zone, northwest Italy. – Geology, **23**, 739–742, Washington, D.C.

Ratschbacher, L., Frisch, W., Neubauer, F., Schmid, S.M. & Neugebauer, J. (1989): Extension in compressional orogenic belts: The Eastern Alps. – Geology, **17**, 404–407, Washington, D.C.

Röggla, M. (2007): Petrographie und Petrologie des Anger Kristallins, Steiermark. – Unpublished Master Thesis, Naturwissenschaftliche Fakultät der Karl-Franzens-Universität-Graz, 168 pp, Graz.

Rudnick, R.L. & Gao, S. (2003) Composition of the Continental Crust. – In: Rudnick, R.L. (Ed.): The Crust, 1–64, Oxford (Elsevier-Pergamon).

Sander, B. (1921): Zur Geologie der Zentralalpen. – Jahrbuch der Geologischen Staatsanstalt, **71**/3–4, 174–224, Wien.

Scharf, A., Handy, M.R., Favaro, S., Schmid, S.M. & Bertrand, A. (2013): Modes of orogen-parallel stretching and extensional exhumation in response to microplate indentation and roll-back subduction (Tauern Window, Eastern Alps). – International Journal of Earth Science (Geologische Rundschau), **102**/6, 1627–1654, Heidelberg.

Schmid, S., Scharf, A., Handy, M. & Rosenberg, C. (2013): The Tauern Window (Eastern Alps, Austria): a new tectonic map, with cross-sections and a tectonometamorphic synthesis. – Swiss Journal of Geosciences, **106**, 1–32, Basel.

Schuster, R. & Stüwe, K. (2008): The Permian Metamorphic Event in the Alps. – Geology, **36**/8, 303–306, Washington, D.C. http://dx.doi.org/10.1130/G24703A.1

Schuster, R., Scharbert, S., Abart, R. & Frank, W. (2001): Permo-Triassic extension and related HT/LP metamorphism in the Austroalpine – Southalpine realm. – Mitteilungen der Gesellschaft der Geologie- und Bergbaustudenten in Österreich, **44**, 111–141, Wien.

Schuster, R., Koller, F., Hoeck, V., Hoinkes, G. & Bousquet, R. (2004): Explanatory notes to the map: Metamorphic structure of the Alps – Metamorphic evolution of the Eastern Alps. – Mitteilungen der Österreichischen Mineralogischen Gesellschaft, **149**, 175–199, Wien.

Schuster, R., Ilickovic, T., Mali, H., Huet, B. & Schedl, A. (2017): Permian pegmatites and spodumene pegmatites in the Alps: Formation during regional scale high temperature/low pressure metamorphism. – Abstracts and proceedings of the Geological Society of Norway (8th International Symposion on Granitic Pegmatites, Kristiansand, 14.–19.06.2017), **2/2017**, 122–125, Oslo.

Schuster, R., Huet, B., Knoll, T. & Paulick, H. (2019): Anatectic origin of albite-spodumene pegmatites: a geochemical model. – EGU General Assembly 2019, Geophysical Research Abstracts, **21**, EGU2019–7277, Katlenburg-Lindau.

Stöckert, B. (1987): Das Uttenheimer Pegmatitfeld (Ostalpines Altkristallin, Südtirol) Genese und alpine Überprägung. – Erlanger geologische Abhandlungen, **114**, 83–106, Erlangen.

Stüwe, K. & Schuster, R. (2010): Initiation of subduction in the Alps: Continent or ocean? – Geology, **38**, 175–178, Boulder.

Thöni, M. (1999): A review of geochronological data from the Eastern Alps. – Schweizerische Mineralogische und Petrographische Mitteilungen, **79**, 209-230, Basel.

Thöni, M. (2006): Dating eclogite-facies metamorphism in the Eastern Alps – approaches, results, interpretations: a review. – Mineralogy and Petrology, **88**/1/2, 123–148, Wien.

Thöni, M. & Miller, C. (2000): Permo-Triassic pegmatites in the eo-Alpine eclogite-facies Koralpe complex, Austria: age and magma source constraints from mineral chemical, Rb-Sr and Sm-Nd isotopic data. – Schweizerische Mineralogische und Petrographische Mitteilungen, **80**, 169–186, Zürich. http://dx.doi.org/10.5169/seals-60959

Thöni, M., Miller, C., Zanetti, A., Habler, G. & Goessler, W. (2008): Sm-Nd isotope systematics of high-REE accessory minerals and major phases: ID-TIMS, LA-ICP-MS and EPMA data constrain multiple Permian-Triassic pegmatite emplacement in the Koralpe, Eastern Alps. – Chemical Geology, **254**, 216–237, Amsterdam. http://dx.doi.org/10.1016/j.chemgeo.2008.03.008

Turekian, K.K. & Wedepohl, K.H. (1961): Distribution of the elements in some major units of the earth's crust. – Geological Society of America Bulletin, **72**, 175–182, Boulder.

## 6. DISCUSSION OF THE ARGUMENTS AGAINST THE ANATECTIC MODEL

In his seminal paper, Černý (1991) raised nine issues against the possibility for rare element pegmatite to derive from an anatectic melt. We do not doubt that these arguments are relevant for many pegmatite occurrences. Nevertheless, some of his arguments against the anatectic model could be answered on the basis of our research. In this chapter, we discuss each of the issues raised by Černý (1991) in the light of our data and model presented in the previous chapters of this work. We can show that these arguments are actually not entirely relevant for the investigated Austroalpine Unit Pegmatite Province and the supporting geochemical model. In the following, each argument is discussed after quoting the text of Černý (1991). Please note that this discussion only pertains to lithium and more research is needed for testing the anatectic model for other classes/types of economically relevant pegmatite. Notice that London (2018) also suggests that some arguments against the anatectic model might not be relevant.

### THE LITHIUM-RICH PROTOLITH

"Lithologies that may serve as protholiths extraordinary enriched in rare elements (such as evaporites) are scarce in high-grade metamorphic terranes (and just about any Archean terranes), they do not cover the full spectrum of elements represented in different pegmatite types and many of them (e.g. evaporites) would be prone to devolatilization coupled with dispersion early in prograde metamorphism (Černý, 1991b)."

Lithium may indeed be concentrated in evaporites at 1000s ppm levels (Warren, 2009) but can also be enriched in Al-rich pelite though at 100 ppm level (Chan et al., 2006). The Li-rich metasediments that form the protolith of the anatectic melt in the AUPP have a common shale major element chemistry and do not evidence for an evaporitic origin. Hence, the Li concentration in rather common Al-rich pelite may be distinctly higher than in the average crust and our investigations show that this may be maintained after metamorphism in the amphibolite-facies. Even though Li can be lost through devolatilization during prograde metamorphism (Zack et al., 2003; Marschall et al., 2007; Qiu et al., 2011), staurolite is a typical phase of amphibolite-facies Al-rich metapelite and it may contain up to 5900 ppm Li (Dutrow et al., 1986). Therefore, large amounts of Li can be stored in metapelite until staurolite breaks down in presence of melt, transferring Li efficiently into a low-percentage granitic melt. We reckon that the albite-spodumene pegmatite of the AUPP do not contain the full spectrum of rare elements. Especially, they are commonly very poor in REE, Ti, U, Th, Sn, Ta, Nb, Rb, Cs, Be, B and/or F that are considered as typical for the different types of Li-rich pegmatite (Ercit et al., 2005). In the AUPP the phases containing these elements are refractory (biotite, garnet) or accessory (e.g. zircon, rutile, monazite, apatite) and detectable with the SEM. This discrepancy might reflect two different genetic processes. Pegmatite with a large spectrum of rare elements would derive from fertile granite intrusions or anatectic melts formed above the temperature of biotite dehydration melting (see above) while albite-spodumene pegmatite devoid of rare elements other than Li would derive from anatectic melts formed below the temperature of biotite dehydration melting.

### VALIDITY OF THE PARTITIONING COEFFICIENTS

"Extremely low-percentage melting would be required to generate anatectic magmas even remotely similar to complex pegmatite and would do so only if partition coefficients that work at <20% melting could be realistically extrapolated to about <3% melting (Černý, 1991b)."

We reckon that experimental work has to be carried out for measuring the Li distribution between the solid phases and melt at different pressures, temperatures and melt fractions in well-controlled environments. In absence of such studies, we established a set of coefficients that correspond to Li partitioning at both sub- and suprasolidus conditions in natural and experimental systems. This set is clearly preliminary but we believe that if our partitioning coefficients study are not accurate, they tend to provide conservative estimates for Li

concentration in the melt (see Chapter 4). Especially, we have chosen a rather high partitioning coefficient between melt and biotite experimentally determined at temperatures slightly above the solidus (Icenhower & London, 1995). This coefficient should therefore be valid for partitioning with low-fraction melt. Our model shows that very large concentrations up to a few 1000 ppm Li can be reached for very low melt fractions of 4-5 vol%. This is consistent with the argument pointed out by Černý (1991) and initially noticed by Stewart (1978). However, the model also shows that Li concentrations of a few 100s ppm Li can be achieved for melt fractions of 10-20 vol%, even with conservative partitioning coefficients.

THE NATURE OF THE LITHIUM CARRIER IN METASEDIMENT

"In metamorphic rocks, lithophile rare elements, such as Li, Ta, Nb, Ti, Sc and Sn, are bound in mafic silicates and accessory oxide minerals, and at least biotite and hornblende (if not pyroxenes and refractory oxide minerals) would have to be broken down. At that stage, partial melts would be Ca-enriched and rare-element concentrations much below their abundances typical of pegmatites (Černý, 1991)."

A major argument of our model is that staurolite is the main Li carrier in amphibolite-facies Al-rich metapelite in agreement with Dutrow et al. (1986). This phase can remain stable or metastable at the onset of melting (see Chapter 3), demonstrating that not only biotite, amphibole or pyroxene need to break down for transfer Li into an anatectic melt. Due to the small amount of Ca in the protolith and the peritectic growth of garnet and biotite the Ca, Mg and Fe content in the melt are low, as reflected by the presented analyses. As the major carriers of Ta, Nb, Ti, Sc, and Zr (biotite, accessory minerals) do not contribute to the melt, these elements are depleted in most of the pegmatite and leucogranite of the AUPP.

LI BALANCE BETWEEN METAPELITE AND PEGMATITE

"Concentrations of rare elements encountered in complex pegmatite would require substantial removal of these elements from very large volumes of source rocks such as metapelites (Černý, 1991)."

The Permian event affected a large crustal domain now incorporated in the Adria derived units of the Alps, including the Austroalpine Unit (Schuster & Stüwe, 2008). Several kilometers of the lower part of the crust experienced upper amphibolite- and granulite-facies conditions as an effect of heat conduction related to lithospheric stretching and heat advection due to magmatic underplating (Henk et al, 1997). Additionally, the available geochronological data argues for protracted crustal melting over 40 Ma. Hence, as observed in the Ivrea Zone, which is one of the deepest exposed section of the Permian crust, melting might have been generalized in the lower crust (Kunz et al., 2018). We here present a simple mass balance calculation based on the results of our model. We consider the Weinebene deposit (Saualpe-Koralpe Complex) that hosts the largest albite-spodumene pegmatite swarm of the AUPP (Göd, 1989; Chapter 4). There, 7 dikes with economic potential have an average thickness of 2 m and have been identified over a maximum distance along strike of 1.5 km and a maximum down dip distance of 450 m. This corresponds to total area of 4500 m2 per section perpendicular to the strike direction. Assuming a fractionation degree of 90% or 99% (see Chapter 4) and an extracted melt fraction of 20 vol% (see Chapter 4), this implies an area of molten metapelite of approximately 0.23 to 2.3 $km^2$. The lower and upper bounds represent melt collection and extraction from an area of 1 km width over a thickness of 270 m and 2.7 km, respectively. Both bounds appear realistic owing to the thermal state of the crust during the Permian event. Notice that this calculation considers the largest albite-spodumene pegmatite deposit of the AUPP and maximum values for the dike down dip depth. This implies that the smaller albite-spodumene pegmatite deposits correspond to smaller estimates of molten area.

MECHANISMS OF MELT SEGREGATION AND EXTRACTION

"Segregation of low-percentage melts (<3%) from enormous volumes of protolith into restricted spaces occupied by complex pegmatite would be mechanically difficult, and probably impossible (Černý, 1991)."

Segregation and migration of low-percentage melt is indeed unlikely (see Chapter 4). However, the argument of Černý (1991) is based on the idea that only low-percentage anatectic melt can be sufficiently rich in lithium for crystallizing Li-rich pegmatite (Stewart, 1978). As noticed by London (2018) this roots in the assumption made by Stewart (1978) that fractional crystallization of granitic melts to rare-element-rich compositions at low temperatures is reversible. Consequently, this process could not significantly contribute to enrich the melt. This notion is actually not relevant (London, 2018 and references therein), implying that larger-percentage melt could be a relevant source after fractional crystallization. Our geochemical model actually demonstrates that for realistic values of 7-20 % melt, Li can be sufficiently enriched in the melt by fractional crystallization for producing albite-spodumene pegmatite (see Chapter 4). The calculation presented above additionally shows that the volume of molten protolith do not have to be "enormous". What is more, the Permian metamorphic record and our field observations imply that melt migrated through at least 7 km of crustal thickness which do not correspond to a "restricted space". We admit that collection and channelizing of Li-rich anatectic melt from a volume of migmatitic metasediment remains to be understood.

MECHANISMS OF MELT EMPLACEMENT

"Passive flow of such melts down a pressure gradient into open space to be filled by pegmatite melt cannot be reconciled with the observed forcible mode of emplacement (Černý, 1991)."

The driving force of migration is probably buoyancy (see Chapter 4) as considered by Černý (1991). However, his concept of emplacement assumes open space (London, 2008), which we do not observe in the AUPP as the investigated albite-spodumene pegmatite are no miarolitic. Instead, the field observations suggest that anatectic melt migrates through a network of channels parallel and oblique to the schistosity and/or pervasively. The very inhomogeneus textures of the leucogranite bodys argues for a repeated feeding by melt pulses with different grade of fractionation over an extended time. The melt finally emplaces either as sills parallel to the schistosity or as dikes discordant to it that reactivate brittle fractures.

CHEMICAL INTERACTION BETWEEN MELT AND HOST-ROCK

"Were such a segregation feasible, the melts passing through contrasting metamorphic lithologies would react with them, and lose most of their content of rare elements in the process (Černý, 1991)."

In the AUPP several features argue for interaction of the melts with the country rock. (1) Coarse-grained muscovite commonly occurring in the paleosome of migmatite as well as in micaschist and paragneiss of the lowest part of intermediate level are interpreted as an evidence of interaction between the melt and its solid matrix. (2) The same applies to anomalously large alkali-feldspar in paragneiss and tourmaline nests in the host rock surrounding pegmatite in the higher structural level. (3) Li-bearing dravitic tourmaline has been described at the contact between marble and evolved pegmatite, partly spodumene-bearing (Ertl et al., 2010). (5) Elevated Li concentrations and holmquistite (a Li bearing amphibole) have been described in amphibolite hosting the albite-spodumene pegmatite dikes of the Weinebene spodumene deposit (Göd, 1989). No Li exchange with the surrounding paragneiss has however been described there. In spite of these local evidence, the systematic increase of Li concentration in the melt through magmatic fractionation documented in the whole rock composition and muscovite suggests that loss of Li during melt migration was not significant. Eventually, if loss of

rare elements during melt migration would be a limiting factor, this would also apply to pegmatitic melts related to fertile granite intrusions, because the latter also migrate up to a few kilometers from their source (Černý, 1991, London, 2018).

### Evidence from radiogenic isotope geochemistry

"Localities examined in sufficient detail show systematics of radiogenic isotopes in pegmatite sharply discordant with those of the host rock and their deep seated analogs (Černý, 1991)."

A large set of Sr and Nd isotopic compositions is available for metapelite and different pegmatite types of the Austroalpine Unit. In agreement with the statement above, the isotopic values of metapelite and pegmatite recalculated to the time of pegmatite formation (ca. 260 Ma) are different. This is not surprising because there is no isotopic equilibrium between the paleosome and melt during partial melting for the following reasons. Most minerals with significant amounts of REE and with elevated Sm/Nd ratios (garnet, zircon or monazite) remained in the paleosome. For this reason, the paleosome archived more radiogenic 143Nd from the 147Sm decay, and consequently lower 143Nd/144Nd ratios and Nd values than the melt. The situation for the Sr isotopic system is more complex, because several minerals with high concentrations in Sr or Rb but very different Rb/Sr ratios were present in the metapelite (muscovite, biotite, plagioclase, K-feldspar, apatite). Depending on the modal amount of these minerals in the metapelite and the amount of melt produced, different initial isotopic ratios could have developed (e.g. Bea, 1996). In any case partial melting induced isotopic fractionation and different initial Nd and Sr isotopic signatures. The isotopic discordance between pegmatite and their sedimentary source is therefore not an argument against the anatectic model.

### Field evidence

"Last but not least, not a single case of 'aborted segregation' of highly fractionated pegmatite melts in statu of metamorphic/anatectic nascendi has been observed; on the contrary, all partial melts show primitive geochemistry (such as abyssal- or muscovite-class pegmatite stringers), and dispersed rare-element distribution around pegmatites is proven to be exomorphic (Černý, 1991)."

All elements forming the complete evolution from the anatectic Al-rich metapelite to the crystallization of albite-spodumene pegmatite are preserved and visible in outcrops of the Austroalpine Unit Pegmatite Province. They have been overlooked or misinterpreted for a long time and this can be true also in other pegmatite regions. As argued in Chapter 4 leucosome of patchy migmatite represent segregated melts, potentially in compaction melt bands. Net-textured migmatite and pegmatite dikes represent localized melt channels whereas the anomalously large muscovite and alkali-feldspar crystals are interpreted as leftovers from pervasively migrating melt. The early products of this process indeed show a primitive geochemistry and mineralogy compatible with the abyssal- and the muscovite-class. However, the melt evolution is compatible with a continuous chemical fractional crystallization trend documented by trace element analyses of rock and muscovite. In evolved pegmatite some additional minerals like beryl, andalusite, minor ore minerals and spodumene appear, but in general the mineral composition remains simple.

## REFERENCES


Bea, F., 1996. Controls on the trace element composition of crustal melts. Transactions of the Royal Society of Edinburgh-Earth Sciences. 87(1), 33-42.

Černý, P., 1991. Rare-element Granitic Pegmatites. Part II: Regional to Global evironments and Petrogenesis. Geoscience Canada. 18(2), 68–81.

Chan, L. H., Leeman, W. P., Plank, T., 2006. Lithium isotopic composition of marine sediments. Geochemistry, Geophysics, Geosystems. 7(6).

Dutrow, B. L., Holdaway, M. J., Hinton, R. W., 1986. Lithium in staurolite and its petrologic significance. Contributions to Mineralogy and Petrology. 94(4), 496-506.

Ercit, T. S., Linnen, R. L., Samson, I. M., 2005. REE-enriched granitic pegmatites. Rare-element geochemistry and mineral deposits: Geological Association of Canada. GAC Short Course Notes. 17, 175-199.

Ertl, A., Schuster, R., Hughes, J.M., Ludwig, T. Meyer, H.-P., Finger, F., Dyar, M.D., Ruschel, K., Rossman, G.R., Klötzli, U., Brandstätter, F., Lengauer, Ch.L., Tillmanns, E., 2012. Li-bearing tourmalines in Variscan granitic pegmatites from the Moldanubian nappes, Lower Austria. European Journal of Mineralogy. 24, 695–715.

Göd, R., 1989. The spodumene deposit at “Weinebene”, Koralpe, Austria. Mineralium Deposita. 24(4), 270-278.

Henk, A., Franz, L., Teufel, S., Oncken, O., 1997. Magmatic underplating, extension, and crustal reequilibration: Insights from a cross-section through the Ivrea Zone and Strona-Ceneri Zone, northern Italy. The Journal of Geology. 105(3), 367-378.

Icenhower, J., London, D., 1995. An experimental study of element partitioning among biotite, muscovite, and coexisting peraluminous silicic melt at 200 MPa (H2O). American Mineralogist. 80(11-12), 1229-1251.

Kunz, B. E., Manzotti, P., von Niederhäusern, B., Engi, M., Darling, J. R., Giuntoli, F., Lanari, P., 2018. Permian high-temperature metamorphism in the Western Alps (NW Italy). International Journal of Earth Sciences. 107(1), 203-229.

London, D., 2008. Pegmatites, in: Canadian Mineralogist Special Publication 10, Mineralogical Association of Canada, Quebec. pp. 347.

London, D., 2018. Ore-forming processes within granitic pegmatites. Ore Geology Reviews. 101, 349-383.

Marschall, H. R., von Strandmann, P. A. P., Seitz, H. M., Elliott, T., Niu, Y., 2007. The lithium isotopic composition of orogenic eclogites and deep subducted slabs. Earth and Planetary Science Letters. 262(3-4), 563-580.

Qiu, L., Rudnick, R. L., McDonough, W. F., Bea, F., 2011. The behavior of lithium in amphibolite-to granulite-facies rocks of the Ivrea–Verbano Zone, NW Italy. Chemical Geology. 289(1-2), 76-85.

Schuster, R., Stüwe, K., 2008. Permian metamorphic event in the Alps. Geology. 36(8), 603-606.

Stewart, D. B. (1978). Petrogenesis of lithium-rich pegmatites. American Mineralogist. 63(9-10), 970-980.

Zack, T., Tomascak, P. B., Rudnick, R. L., Dalpé, C., McDonough, W. F., 2003. Extremely light Li in orogenic eclogites: the role of isotope fractionation during dehydration in subducted oceanic crust. Earth and Planetary Science Letters. 208 (3-4), 279-290.

## 7. INNOVATION AND APPLICATION POTENTIAL

The new model for the formation of deposits presented in this PhD thesis has the potential to trigger increased exploration efforts in areas that were previously ignored due to their geological conditions. The realization that certain metamorphic conditions can be of fundamental importance for the formation of lithium deposits opens up exploration opportunities, particularly in orogens such as the Alps and Pyrenees, where uplift and erosion have opened up corresponding rock units from prospective depths. This shows that basic geological research has the potential to develop innovative exploration models that have great application potential in the exploration of such deposits.

## 8. CONCLUSION

Our investigations in the Austroalpine Unit Pegmatite Province yield the following main conclusions (Chapter 3-4)

- Field observations show that both rock types occur in the same lithostratigraphic complexes always associated with simple pegmatites.
- The magmatic mineral assemblages consists of K-feldspar, quartz, plagioclase, muscovite, garnet and tourmaline and additional spodumene in the pegmatites. As accessories rare beryl, REE minerals (monazite, allanite, xenotime), apatite, zircon, uraninite as well as traces of Nb-Ta phases and cassiterite appear.
- They have a peraluminous, granitic composition, similar element distribution patterns and show continuous fractionation trends for trace elements including Be, Li, Rb, Cs, Sn, Ge, Ba and REE.
- Magmatic garnet is rich in Mn and Fe and the occurrence of tourmaline in the absence of biotite may be due to a low TiO2 content in the melts. The composition of tourmaline in spodumene pegmatites indicates that they crystallized from evolved melts. Trace elements (Rb, Li, Cs, Tl or Ba) in magmatic muscovite show similar fractionation trends with more fractionated signatures in the spodumene pegmatites.
- With respect to the trace elements in muscovite classification diagrams of Černý & Burt (1984) the leucogranites fall in the fields of less evolved muscovite-bearing and muscovite-barren pegmatites, whereas spodumene pegmatites barely reach fields of moderately evolved spodumene pegmatites.
- The ε(t)Nd of about –8 and initial 87Sr/86Sr ratios in the range of 0.7098–0.7353 indicate a crustal origin of the primary melts. 147Sm/144Nd ratios are lowest in tourmaline followed by whole rock powder, quartz+feldspar and finally garnet fractions. In garnet, the ratios are very high (up to 7.7), indicating high purity of the analyzed material.
- Our Sm-Nd garnet ages indicate that the investigated rocks intruded in Permian time at 255–280 Ma. This range fits within those reported for the simple pegmatites.
- The spodumene pegmatites from the Austroalpine Unit are inferred to have intruded at more than 10 km depth in country rocks at upper greenschist- to amphibolite-facies conditions.
- All these features taken together indicate a contemporaneous and cogenetic formation of spodumene pegmatites and leucogranites, whereby the spodumene pegmatites are more fractionated and occur in higher structural levels.
- Field observations of Permian crustal profiles over more than 400 km, together with geochronological and geochemical investigations indicate that the migmatite, simple pegmatite, leucogranite, evolved pegmatite and albite-spodumene pegmatite are contemporaneous and cogenetic. They are all associated to Permian lithospheric extension.
- The three pegmatite types and leucogranite derived from anatectic melt produced by melting of Al-rich metasediments at temperature conditions up to muscovite dehydration melting and below those of biotite dehydration melting.

- Melt segregation in the migmatite and extraction from it was most likely assisted by deformation. Melt ascent through the crust occurred over several km.
- Simple pegmatite, leucogranite, fractionated pegmatite and albite-spodumene pegmatite represent consecutive stages of crystallization of the anatectic melt, at progressively shallower crustal levels.
- Geochemical investigation indicates continuous fractional crystallization during melt ascent, accompanied by progressive enrichment of Li in the melt.
- The Li source for the albite-spodumene pegmatite was a Li-Al-rich metapelite with Li concentrations between 70-270 ppm Li, derived from a shale precursor.
- Staurolite is by far the Li-richest phase within the metapelite with concentrations between 367-2973 ppm Li. The Li concentration sequence in the analyzed samples is staurolite > biotite > muscovite > garnet.
- This fertile metasediment released significant amounts of Li while it experienced partial melting at upper amphibolite facies conditions for the first time.
- The mechanism of Li transfer from the metapelite into the anatectic melt is strongly controlled by the breakdown of staurolite in the presence of melt. This indicates that partial melting initiated in the range between 650-750°C and 0.6-0.8 GPa, i.e. 18-26 km depth.
- Efficient melt transfer yielded Li concentration in ascending melt comprised between 200 and 1000 ppm. This range is consistent with the composition of Li-rich large muscovite in migmatite.
- For modest concentrations of 200 to 500 ppm Li in the anatectic melt, a fractionation degree of 91 to 99% is needed to allow spodumene to crystallize in the residual melt. For 1000 ppm Li, the required fractionation degree ranges between 81% and 91%.
- Albite-spodumene pegmatite was emplaced as residual melt at upper greenschist facies conditions at 12-15 km depth.
- Our case study provides the basis of an anatectic model of Li-pegmatite and an alternative explanation for the formation of Li-pegmatite if no fertile parent granite can be identified.

# 9. DISSEMINATION RESULTS

## 9.1. PUBLICATIONS

Knoll, T., Schuster, R., Mali, H., Onuk, P., Huet, B., Horschinegg, M., Ertl, A. & Gister, G. (2018): Spodumene pegmatites and related leucogranites from the Austroalpine Unit (Eastern Alps): field relations, petrology, geochemistry and geochronology. – The Canadian Mineralogist.

Knoll, T., Schuster, R., Mali, H., & Huet, B. (2021). Die Genese der permischen Lithium-Pegmatite des Ostalpinen Kristallins. Berg-und hüttenmännische Monatshefte: BHM.

Schuster, R., Knoll, T., Mali, H., Huet, B., Griesmeier, G.E.U., 2019. Field trip guide: a profile from migmatites to spodumene pegmatites (Styria, Austria). Berichte der Geologischen Bundesanstalt.

Knoll, T., Huet, B., Schuster, R., Mali, H., Ntaflos, T., & Hauzenberger, C. (2023). Lithium pegmatite of anatectic origin-A case study from the Austroalpine Unit Pegmatite Province (Eastern European Alps): geological data and geochemical model. Ore geology reviews, 105298.

## 9.2. CONFERENCE CONTRIBUTIONS

Ilickovic, T., Schuster, R., Mali, H., Petrakakis, K. & Schedl, A. (2015). New sight on Li-rich Pegmatites within the Austroalpine unit (Eastern Alps) and their evidence for an anatectic origin. – Udruženje/Udruga Geologa U Bosni I Hercegovini, Zbornik Radova, Knjiga Sažetaka, 1 Kongres Geologa Bosne I Hercegovine sa Medunarodnim Učešćem, Tuzla, 21.-23.10.2015, 96.

Ilickovic, T., Schuster, R., Mali, H., Petrakakis, K., Schedl, A. & Horschinegg, M. (2016): Spodumene bearing pegmatites in the Austroalpine unit (Eastern Alps). New field observations and geochronological data. – Abstract Volume GeoTirol 2016, Annual Meeting DGGV 25.-28. September 2016 Innsbruck/Austria, 138.

Mali, H., Ilickovic, T., Schuster, R., Onuk, P., & Schedl, A. (2017). Verteilung der Spodumen-Pegmatite sowie differenzierter Pegmatite und Leukogranite im Ostalpinen Kristallin. – Arbeitstagung der Geologischen Bundesanstalt, Bad Ischl 19.–22. Juni 2017, 278-279, Geologischen Bundesanstalt (Wien).

Ilickovic, T., Schuster, R., Mali, H., Petrakakis, K., Schedl, A. & Horschinegg, M. (2017a): Genesis of spodumene bearing pegmatites in the Austroalpine unit (Eastern Alps): isotopic and geochemical investigations. – Arbeitstagung der Geologischen Bundesanstalt, Bad Ischl 19.–22. Juni 2017, 249-250, Geologischen Bundesanstalt (Wien).

Ilickovic, T., Schuster, R., Mali, H., Petrakakis, K. & Schedl, A. (2017b). Spodumene bearing pegmatites in the Austroalpine unit (Eastern Alps): Distribution and new geochronological data. – EGU General Assembly 2017, Geophysical Research Abstracts, 19: EGU2017-7235.

Ilickovic, T., Schuster, R., Mali, H., Onuk, P., & Horschinegg, M. (2017c). Genesis of spodumene bearing pegmatites in the Austroalpine unit (Eastern Alps): isotopic and geochemical investigations. – Peg17, Kristiansand, Norwegen 13-20. Juni 2017.

Ilickovic, T., Schuster, R., Mali, H., Huet, B. & Horschinegg, M. (2017d). Genesis of Permian pegmatites and spodumene bearing pegmatites during regional scale, high temperature/low pressure metamorphism in the Austroalpine unit. – Abstract Volume 2nd Emile Argand Conference on Alpine Geology 2017 Zlatibor, 47.

Schuster, R., Ilickovic, T., Mali, H., Huet, B. & Schedl, A. (2017a). Permian pegmatites and spodumene pegmatites in the Alps: Formation during regional scale high temperature/low pressure metamorphism. – Peg17, Kristiansand, Norwegen 13-20. Juni 2017.

Schuster, R., Ilickovic, T., Mali, H. (2017b). Unrevealing the internal structure of Austroalpine basement nappes by using the mineral compositions and fractionation trends of Permain pegmatites (Eastern Alps/Austria). – Abstract Volume 2nd Emile Argand Conference on Alpine Geology 2017 Zlatibor, 96.

Huet, B., Knoll, T., Schuster, R. & Paulick, H. (2018). Albite-spodumene pegmatites without large granite intrusions? Exploring the feasibility of the alternative anatectic model. – PANGEO 2018 Wien.

Knoll, T, Mali, H., Paulick, H., Schuster, R., Huet, B. & Horschinegg, M. (2018a). Metamorphic origin of spodumene pegmatites in the Eastern Alps (Central Europe). – Abstract Volume Resources for Future Generations, June 16-21, 2018 Vancouver, BC, Canada.

Knoll, T., Schuster, R., Huet, B., Mali, H. & Paulick, H. (2018b). Spodumene pegmatites, pegmatites and leucogranites from the Austroalpine Unit (Eastern Alps). – Abstract Volume XXI International Congress of the CBGA, Salzburg, Austria, September 10–13, 2018.

Knoll, T., Schuster, R., Mali, H., Huet, B., Horschinegg, M. & Paulick, H. (2018c). The relationship between spodumene pegmatites, pegmatites and leucogranites from the Austroalpine Unit (Eastern Alps). – PANGEO 2018 Wien.

Knoll, T., Huet, B., Schuster, R., Paulick, H. & Mali, H. (2020). An anatectic model for albite-spodumene pegmatites from the Austroalpine Unit (Eastern Alps). – GeoUtrecht, 25.08.2020, online.

Knoll, T., Schuster, R., Mali, H., Huet, B., Konzett, J., Melcher, F., Horvat, CH., Hollinger, CH., & Stockinger, V. (2020). Lithium Pegmatite in den Ostalpen. – MRI-Kolloquium, 5.-6.11.2020, online.

Huet, B., Knoll, T., Schuster, R. & Mali, H. (2021). Lithium pegmatite of anatectic origin: a petrological and geochemical model. – Mitteilungen der österreichischen Mineralogischen Gesellschaft, 167: 107.